

UNIVERSITY OF OKLAHOMA

GRADUATE COLLEGE

EFFECT OF POST-FILL PRESSURE AND NANOCCLAY ON VOID
MORPHOLOGY IN RESIN TRANSFER MOLDED COMPOSITES

A Dissertation

SUBMITTED TO THE GRADUATE FACULTY

in partial fulfillment of the requirements for the

degree of

DOCTOR OF PHILOSOPHY

By

YOUSSEF KHALID HAMIDI

Norman, Oklahoma

2004

UMI Number: 3148880



UMI Microform 3148880

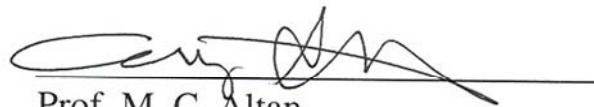
Copyright 2005 by ProQuest Information and Learning Company.
All rights reserved. This microform edition is protected against
unauthorized copying under Title 17, United States Code.

ProQuest Information and Learning Company
300 North Zeeb Road
P.O. Box 1346
Ann Arbor, MI 48106-1346

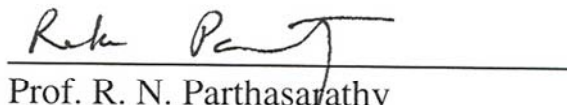
EFFECT OF POST-FILL PRESSURE AND NANOCCLAY ON VOID
MORPHOLOGY IN RESIN TRANSFER MOLDED COMPOSITES

A Dissertation APPROVED for the
SCHOOL OF AEROSPACE AND MECHANICAL ENGINEERING

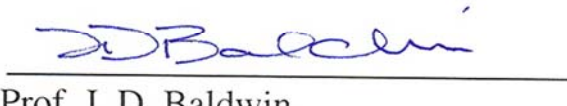
By



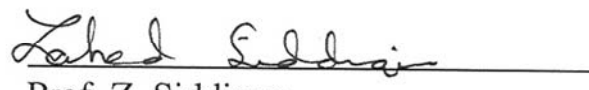
Prof. M. C. Altan



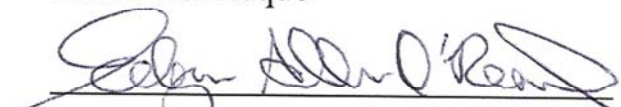
Prof. R. N. Parthasarathy



Prof. J. D. Baldwin



Prof. Z. Siddique



Prof. E. A. O'Rear

To the memory of my late Grandfather Moulay Cherif

To my Grandmother Lalla Khadija

To my Mother Lalla Fatima

To my Father Sidi Mohamed Bencherif

To my brothers Aziz and Y. Amin

And to my sisters Siham, Sana, and Asma

Thank you for being my Family

Youssef Khalid

Acknowledgments

Praise and gratitude to Almighty **Allah**, the **Creator** and the **Sustainer** of the worlds, the **Most Gracious**, the **Most Merciful**, the **Master of the Day of Judgment**. I would like to start by thanking **Allah Almighty** for all his blessings, bounties, and mercy. Thee do we worship and Thine aid we seek.

I would like to express my gratitude, appreciation, and admiration to my advisor, Dr. M. Cengiz Altan. I would also like to thank the other members of my committee, Dr. J. D. Baldwin, Dr. R. N. Parthasarathy, Dr. E. A. O'Rear, and Dr. Z. Siddique for their contributions and encouragements.

I would like to thank Dr. Harry J. Barraza for many useful ideas, and mostly for his friendship. I wish also to thank Levent Aktas, Dr. Kristian A. Olivero, and the rest of the Composites Research Laboratory at OU for their contribution.

A special debt of gratitude to my friends, especially Abdelhamid Hamidi Alaoui, Ibrahim Krabatou, M. Hafid Amini, Hicham Mansouri, Dr. Mohammed Eissa, and Salah Mahmoud, whose support and encouragements made my stay in Oklahoma easier.

This research has been further facilitated by the expertise of Mr. Billy Mays and Mr. Greg Williams at the AME machine shop. Their assistance has been very valuable.

Table of Contents

Title Page	i
Copyright Page.....	ii
Acknowledgments.....	v
Table of Contents.....	vi
List of Tables	ix
List of Figures.....	x
Abstract.....	xiii
1 Introduction.....	1
1.1 Polymer Composites	1
1.2 Materials.....	1
1.2.1 Thermoplastics	1
1.2.2 Thermosets	3
1.3 Manufacturing Methods	4
1.3.1 Wet Lay-Up.....	5
1.3.2 Filament Winding.....	6
1.3.3 Pultrusion.....	7
1.3.4 Molding Processes.....	8
1.3.4.1 Compression Molding	8
1.3.4.2 Autoclave Molding	10
1.3.4.3 Injection Molding	12
1.3.4.4 Liquid Composite Molding.....	13
1.4 Properties and Applications of Polymer Composites	14
1.4.1 Mechanical Properties	14
1.4.2 Electrical and Thermal Conductivity.....	15
1.4.3 Gas Diffusion and Fire Retardency	16
1.5 Defects in Polymer Composites	16
1.5.1 Defects Induced During Fabrication of Composites.....	17
1.5.1.1 Micro Voids and Dry Spots	17
1.5.1.2 Wrinkling.....	19
1.5.1.3 Defects in injection molding.....	19
1.5.2 Defects Induced During Service Life of Composites	20
1.5.2.1 Matrix Cracks and Fiber Fractures	20
1.5.2.2 Delamination	21
1.6 References.....	22
2 Preform Wetting and Void Formation in RTM Composites	25
2.1 Preform Types Used in RTM	25
2.2 Mold Filling in RTM.....	26
2.3 Void Formation and Removal in RTM	28
2.3.1 Experimental Studies on Void Formation	28
2.3.2 Theoretical and Numerical Models for Void Formation	30
2.3.3 Void Removal Studies.....	31
2.4 Fiber Wetting in RTM.....	33
2.4.1 Equilibrium Contact Angle.....	33
2.4.2 Dynamic Contact Angle	35
2.4.3 Capillary pressure.....	37
2.5 Contact Angle and Surface Tension Measurements.....	38
2.5.1 Contact Angle Measurement	38
2.5.1.1 Sessile Drop Technique	38
2.5.1.2 Wilhelmy Technique	40
2.5.1.3 Oscillating Jet Method.....	41
2.5.2 Surface Tension Measurement	41

2.5.2.1	Capillary Rise Method	41
2.5.2.2	Ring Method	42
2.5.2.3	Drop Volume and Drop Weight Method	43
2.5.2.4	Wilhelmy Technique	43
2.6	Void Content Measurement Techniques	44
2.6.1	Density Measurement Technique	44
2.6.2	Water Absorption	45
2.6.3	Ultrasonic C-Scan	45
2.6.4	Radiography	46
2.6.5	Microscopic Image Analysis	46
2.7	References	48
3	Voidage Reduction in Resin Transfer Molded Composites	52
3.1	Abstract	52
3.2	Introduction	53
3.3	Experimental Studies	62
3.3.1	Procedure for Composite Fabrication	62
3.3.2	Transient and Packing Pressure Measurements	65
3.3.3	Modified Capillary Number Determination	66
3.3.4	Voids Characterization	69
3.4	Results and Discussion	73
3.4.1	Transient Inlet Pressure	73
3.4.2	Effect of Injection Rate on Void Content of Resin Transfer Molded Disks	77
3.4.3	Effect of Post-Fill Pressure on Void content	85
3.4.4	Effect of Post-Fill Pressure on Void Size Distribution	87
3.5	Conclusions	90
3.6	References	92
4	Through-The-Thickness Morphological Void Distribution of the RTM composite Molded at Zero Packing Pressure	95
4.1	Abstract	95
4.2	Introduction	96
4.3	Experimental Studies	100
4.3.1	Procedure for Composite Manufacturing	100
4.3.2	Capillary Number Determination	103
4.3.3	Void Characterization	104
4.4	Results and Discussion	106
4.4.1	Location of Voids and Average Void Content	106
4.4.2	Variation of Void Content Through-The-Thickness	110
4.4.3	Variation of Void Size	112
4.4.4	Variation of Void Shape	117
4.5	Concluding Remarks	124
4.6	References	125
5	Three-Dimensional Features of Void Morphology in Resin Transfer Molded Composites	127
5.1	Abstract	127
5.2	Introduction	128
5.3	Experimental Setup	135
5.3.1	Molding Procedure	135
5.3.2	Transient Filling Pressure Measurement	138
5.3.3	Capillary Number Determination	139
5.3.4	Void Characterization	140
5.4	Results and Discussion	146
5.4.1	Inlet Filling Pressure	146
5.4.2	Average Void Content	148
5.4.3	Location of Voids	151
5.4.4	Variation of Void Size	156

5.4.5	Variation in Void Shape	162
5.4.6	Voidage Variation Along the Radius of the Molded Disk	168
5.5	Conclusions	182
5.6	References	183
6	Effect of Packing on Void Morphology in Resin Transfer Molded E-Glass/Epoxy Composites	187
6.1	Abstract	187
6.2	Introduction	188
6.3	Experimental Setup	193
6.3.1	Molding Procedure	193
6.3.2	Sample Preparation for Microscopic Image Analysis	194
6.3.3	Void Characterization	196
6.4	Results and Discussion	196
6.4.1	Inlet Mold Filling Pressure	196
6.4.2	Assessment of Void Removal	199
6.4.3	Effect of Packing on Void Location	203
6.4.4	Effect of Packing on Void Size	206
6.4.5	Effect of Packing on Void Shape	212
6.4.6	Effect of Packing on Radial Voidage Variation	220
6.5	Conclusions	226
6.6	References	227
7	Effect of Nanoclay Content on Void Morphology in Resin Transfer Molded Composites	231
7.1	Abstract	231
7.2	Introduction	232
7.3	Experimental	237
7.3.1	Materials	237
7.3.2	Preparation of the Clay-Epoxy Mixtures	237
7.3.3	Molding Procedure	238
7.3.4	Microscopic Image Analysis	239
7.4	Results and Discussion	240
7.4.1	Effect of Nanoclay Content on Mold Filling Parameters	240
7.4.2	Effect of Nanoclay Content on Void Occurrence	244
7.4.3	Effect of Nanoclay Content on Void Location	247
7.4.4	Effect of Nanoclay Content on Void Size	251
7.4.5	Effect of Nanoclay Content on Void Shape	255
7.4.6	Effect of Nanoclay Content on Radial Voidage Variation	259
7.5	Conclusions	264
7.6	References	265
8	Conclusions and Recommendations	269

List of Tables

Table 3.1: Physicochemical and flow parameters for low- and high-speed RTM processing of composites containing 17.5% by volume of randomly-oriented, E-glass fibers.	82
Table 5.1: Variation in voidage through-the-thickness of the composite disk molded without post-fill pressure at 17.5% fiber content.	150
Table 5.2: Modified capillary number variation along the radial flow direction.	155
Table 6.1: Effect of applying a 570 kPa post-fill pressure on shape ratio distribution for the overall composite and for transition voids.	219

List of Figures

Figure 1.1: Common thermoplastic resins used as the matrix phase in polymer composites.....	2
Figure 1.2: Typical wet lay-up operation.	5
Figure 1.3: Typical filament winding process schematic.	6
Figure 1.4: Schematic of pultrusion process.	8
Figure 1.5: Schematic of compression molding.	9
Figure 1.6: Example of a small autoclave.....	10
Figure 1.7: Temperature profile utilized during autoclave curing of 24 plies of AS4/3501-6 graphite/epoxy prepregs.	11
Figure 1.8: Schematic of Injection Molding.....	12
Figure 1.9: Typical resin transfer molding process.....	13
Figure 1.10: Geometries for testing stress-strain of composites.....	15
Figure 1.11: Representative microscopic images of voids obtained from a glass/epoxy RTM composite.....	17
Figure 1.12: SEM micrographs of failed surfaces of an E-glass/epoxy composite [27].	21
Figure 2.1: Three-phase equilibrium contact angle.....	34
Figure 2.2: Schematic of image analysis setup for contact angle measurement using the sessile drop technique.	39
Figure 2.3: Concept of the Wilhelmy technique for measuring advancing and receding contact angles.	40
Figure 3.1: Experimental molding setup used to manufacture RTM composite disks.	63
Figure 3.2: Representative micrographs from composites molded with different post-fill pressure specimens at 200x magnification. (a) Circular voids of different shapes located in matrix-rich area; (b) Ellipsoidal void in the inter-tow space; (c) Irregular void engulfing a tow of fibers; (d) Example of high voidage area in composites molded without a post-fill pressure.....	72
Figure 3.3: Advancing fluid front superficial velocity at different radial positions inside the mold cavity preloaded with 17.5% E-glass fibers by volume.....	74
Figure 3.4: (a) Inlet pressure profiles during mold filling of composite disks; (b) Close-up of air vent region of the mold.....	76
Figure 3.5: Effect of injection velocity on void formation in RTM composites. Data for model fluids taken from Rohatgi et al. [34]: □ Silicone oil; Δ DOP oil; ○ Ethylene glycol.....	80
Figure 3.6: Effect of capillary number on void formation in RTM composites. Data for model fluids taken from Rohatgi et al. [34]: □ Silicone oil, macro-voids; ■ Silicone oil, micro-voids; Δ DOP oil, macro-voids; ▲ DOP oil, micro-voids; ○ Ethylene glycol, macro-voids; ● Ethylene glycol, micro-voids.....	83
Figure 3.7: Void content reduction due to different post-fill pressures applied to RTM composites molded with different fiber contents at different fill velocities.....	86
Figure 3.8: Void size distributions for RTM composites containing 17.5% fibers by volume molded at different post-fill pressures.....	89
Figure 4.1: Experimental molding apparatus used to fabricate RTM composite disks.....	101
Figure 4.2: Representative microscopic images obtained at 200 x magnifications from the RTM composite molded without post-fill pressure at 17.5% fiber content depicting examples of voids from different zones: (a) typical composite cross-section with different fiber orientations; (b) two matrix voids; (c) five preform voids; (d) one transition void.....	107
Figure 4.3: Void content contributions of different locations (void zones) within the composite disk molded without post-fill pressure at 17.5% fiber content.....	109
Figure 4.4: Variation in void content through-the-thickness of the composite disk molded without post-fill pressure at 17.5% fiber content.	111
Figure 4.5: Void size distributions based on equivalent diameter at the surface (next to mold walls) and inner layers of the RTM composite molded without post-fill pressure at 17.5% fiber content.	114
Figure 4.6: Representative microscopic images obtained at 200 x magnifications from the RTM composite molded without post-fill pressure at 17.5% fiber content depicting voids with different sizes: (a) example of a large void adjacent to a fiber bundle; (b) two small and a barely	

medium void (from top to bottom); (c) a medium void; (d) voids from different size categories.	116
Figure 4.7: Size distributions of voids from different locations (void zones) within the composite disk molded without post-fill pressure at 17.5% fiber content.....	118
Figure 4.8: Void content contributions of voids with different shapes encountered in the RTM composite molded without post-fill pressure at 17.5% fiber content.....	120
Figure 4.9: Size distribution of voids with different shapes encountered in the RTM composite molded without post-fill pressure at 17.5% fiber content.....	122
Figure 5.1: Experimental molding setup used to manufacture the RTM composite disk.....	137
Figure 5.2: Spatial arrangement of investigated samples of the RTM composite molded without post-fill pressure at 17.5% fiber content: (a) location of samples within the composite disk, (b) First sample partitioned into five 15 mm-long radial regions for planar void analysis, (c) Second sample partitioned into five 8 mm-radial regions and eight through-the-thickness layers.....	144
Figure 5.3: Inlet pressure profile during mold filling of the composite disk molded without post-fill pressure at 17.5% fiber content.	147
Figure 5.4: Representative microscopic images obtained at 50x magnification from through-the-thickness (left column) and planar (right column) views of the RTM composite molded without post-fill pressure at 17.5% fiber content.	149
Figure 5.5: Representative microscopic images obtained at 200x magnification from the RTM composite molded without post-fill pressure at 17.5% fiber content depicting examples of voids from different zones: (a) typical composite cross-section with different fiber orientations and two <i>transition voids</i> ; (b) examples of <i>transition</i> and <i>matrix voids</i> ; (c) three <i>transition voids</i> and two <i>preform voids</i> ; (d) three <i>preform void</i>	152
Figure 5.6: Planar and through-the-thickness void content contributions of voids located at different locations of the composite molded without post-fill pressure at 17.5% fiber content.	154
Figure 5.7: Planar and through-the-thickness size distributions based on equivalent diameter of voids encountered in the RTM composite molded without post-fill pressure at 17.5% fiber content.	157
Figure 5.8: Representative microscopic images obtained at 200x magnifications from the through-the-thickness view (left column), and planar view (right column) samples of the RTM composite molded without post-fill pressure at 17.5% fiber content.....	159
Figure 5.9: Size distribution of voids obtained from planar and through-the-thickness views of the RTM composite molded without post-fill pressure at 17.5% fiber content when: (a) considering the whole composite; (b) considering only <i>preform voids</i>	161
Figure 5.10: Planar and through-the-thickness areal void density distributions for different void shapes encountered in the RTM composite molded without post-fill pressure at 17.5% fiber content.	165
Figure 5.11: Average planar and through-the-thickness size distributions of voids with different shapes encountered in the RTM composite molded without post-fill pressure at 17.5% fiber content.	167
Figure 5.12: Planar and through-the-thickness radial distributions of void content within the RTM composite molded without post-fill pressure at 17.5% fiber content.....	171
Figure 5.13: Through-the-thickness radial voidage distribution for different void locations in the RTM composite molded without post-fill pressure at 17.5% fiber content.	172
Figure 5.14: Planar <i>preform void</i> size distribution along the flow direction in the RTM composite molded without post-fill pressure at 17.5% fiber content.....	175
Figure 5.15: Planar <i>preform void</i> content and void areal density variation along the flow direction in the RTM composite molded without post-fill pressure at 17.5% fiber content.	176
Figure 5.16: Areal density of different-sized mobile voids (i.e., combined matrix and transition) along the flow direction based on through-the-thickness view of the RTM composite molded without post-fill pressure at 17.5% fiber content.	178
Figure 5.17: Irregular void size distribution along the flow direction, determined from through-the-thickness view of the RTM composite molded without post-fill pressure at 17.5% fiber content.	181
Figure 6.1: Spatial arrangement of investigated samples for both packed and unpacked composite disks: (a) sample locations within the composite disk, (b) Planar sample partitions of five 15	

mm-long radial regions, (c) Through-the-thickness sample partitions of five 15 mm-long radial regions.	195
Figure 6.2: Inlet pressure profiles during mold filling of the unpacked and packed composite disks containing 17.5% fiber content by volume.	198
Figure 6.3: Representative image of voids in different composite locations obtained at 200x magnification from through-the-thickness (left column) and planar (right column) views of the unpacked (top row) and packed (bottom row) composite disks.	200
Figure 6.4: Through-the-thickness and planar void contents and void areal densities for the unpacked and packed composite parts.	202
Figure 6.5: Contributions from voids in different locations within the composite disks to the void contents of unpacked and packed parts viewed from: (a) the planar view, and (b) the through-the-thickness view.	205
Figure 6.6: Void size distributions for the unpacked and packed composite disks from: (a) the planar view; and (b) the through-the-thickness view.	208
Figure 6.7: (a) Planar and (b) through-the-thickness size distributions of voids observed in different locations in the unpacked and packed composite disks.	210
Figure 6.8: Representative image of voids with different shapes obtained at 200x magnification from through-the-thickness (left column) and planar (right column) views of the unpacked composite disk molded without post-fill pressure at 17.5% fiber content.	213
Figure 6.9: (a) Planar and (b) through-the-thickness void shape distributions for the unpacked and packed composite disks.	216
Figure 6.10: Through-the-thickness and planar size distributions of irregular voids obtained from the unpacked and packed composite disks.	218
Figure 6.11: Radial variation of void content in the unpacked and packed composite disks: (a) obtained from the planar surface, and (b) obtained from the through-the-thickness surface.	221
Figure 6.12: Through-the-thickness radial variation of <i>conformity parameter</i> from average void content reduction rates due to the application of 570 kPa post-fill pressure.	223
Figure 7.1: Spatial arrangement of nanocomposite samples into five radial regions for microscopic analysis.	239
Figure 7.2: Effect of nanoclay volume fraction on the viscosity of the clay-epoxy mixture. Epoxy viscosity, $\mu_0 = 0.65$ Pa·s.	243
Figure 7.3: (a) A representative microscopic image obtained at 50x from the composite molded without nanoclay at 13.6% fiber content by volume; and representative SEM images obtained at 50x from nanocomposites with (b) 2, (c) 5, and (d) 10% nanoclay content by weight.	246
Figure 7.4: Void contents and void areal densities of composites with different clay contents molded with 13.6% volume fraction of E-glass fibers.	249
Figure 7.5: Contributions from voids encountered at different locations to overall voidage in nanocomposites with different clay contents: (a) void content, (b) void areal density.	250
Figure 7.6: Void size distributions for the composites containing different nanoclay contents molded with 13.6% volume fraction of E-glass fibers.	253
Figure 7.7: Effect of nanoclay content on average void sizes and on their respective standard deviation for voids encountered in different location of all nanocomposites molded with 13.6% volume fraction of E-glass fibers.	254
Figure 7.8: Representative images obtained at 200x magnification of different voids encountered within the composite molded with 13.6% volume fraction of E-glass fibers and containing: (a): 0%; (b): 2%; (c): 5%, and (d): 10% nanoclay by weight.	256
Figure 7.9: Contributions to void content from voids with different shapes as a function of nanoclay content.	258
Figure 7.10: Radial variation of void content in the composites molded with 13.6% volume fraction of E-glass fibers and containing 0, 2, 5, and 10% nanoclay.	261
Figure 7.11: Radial variation of preform void content in the composites molded with 13.6% volume fraction of E-glass fibers and containing 0, 2, 5, and 10% nanoclay.	263

Abstract

Resin transfer molded (RTM) composites usually suffer from the formation of flow-induced defects such as voids. Detrimental effects of voids on performance of molded parts have been studied extensively. Yet, knowledge of effective void removal strategies, along with detailed morphological void distribution within molded composites is very limited. In this investigation, effects of post-fill pressure on void content is investigated for random-mat, E-glass/epoxy RTM disks. Measured void contents agree well with results obtained in other studies for similar ranges of modified capillary number values. Packing helped significantly reduce void contents in RTM parts. In addition, voids are found to concentrate primarily within or adjacent to the fibers. Three-dimensional features of the formed voids are included in more detailed analyses of morphology variations of voids within the composite from both through-the-thickness and planar surfaces.

Effects of applying a packing pressure on void morphology are investigated for similar composites. Packing pressures of zero and 570 kPa are applied and voidage is evaluated from both through-the-thickness and planar views. The packed composite is found to contain almost 92% less void content than the unpacked composite, accompanied by a 40% drop in average void size. Along the flow direction, removal of voids seems to depend on their arrangement at the end of the filling stage.

Finally, effect of nanoclay content on void morphology in RTM nanoclay/E-glass/epoxy composites are investigated. Cloisite[®]25A nanoclay loads of 0, 2, 5, and 10 wt% are mixed with a low-viscosity epoxy resin prior to filling. Void occurrence is observed to

increase considerably with increasing nanoclay content from 2.1% in the composite without nanoclay to 5.1 and 8.3% in 5%- and 10%-nanocomposites, respectively. However, the composite with 2 wt% nanoclay yields the lowest void content of 0.7%. Voids are observed to be smaller after the addition of nanoclay at all concentrations.

1 Introduction*

1.1 *Polymer Composites*

Polymer composites are mixtures of a polymer, which is the major or continuous phase, and a filler, which can be either metal, ceramic, or even another polymer. Both thermosetting and thermoplastic resins can be used as the polymer phase; the former has the advantage of low viscosity while the latter has the advantage of the possibility of recycling and reuse. Essentially all commercially important polymers have applications where the polymer is filled, although certainly some materials are more commonly filled than others. Typically, the reason that a particular polymer is a good or bad candidate for use as the continuous phase of a composite is its ability to form strong interactions with a particular filler. Composites are a fast growing segment of the polymer industry; composites filled with materials having at least one dimension in the nanometer-size range such as nanoclays or nanotubes represent a step change in technology in the composites area. This chapter is an introduction to this rather diverse field. For more information, please refer to one of the excellent monographs on the subject [1-3].

1.2 *Materials*

1.2.1 *Thermoplastics*

Global worldwide production of thermoplastics is approximately 200 billion pounds per year, or approximately 25 pounds for every person on the planet. Only a small fraction of this amount is filled and used as a composite, but a small fraction of this large number

* Material in this chapter is published in: Encyclopedia of Chemical Processing, Decker Publisher, 2004.

is still a significant amount of material. By far the most important thermoplastic composites are made from flexible thermoplastics, i.e. semicrystalline materials with a glass transition temperature below room temperature. One significant exception to this generalization is polycarbonate; however these glassy materials are, for a glass, flexible at room temperature. The purpose of adding fillers in these flexible materials is to add stiffness, while the cost is typically a reduction in flexibility. Glassy polymers typically do not need more stiffness, while many applications require more stiffness from a flexible material. High-density polyethylene and polypropylene, shown in Fig. 1.1, are used very commonly in polymer composites.

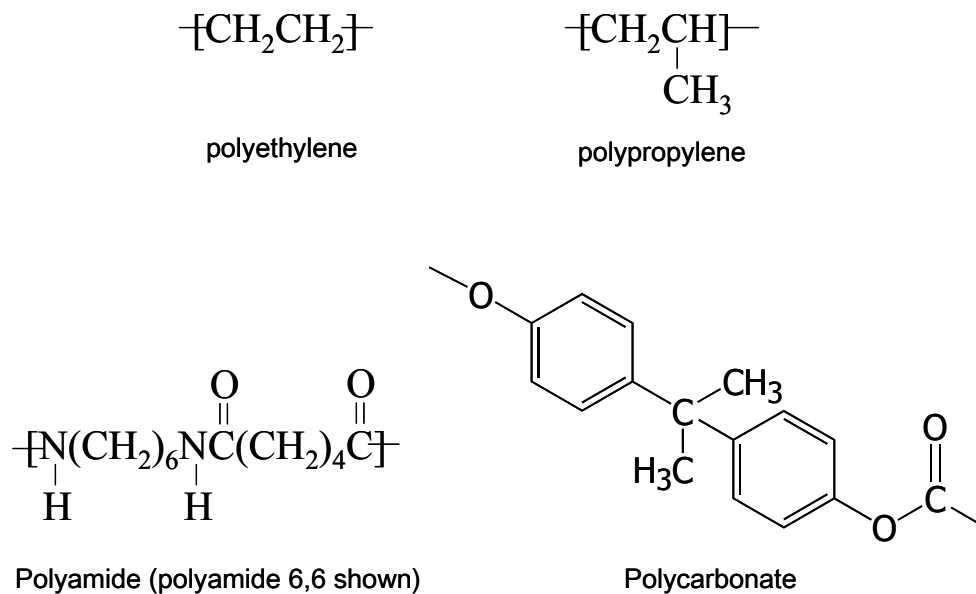


Figure 1.1: Common thermoplastic resins used as the matrix phase in polymer composites.

These materials are commonly mixed with low-cost fillers such as wood, clay, or glass. The decrease in flexibility and toughness caused by the introduction of fillers is large because the adhesion between these materials and the fillers is typically poor. The filler

can be coated with a thin layer to improve the filler-polymer interaction; however, this coating carries a significant cost. The cost of the composite, in the absence of a coating, can be significantly lower than the cost of the neat resin, which explains the popularity of these polymer composites. Good adhesion between relatively polar polymers and polar fillers yields higher performance composites. The most common polar filler is glass; while both polyamides (various types) and polycarbonate, shown in Fig. 1.1, are commonly used as polar thermoplastic resins.

1.2.2 Thermosets

Unlike thermoplastics that are simply melted, thermoset resins chemically react from low viscosity liquids to form solid materials during processing, a process called curing. Structurally, thermosets differ from thermoplastics because of the presence of crosslinks in the former, which means that thermosets cannot be reshaped or recycled once the chemical reaction occurs. One advantage of thermosets over thermoplastics is that wetting the filler becomes much easier with a low viscosity material. By far the most common thermoset composite is automobile tires, which consists of a polymer made from styrene and butadiene monomers and a carbon-black filler. The actual recipe used is much more complicated, and can include other monomers or polymers, as well as other fillers. In the absence of filler, the cured resin is rubbery at room temperature, which makes tires a unique thermosetting composite since most thermosetting composites are made with resins that are stiff at room temperature.

Other types of resins commonly used as thermosets include epoxies, polyesters, and vinyl esters. Unlike thermoplastics, these categories are a bit misleading in the sense that

various structures are classified under one heading. For example, approximately ten different molecules with the epoxy functionality are important commercial products, and each has slightly different mechanical properties and/or environmental stability. The two monomers that typically combine to form an epoxy resin are an epoxide and an amine. Polyesters are made with polyester resins containing unsaturation, and styrene. The structure of the polyester and the styrene (or other co-monomer content) is varied in these systems. Finally, vinyl ester is a term used to describe bifunctional monomers with long organic structures between acrylic end groups.

1.3 *Manufacturing Methods*

The performance of a composite part not only depends on the materials selected, but also the process parameters used during manufacturing. Properties of the polymer matrix, quality of fiber-matrix adhesion, as well as composite microstructure and defects are a function of manufacturing. Various processes for manufacturing commercial composite parts have been developed during the last 50 years. While the aerospace, marine, and defense industries usually require manufacturing methods yielding high-performance composites, automotive and consumer goods industries focus on cost-effective, high-volume production methods. The type of manufacturing method also depends largely on whether the starting material is a low viscosity uncured thermoset or a high viscosity thermoplastic. This section briefly outlines the different composite manufacturing methods currently used in the composites industry.

1.3.1 Wet Lay-Up

Wet lay-up consists of placing a layer of dry reinforcement inside a mold and then applying an uncured, low viscosity thermoset resin as shown in Fig. 1.2. Woven glass fibers are the prevalent reinforcing preform utilized in lay-up processes, although carbon and aramid fibers are also used to a lesser extent [3-5]. Typical fiber volume fraction of composites manufactured via wet lay-up range between 30 and 50%. The resin can be poured, sprayed, or brushed on top of the preform layer either by hand or by machine. The fiber preform layer is rolled on or pressed after the application of resin to evenly distribute the resin and remove air pockets. Resin is applied on top after each layer of fiber mats is properly placed. This process is repeated until the desired thickness is reached. To provide a smooth surface finish on the mold side, a thin layer of mold release is often applied prior to starting the lay-up. Thereafter, pressure and heat are applied to allow the composite to cure. Pressure can be applied either mechanically or pneumatically; for more details on the molding processes, see section 1.3.4.

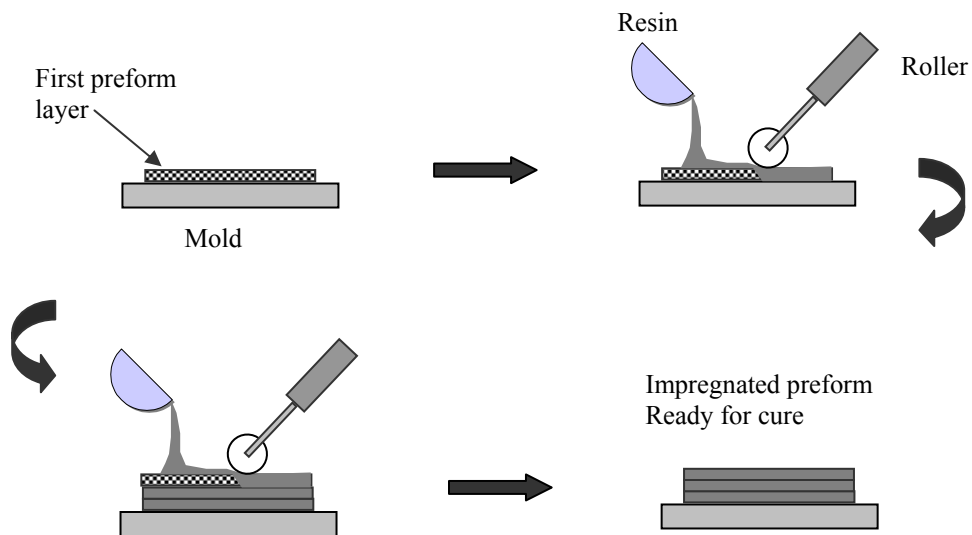


Figure 1.2: Typical wet lay-up operation.

The material may not be cured to a final product; in some cases the material is partially cured to yield a product that is still soft, but the resin has enough viscosity to not drip out of the material. This material is termed prepreg, and the prepreg can be shipped from one location to another where it is then formed and made into a final product.

1.3.2 Filament Winding

In the filament winding process, a continuous tape of polymer-impregnated fibers is wrapped over a rotating mandrel to form a composite part. Preform tapes can be either in pre-impregnated or impregnated in a thermoset resin bath right before winding. Successive layers are added at the same or different winding angles until the desired thickness is reached. The schematic of a typical filament winding process is shown in Fig. 1.3.

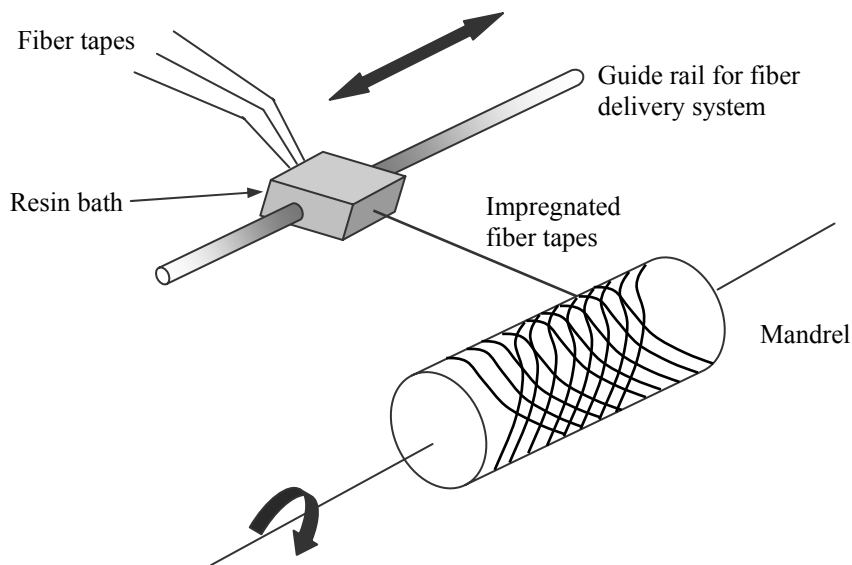


Figure 1.3: Typical filament winding process schematic.

Most winding machines operate similar to a lathe; the mandrel is mounted horizontally and rotates at a constant speed while the carriage delivering the fibers moves along the

length of the composite part. Typical winding speeds range between 50 and 100 m/min. After the winding is complete, the composite part is allowed to cure either at room temperature, in an oven, or inside an autoclave. Steel and aluminum mandrels are usually used to facilitate the removal of the fabricated composite part after cure. However, inflatable and collapsible metal mandrels are also used in closed-end products.

Parts with diameters as small as 25 mm and as large as 6 meters are made by filament winding. In addition, a variety of fiber orientations can be achieved, leading to more control of design properties of the fabricated composites. Continuous fibers of glass, carbon, and aramid are used in filament winding while glass/polyester systems are more widely used because of their lower cost. The filament winding process can be automated yielding cost-effective, high-volume production. Most shapes fabricated by this technique are axisymmetric and include glass-fiber pipes, pressure vessels, rocket motor cases, sailboard masts and other similar products.

1.3.3 Pultrusion

Pultrusion is a low-cost, high-volume process used to manufacture long, constant cross-section shapes from thermoset resins, and consists of pulling continuous dry fibers through a resin bath as shown in Fig. 1.4. Thereafter, impregnated fibers are pulled through a heated die for cure. The cross-section of the die dictates the final shape of the product. The length and temperature of the die are determined by the pulling speed, the dimensions of the part, and the curing characteristics of the resin. At the exit of the heated die, the composite cools rapidly and 2 to 3% volumetric shrinkage is observed.

The composite is continuously produced and a moving saw can be used to cut the part at the desired length without stopping the production.

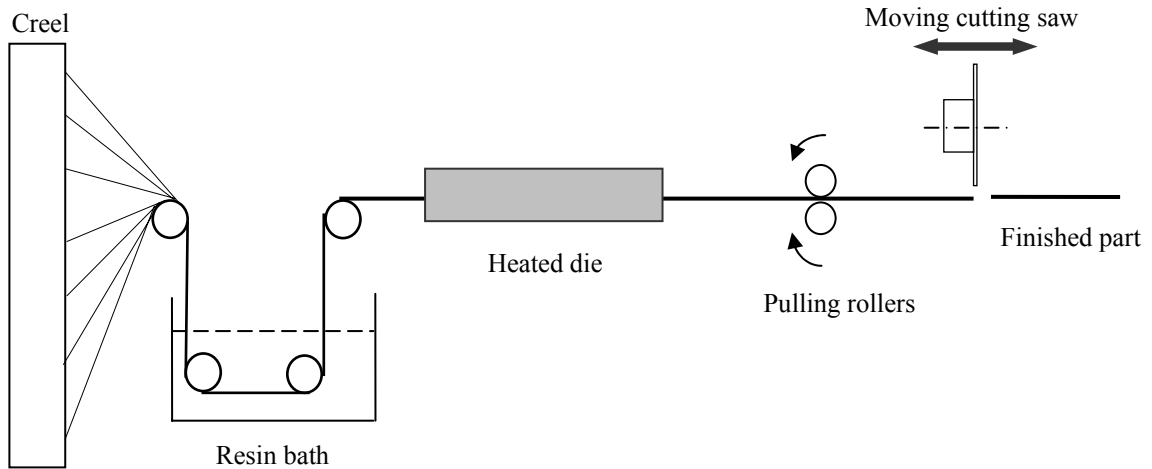


Figure 1.4: Schematic of pultrusion process.

Glass, carbon, and aramid fibers are used as unidirectional or fabric mat reinforcements, with E-glass/polyester being the most commonly used system [3,6]. The limitation of pultrusion is that only constant cross-section parts can be fabricated. However, a variety of hollow and solid profiles of any length can be manufactured.

1.3.4 Molding Processes

1.3.4.1 Compression Molding

Compression molding consists of placing a pre-determined amount of composite inside matching male and female metal molds. The mold walls are then heated, closed and pressurized mechanically until the composite deforms into the desired shape. After the charge fills the mold cavity, the pressure is released and the molded part is ejected from the mold. A schematic of this process is presented in Fig. 1.5.

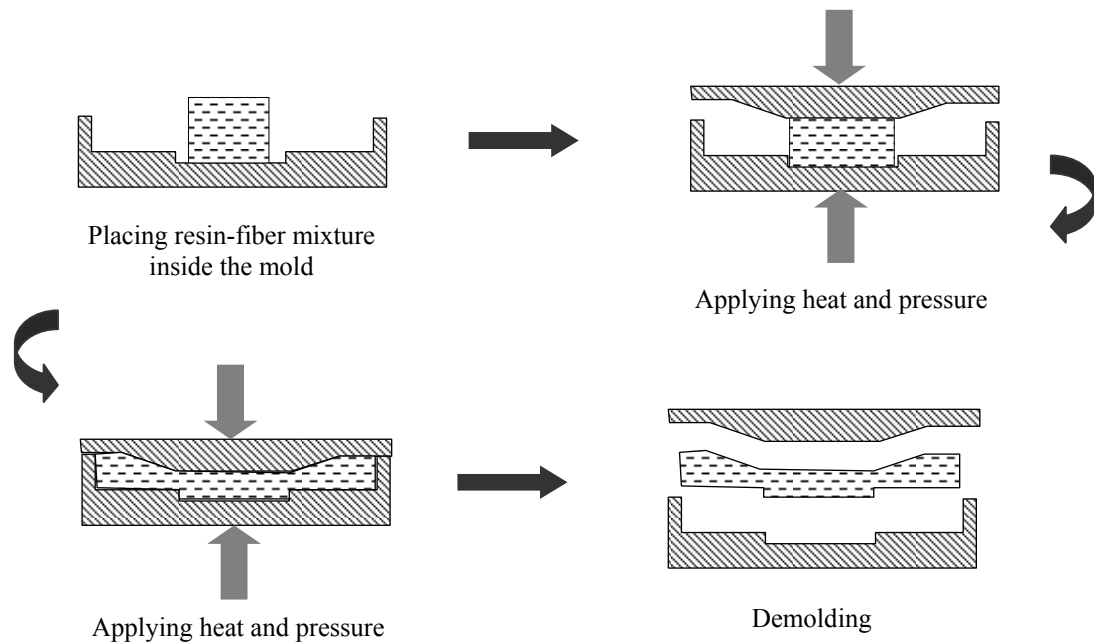


Figure 1.5: Schematic of compression molding.

Discontinuous fibers are commonly used in compression molding with fiber contents often limited at 30% in order to maximize the surface quality of the final product while achieving complete filling of the mold cavity [6-7]. Sheet molding compound (SMC) and bulk molding compound (BMC) are the most commonly used materials in compression molding. SMC is obtained by mixing chopped fibers, liquid resin, and fillers into a 2 to 5 mm-thick sheet product. A typical SMC compound contains glass fibers, polyester resin, and calcium carbonate [3,6]. Compression molding is also used for thermoplastics; however injection molding is preferred unless mats are used. Compression molding usually requires a large initial investment and produces semi-structural parts. The simplicity of the process minimizes part set-up time, reduces secondary finishing, and allows high-volume production with a low scrap rate.

1.3.4.2 Autoclave Molding

Instead of using mechanical force to pressurize a composite and force consolidation and/or shape, air pressure can be used if a low viscosity thermoset is used as the resin. An autoclave is a large pressure vessel that allows the simultaneous application of heat and pressure during the manufacture of thermosetting composite laminates. Internal work space of commercial autoclaves can be as large as 10 meters in diameter and 30 meters in length. Figure 1.6 depicts a small autoclave with a 90 cm-diameter internal work space.



Figure 1.6: Example of a small autoclave.

Typically, prepreg layers are cut to the desired shape and stacked in predefined orientations. Thereafter, the stacked prepreps are placed on a mold die and covered with a vacuum bag sealed at the edges. A vacuum is usually drawn before an external pressure of the order of 0.1 to 0.7 MPa is applied to the vacuum bag inside autoclave. Simultaneously, the desired temperature profile is applied to ensure the complete cure of the composite part. An example of a temperature profile applied for 24 plies of AS4/3501-6 graphite/epoxy prepreps is depicted in Fig.1.7.

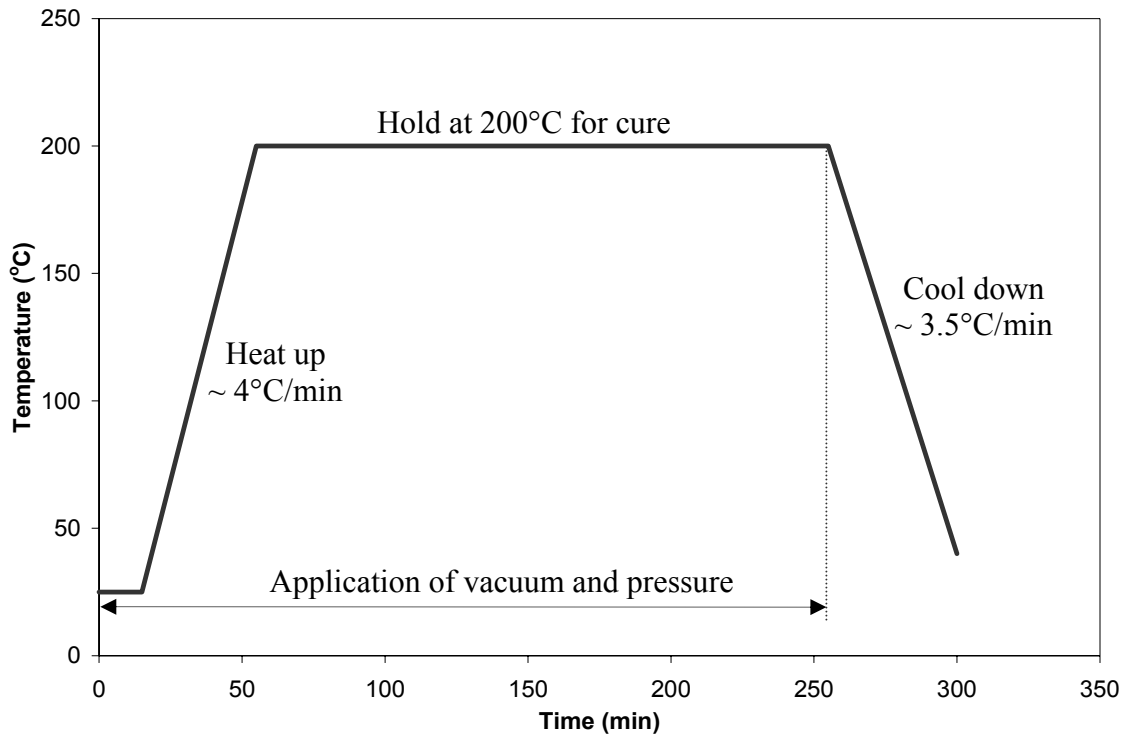


Figure 1.7: Temperature profile utilized during autoclave curing of 24 plies of AS4/3501-6 graphite/epoxy prepregs.

During most curing processes, an internal autoclave fan circulates the air inside ensuring uniform temperatures aided by convective heating. The external pressure and vacuum inside the bag create sufficient pressure differential to facilitate consolidation of the laminate and ensure good bonding between layers. During cure, the excess resin is absorbed by a bleeder placed above the prepregs within the vacuum bag. The application of vacuum also helps remove volatiles and excess air. Although autoclave processing requires high initial and operating costs, high-performance composites suitable for aerospace and similar structural applications are typically produced using this technique.

1.3.4.3 Injection Molding

Injection molding is a high-volume, low-cost manufacturing process for thermoplastics, including thermoplastic composites, and is shown schematically in Fig. 1.8.

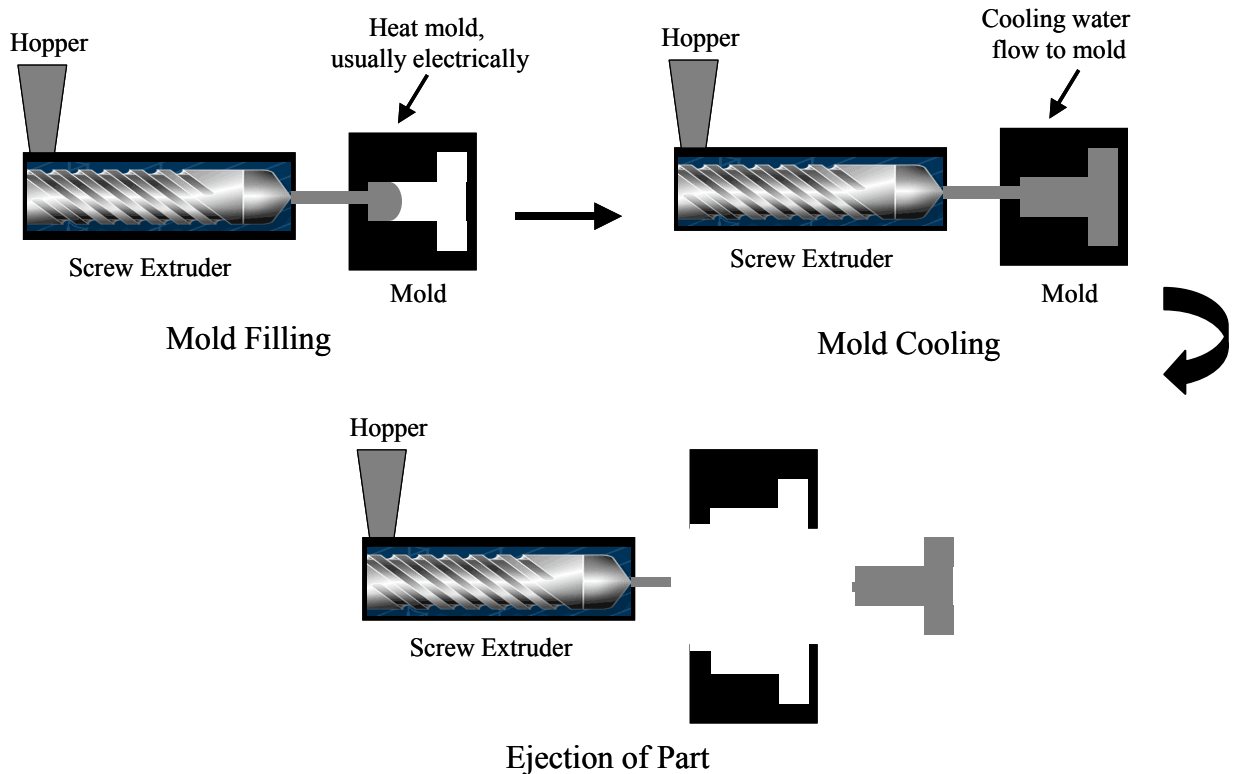


Figure 1.8: Schematic of Injection Molding

Mixing of discontinuous fillers with a thermoplastic is the first step; this mixing typically occurs in a twin-screw extruder and the material is extruded and chopped into pellets. These pellets of thermoplastic resin mixed with chopped fibers or particles are then melted in a single-screw extruder, and the molten mixture is injected into a closed mold cavity. The injection pressure must be quite high in order to ensure complete filling and compensate for shrinkage due to cooling. After filling, the mold is then cooled down for solidification before the composite part is removed. Common volume fractions of

particles range between 18 to 35%. Typical cycle times on the order of 30 seconds with the largest fraction of the time being spent during the cool down step. Composites of complex geometries are conveniently fabricated to essentially their final shape. However, the required operating pressures (i.e. 50-100 MPa) limit injection molding to small to medium-sized composite parts [8].

1.3.4.4 Liquid Composite Molding

Liquid composite molding (LCM) processes such as resin transfer molding (RTM) have been long established in the automotive and aerospace industries as versatile technologies for manufacturing medium to large composite parts with complex geometries at low cost [9-11]. All LCM processes involve the injection of a liquid resin into a dry fiber preform, and is essentially the thermosetting equivalent to injection molding; except that the preform is typically placed in the mold prior to injection of the resin. Because of the lower viscosities of thermosets, the high pressures required for injection molding are not required for LCM. However; the cycle times are typically much longer because of the prolonged time required for the part to harden, which in turn is due to the much slower kinetics of a chemical reaction in LCM vs. cooling in injection molding. RTM, for instance, consists of injecting a reactive thermosetting resin into a closed mold cavity preloaded with a fibrous preform as shown in Fig. 1.9.

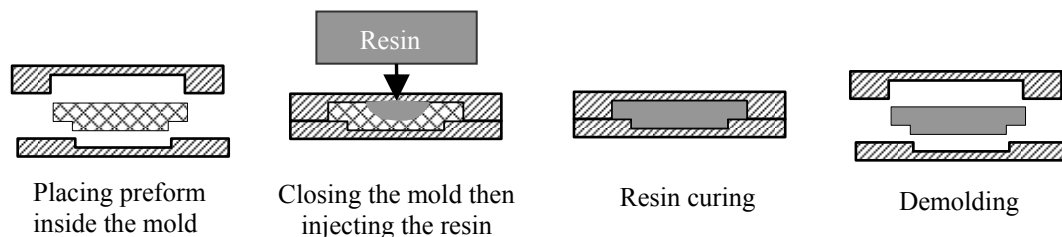


Figure 1.9: Typical resin transfer molding process.

Preforms used in LCM may consist of a 3D braided structure or multiple layers of 2D fabrics and mats. Glass, carbon, and aramid fibers are used as reinforcement, E-glass fibers being the most common [3,11]. High-performance carbon/epoxy systems are particularly used more often in the aerospace industry [3,8,11]. RTM can produce composite parts with volume fractions reaching 60%; however, typical applications may contain 25 to 35% fibers by volume. After the cure reaction is complete, the solidified composite part is removed from the mold. In other variants such as vacuum assisted resin transfer molding (VARTM), the impregnation is vacuum-driven, and thus half of the mold is often replaced with a vacuum bag. Since the pressure differential is much lower in VARTM, the cost of the mold can be reduced substantially, especially when fabricating larger parts.

1.4 *Properties and Applications of Polymer Composites*

1.4.1 Mechanical Properties

An increase in stiffness is probably the single most important reason that fillers are added to polymers. Stiffness is quantified using the modulus, which is the slope of a stress vs. strain curve at zero strain. The modulus, and other mechanical properties such as tensile strength and toughness, can be measured using different geometries; the two most common for composites are tensile and bending as shown in Fig. 1.10.

Bending studies are typically more informative for fiber-reinforced composites since this geometry provides a better test of adhesion between the polymer and the filler, while tensile studies are more commonly used for particulate composites, if the matrix is

flexible enough to allow tensile tests. For most systems, an increase in stiffness is typically accompanied by an unwanted decrease in flexibility and/or tensile strength; and most important commercial fillers for a particular polymer have a lower reduction in these properties at a given volume fraction than other fillers. The applications of composites that depend primarily on mechanical property specifications are too numerous to list, some examples are airplane and automotive components. Other important mechanical properties that often justify the use of a filled system vs. one without any filler are abrasion resistance, e.g. automobile tires, and resistance to creep e.g. weight-bearing structural components.

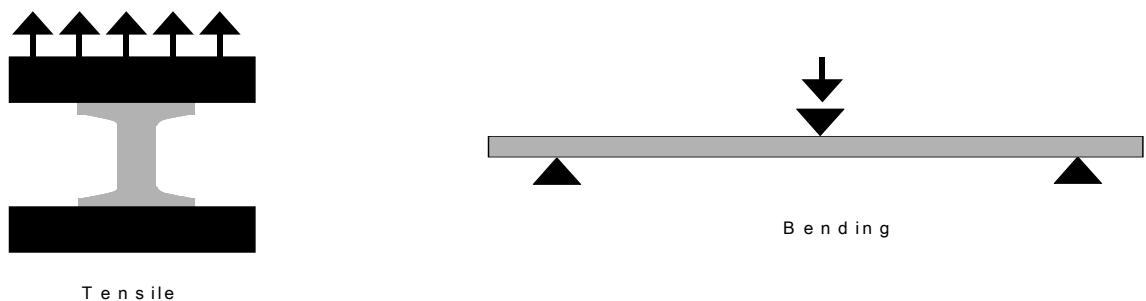


Figure 1.10: Geometries for testing stress-strain of composites

1.4.2 Electrical and Thermal Conductivity

Another common reason to add fillers to a polymer is to increase either electrical conductivity or thermal conductivity. Polymers typically have electrical conductivity from 10^{-15} S/cm to 10^{-18} S/cm; through the addition of a moderately conductive filler such as carbon black conductivities of 10^{-2} - 10^0 S/cm are possible; highly conductive fillers such as silver can raise this value to 10^1 - 10^2 S/cm. Applications include static dissipative devices and surge protectors. The impact of adding a highly thermally conductive filler to a polymer is much smaller at low volume fractions versus the impact of an electrically

conductive filler on electrical conductivity. However, if a highly loaded stiff product is acceptable, polymer composites are capable of dissipating substantial amounts of heat.

1.4.3 Gas Diffusion and Fire Retardency

Nanotechnology has been identified as one of the key technologies that will lead to important advances in the quality of life, and important advances have been made using nanotechnology in the polymer composite area. The use of nanoclays, which are nanometer-thick layered silicates, if exfoliated (i.e. separated apart), have enabled the manufacture of polymer-filled materials with vastly improved resistance to burning and gas diffusion. Applications that make use of the unique properties of composites filled with exfoliated clays are just beginning to appear. Manufacture of nanocomposites has proven to be quite difficult; since agglomerates of clay platelets must be separated in order for the improved resistance to diffusion and flame to occur. Thermoplastic resins with specific clay-polymer interactions, e.g. nylon, have proven to be the most effective matrix for nanocomposites.

1.5 Defects in Polymer Composites

The presence of defects in polymer composites adversely affects their mechanical properties and environmental resistance [12-14]. Conversely, environmental factors can lead to the worsening of already present defects. Defects in composites either originate during the manufacturing process as a result of incomplete wetting, improper process pressure, inadequate heating, or excessive temperature overshoot; or during the service life of the composite due to external factors including cyclic loading, low-energy impact, moisture, and elevated temperatures. Poor choice of process parameters leads to voids,

inclusions, resin burn out, and dry spots whereas external factors lead to defects such as sub-surface damages, ply cracking, and delamination.

1.5.1 Defects Induced During Fabrication of Composites

1.5.1.1 Micro Voids and Dry Spots

Depending on the manufacturing method, fiber type and content, and properties of the impregnating polymer, various mechanisms lead to the formation of large dry areas, called dry spots, and air inclusions or micro voids in the final composite part made with thermosetting resins. The common causes for void formation in polymer composites include volatilization of dissolved gases or moisture in the resin during impregnation or curing, partial evaporation of mold releasing agent into the preform, and initial air bubble content in the resin mixture. In wet lay-up and pultrusion, uneven application of the resin is the primary cause of void and dry spot formation; whereas in autoclave curing of composite laminates, voids are mainly caused by entrapped air between layers in prepregs. In LCM processes, on the other hand, voids form during mold filling primarily due to mechanical entrapment of air at the advancing flow front [15-19].

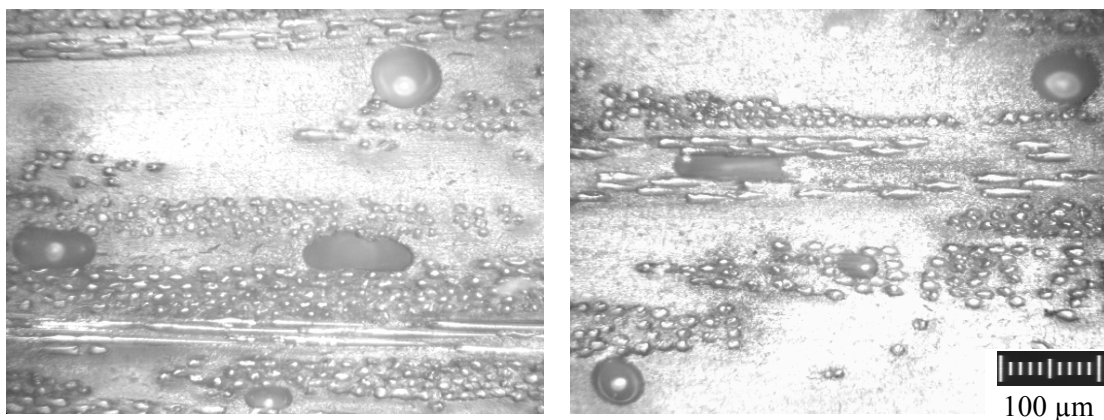


Figure 1.11: Representative microscopic images of voids obtained from a glass/epoxy RTM composite.

Void presence in composites, even in small amounts, is detrimental to their mechanical performance. Judd and Wright [12] reported that regardless of the manufacturing process, void presence induces reduction in interlaminar shear strength, tensile and flexural strength and modulus, torsional shear, fatigue resistance, and impact properties of a composite part. Ghiorse [13] indicated, for carbon/epoxy laminates, that each 1% increase in void content induced a 10% reduction in flexural and interlaminar shear strength, and a 5% reduction in flexural modulus. Voidage is also known to affect both the rate and equilibrium level of moisture absorption in composites [14]. Harper et al. [14] reported that an increase from 1 to 5% in void volume fraction induces an increase of around 280% in the initial absorption rate, and 50% in the equilibrium mass gain for an AS4/3502 graphite/epoxy composite.

Although it is not practically possible to manufacture void-free composites, different techniques have been successfully utilized for most manufacturing processes to fabricate composite parts with acceptable void content. Some of the void reduction techniques include: (i) degassing the resin mixture prior to impregnation, (ii) utilization of vacuum to remove the air entrapped between prepreg layers, (iii) proper selection of fiber/resin systems to lower gas emission during impregnation and cure, and (iv) utilization of lower viscosity resins at higher temperatures to facilitate the impregnation. Most industrial applications consider 1% void content as a threshold for acceptance of composite parts [16,17]. However, in highly structural applications, an acceptance threshold of 0.5% in void content is often applied [20].

1.5.1.2 Wrinkling

A number of mechanisms are known to induce wrinkling in continuous-fiber polymer composites. These mechanisms include mismatch in thermal expansion between the fiber, matrix, and tool plate materials; the temperature changes experienced by the part during processing; and volumetric shrinkage of the matrix [21-24]. The difference between thermal expansion coefficients of fiber, matrix, and tool plate can be several orders of magnitude. Thus, residual stresses often develop during the cool-down of the part. Elevated cooling rates can lead to compressive stresses in the laminate surface, while slower cooling rates allow time for stresses to relax and avoid significant temperature gradients through-the-thickness of the part [21].

1.5.1.3 Defects in injection molding

Incomplete filling and weldlines are the most common defects in injection molded composites. High fiber contents and low heating temperatures often lead to highly viscous fiber-resin mixtures that require elevated injection pressures. If adequate pressure is not supplied or the solidified composite blocks parts of the injection gate or runners, only a fraction of the needed volume is injected into the mold cavity. This problem can usually be solved by using higher melting temperatures to reduce the mixture viscosity, and also by enlarging the injection gates. Another defect encountered in most injection molded parts is the formation of weldlines [25]. When a weldline is formed by the merging of separate fluid fronts, fibers at both sides do not penetrate across the neighboring front, thus forming an unreinforced, structurally weak plane. This problem is often accentuated for parts containing longer fibers and higher fiber contents

[4]. Fiber breakage is another defect affecting the performance of injection molded parts. The mixing and shearing of the extruder screw often reduces the fiber length yielding a composite part molded with reduced mechanical properties. Low screw speeds and injection pressure can be utilized in order to avoid excessive fiber breakage [4].

1.5.2 Defects Induced During Service Life of Composites

1.5.2.1 Matrix Cracks and Fiber Fractures

Although matrix cracks can be induced by residual stresses developed during curing [23], most matrix cracks are initiated during the service life of composites. Given that the matrix usually sustains a lower stress before failure compared to the fiber reinforcements, micro cracks are often generated in the matrix after the application of high loads. Depending on the fiber orientation, content, and the direction of the applied load, multiple matrix cracks with different orientations can form inside the composite. If the matrix cracks propagate above a certain limit, fibers start supporting most of the applied load before they fail under different mechanisms. Short fibers frequently fail under pull-out, i.e. extraction of the fiber from the matrix, while continuous fibers tend to fracture under excessive loads. Depending on the strength of the matrix-fiber adhesion, a combination of both mechanisms is usually present in fractured composites [26]. Environmental effects, such as the infusion of water, can lead to a reduction in matrix-fiber adhesion which in turn leads to premature failure. Figure 1.12 shows SEM micrographs of failed surfaces of an E-glass/epoxy composite [27]. Fibers failing under both pull-out and fracture can be seen in Fig. 5.2.

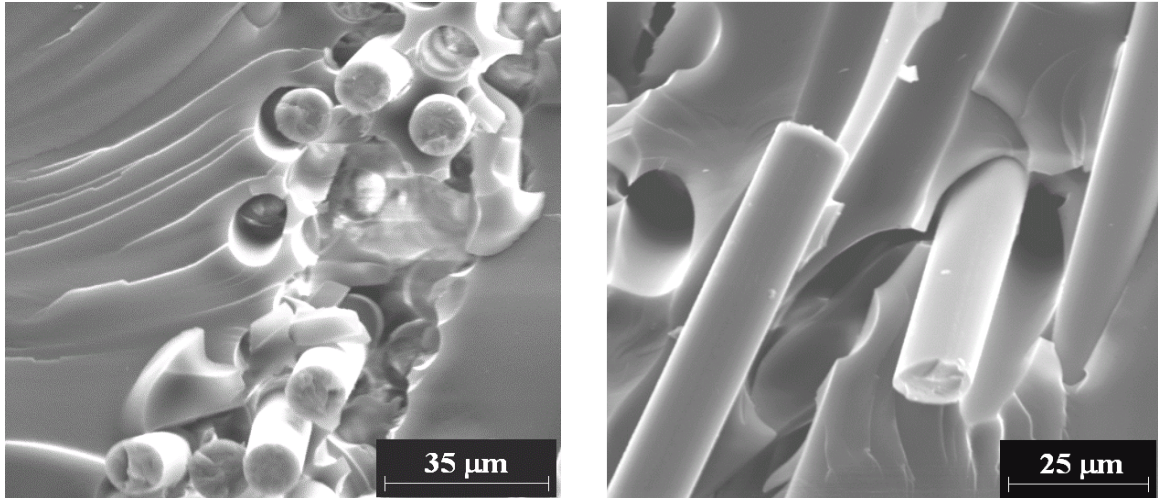


Figure 1.12: SEM micrographs of failed surfaces of an E-glass/epoxy composite [27].

1.5.2.2 Delamination

Delamination is the debonding of adjacent composite layers and is one of the most prevalent life-limiting defects in thermosetting composite laminates. Delamination is usually induced during service life of the composite from a low-energy impact or fatigue loading. However, delamination can also originate from other pre-existing defects such as matrix cracks and voids. In addition to reducing the structural integrity of the material, delamination also results in deterioration of long-term performances [28-29]. Non-destructive evaluation (NDE) methods have been commonly used to detect delaminations to prevent their excessive propagation leading to the final failure of the laminate [30]. Techniques such as X-ray and ultrasonic inspections are widely used, particularly in the aircraft industry where structural composite laminates are often used. NDE tests usually help define regular inspection intervals and determine the need for repair.

1.6 References

1. Astrom B. T., and Astrom T., *Manufacturing of Polymer Composites*, Chapman and Hall, 1997.
2. Gay D., Hoa S. V., and Tsai S. W., *Composite Materials: Design and Applications*, CRC Press, 2002.
3. Mazumdar S. K., *Composites Manufacturing: Materials, Product, and Process Engineering*, CRC Press, 2001.
4. Campbell F. C., *Manufacturing Processes for Advanced Composites*, Elsevier, 2004.
5. Hancox N. L., *Fiber Composite Hybrid Materials*, MacMillan Publishing, 1981.
6. Shibley M., *Handbook of Composite Materials*, Van Nostrand Reinold, 1982.
7. Swanson S. R., *Introduction to Design and Analysis with Advanced Composite Materials*, Prentice-Hall, 1997.
8. Bader M. G., Smith W., Isham A. B., Rolston J. A., and Metzner A. B., Processing and Fabrication Technology. *Delaware Composites Design Encyclopedia*, Vol. 3, Technomic Publisher, 1990.
9. Abraham D. and McIlhagger R., *Composites Part A*, 29(5), 533, 1998.
10. Abraham D., Matthews S., McIlhagger, R., *Composites Part A*, 29(7), 795, 1998.
11. Johnson F., *Resin Transfer Molding, Composite Materials Technology- Process and Properties*, Hanser Publisher, 1990.
12. Judd N. C. W. and Wright W. W., *SAMPE Journal*, 14(1), 10, 1978.
13. Ghiorse S. R., *SAMPE Quarterly*, 23(1), 54, 1993.
14. Harper D., Staab G. H., and Chen R. S., *Journal of Composite Materials*, 21, 280, 1987.

15. Hamidi Y. K., and Altan M. C., *Journal of Materials Science Letters*, 22(24), 1813, 2003.
16. Barraza H. J., Hamidi Y. K., Aktas L., O'Rear E. A. and Altan M. C., *Journal of Composite Materials*, 38(3): 195, 2003.
17. Olivero K. A., Barraza H. J., O'Rear E. A., and Altan M. C., *Journal of Composite Materials*, 36(16), 2011, 2002.
18. Mahale A. D., Prud'Homme R. K., and Rebenfeld L., *Polymer Engineering and Science*, 32(5), 319, 1992.
19. Patel N., Rohatgi V., and Lee J. L., *Polymer Engineering and Science*, 35(10), 837, 1995.
20. Goodwin A. A., Howe C. A., and Paton R. J., *Proc. of ICCM-11, Australian Composite Structures Society*, Vol. IV, 11, 1997.
21. Kugler D., and Moon T. J., *Journal of Composite Materials*, 36(12), 1451, 2002.
22. Meink T. E., Huybrechts S., and Herman Shen M.-H., *Journal of Composite Materials*, 36(9), 1025, 2002.
23. Dharia, A. K., Hays, B. S., and Sferis, J. C., *33rd International SAMPE Technical Conference*, Nov. 2001.
24. Coffin W., and Pipes R. B., *AIP Conference Proceedings, Materials Processing and Design*, 2004.
25. Papathanasiou T. D., and Guell D. C., *Flow-Induced Alignment in Composite Materials*, Woodhead Publishing, 1997.
26. Morley J. G., *High-Performance Fiber Composites*, Academic Press, 1987.

27. Barraza H. J., *Admicellar-Polymerized Thin Elastomeric Coatings for Engineered Interfaces for Enhanced Composite Performance*, PhD Dissertation, the University of Oklahoma, 2003.
28. Reddy A. D., Rehfield L. W., and Haag R. S., *Effects of Defects in Composite Materials*, ASTM STP 863, 71, 1984.
29. De Charentenay X., Harry J. M., Prel Y. J., and Benzeggagh M. L., *Effects of Defects in Composite materials*, ASTM STP 863, 84, 1984.
30. DiScalia L., and Green R. E. Jr, *Journal of Composite Materials*, 34(21), 1860, 2000.

2 Preform Wetting and Void Formation in RTM Composites

2.1 *Preform Types Used in RTM*

The assembly of reinforcing fibers, pre-shaped and oriented for placement in the RTM mold cavity to its near-net configuration before injecting the resin is commonly called a preform. Different preform types are available for RTM applications including random mats, woven, and non-woven products, as well as 2- and 3-D braidings. Selection of a preform fiber architecture directly affects the processability and mechanical performance of the RTM part. The following is a brief description of common preform types used in RTM composites.

Random mats consist of continuous or chopped fibers placed randomly and held loosely together by a binder adhesive. Because of the randomness, random preforms are isotropic, and fluid flow is thus relatively easy to predict. Other advantages of this preform include its high permeability yielding a thorough wet-out as well as an easy handling for placement in the mold cavity. However, random preforms can only achieve limited fiber volume fractions, have relatively poor stiffness and strength, and lack any control on fiber orientation. Unidirectional preforms, on the other hand, consist of parallel fibers held loosely in place by stitches in a plane. Although this preform type often yields high stiffness and strength in the fiber direction, they produce parts with poor integrity in other directions. In addition, fiber wash may occur during resin injection. Another preform architecture often used in RTM composites is two-dimensional woven.

Two-dimensional fabrics are fabricated from at least two sets of tows that are interwoven. Weaves can be classified according to the spacing between the tows: weaves with big open spaces between the tows are called open weaves, while weaves with no space between the tows are referred to as closed weaves. Balanced properties in the plane of the fabric can be achieved, although there can be some asymmetry depending on the type of weave pattern. Even though composites made with woven preforms exhibit good impact resistance, these materials have poor conformability for placement in odd-geometry molds. Furthermore, the weave introduces undulation of the yarns that degrades the strength and effective stiffness of the composite. Other fiber forms include 2- and 3-dimensionally braided preforms used for specialized applications. In order to eliminate the time-consuming lay-up step from the RTM process and ensure uniformity, three-dimensional braiding can be utilized to produce 3-D preforms. However, weaving can be costly and once performed, eliminates any possibility of varying the preform architecture.

2.2 *Mold Filling in RTM*

The flow of resin through the porous fiber preform during mold filling in RTM process is similar to that of water infiltration into soil. In both processes, a wetting fluid flows through an unsaturated porous medium; while this dry medium initially contains a non wetting phase, i.e. air. However, there is a basic difference between resin injection in RTM, that consists of two types of flow, and water ingress into soil that is a simple infiltration flow. The first type of flow during preform impregnation is a macroflow involving the flow in the larger gaps between fiber tows. The second is a microflow involving the infiltration into the small gaps between single fibers inside the fiber tows.

The macroflow is induced by the applied pressure or injection rate and is thus governed by viscous forces. The microflow, on the other hand, is a spontaneous process in which the interaction between the liquid and solid phases is the driving force. Microflow is mostly controlled by the capillarity and the surface tension effects. The difference between these two flows is what causes void entrapment in the RTM composites as will be developed in the next sections.

Darcy's law [1], often utilized to model fluid transport through porous media, states that the flow velocity is directly proportional to the pressure gradient with a permeability tensor as:

$$\mathbf{u} = -\frac{1}{\mu} \mathbf{K} \nabla p, \quad (2.1)$$

where \mathbf{u} is the average Darcy velocity, μ is the dynamic viscosity, ∇p is the pressure gradient, and \mathbf{K} is the second-order permeability tensor. Based on Darcy's law, the permeability tensor is a constant for a particular geometry of the porous medium and is independent of flow rate and liquid properties; certain experiments, however, have shown otherwise [2-4]. These discrepancies originate from the different rate of advancement of the fluid between and within the fiber tows. Darcy's law does not take into account the capillarity or any of the surface tension effects that govern the flow within the fiber tows as described above. Therefore, Darcy's law alone cannot predict the overall flow process in RTM. Capillary models such as those proposed by Carman [2] and Gutowsky et al. [3] include the fiber radius and porosity in order to predict the permeability more accurately. Yet, several discrepancies with experimental data have been also reported [5-

8]. Theoretical models have also been developed for different idealized media structures [6-8]. Most models may not give accurate prediction of the impregnation process since fibrous mats used in RTM are often more complex than the idealized unit cell patterns used in theoretical derivations. In any case, permeability studies focus on the macroscale flow and often do not yield good prediction models for porosity and void formation. In the following section, relevant void formation mechanisms in RTM are discussed.

2.3 Void Formation and Removal in RTM

Reducing void occurrence in RTM composites involves two different steps. The first involves understanding void formation mechanisms during mold filling, while the second consists of developing effective methods for void removal. The following is a description of void formation mechanisms as well as removal techniques used in RTM.

2.3.1 Experimental Studies on Void Formation

Voidage in RTM composites can originate from mechanical entrapment, volatilization of dissolved gas in the resin during mold filling or curing, partial evaporation of mold releasing agent into the preform, and initial air bubble content in the resin mixture [9]. Using resin systems involving fewer volatiles during molding, as well as degassing prior to injection helps make mechanical air entrapment the primary void formation mechanisms in RTM composites [10-12]. As described above, the flow is driven by viscous forces at the fiber tow level; while capillary forces drive the flow impregnating fiber tows at a single fiber scale. Depending on the molding parameters, either viscous or capillary flow is likely to lead the flow, causing mechanical entrapment of air bubbles. A more detailed analysis of this phenomenon (i.e., fingering) has often been achieved using

the capillary number, Ca , defined as the non-dimensional ratio of viscous forces to capillary forces [10-13]:

$$Ca = \frac{\mu V}{\gamma}, \quad (2.2)$$

where μ , V , and γ are the impregnating resin viscosity, the macroscopic fluid front velocity, and the resin surface tension, respectively.

The capillary flow leads at lower capillary number values, hence promoting inter-tow void entrapment in the macro-space between fiber tows. In contrast, viscous flow leads at higher values of Ca , thus promoting intra-tow void entrapment within fiber tows [10-13]. Mahale et al. [10] studied void entrapment during planar radial flow into non-woven multifilament glass fiber networks, and reported the existence of a critical capillary number value of 2.5×10^{-3} , below which void content increases exponentially with decreasing capillary number. Above this critical value, much less void entrapment was observed. However, these critical capillary number values remain specific to the set of material used in their experiment.

To avoid dependence on utilized material, a modified capillary number, Ca^* , has been defined by introducing liquid-fiber contact angle, θ , into the non-dimensional number as [11,12]:

$$Ca^* = \frac{\mu V}{\gamma \cos \theta}. \quad (2.3)$$

The authors included the contact angle in order to generalize the capillary number definition for any type of liquid-fiber system. Experimental observations of measured void contents for various model fluids injected at different velocities supported this generalization. When plotted as a function of modified capillary number, all the experimental voidage data followed a single master curve. This master curve also indicated the existence of a preferential range of modified capillary number of micro-equilibrium between viscous and capillary flows between 2.5×10^{-3} and 2.5×10^{-2} , where the void content is minimal. Detailed analysis of these phenomena is performed in the following chapter.

2.3.2 Theoretical and Numerical Models for Void Formation

Numerous researchers [13-19] developed theoretical and numerical models to predict void formation during injection. Chan and Morgan [13] developed a one-dimensional model for parallel flow through unidirectional preforms based on Darcy's law. This model predicts a localized void formation at the resin front region but is undermined by the assumption of a simplified fiber arrangement pattern. Chui et al. [14] proposed a theoretical model based on a simple unsaturated flow in porous media, predicting a voidage-pressure dependence in RTM processes. The model of Chui et al. [14] thus suggests that increases in local pressure would minimize void occurrence. This dependence of void presence on injection pressure was confirmed experimentally by Lundström [15]. Patel and Lee [16,17] also developed a model for void formation in LCM processes based on the multi-phase Darcy's law. In addition, a criterion for the transport of trapped voids based on the local pressure, void size, and contact angle was formulated. Binetruy et al. [18], on the other hand, developed a simple analytical model

for tow impregnation when the macroscopic flow is parallel to the fiber direction. More recently, Kang et al. [19] formulated a mathematical model to describe microscopic perturbations in the resin flow front that induce void formation during injection.

Once voids are formed, they are subjected to transport phenomena during filling that change their spatial distribution and geometrical morphology. To understand void transport mechanics through fiber reinforcement, bubble motion through constricted micro-channels has been investigated by several researchers [16-17,20-21]. Both bubble size and the resin-fiber contact angle are reported to affect void mobility [21,22]. Adhesion force between bubbles and fibers originates from the surface tension and the difference between advancing and receding contact angles [21]. In addition, larger voids exhibit larger perimeters and thus have larger adhesion force [21,22].

2.3.3 Void Removal Studies

Numerous techniques are used to reduce void occurrence in RTM composites [9-14,23-34]. Lundström et al. [23-24], among others, utilized vacuum assistance to lower void content. The mold cavity is vacuumed prior to injection in order to lower the internal air pressure, thus easing void dissolution into the resin, and also enhancing void mobility during molding. The authors reported that increasing the pressure difference between the inlet and outlet of the mold cavity from 0.17 to 0.50 MPa resulted in a decrease in void content from 6.5 to 3.8%. Yet, low void contents are only reached when costly, very high vacuum levels are used [24].

Degassing the injected resin is also used to reduce voidage in molded composites, since high initial bubble content results in elevated void presence [25-28]. However, even with a degassed resin, voids will still be mechanically entrapped by the fluid front as described earlier. Another commonly used method for void removal is bleeding, which consists of continuing the resin discharge after impregnation is completed in an attempt to purge the formed voids [14,23,29]. Bleeding might be useful when the formed voids can be transported, i.e. when voids are dominantly inter-tow voids. However, inter-tow voids are formed mostly at slow injection rates not seen in most industrial molding applications [9-11]. In addition, intra-tow voids formed in RTM processes with faster impregnation rates are found to be very difficult to purge by bleeding [12].

Another void removal method is compressing the mold walls after resin injection is complete [30]. Squeezing the mold walls is anticipated to expel voids and help fabricate void-free composites. The method drives out voids only to the end of the cavity [31], and yet requires expensive tooling that might make the molded parts much more expensive. Articulated tooling, a variant of compressing mold walls, was recently proposed by Choi and Dharan [32]. This technique calls for a segmented articulated mold wall, utilized to sequentially impregnate dry preform areas in a step-wise sequential manner. A five fold reduction in mold fill time and reduced void generation were observed [32]. Nonetheless, like compression, articulated tooling requires higher initial investment, and possibly yields undesirable surface marks and defects.

Packing is performed by increasing the pressure after the molding cavity is filled. This method has also been used to reduce void occurrence in RTM composites [23,29,33-34].

Forcing more resin into a previously filled mold cavity would shrink the existing voids or even dissolve them into the resin matrix. In an earlier study by Olivero et. al [33], void content was found to decrease exponentially with increasing applied packing pressure up to 700 kPa for resin transfer molded glass/epoxy composites at 21% fiber content [33]. Packing facilitates void removal for RTM and similar processes without additional tooling or investment. Hence, packing can be a cost-effective void removal technique that might improve most LCM processes. Concerns with packing reside in the possible spatial concentration of voidage or creation of large irregular voids with sharp corners that are prone to early failure cracks [31,35]. Effects of packing on void occurrence, spatial as well as morphological void distribution are investigated in the following chapters.

2.4 *Fiber Wetting in RTM*

As described above, fiber wetting and void formation in RTM depend on the equilibrium between viscous and capillary flows, which in turn depend to a large degree on the physicochemical properties of the resin-fiber system. The following is a brief description of the different relevant characteristics involved in this process.

2.4.1 Equilibrium Contact Angle

When a liquid is in contact with a solid surface, the equilibrium condition for wetting is determined by the three phase of equilibrium: solid, liquid, and air. As shown in Fig. 2.1, the equilibrium point of contact is the intersection of three interfaces: solid-liquid, liquid-gas, and solid-gas. The equilibrium conditions are given by the Young-Dupré equation [36-37] as:

$$\gamma_S - \gamma_{SL} = \gamma_L \cos \theta, \quad (2.4)$$

where γ_S is the solid surface energy, γ_{SL} the solid-liquid interface tension, γ_L the liquid surface tension, and θ is the equilibrium contact angle.

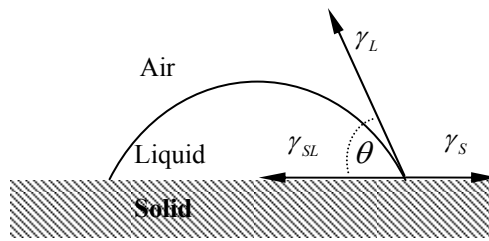


Figure 2.1: Three-phase equilibrium contact angle.

The contact angle is usually considered a measure of wettability, i.e. degree of wetting. Based on the magnitude of the contact angle, the liquid can be classified as: (i) spreading for $\theta = 0^\circ$; (ii) wetting for $0^\circ < \theta \leq 90^\circ$, or (iii) non-wetting when $\theta \geq 90^\circ$. The higher the value of the adhesion tension, $\gamma_L \cos \theta$, the more readily the wetting proceeds [38]. In order to ensure wetting, the liquid phase should have a surface free energy or a surface tension lower than the free energy of the solid surface. Measuring the contact angle with liquids of known surface tension also provides means of quantifying the interaction between solids and liquids. The property determining the extent of this interaction is W_a , the work of adhesion between the solid and the liquid, defined as [39]:

$$W_a = \gamma_L (1 + \cos \theta). \quad (2.5)$$

2.4.2 Dynamic Contact Angle

When the liquid and the solid are in motion with respect to one another, the solid-liquid-air interface is under transient conditions and a dynamic contact angle develops. Even at very low velocities, the dynamic contact angle is considerably larger than the equilibrium value. The dynamic contact angle can be either advancing or receding depending on whether the solid surface is advancing or receding over the liquid. Usually, the values of the advancing and receding contact angles are not the same, except in cases of perfect wetting, i.e. $\cos \theta = 1$. Advancing contact angles are normally greater than or equal to the receding contact angles. The difference is called the contact angle hysteresis and is well understood in the literature [40-42]. Some of the sources of this hysteresis include surface roughness, surface heterogeneity, surface deformation and relaxation effects, and increased liquid penetration due to diffusion [40-42]. Since the nature of RTM process is to make the resin advance through the fiber preform, advancing contact angles are more relevant.

The dynamic contact angle is influenced by the resin viscosity and surface tension. Several studies investigated the effects of viscosity and surface tension on the measured contact angle using the capillary number, Ca , defined in Eq. (2.2). The dynamic contact angle is observed to remain constant at very low values of the capillary number, and then increases with increasing capillary number. The contact angle dependence on the viscous drag was observed in the range of $10^{-6} < Ca < 10^{-5}$ [43].

Elmendorf and During [44] developed a model that explains the physics behind the spreading of a liquid over a solid surface. According to this model, the liquid closest to the solid experiences the largest molecular attraction and thus tends to move faster than the bulk liquid, which causes a concavity in the liquid surface. Away from the solid surface, the shape of the liquid surface that determines the dynamic contact angle is governed by the balance of surface tension and viscous forces. The authors used their model to obtain a correlation between the dynamic contact angle θ_d , the equilibrium contact angle θ_e , and the capillary number, Ca , as:

$$\theta_d^3 - \theta_e^3 = 53 \cdot Ca , \quad (2.6)$$

Another correlation for dynamic contact angle for resins with viscosities in the range of $10 - 1000 \times 10^{-3}$ Pa·s moving at velocities of the order of 1–100 mm/s is given by the Friz equation [45]:

$$\tan \theta_d = m Ca^n , \quad (2.7)$$

where m and n are empirical constants.

Contact angle analysis is further complicated by the nature of the resin system and the fiber surface. Resin systems are usually mixtures of different elements, and composition gradients as well as chemical reaction and evaporation of volatile chemicals may also affect the surface energies and may lead to local changes of the dynamic contact angle. In addition, if the fiber sizing interacts either physically or chemically with the resin, changes in fiber wettability would occur. The effect of fiber sizing on contact angle was quantified by Larson and Drzal [46], among others. The authors observed that

evaporation of styrene from a vinyl ester resin significantly increased the surface free energy of the resin and changed the liquid-fiber interaction from wetting to non-wetting. Contamination of glass fibers with styrene vapor and liquid resulted in an increase in contact angle, and zones of poor wetting with increased voidage were observed in the molded composite [45].

2.4.3 Capillary pressure

In addition to the dynamic contact angle, another important parameter to be considered in flow through porous media is the capillary pressure, P_c . In soil mechanics, capillary pressure is called suction since it provides the driving force for the liquid to infiltrate the porous media. Capillary pressure is a decreasing function of the wetting phase saturation, i.e., the capillary pressure is at the maximum when the fibers are dry, and then decreases as the fibers are impregnated. Assuming that the single fibers inside fiber tows have cylindrical capillaries, a simple relationship was obtained for evaluating the capillary pressures [47]:

$$P_c = \frac{4 \gamma \cos \theta}{d}, \quad (2.8)$$

where d is a measure of the size of the capillary or the flow channel. The above equation is known as the Young-Laplace equation. However, it is very difficult to obtain realistic estimates for d since a typical fiber preform consists of a large number of capillaries of varying shapes and sizes. One way to estimate d is to utilize the concept of hydraulic diameter, D_h .

2.5 Contact Angle and Surface Tension Measurements

Surface tension and contact angles play a significant role in characterizing fiber wettability and penetration of resin into the fibers. Almost all the equations mentioned in the previous section incorporate these parameters; their accurate determination is thus vital. The next section is hence devoted to describe some of the experimental techniques used to measure the contact angle and surface tension.

2.5.1 Contact Angle Measurement

2.5.1.1 Sessile Drop Technique

Most of the established experimental techniques for measuring surface wetting properties have been developed for flat solid surfaces similar to the one shown in Fig. 2.1. Therefore, direct measurements can be performed using a microscope fitted with a camera as shown in Fig. 2.2. Accurate measurement of contact angles using the sessile drop technique can be computed via image analysis software. In this technique, a small hole is drilled in the solid using a sharp needle and a drop is grown from the bottom. Figure 2.2 shows the schematic of a typical setup for sessile drop measurements. The image of the drop is transmitted through a camera-fitted microscope to a computer for image analysis and computation. Advancing and receding contact angles can also be obtained using this method by forming the drop using a motor driven syringe.

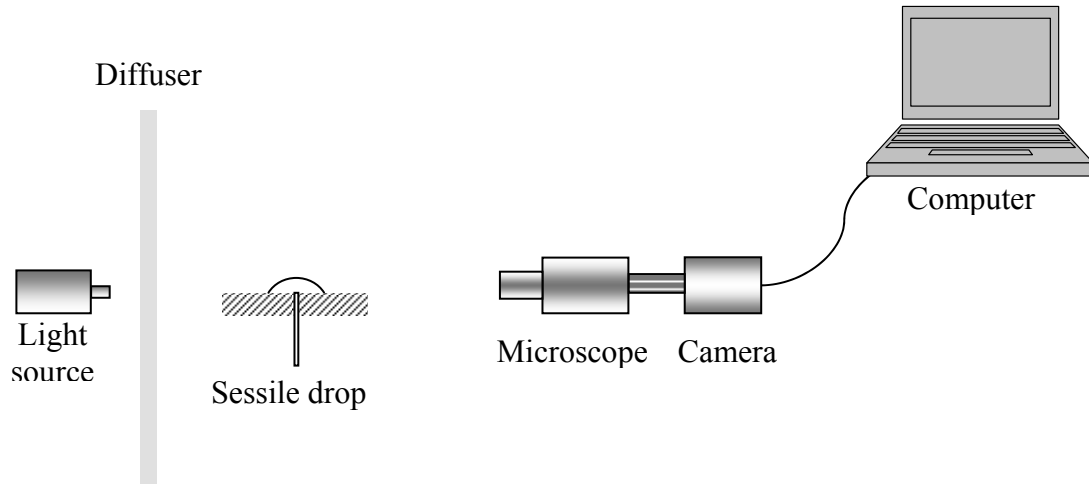


Figure 2.2: Schematic of image analysis setup for contact angle measurement using the sessile drop technique.

Measuring the contact angles on single fibers or fiber tows requires placing a drop of the resin on a horizontally mounted specimen. The contact angle also needs to be observed from a point in the same horizontal plane and perpendicular to the long axis of the sample. These requirements are necessary since certain liquids have the tendency to completely surround the single fiber, or fiber tow; while others remain on one side of the fiber with a clamshell profile. Therefore, this approach requires considerable precaution to make sure that the observed and measured value is the true contact angle. For composite manufacturing processes, resin-fiber tow contact angle is more relevant than that of a single fiber since the resin is in contact with fiber tows during impregnation.

Similar methods are also utilized to measure contact angles. In the pendent drop method, for instance, the drop of the liquid is hanging from the solid instead of being placed on top of a flat surface. The pendant drop of liquid is then photographed, and its image is processed to obtain the dimensions of the drop. The contact angle as well as the surface tension can be obtained by this method.

2.5.1.2 Wilhelmy Technique

Due to the inherent difficulties involved in the accurate measurement of contact angles using direct methods, an indirect method was developed based on the Wilhelmy principle. Since the development of this technique, it has been applied extensively to study the dynamic wetting behavior of fibers for various liquid-fiber systems. This method does not involve direct observation of the shape of the liquid surface on the solid; instead, it requires measuring the force that the liquid exerts on the fiber surface.

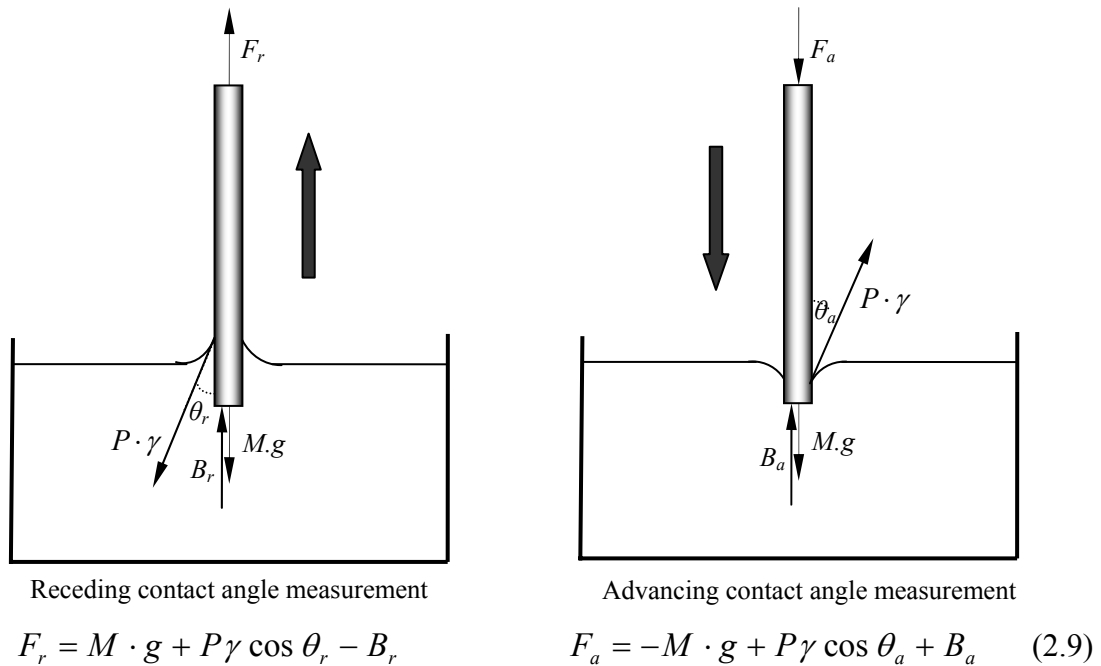


Figure 2.3: Concept of the Wilhelmy technique for measuring advancing and receding contact angles.

When the perimeter and the surface tension are known, the contact angle can be directly obtained from the measured values. Measuring the involved forces can be performed using a microbalance. Figure 2.3 depicts this concept in terms of the forces acting on the fiber in advancing and receding modes.

2.5.1.3 Oscillating Jet Method

Another technique used to measure the contact angle is the oscillating liquid jet method. When a liquid jet emerges from an elliptical orifice, the surface tension of the liquid attempts to restore a circular shape to the jet. However, overshoots due to liquid inertia induce an oscillation around the circular shape. If the jet is illuminated by parallel beams of light perpendicular to the jet axis, the jet acts as a lens and focused patterns of stripes appear on the screen at a suitable distance from the jet. Knowing the parameters of the Jet, the contact angle and surface tension can be calculated from any point of the jet [48].

2.5.2 Surface Tension Measurement

Surface tension of a liquid is a thermodynamic property, and for a pure liquids depends only on temperature with respect to which it shows monotonic decrease [43]. Surface tension of polymer resins has been observed to change with the evaporation of volatiles [46]. Most of the techniques used to measure the contact angle can be used to measure the surface tension of a liquid using a solid with a very high surface energy such as platinum. The following is a description of the common methods for surface tension measurement.

2.5.2.1 Capillary Rise Method

The capillary rise method is based on the measurement of the height of liquid column, h , in a capillary of radius r immersed in a liquid. Since the measurements do not involve disturbance of the liquid surface, slow time effects can be followed. Surface tension is then calculated using the densities ρ_L and ρ_G of the liquid and the gas, respectively, as:

$$\gamma = \frac{r h (\rho_L - \rho_G) g}{2 \cos \theta}, \quad (2.10)$$

In practice, the capillary rise method should only be used when the contact angle is zero not to include the uncertainties involved with the contact angle measurements. A variation of this method is to measure the difference in capillary rise, Δh , for capillaries of different sizes (r_1 and r_2); thus eliminating the reference to the flat liquid surface. In this case, the surface tension is calculated as:

$$\gamma = \frac{r_1 r_2 \Delta h (\rho_L - \rho_G) g}{2 (r_1 - r_2)}, \quad (2.11)$$

2.5.2.2 Ring Method

In this method, the force required to detach a ring from a liquid surface is measured, usually by suspending the ring from the arm of a balance. The detachment force, F , is related to the surface tension by the expression:

$$\gamma = \frac{\beta F}{4 \pi R}, \quad (2.12)$$

where R is the mean radius of the ring and β is a correction factor [49]. To ensure a zero contact angle, platinum rings should be cleaned with a strong acid, or by flaming. The correction factor accounts for the non-vertical direction of the tension forces as well as the complex shape of the liquid supported by the ring at the point of detachment.

2.5.2.3 Drop Volume and Drop Weight Method

Drops of liquid are allowed to detach themselves slowly from the tip of a vertically mounted narrow tube, and their weight, m , or their volume, V , is measured. At the point of detachment:

$$\gamma = \frac{\beta m g}{4 \pi r} = \frac{\beta \rho V g}{4 \pi r}, \quad (2.13)$$

where r is the drop radius, and β is an empirical correction factor reported to depend on the ratio $r/V^{1/3}$. This correction is needed since at the point of detachment, the drop does not completely leave the tip, and the surface tension forces are rarely vertical.

2.5.2.4 Wilhelmy Technique

This technique was described earlier as a method of measuring contact angles. The same technique can be utilized to measure surface tension when the immersed rod or plate has a zero contact angle. Often, flamed glass or platinum plates are used since they have very high surface energies. Equation (2.9) is used to calculate the surface tension given the perimeter of the plate. The underlying assumption in this method is that the plate makes a zero contact angle with the liquid whose surface tension is to be measured. The Wilhelmy technique is used in this study to measure both the utilized resin surface tension and the resin-fiber contact angle; and details of the measurements are given in chapter 3.

2.6 Void Content Measurement Techniques

Since void presence severely deteriorates the mechanical properties as discussed in section 1.5.1.1, several techniques for determining void content in composites have been developed. Most experimental studies on void formation in RTM determine void content during mold filling via monitoring flow front progression during mold filling. Post-cure studies, on the other hand, use different methods to estimate void content after fabrication of the composite part. A brief description of the main features of the common void content measurement techniques is summarized below.

2.6.1 Density Measurement Technique

This method is relatively simple to utilize and does not require any sophisticated equipment. Void volume is calculated from the densities of the fiber, resin, and composite as well as to the volume fraction of the fiber and the resin by the expression:

$$V_v = \frac{W_c}{\rho_c} - \left(\frac{W_f}{\rho_f} + \frac{W_r}{\rho_r} \right), \quad (2.14)$$

where V , W , and ρ are respectively the volume, weight, and density; while subscripts c , f , and r denote the composite, fibers, and resin, respectively. Therefore, precise knowledge of void content requires accurate determination of various densities as well as the resin and fiber weight fractions. The densities are obtained from either the water buoyancy technique described in ASTM D792, or the density gradient technique explained in ASTM D1505. The fiber and resin contents are usually obtained from chemical or thermal methods. The former involves acid digestion of the resin while the latter involves removal of the resin by thermal degradation. Weight changes are monitored in

both cases by gravimetry. A variation of 0.1% in ρ_c , ρ_f , ρ_r , V_f , or V_r induces a 2.5% in the calculated void content [50]. The uncertainty of fiber density may introduce an error as large as $\pm 0.5\%$, and this method is known to give negative values of void contents [50-51]. In addition, this technique can only estimate the overall void content based on small samples. Furthermore, it provides no information on the size, shape, location, or distribution of voids.

2.6.2 Water Absorption

This method is based on the volume absorbed by the composites samples. It requires the determination of the equilibrium water uptake of a composite without voids and the composite for which the void content is to be measured. Void volume is then calculated as:

$$V_v = \frac{1}{\rho_w} (W_c - W_0), \quad (2.15)$$

where ρ is the density of water, W_c is the weight of the water absorbed by the composite and W_0 the weight of the water absorbed by the composite not containing any voids. The validity of this method depends on complete saturation of the voids as well as the fabrication of a void-free composite. The accuracy of this technique is estimated to be worse than the density measurement method.

2.6.3 Ultrasonic C-Scan

This method is widely used in the industry for qualitative, non-destructive evaluation of defects in composites. It can be applied by transmitting a short pulse of ultrasonic energy through the specimen and measure the attenuation or decibel drop caused by the passage

of the ultrasonic pulse. This technique has the advantage of accessing the whole specimen instead of small sections. Since voids are known to be strong scatterers of ultrasonic elastic waves, they cause a dramatic decrease in the amplitude of the transmitted signal and an increase in the ultrasonic attenuation. However, a previous step of calibration is necessary with reference to another technique, and also attenuation is influenced by other composite parameters such as delaminations, fiber volume fraction, and degree of cure. Hsu [52] showed that void volume fraction in unidirectional and woven carbon fiber reinforced epoxy laminates is directly proportional to the slope of the attenuation with respect to frequency. The authors reported that void contents determined from attenuation slope compared well with those determined via density methods.

2.6.4 Radiography

Radiographic techniques have also been used in some instances. The samples are first impregnated with molten sulfur and then radiograph images are taken using a tungsten target. A stereo pair of radiographs is taken to facilitate examination of void distribution throughout the composite sample. It has been demonstrated that voids of micron size can be detected. However, the accuracy of this technique is highly dependent on complete filling of voids with the molten sulfur [51].

2.6.5 Microscopic Image Analysis

Adapted from metallography, this technique involves using a reflecting type microscope to analyze the studied specimen. Usually, a small sample of the composite is cut and mounted on a block. It is then polished sequentially on silicon carbide with decreasing

grit size. The prepared specimen is then scanned by a microscope fitted with camera. By assuming a random distribution of the voids within the composite sample, the voids fraction in the studied cross-section is taken as equivalent to the void volume fraction. Frames are often obtained at very localized areas that are assumed to represent the whole composites. In spite of all these assumptions, microscopic image analysis is demonstrated to be the best method to measure void contents in composite materials [33-35,51,53]. In addition, this technique provides additional information on void size, shape, and distribution. In this study, microscopic image analysis is utilized over the entire cross sections of the studied composites to ensure the most accurate measurement of void content. In addition, all void measurements are conducted manually to eliminate errors induced by usage of luminosity threshold; although this practice is commonly used and allows faster image processing. In order to insure that no errors were introduced in the current studies by personalized judgment, tow sample regions were entirely processed for voids by two operators, and measured void contents were within at most 5% of each other for each region.

2.7 References

1. Darcy H. P. G., *Les Fontaines Publiques de la Ville de Dijon*, Delmont, Paris, 306, 1856.
2. Carman P. C., *Transaction of the Institute of Chemical Engineers*, 15, 150, 1937.
3. Gutowski T. G., Morigaki T., and Cai Z., *Journal of Composite Materials*, 21(2), 172, 1987.
4. Dave R. and Houle S., *Proc. of the American Society for Composites*, 5th Technical Conference, 1990.
5. Gebart B. R., *Journal of Composite Materials*, 26(8), 1100, 1992.
6. Brusckie M. V., and Advani S. G., *Polymer Composites*, 11(6), 398, 1990.
7. Ngo N. D., and Tamm K. K., *International Journal of Heat and Mass Transfer*, 44(16), 3135, 2001.
8. Williams J. G., Morris C. E. M., and Ennis B. C., *Polymer Engineering and Science*, 14(6), 413, 1974.
9. Patel N., and Lee L. J., *Polymer Composites*, 16(5), 386, 1995.
10. Mahale A. D., Prud'Homme R. K., and Rebenfeld L., *Polymer Engineering and Science*, 32(5), 319, 1992.
11. Patel N., Rohatgi V., and Lee J. L., *Polymer Engineering and Science*, 35(10), 837, 1995.
12. Rohatgi V., Patel N., and Lee J. L., *Polymer Composites*, 17(2), 161, 1996.
13. Chan A. W., and Morgan R. J., *SAMPE Quarterly*, 23(4), 48, 1992.

14. Chui W. K., Glimm J., Tangerman F. M., Jardine A. P., Madsen J. S., Donnellan T. M., and Leek R., In: *Proc. of the 9th International Conference of Numerical Methods in Thermal Problems*, 1323, 1995.
15. Lundström T. S., *Composites Part A*, 28, 201, 1997.
16. Patel N., and Lee J. L., *Polymer Composites*, 17(1), 96, 1996.
17. Patel N., and Lee J. L., *Polymer Composites*, 17(1), 104, 1996.
18. Binetruy C., Hilaire B., and Pabiot J., *Journal of Composite Materials*, 32(3), 223, 1998.
19. Kang M. K., Lee W. I., and Hahn H. T., *Composite Science and Technology*, 60, 2427, 2000.
20. Lundström T. S., *Polymer Composites*, 17(6), 770, 1996.
21. Shih C-. H., and Lee L. J., *Polymer Composites*, 23(1), 120, 2002.
22. Blackmore B., Li D., and Gao J., *Journal of Colloid and Interface Sciences*, 241(2), 514, 2001.
23. Lundstrom T. S., and Gebart B. R., *Polymer Composites*, 15, 25, 1994.
24. Lundstrom T. S., Gebart B. R., and Lundemo C. Y., *Journal of Reinforced Plastics and Composites*, 12, 1339, 1993.
25. Johnson C. F., *Composite Materials Technology- Process and Properties*, Hanser Publisher, NewYork, Ch. 5, 1990.
26. Howe C. A., Paton, R. J., and Goodwin A. A., *Proc. of ICCM-11, Composites Processing and Microstructure*, Australian Composite Structures Society, Gold Coast, Australia, 46, 1997.
27. Bowles K. J., and Frimpong S., *Journal of Composite Materials*, 26, 1487, 1992.

28. Stabler W. R., Tatterson G. B., Sadler, R. L., and El-Shiekh A. H. M.. *SAMPE Quarterly*. 23(1), 38, 1992.
29. Han K., and Lee L. J., *Journal of Composite Materials*, 30, 1458, 1996.
30. Ikegawa N., Hamada H., and Maekawa Z., *Polymer Engireeng and Science*, 36, 953 (1996).
31. Wisnom M. R., Reynolds T., and Gwilliam N., *Composites Science and Technology*, 56, 93, 1996.
32. Choi J. H., and Dharan C. K. H., *Journal of Composite Materials*, 36, 2267, 2002.
33. Olivero K. A., Barraza H. J., O'Rear E. A., and Altan M. C., *Journal of Composite Materials*, 36, 2011, 2002.
34. Barraza H. J., Hamidi Y. K., Aktas L., O'Rear E. A., and Altan M. C., *Journal of Composite Materials*, 38, 195, 2004.
35. Harper B. D., Staab G. H., and Chen R. S., *Journal of Composite Materials*, 21, 280, 1987.
36. De Ruijter M., Kolsch P., Voue M., De Coninck J., and Rabe J. P., *Colloids and Surfaces, Part A: Physicochemical and Engineering Aspects*, 144, 235, 1998.
37. Miller B., *Surface Characteristics of Fibers and Textiles, Part II*, Ch. 11, 417, M. J. Scick, Ed., Marcel Dekker, 1977.
38. Carino L. and Mollet H., *Powder Technology*, 11, 189, 1975.
39. Kamath Y. K., Dansizer C. J., Hornsby S., and Weigmann H. D., *Textile Research Journal*, 205, April 1987.
40. Wang J.-H., Claesson P. M., Parker J. L., and Yasuda H., *Langmuir*, 10, 3887, 1994.
41. Wang B.-X. and Yu W.-P., *Fluid Phase Equilibria*, 75, 197, 1992.

42. Sauer B. B. and Carney T. E., *Langmuir*, 6, 1002, 1990.
43. Ahn K. J. and Sefris J. C., *Polymer Composites*, 12(3), 146, 1991.
44. Elmendrop J. J. and During, F., *Proc. of the 49th SPE ANTEC*, 1361, 1991.
45. Hayward J. S. and Harris B., *Composites Manufacturing*, 1(3), 161, 1990.
46. Larson B. K. and Drzal L. T., *Proc. of the 50th SPE ANTEC*, 752, 1992.
47. Skartsis L., Khomami B., and Kardos J. L., *SAMPE Journal*, 28(5), 19, 1992.
48. Kubiak A., and Dejmek P., *Journal of Dispersion Science and Technology*, 14(6), 661, 1993.
49. Shaw D. J., *Introduction to Colloid and Surface Chemistry*, Butterworth, 1980.
50. Judd N. C. W. and Wright W. W., *SAMPE Journal*, 14(1), 10, 1978.
51. Shih C-H., *Liquid Composite Molding of Tackified Fiber Reinforcement: Preforming and Void Removal*. PhD Thesis, Ohio State University, Department of Chemical Engineering, 2000.
52. Hsu, D., *Proc. of the 46th SPE ANTEC*, 1273, 1988.
53. Ghiorse S. R., U. S. Army Materials Technology Laboratory, Report MTL TR 91-13, 1991.

3 Voidage Reduction in Resin Transfer Molded Composites

3.1 *Abstract*

Resin transfer molding (RTM) is regarded as successful process in manufacturing near-net-shape, geometrically complex composite parts. High-speed processing is essential to achieve lower production cost in the fabrication of fiber-reinforced composites with the current RTM practices. A major consequence of increasing the resin injection velocity is the formation of defects such as voids and dry regions that decrease the load-bearing capability of molded composites. Detrimental effects of voids on the structural integrity of molded parts have been studied extensively. In contrast, knowledge of effective void removal strategies, along with detailed spatial and morphological void distribution within a molded composite is very limited. In this investigation, various post-fill pressure levels are applied to molded disk-shaped random-mat E-glass/epoxy parts as a method to reduce their voidage content. Microscopic image analysis over cross-sections cut from these composites revealed that significant changes in voidage concentration take place with the packing pressure. For instance, overall void content dropped more than 88% with the application of a post-fill pressure as low as 300 kPa. In addition, as the packing pressure increases, large voids gradually disappear.

3.2 Introduction

Liquid molding technologies such as Resin Transfer Molding (RTM), Vacuum Assisted Resin Transfer Molding (VARTM), and Resin Infusion, among others, are often regarded by composite manufacturers as excellent alternatives to current autoclave-cured laminated composites. In general, these liquid molding processes have lower operational costs and higher production rates that make them particularly attractive for high-throughput industries such as automotive and consumer products. Some authors even predict that high-speed liquid molding will be the mainstream fabrication process for aerospace parts in the next decade [1,2]. In resin transfer molding, an uncured liquid resin is mechanically injected into a mold containing an inorganic porous or fibrous reinforcement. The resin is expected to displace the air inside the mold, quickly filling up all empty spaces within the preform. In the case of fibrous reinforcements, the network of channels for the resin flow is not uniform and contains a wide distribution of inter-tow and intra-tow channel spacing as well as a broad range of channel orientations (i.e. random fiber preforms). Such heterogeneous microstructure forms high and low permeability zones within the reinforcement; and at the same time, creates an imbalance between viscous and surface forces during the flow of the polymeric mixture. Permeability variations at the flow front, coupled with non-isothermal effects coming from the curing kinetics, are responsible for transient phenomena that decrease impregnation quality and ease of spreading of the resin through the inorganic preform, thus leading to macroflow- and microflow-driven defects like dry spots and voids. In addition, voids can also originate from nucleation and growth of either dissolved gases or low molecular weight by-products formed during the crosslinking reaction [3]. High

voidage is one of the major factors inducing a severe degradation of mechanical properties in composites [4]. It has been reported that a void content as low as 1% may cause reductions between 2 and 10 MPa in the interlaminar shear strength (ILSS) of a composite part [5].

Previous investigations have revealed that void formation during RTM depends primarily on process-related factors such as capillary number, contact angle, and orientation of fibers with respect to the flow direction [6]. Patel and Lee [7] put forward a simple unidirectional model that predicts void formation as the result of the extensive fingering at the flow front (i.e. lead-lag behavior). According to these authors, the lead-lag appears when either the inter-tow or primary flow predominates over the flow between fiber interstices (i.e. capillary flow), and *vice versa*. The manifestation of flow front lead-lag is directly related to the impregnation rates. For instance, at low filling velocity, the flow inside the fiber tows or intra-tow flow is dominant. High capillary pressures cause the microflow within the narrow channels formed by parallel fibers inside a tow to move ahead of the macroflow, which takes place in the inter-tow spacing. At high flow velocity on the other hand, the situation is reversed: the macroflow moves ahead of the microflow. In this latter case, the capillary effect is very small compared to the externally applied pressure, and thus the viscous forces dominate the filling pattern [8].

In addition to molding speed, other factors are known to change the lead-lag intensity and ultimately the quantity and distribution of voids inside a molded part. One such variable is the injection mode. When the liquid injection is carried out at a constant volume flow rate, the front lead-lag should not depend on the distance from the inlet for a constant

cross-section, one-dimensional flow. Consequently, the void fraction along the composite should not vary much with respect to the inlet distance (i.e. only if void compression and advection are assumed negligible). In contrast, when the impregnation is performed at constant inlet pressure the flow rates would decrease with time, and hence, the flow front lead-lag would change as the flow progresses. In this case, a spatially nonuniform void distribution is expected, with increasing number of voids present towards the exits [7]. Similar void occurrence dependence on the distance from the inlet is also expected when the liquid injection is performed at a constant volume flow rate in a constant cross-section mold cavity.

During resin impregnation, and up until the gelling process begins, the entrapped voids are in a transient state where changes in size, shape, and location can be easily induced by applying external driving forces. Several authors [6-10] have studied this particular phenomenon and suggested mechanisms for void mobilization and reduction in RTM composites. Lundström [10] for example, found that a significant drop in void content could be achieved by continuing the resin flow after the reinforcement has been completely wet out. In this way, the resin advects out voids and more time is allowed for dissolving any binder or excessive sizing on the fiber surface. In industrial practice this procedure has commonly been referred to as bleeding. Chen et al. [9] studied the physicochemical variables (i.e. surface tension, viscosity and equilibrium contact angle) controlling void mobilization and concluded that voids entrapped by a resin with lower surface tension are more deformable, and consequently, easier to wash out from the fiber bundles. According to Chen's study, resin viscosity also appears to have a great influence on the momentum transfer mechanism for void mobilization. Higher

viscosities are expected to increase the compressive pressure over the bubbles and help in their mobilization. However, the trade-off is that when the resin viscosity is too high, penetration into the inter-fiber channels becomes much more difficult; and molding pressures rise to almost impractical levels. Recent experiments conducted by Balckmore et al. [11] on the detachment of bubbles in slit microchannels by shearing flows confirm many of the previous observations found in the composite materials literature. One of their major conclusions is that the fluid drag force necessary to move a bubble located in contact with both surfaces inside a narrow channel must always be greater than the adhesion force that keeps it in place. The source of this adhesion force is related to the bubble liquid-air surface tension and the difference between the advancing and receding contact angles as:

$$F_a = 2D_c \gamma (\cos\theta_r - \cos\theta_a), \quad (3.1)$$

where D_c is the bubble contact diameter, γ represents the bubble liquid-air surface tension, θ_r is the receding contact angle, and θ_a corresponds to the advancing contact angle. From Eq. (3.1), it can be easily inferred that at the same flow condition, a larger bubble has a longer perimeter and hence a larger adhesion force. In contrast, small bubbles have lower adhesion forces and therefore become mobile in a straight microchannel at lower fluid shear rates. Analysis of the void size and shape distributions within composite parts clearly shows that small and circular voids tend to concentrate in regions away from the inlet, which is definitely a consequence of their higher mobility [12,13].

Equation (3.1) may also serve as a theoretical explanation to the findings of Chen et al. [9] and other authors regarding the effect of surface tension on void mobilization. However, no simple generalization can be made in the case of composites liquid molding because lower surface tensions may help in void advection, but at the same time, a liquid with lower surface tension would exhibit poor wetting on inorganic preforms and therefore induce higher void occurrence. In order to account for the effects of both physicochemical and flow-related variables on void migration, the capillary number, Ca , defined as the nondimensional ratio of the viscous forces to the capillary forces, has often been used [9]:

$$Ca = \frac{\mu V}{\gamma}, \quad (3.2)$$

where μ , V , and γ are the polymer viscosity, the macroscopic fluid front velocity, and surface tension of the reacting mixture, respectively. Recently, Patel et al. [6] introduced the idea of using a modified capillary number, Ca^* , as the nondimensional parameter to relate the viscous forces and surface forces during fluid flow with the wettability characteristics of the substrates, given by the equilibrium contact angle, θ . The expression for the modified capillary number is given by,

$$Ca^* = \frac{\mu V}{\gamma \cos \theta}. \quad (3.3)$$

When plotting the void area fraction measured in experiments with various model fluids injected at different velocities, Patel et al. [6] found that, regardless of the type of fluid or solid wettability, all the voidage data collapsed into a single master curve having the

modified capillary numbers as the independent variable. Further experimentation carried out by the same authors [7], as well as by Manhale et al. [14], indicate the existence of a critical capillary number for void formation lying in the range of 2.5×10^{-3} . Similarly, Patel et al. [7] defined a critical capillary number value for void elimination through advection that depends on the fiber geometry and is an order of magnitude higher (e.g. 1.0 to 2.2×10^{-2}) than the critical capillary number for void formation. To attain these capillary numbers, injection of liquid must be performed at high flow rates. Model experiments with parallel plate microchannels [11] also showed that for a given channel spacing (H), a critical capillary number needs to be reached in order to generate a detaching shear force sufficient to mobilize a bubble of a particular contact diameter, D_c . This critical capillary number was found to decrease linearly as D_c/H increased, reaching a plateau as the channel spacing became smaller.

A substantial decrease of the interlaminar adhesion properties with increasing levels of voidage has been long recognized in literature, and empirical correlations of exponential type have been put forward to represent the void-property relation [13,15]. In most cases, these analytical predictions assume a simple relationship between mechanical performance and the bulk or overall void content as the sole independent parameter. However, given that voids are likely to originate from different sources during filling, other void characteristics such as void shape, size, and spatial distribution must be taken into account in composite durability predictions, as these individual parameters will contribute to mechanical properties and failure mechanisms in different ways. For instance, Lundström and Gebart [10] report the coexistence of two types of voids formed in RTM composites with unidirectional glass fibers: slender cylinders, located

preferentially inside the fiber bundles; and, large spherical voids, found in the interstices between the fiber bundles. The authors noted that large bubbles, in particular, aligned themselves perpendicularly to the flow direction as a result of the periodic constrictions formed by the weave pattern of the reinforcement (i.e. the reinforcement had 5% of the fibers perpendicular to the rest of the fibers). This particular example shows the strong dependence of void morphology on parameters such as the reinforcement volume fraction and architecture. Howe et al. [16], on the other hand, characterized the types of voids formed in carbon/epoxy composite parts manufactured by two different molding schemes: autoclave molding of prepregs and RTM. They found that, at similar fiber volume fractions, voids in the autoclaved laminates were mostly asymmetric and exhibited sharper edges; whereas in the RTM parts voidage was predominantly near-spherical or elliptical. Comparing the reductions in the interlaminar shear strength (ILSS) values caused by voids in each molding scheme, Howe et al. [16] concluded that voids with a more circular shape had less effect on reducing the ILSS than asymmetric voids.

In terms of the void concentration, Varna et al. [12] indicated that RTM-specimens with low void content can achieve high strength levels when tested under uniaxial tension, but also argued that the formation of large transverse cracks can make them brittle, thus leading to low strain to failure. Meanwhile, for laminates with slightly more voids, the fracture mechanism is initiated with the appearance of many small cracks connecting large spherical voids; although, some of these cracks connected small cylindrical voids only. Often times, claim the authors [12], a small crack is arrested at a weft bundle, and the crack tip is somewhat displaced with respect to the first crack. This irregularity in the

crack growth mechanism results in a lower stress concentration and stress level at the fiber bundles, which in turn explains the nominally higher transverse strain to failure of specimens containing slightly more voids. Very few works in the literature have addressed the topic of interlaminar shear strength reduction by discrete voids, or the influence of void shapes in the failure initiation mechanisms. Wisnom et al. [17], for example, observed that in glass/epoxy and carbon/epoxy specimens with discrete inclusions, longer voids could cause premature failure to initiate from the defect, not only by a stress concentration mechanism, but also from the reduction in the load-bearing cross-sectional area.

Successive steps of packing and bleeding - among other procedures - have been recommended to composite manufacturers as a way to obtain parts with low void content [18]. Usually, after the mold is full, the resin injection is stopped and the vents are closed. Thereafter, packing starts by continuing resin injection while keeping the exit vents closed. After the packing is complete, the vents are released to let the resin bleed. Although effective removal of macrovoids and significant voidage reductions are attained by this method, the packing and bleeding sequence increases the total cycle time as well as the fixed costs represented in the wasted resin (ca. US 40 – 50 per pound). The utilization of surfactants in the flow front [9,19], surface waxing of mold walls [20], and vibration-assisted RTM [20,21] are also alternatives for void reduction that have been implemented with mixed results. An optimum condition of fluid impregnation wherein both micro- and macro-flows are balanced seems imperative for minimizing void formation during a given mold filling process. As described before, experiments with

different fiber architectures and model fluids favor the existence of a critical range of capillary numbers where lower void contents can be achieved [7,9,22].

Notwithstanding the physical barriers imposed by the surface and viscous forces, there have been successful attempts to overcome void formation at high-speed molding. Among such strategies, the change of the inlet location [23,24] and the utilization of higher injection pressures [5,25] have demonstrated a significant reduction both in mold filling times and void inclusions. Further, other alternatives that can be readily implemented like preheating the preform to remove volatiles from the sizing system prior to resin injection [26]; and also, applying a “post-fill” cure pressure or “packing pressure” after the mold fill operation, have been also shown to be effective in superseding fluid front influences which otherwise would trigger void formation [13,26,27].

To the best of the author’s knowledge, a systematic investigation to discern the effects of different post-fill pressure levels on void reduction in RTM composites has not yet been undertaken. In the current work, the extent of processing-induced defect reduction attained by applying a post-fill cure pressure at the four different levels: 0, 300, 568 and 781 kPa is studied. All composite parts are reinforced with commercial E-glass-fiber random-mats, and molded with a high-speed molding setup that allowed the filling of a 58 cm³ mold at a constant flow rate in an average of less than 10 seconds. These fill times are consistent with current industrial molding cycles for small to medium sized RTM parts.

3.3 *Experimental Studies*

3.3.1 **Procedure for Composite Fabrication**

Figure 3.1 depicts the major components of the high-speed molding setup used to fabricate random-mat E-glass/epoxy RTM composites. This setup includes a hydraulic press and a rectangular aluminum mold containing the fiber preform. The molding press consists of two hollow cylinders, two plungers and a 40-ton hydraulic (ARCAN, Model CP402) press that provided the force necessary to inject the reacting mixture into a disk-shaped mold cavity. Prior to the injection, EPON 815C epoxy resin (Shell Chemicals) and EPICURE 3282 curing agent are separately loaded into two hollow stainless-steel cylinders. These cylinders had inner diameters of 55.5 mm for the resin and 25.5 mm the curing agent, such that a mixing ratio of 4.7 to 1 by volume is achieved with the constant displacement rate of the plungers. During mold filling, a linear velocity of 2×10^{-3} m/s of the hydraulic ram is maintained through most of the 152.4 mm stroke, which yields an injection rate of approximately $5.32 \text{ cm}^3/\text{s}$.

The resin and curing agent flows merge in a T-connector and thereafter pass through a Statomix[®] inline mixer (ConProTec, Inc.) comprising 32 alternating helical segments placed inside a 155 mm-long polypropylene tube with 5 mm inner diameter and 8 mm outer diameter. Transient pressure profiles of the completely mixed polymer ($\mu = 0.96$ cP) are recorded with a pressure transducer located at the injection port. The center-gated disk-shaped aluminum molds are made of two square walls with dimensions: 228.6 mm x 228.6 mm x 6.35 mm, separated by a 3.18 mm-thick aluminum spacer plate.

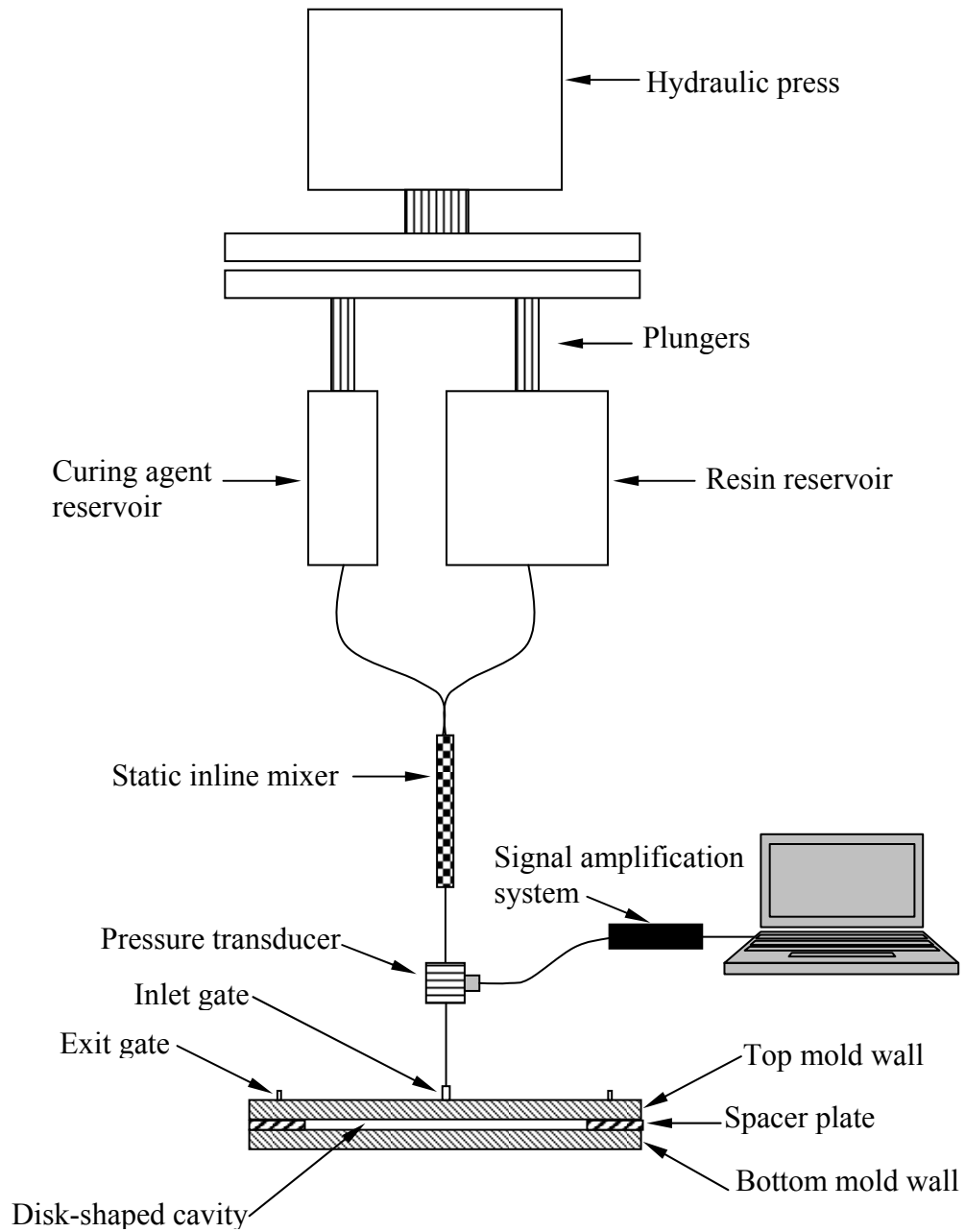


Figure 3.1: Experimental molding setup used to manufacture RTM composite disks.

To create the mold cavity, a 152.4 mm diameter disk is cut out of the center of the aluminum spacer plate. Both the top and bottom aluminum parts had a circular groove of 184 mm in diameter and 0.3 mm in depth carved out to accommodate a 4-mm O-ring rubber seal. Inlet gate and exit vents are drilled and tapped on the top mold wall. The inlet is located in the center of the disk and has either plastic or brass barbed fittings connected to the feeding hose (ID=6.2 mm). The four symmetrical exit vents (ID=1.6 mm) are positioned 90 degrees apart at a radius of 88.9 mm.

The reinforcement utilized in this study is a randomly-oriented, chopped glass fiber mat (FiberGlast part # 250), having a planar density of 0.459 kg/m². Among the attractive features of this preform are the planar isotropy and relatively low cost. Four circular layers (152.4 mm diameter) of the preform were cut and stacked into the mold cavity, which represented a fiber volume fraction of approximately 17.5% in all composite parts fabricated. To impregnate the preform, the resin and curing agent mixture is injected into the mold cavity by a constant displacement of the plungers as described above. On average, filling the mold cavity with the preform took less than 10 s, after which the exit gates are securely clamped and no resin bleeding is allowed to occur. Thereafter, the hydraulic press is further operated for a few additional seconds until the desired post-fill pressure is reached at the inlet.

A total of four post-fill pressures, i.e. 0; 300; 568; and 781 kPa, is used to investigate post-fill pressure effects on overall void content as well as the shape, size and spatial distribution of voids. Pressure values presented here are measured with an accuracy of

less than ± 1 kPa. In order to prevent anomalies due to imperfect sealing, expansion of the hoses, or even the deflection of the mold walls that could cause a significant drop in the post-fill pressure, continued monitoring of pressure levels lasts for at least one minute before the inlet gate is finally clamped. Molded disks were cured inside the molds at room temperature for 48 hours until the disks reached their “green state”, and then were taken out of the molds. Finally, to ensure complete cross-linking of the resin, the disks were left to post-cure at room temperature for a minimum of one month before further cutting composite samples and polishing for void analysis.

3.3.2 Transient and Packing Pressure Measurements

The relationship between volumetric flow rate and fill pressure during liquid composite molding is an important design parameter, which is in most cases described by a flow through porous media model given by the Darcy’s law. In the current study, the impregnating resin was injected at a constant volumetric rate. Therefore, given the circular geometry of the mold cavity, the filling pressure steadily increased as the flow front moved radially outward. To quantify the transient pressure profiles during filling, as well as the post-fill pressure levels, a pressure acquisition and monitoring system was installed at the inlet port of the mold as depicted in Fig. 3.1. The acquisition system consisted of a flash diaphragm pressure transducer (Sensotec BP357BR Model S), mounted on the hose between the mixer and the mold inlet gate; a custom built signal amplification system based on an AD620 in-amp; and an Omega Daqbook acquisition software installed on a laptop computer. During mold filling, the resin flow pressure at the mold inlet was converted to a voltage signal by the pressure transducer. This output signal was conditioned for the data acquisition system through the amplifying system,

which amplifies the voltage, isolates the signal and lowers the transducer output impedance. Pressure data were recorded at a frequency of 10 Hz.

3.3.3 Modified Capillary Number Determination

As was mentioned in the introduction, fluid front progression during preform impregnation is governed by macro- and micro-scale phenomena that are directly linked to void occurrence. To date, most attempts to understand the mechanics of void formation at the flow front have been based on flow visualization experiments performed with model fluids over fibrous reinforcements of different architectures. These studies have demonstrated the existence of so-called critical modified capillary numbers for void formation and advection, which are assumed to be scalable to actual liquid composite molding. It is not clear from the current literature if these master curves relating void area fraction with modified capillary number are directly applicable to RTM molding operations involving reacting polymeric systems. For this reason, herein we investigated the range of modified capillary numbers reached with the mold press depicted in Fig. 3.1, which will be referred to as high-fill velocity impregnation, and correlated them to the overall void volume fraction. An analogous comparison is established with data from previous experiments [13] obtained at lower injection flow rates (i.e. low-fill velocity) in a molding system comprising the same polymer, fiber type and fiber volume fraction. First, the surface tension of the epoxy, curing agent and the reacting mixture were measured in order to calculate the variability limits of the modified capillary number (i.e. Ca^*) during mold filling with respect to changes in the liquid surface energies. The method followed for these measurements is based on the well-known Wilhelmy equation,

which expresses the force, F , exerted by the tested liquid over a partially immersed solid probe, as:

$$F = W + P\gamma \cos \theta - B, \quad (3.4)$$

where W and P are the weight and perimeter of the solid probe, respectively; and B is the buoyancy force. This latter parameter is usually neglected if the solid is slightly immersed and dimensionally uniform. All measurements were carried out in a dynamic contact angle analyzer (Cahn Instruments, Inc., DCA-322), and the experimental procedure followed was very similar to that used for measuring contact angles on fibrous reinforcements [28]. First, an approximately 5 mm-long flamed platinum rod with 254 μm diameter was hung from the arm of a highly sensitive microbalance (i.e. 0.1 μg accuracy). The clean platinum rod has a high surface energy, and thus, it is expected that the contact angle of both the monomers and the pre-polymer against the metal surface would be zero. Once the experiment started, 3 mm along the platinum rod axis was immersed into the liquid at a very slow stage velocity of 12 $\mu\text{m/s}$. Force and time data generated during each run were automatically recorded on a computer; and with aid of a software (WinDCA 1.01), the surface tension was calculated from the most stable force reading when the liquid has receded over the platinum rod surface. Measurements for the polymer required a preliminary step consisting of loading the exact volume ratio of resin to curing agent into a 60 ml plastic syringe, and then manually injecting the mix through a Statomix[®] inline mixer, similar to the one used during composites molding for further mixing. Surface tension of epoxy polymers is known to vary with the conversion grade of the reaction, a.k.a. as the degree of cure. Thus, the data presented here correspond to

the average of measurements taken at approximately the same time interval on at least five different batches of resin/curing agent mix. Reported results for the resin and curing agent correspond to the average of individual measurements performed with 4 to 6 fresh samples.

Given that the injection is performed at constant volumetric flow rate, the radial superficial velocity is an inverse function of the radial distance from the injection port. Hence:

$$V_{ave} = \frac{Q}{A} = \frac{Q}{2\pi H r(1-V_f)}, \quad (3.5)$$

where Q is the resin flow rate, A is the cross-sectional area of the resin flow at a given time; H is the thickness of the mold, r is the radius at which the capillary number is calculated, and V_f the fiber volume fraction of the molded composite. As mentioned before, Patel et al. [6] proposed the idea of a modified capillary number to account for the effect of contact angle between fiber and resin. The same approach has been also used recently by others [29] to correlate microvoid formation during RTM molding. In the current work, we recurred to single-fiber experiments based on the Wilhelmy technique to measure the wettability characteristics of the commercial fiber by the resin. In this case, the liquid probe had a known surface tension and the only parameter to evaluate was the contact angle between the glass fiber and the liquid. Instead of a single equilibrium contact angle, θ , this test allows to record both the advancing (θ_a) and (θ_r) receding contact angles.

The fact that the Wilhelmy method provides an estimate of a dynamic contact angle constitutes a major advantage when trying to extrapolate the results to a macroscopic scale (e.g. moving liquid fronts during composite fabrication imply dynamic contact angles). Therefore, herein all calculations involving the modified capillary number include the advancing contact angles measured for the pure epoxy resin and fibers from the random-mat preform. These advancing contact angles have been already presented elsewhere [28]. It is worth noting that the fibers were relatively small in diameter (e.g. 13 μm), and hence bending of the fibers was realized as a source of errors when submerging the fibers into test liquids. In consequence, a stage velocity of 2 $\mu\text{m/s}$ was set for all experiments to avoid disturbances in the recorded force coming from viscous friction. For this reason, contact angle measurements with the reacting mixture proved impractical, as the necessary experimentation time was much longer than the gelling time. Surface tension, viscosity and other physicochemical parameters of the monomers and polymers used in the current study are presented in Table 3.1.

3.3.4 Voids Characterization

Voidage evaluation in composite materials by means of microscopic image analysis has been demonstrated to be among the most accurate methods for measuring the true void content [30]. Furthermore, the image analysis technique has the advantage of providing detailed information of other important parameters such as voids distribution, shape, and size that cannot be assessed by either physical (e.g. relative density) or chemical (e.g. acid digestion) methods. Usually, voidage measurements by microscopic imaging imply the random acquisition of pictures over the area of interest followed by the statistical averaging of the void areas measured in each picture.

In the current work, unlike most previous work, image analysis was performed over the entire cross-sections of specimens cut from the center of completely cured disks molded at each post-fill pressure. Hence, all voids that could be identified at the working magnification were included in void content calculations. The specimens had an average length and thickness of 75 mm and 3.98 mm, respectively, and were embedded into a quick cure acrylic resin (Allied High Tech. Products, part # 170-10000). Once embedded, the samples were polished with a series of polishing pastes (Clover Compound) with grits sizes ranging from 180 (e.g. 80 μm average particle diameter) to 1200 (15 μm) in six successive steps. After each step, the samples were set for 40 minutes in an ultrasonic cleaner at moderate sonication (19 W) to completely remove residues of the polishing compound.

The microscopic image analysis started by dividing each 75-mm long sample into five 15-mm long regions along the radial direction. Each cross-section was then entirely scanned at 200x magnification using a MEIJI optical microscope. At this particular magnification, every frame displays approximately $0.71 \times 0.53 \text{ mm}^2$, which needed the capture of eight frames to scan across each sample thickness (i.e. 3.98 mm) at a particular radial location. Each time a void was clearly identified the picture of the region containing the void was taken. A total of approximately 1400 frames containing voids were taken from all radial locations in all samples analyzed.

In addition to the image analysis in the radial direction, voidage distribution through the specimen thickness was also recorded. To do that, frames from the top layer (defined as

the area within 1.07 mm from the top surface), bottom layer (1.07 mm from the bottom surface), or inner layer (intermediate region) of the cross-sections were investigated. As described before, the voids entrapped within a particular cross section were identified and their images captured using a PC-based CCD camera attached to the optical microscope. Each picture was then processed using the image analysis software UTHSCSA Image Tool[®], which allowed simultaneous measurements of voids' area (A) and maximum length (L_{max}). Due to the planar randomness of the preform and the shape of the mold, the flow is assumed to depend only on the radial location for each disk. Hence, the void volume fraction at each cross section was assumed to be linearly equivalent to the ratio of the total void area by the entire area of the cross section [31].

Figure 3.2 depicts images of composite cross-sections with various voidage levels, as well as voids with different sizes and shapes representative of the voids encountered within the studied composites. In these images, the continuous phase (i.e. polymeric matrix) appears as a gray background, whereas the white circular and elliptical objects correspond to glass fibers oriented perpendicularly and in an angle, respectively, to the cross-section. The groups of fibers observed in close proximity to one another exhibit similar orientations and correspond to fiber tows bundled together within the random mats.

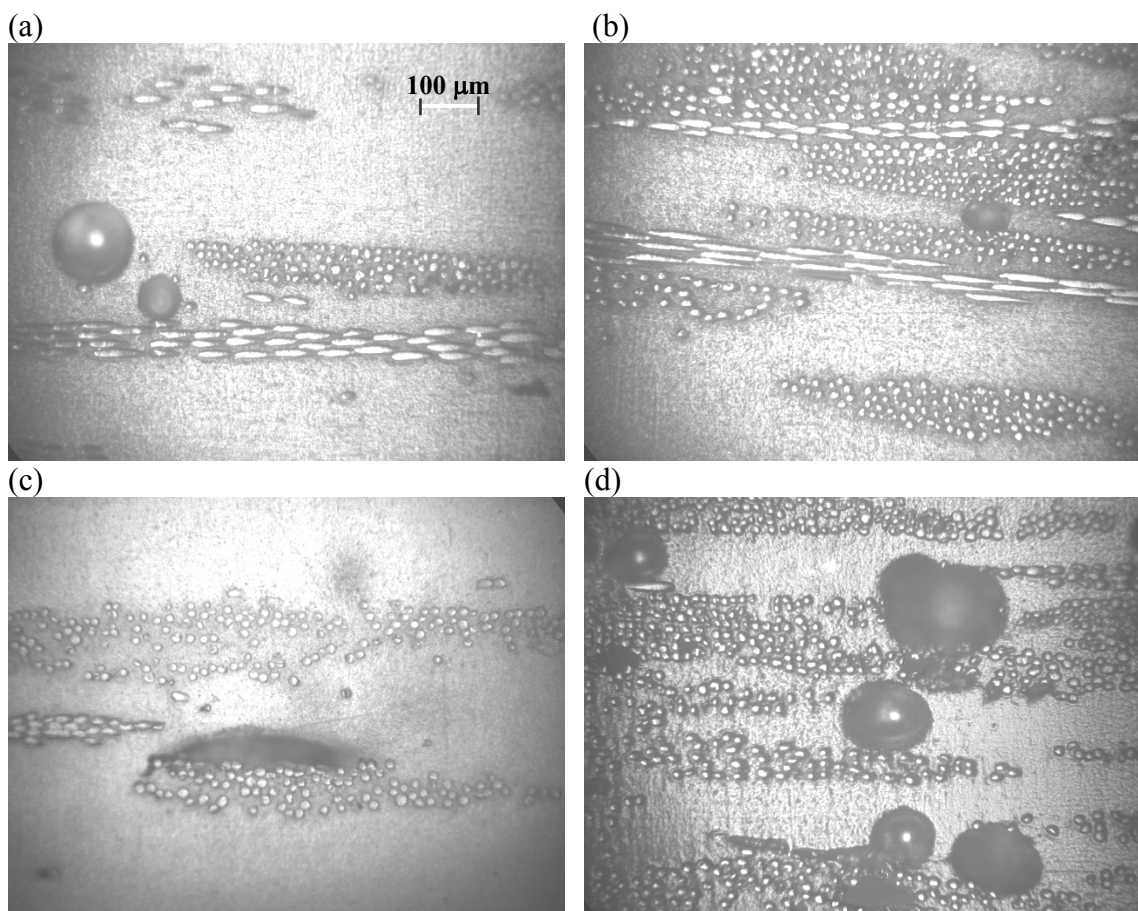


Figure 3.2: Representative micrographs from composites molded with different post-fill pressure specimens at 200x magnification. (a) Circular voids of different shapes located in matrix-rich area; (b) Ellipsoidal void in the inter-tow space; (c) Irregular void engulfing a tow of fibers; (d) Example of high voidage area in composites molded without a post-fill pressure.

3.4 *Results and Discussion*

3.4.1 **Transient Inlet Pressure**

Positive displacement of the plungers by the molding press ensured that infusion of the reacting polymer through the random-fiber preform would take place at a constant volumetric flow rate. Due to the circular mold geometry, the resin front advances through the dry preform and towards the exits; and in most cases, a radial liquid front symmetry can be assumed. Three transient positions of the advancing flow front inside the mold are depicted in the top part of Fig. 3.3. Very close to the entrance, the impregnating front moves at high velocities yielding much faster local velocities at the mold cavity mid-plane. Further away from the injection port, the advancing front velocity decreases monotonically at radial positions (i.e. bottom part of Fig. 3.3). The total energy of the liquid is reduced due to the mold geometry, together with the resistance exerted by the dry preform surface. This energy dissipation becomes greater as the dry surface area opposing the flow increases radially, until the fluid impregnates the whole solid and finally reaches the vents.

In order to maintain a constant impregnation rate, the pressure applied to the liquid must also increase so sufficient energy is provided to impregnate the solid. Transient inlet pressure readings of four different mold-filling experiments are shown in Fig. 3.4a. In this figure, four different zones that are common to all filling experiments can be identified, *inter alia*, the injection or fill zone, the peak pressure zone, the plateau region and the step zone. Within the fill zone, pressure increases at a very steep rate.

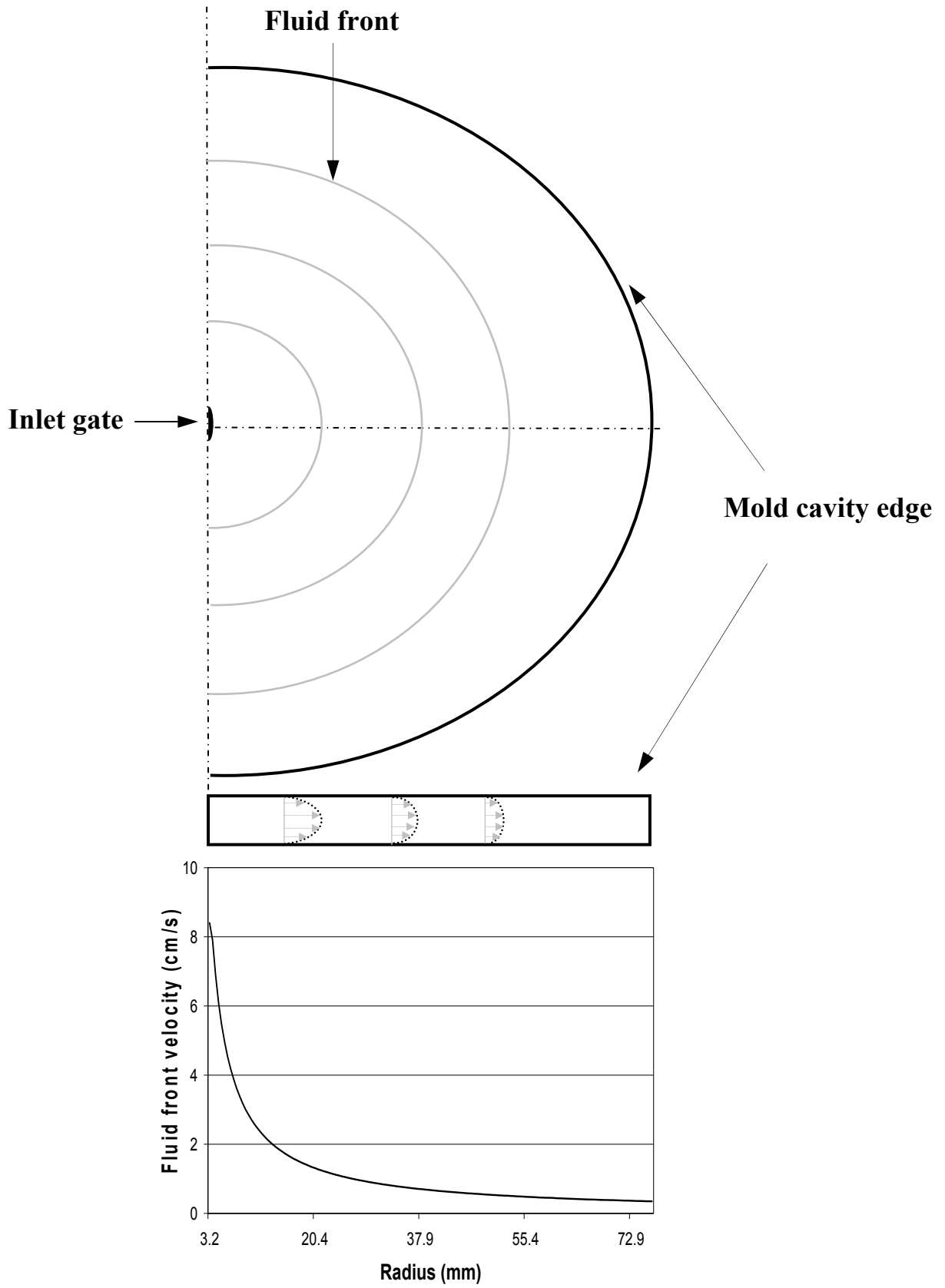
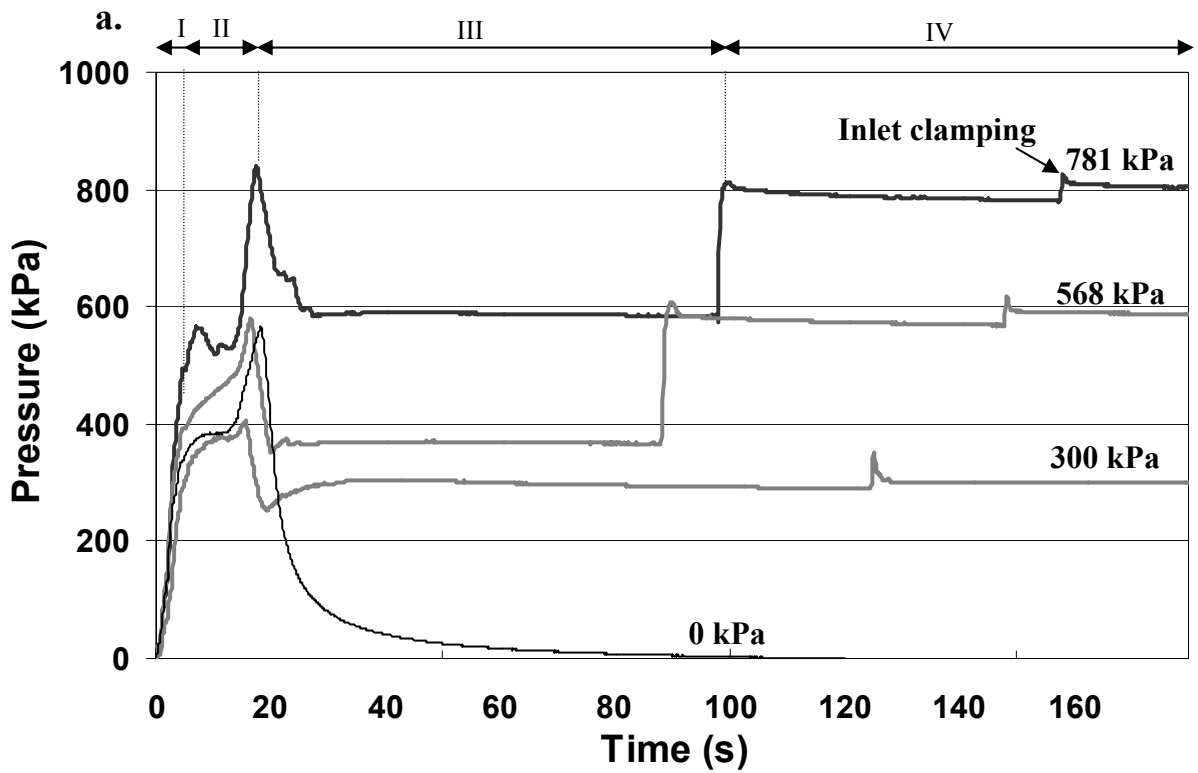


Figure 3.3: Advancing fluid front superficial velocity at different radial positions inside the mold cavity preloaded with 17.5% E-glass fibers by volume.

Note, however, that the change in injection pressure with respect to time was the same for all molded composites. Thus, considering that these parts had the same fiber volume fraction, it can be concluded that, independent of random variations in permeability, the flow field was approximately the same for all filling operations. This latter result is significant because it precludes the probability of obtaining different voidage levels in molded parts due to uncontrolled flow behavior during filling. After the fill zone, pressure readings start showing some discrepancies between different experimental runs. Note that although each molding experiment took approximately the same time to reach the peak pressure (i.e. 18 s), the peak value was not the same among experiments. In Fig. 3.4b, a close-up of the mold vent region illustrates the relative dimensions of the narrow opening and the mold cavity. Narrower flow channels formed between the spacer plate and the top mold wall impose greater resistance to flow that translates into higher-pressure drops. Thus, peak values recorded in Fig. 3.4a are more suggestive of random variations in the constricted channel spacing than to any direct relationship with the process variables.

It can be inferred from Fig. 3.4b that channel spacing will depend on the deformability of the rubber o-ring utilized to seal the mold. The applied force and the condition of the o-ring during mold assembly are believed to affect the thickness of this narrow channel, and thus the peak pressure reached in zone II. Once the resin starts flowing through the narrow channel and out to the vents, the molding press is turned off, stopping resin injection. This event marks the onset of zone III.



b.

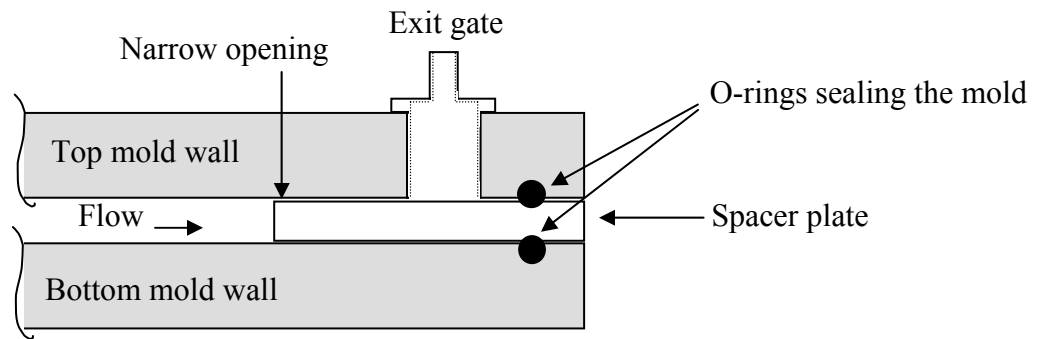


Figure 3.4: (a) Inlet pressure profiles during mold filling of composite disks; (b) Close-up of air vent region of the mold.

As seen in Fig. 3.4b, between the time injection ceases, and the moment all exit vents are securely closed, there is a monotonic decrease in the recorded pressure that is consistent with the tendency of the system to attain a balance between inlet and outlet pressures. Thereafter, the pressure levels-off to a plateau pressure value, and remains constant until the commencement of the step zone (i.e. zone IV). In the case of experiments with zero post-fill pressure, no compressing action took place, and as a consequence, the pressure continued decaying asymptotically.

Zone IV began when the resin inside the mold was compressed to the desired post-fill pressure level (e.g. step zone). Two or three minutes after the post-fill pressure is applied the injection port was clamped. The sudden contraction of the mold opening is registered in the pressure charts (Fig. 3.4a) as a minute pressure peak (ca. 60 kPa) towards the end of the experiment. In summary, the transient pressure have shown that both the mold filling, as well as the establishment of a final post-fill pressure, were adequately controlled with the current molding setup and molding procedures.

3.4.2 Effect of Injection Rate on Void Content of Resin Transfer Molded Disks

One of the advantages of RTM over similar composites fabrication techniques lies in the possibility of attaining short cycle times. Therefore, a critical step during RTM molding is to impregnate the preform as quickly as possible while minimizing undesirable features such as a race-tracking, high void content, or incomplete wet-out that may result in premature failure or poor overall performance [32,33]. In an earlier study [13], the effect of volume flow rate and post-fill cure pressure on the mechanical properties and overall

void content of RTM composites with identical mold geometry, fiber architecture, volume fraction and epoxy system, was investigated. Therein, four different constant injection rates of 0.067, 0.2, 0.6 and 1.0 cm³/s representing more than an order of magnitude change in fill times were used. Corresponding fill times for these injection rates were: 900, 300, 100 and 60s, respectively. Tensile strength and stiffness reductions on the order of 14 and 13% due to increased fill rates suggested that an injection rate increase had detrimental effects possibly associated to increased void formation. Conversely, significant improvements in the order of 13 to 15% were observed for the strength and elastic modulus when a range of post-fill cure pressures between 228 and 683 kPa was applied. With the objective of evaluating to what extent the application of a post-fill cure pressure can be regarded as an efficient method to reduce the flow-induced voidage in composite materials, data from molding experiments carried out at low-speed (i.e. 0.20 cm³/s) in the previous work [13] are compared to analogous RTM experiments conducted at injection rates almost thirty times higher (i.e. 5.32 cm³/s). There is approximately a 30-fold reduction in the fill time between the low- and high-speed molding schemes, which we consider to be significant in terms of extrapolating these results to the industrial fabrication scale.

With the exception of the work by Rohatgi et al. [34], not many of the flow front visualization studies presented in the literature have dealt with void formation when the impregnation velocity is high. Figure 3.5 shows data taken from Rohatgi's work corresponding to the trend in area void fraction as a function of liquid injection velocity for silicone oil, diphenyl-octyl-phthalate (DOP) and ethylene glycol when flowing axially over a unidirectional stitched fiberglass mat (CoFab A108).

In the same figure, the range of liquid front velocities inside the molds (i.e. maximum velocity at the entrance, and minimum close to the exit ports) has been incorporated during the high-fill and low-fill velocity processing of random-fiber/epoxy composites (i.e. abscissa); and in the ordinate, we show the overall void content for those parts molded without extra packing (post-fill pressure = 0 kPa). As suspected, the void content in the composite part strongly depends on the liquid front velocity. At low-fill velocity, the void content level is below 1%, which in the composites industry is regarded as a quality threshold value for parts with good mechanical performance [18]. As long as the injection velocity increases, the entrapment of air is more likely to occur and thus the void content inside the part reaches an undesirable level of 2.15 %, as observed in the current study.

It would be easy to conclude that reducing the injection velocity further below the low-speed velocity range used herein could completely eliminate the driving forces for void formation. Such an argument has already been proven wrong by studies on air entrapment during the impregnation of fibrous reinforcement with model fluids flowing at very low velocities. In this case, the main front velocity lags behind the faster capillary flow occurring inside the narrow inter-fiber spacing, and extensive formation of macrovoids takes place [7].

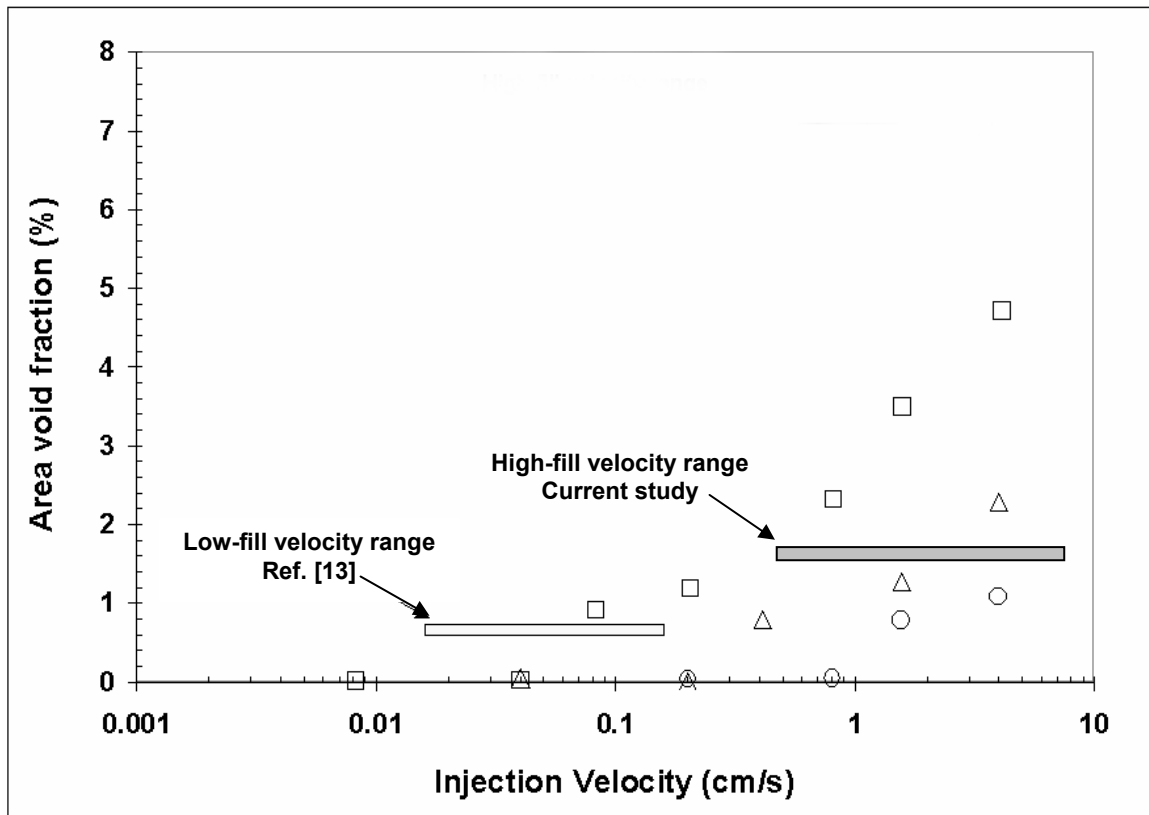


Figure 3.5: Effect of injection velocity on void formation in RTM composites. Data for model fluids taken from Rohatgi et al. [34]: \square Silicone oil; \triangle DOP oil; \circ Ethylene glycol.

The results presented by Rohatgi et al. [34], shown in Fig. 3.6 as data-points, reveal another interesting trend. The area void fraction was - as expected - an increasing function of the injection velocity for all test liquids utilized. However, the major factor determining the ultimate level of air entrapment present was the fluid's physicochemical characteristics. For instance, viscous fluids of relatively low surface tension are more prone to engulf air when the flow front advances at a high speed. When silicone oil (viscosity = 193.4 cP, $\gamma = 21.0 \times 10^{-3}$ N/m) was injected at a velocity of 4 cm/s, the void area of air trapped was close to 5%, whereas at the same velocity, only a 1% area void fraction was trapped by ethylene glycol (viscosity = 19.8 cP, $\gamma = 19.8 \times 10^{-3}$ N/m). These results corroborate our data, in the sense that they explain why the effect of molding speed on the final void content is so dramatic when using the commercial epoxy polymer. As presented earlier, the viscosity of the polymeric mixture used in the current study is on the order of 960 cP, which is five times greater than the model silicone fluid used by Rohatgi et al. In addition, these fluids would exhibit different wettability scenarios with the preform fibers. Therefore, it seems reasonable to assume that with a higher-viscosity fluid, any increase in the front velocity would lead to more extensive entrapping of air than with the silicone oil. In fact, taking an average value for the injection velocity at the two molding schemes (e.g. 0.088 cm/s for the low-speed range and 2.5 cm/s for the high-speed range), and comparing them to similar injection velocities for the silicone oil; it is clear that while for the model fluid there is a five-time increase in area void fraction between the low and high injection velocities, a 3-fold change in void content takes place with the commercial resin. Other factors, such as the difference in fiber volume fraction (e.g. 20% in the current study vs. 43% in Rohatgi et al.) and the fiber orientation (e.g.

random-mat vs. unidirectional) must also be considered in order to explain the slightly lower void contents in our samples.

Using the physicochemical data listed in Table 3.1 for the polymer, and the modified capillary number Ca^* given in Eq. (3.5), we calculated the variability limits of the nondimensional modified capillary number for both the high- and low-speed impregnation flows.

Table 3.1: Physicochemical and flow parameters for low- and high-speed RTM processing of composites containing 17.5% by volume of randomly-oriented, E-glass fibers.

FLUID	VISCOSITY μ (cP) at 25°C	SURFACE TENSION γ (mN/m) at 25°C	ADVANCING CONTACT ANGLE (θ)	Range of Critical Capillary Number (Low-speed fill) Ref. [13]	Range of Critical Capillary Number (High-speed fill)
EPON 815C	500 – 700 [†] (Avg. 600)	40.6±0.5 [‡]	34° ± 5 [‡]	0.0025 - 0.036	0.068 - 0.95
EPICURE 3282	4000 – 4900 [†] (Ca based on 4000 cP)	48.0±1 [‡]	0° (assumed)	0.012 - 0.167	0.317 - 4.4
Polymeric Mixture	960 [‡]	36.3±0.8 [‡]	~ 34° (assumed)	0.009 - 0.064	0.12 - 1.7

[†] Reported value from manufacturer

[‡] Measured.

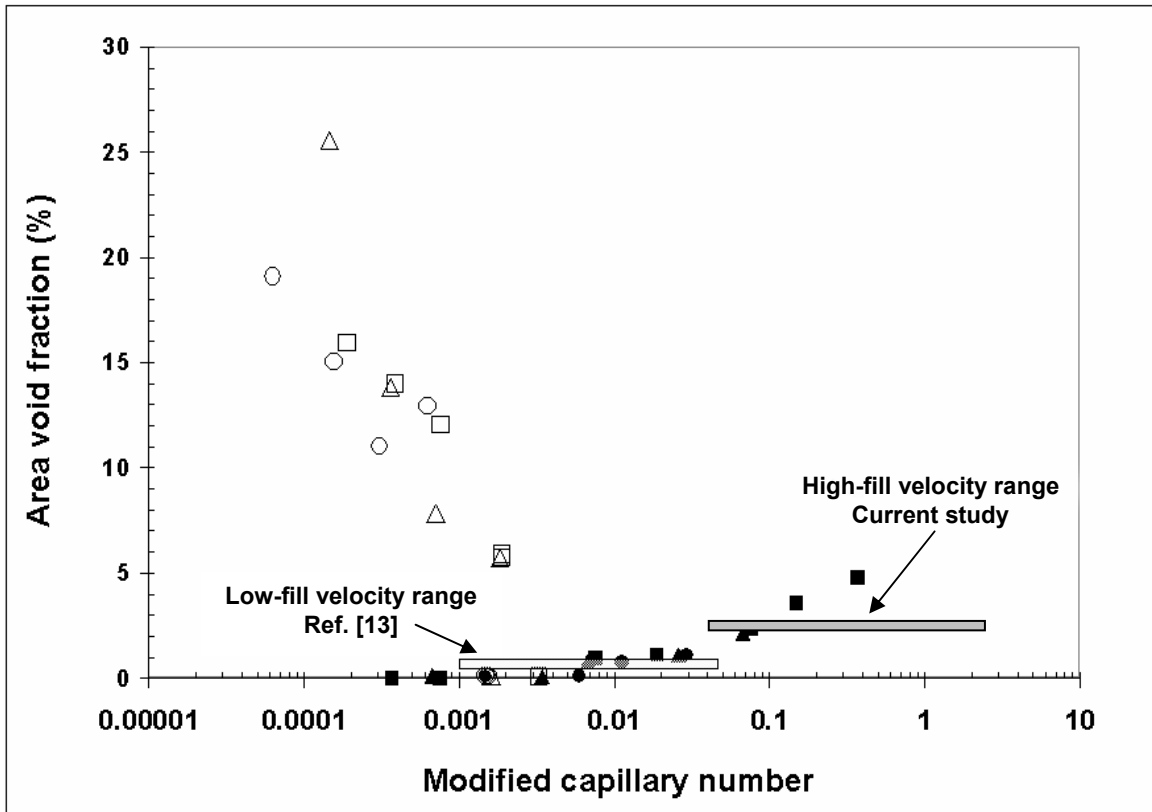


Figure 3.6: Effect of capillary number on void formation in RTM composites. Data for model fluids taken from Rohatgi et al. [34]: □ Silicone oil, macro-voids; ■ Silicone oil, micro-voids; △ DOP oil, macro-voids; ▲ DOP oil, micro-voids; ○ Ethylene glycol, macro-voids; ● Ethylene glycol, micro-voids.

From Rohatgi's data, it can be inferred that reinforcement impregnation at extremely low modified capillary numbers favors extensive voidage accumulation in the parts, primarily composed of circular macrovoids. As the impregnation velocity increases, so does the modified capillary number and the macrovoids start to mobilize and void content values reduce considerably. Critical modified capillary numbers for void mobilization are on the order of 1.0 to 2.2×10^{-3} , as observed in this plot, and also corroborated by other studies [7,14] mentioned in the introduction. Next to the critical modified capillary number of void mobilization there is a zone for "optimum" impregnation wherein the void content fluctuates around 1%. According to theoretical calculations [29] relating capillary number to the time ratio describing the competition between intra-tow and inter-tow flow fronts, the range of low void content is located in a region of capillary numbers between 6×10^{-3} up to 0.03. A further increase in the injection velocities leads to higher capillary numbers, which triggers the entrapment of air, and hence the void area fraction starts augmenting. The types of voids formed at these high capillary numbers are quite distinct, and mostly correspond to ellipsoidal microvoids [34].

Comparing the void area fraction formed at the range of capillary numbers established during the molding process at high speed, with the air entrapment levels occurring within the low-speed velocity range, the main conclusion that can be drawn is that our data matches reasonably well with the trends observed by other authors [9,34]. That is, at capillary numbers well above the so-called "optimum" range the void content was relatively high (i.e. 2.15% for the high-speed velocity range). Whereas, for the low-speed molding, the capillary numbers were all within, or very close to, the "optimum",

and therefore, the void content was almost negligible (e.g. around 0.7%). Note that the results described so far are only for the overall void content of parts molded at either high- or low-speed velocities, but not subjected to a post-fill pressure. These void contents obtained in composites molded without any further packing pressure will later be used as the baseline to compare the extent of void reduction achieved when a post-fill pressure is applied.

3.4.3 Effect of Post-Fill Pressure on Void content

As discussed earlier, void contents from composites molded at different post-fill pressures are assessed by means of microscopic image analysis. Figure 3.7 depicts void content reduction induced by applying different post-fill pressures. Void content reduction is defined as the ratio of the final void content reached after packing, to the baseline void content recorded when no post-fill pressure is applied (i.e. 2.15% baseline void content in the current study, and 0.7% for data from reference [13]). The main trend inferred from Fig. 3.7 is that, independent of the injection mode or initial void content value, the methodology of applying a post-fill pressure significantly reduces the final voidage levels in the composite parts. For instance, applying a post-fill pressure as low as 300 kPa to the part molded at high-fill velocity results in an elevated void content reduction of 88.32%. Similarly, reductions of the order of 91.16 and 97.2 % in voidage are registered when post-fill pressures of 568 and 781 kPa are applied, respectively. However, lower levels of void content reduction (34 to 57%) were observed in composites molded in the prior study [13].

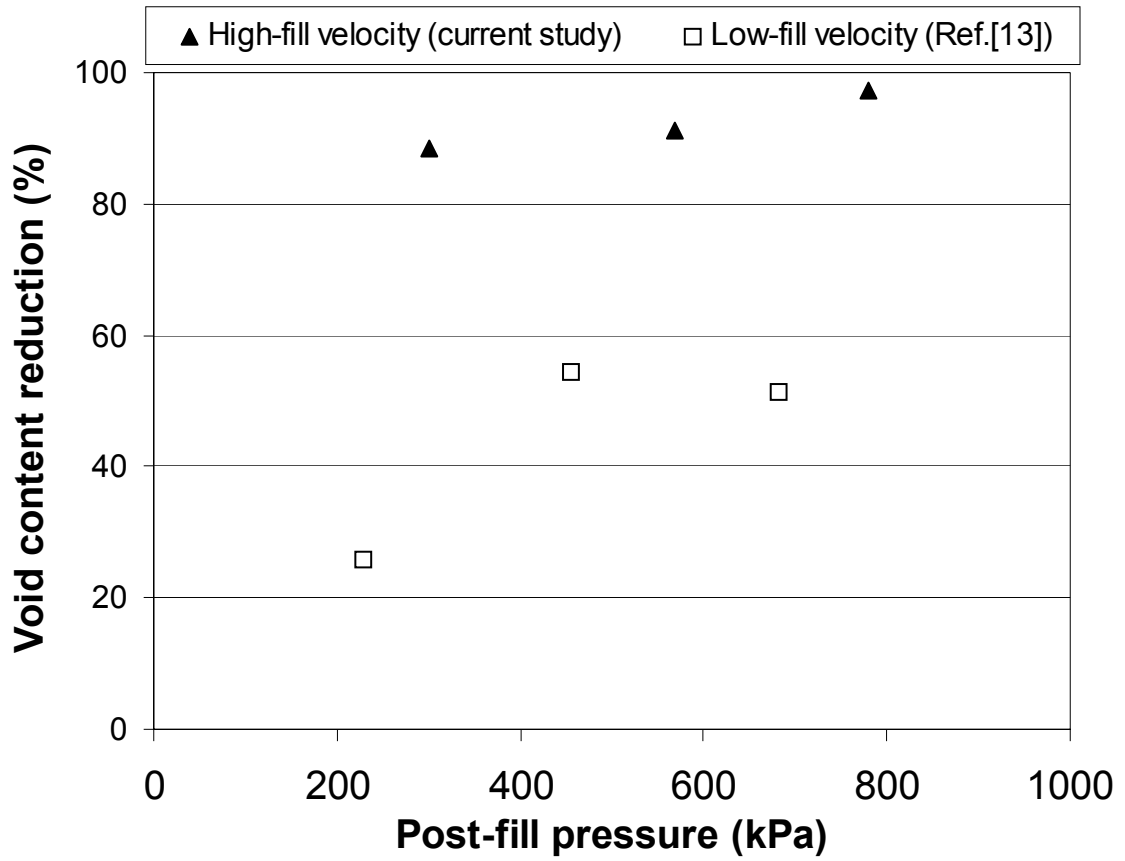


Figure 3.7: Void content reduction due to different post-fill pressures applied to RTM composites molded with different fiber contents at different fill velocities.

This difference in void content reduction is believed to originate from the lower baseline void content of composites molded at low-fill velocity (i.e. 0.7%). Applying a high post-fill pressure is hereby found to be an effective method for void removal in resin transfer molded composites.

3.4.4 Effect of Post-Fill Pressure on Void Size Distribution

Figure 3.4 depicts images of composite cross-sections with various voidage levels, as well as voids with different sizes and shapes. Figure 3.4d exemplifies a high voidage area taken from the composite baseline sample molded at zero post-fill pressure. In order to classify the observed differences in void sizes, captured void surface area data, measured earlier, are utilized by defining an equivalent diameter, D_{eq} , as:

$$D_{eq} = \sqrt{\frac{4A}{\pi}}, \quad (5)$$

where A is the measured area of the void. Three different size categories are arbitrarily defined. Large voids are defined as those voids with an equivalent diameter greater than 100 μm , i.e. $D_{eq} > 100 \mu\text{m}$; while voids with an equivalent diameter lower than 50 μm are regarded as small voids. Intermediate equivalent diameter values, i.e. $50 \mu\text{m} < D_{eq} \leq 100 \mu\text{m}$, correspond to medium size voids.

A typical example of large circular voids is presented in Fig. 3.2a. The void on the left end of the picture has a diameter of ca. 130 μm , which is a large size according to the classification defined above. The other void, shown in the same picture, has a diameter smaller than four times the fiber diameter (i.e. 50 μm). Note that these two voids are

both located within the matrix area. Voids that are trapped in the inter-tow spacing are forced to conform to the channel geometry. As it is seen in Fig. 3.2b, they are mostly small and elliptical. In Fig. 3.2c, a couple of small and irregular voids are depicted. The irregular voids were, in most cases, found either inside the intra-tow areas or engulfing a group of fibers from a tow. It appears as if they were originated from rounded bubbles that are pushed into the tows by a high shear force during the resin flow. Figure 3.2d exemplifies a high voidage area taken from the composite sample molded without applying a post-fill pressure.

Using the size categories herein defined, void size distributions are calculated for the four molded composite disks, and the results are presented in figure 3.8. In this figure, large and medium voids are seen to literally disappear as higher post-fill pressure is applied. Small voids occurrence, on the other hand, sharply increase from barely 40% in the baseline composite to almost 90% in both disks molded at 568 and 781 post-fill pressure. These results are expected since there is some evidence in the literature [18,26-27,35] suggesting that high molding pressures (0.1-0.9 MPa) may reduce void occurrence in composites by a mechanism involving the disruption of void nucleation and growth dynamics, as well as by the increase in the driving force for mass transfer taking place when the pressure outside the voids is higher than that of the air in their interior [3]. Lundström and Gebart [10] talk about a compression effect over the voids inside a laminate when the cure pressure is increased after filling. These authors even suggest that such an increase in the final pressure could have a similar effect as applying vacuum. Some of the mechanisms described above are perhaps contributing to the final void content reduction observed within our samples.

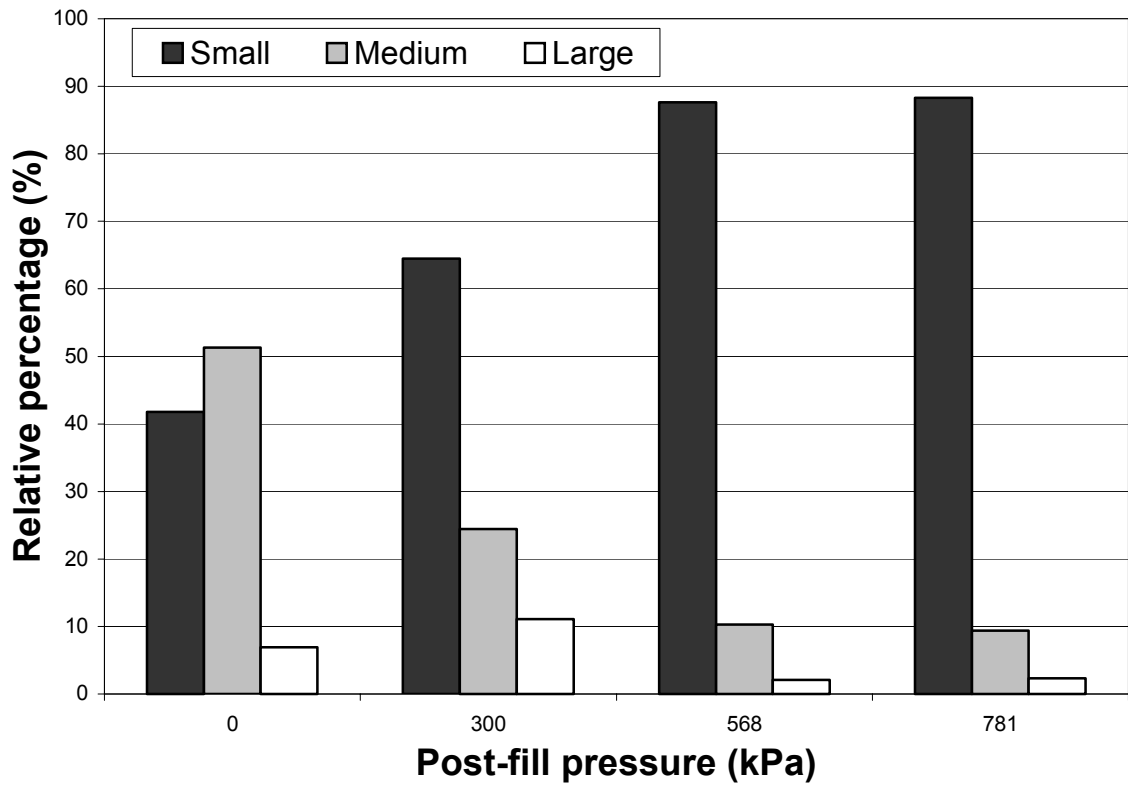


Figure 3.8: Void size distributions for RTM composites containing 17.5% fibers by volume molded at different post-fill pressures.

3.5 Conclusions

The mechanical performance of fiber-reinforced composites is strongly linked to the adhesive strength of their interfaces, as well as to the presence of process-induced defects such as voids and dry areas. To date, there is no commercial method capable of manufacturing completely void-free parts. The existing alternatives to reduce voidage, either incur high operational costs, or have not been successful at all. In this study, an assessment on the extent of voidage reduction, attained when different post-fill pressure levels are applied to the mold after complete filling, has been performed. The first set of results includes the effect of flow front velocities on the formation of voids when post-fill pressure is not applied. Previous data [13], obtained in an RTM setup for low-speed processing (e.g. flow rate $0.2 \text{ cm}^3/\text{s}$), was compared with the current molding procedure (e.g. high-speed processing) that was capable of injecting at flow rates in the order of $5.32 \text{ cm}^3/\text{s}$. A 75% increase in the overall void content takes place in the composites molded at high-speed compared to the same type of parts molded at lower volume flow rates. Furthermore, overall void area fractions in the composites molded with both processing schemes were found to be a function of the modified capillary numbers and flow front velocities, in accordance with data presented in the literature for model fluids.

Transient pressure measurements at the injection port revealed that, both the filling operation as well as the establishment of a final post-fill pressure was adequately controlled with the current molding setup and molding procedures. The major effect observed by applying the extra packing was a reduction of more than 88% in overall void content from the baseline level (i.e. 0 kPa) for composites molded with the short fill time

setup. Finally and in terms of the void size, the most striking observation was that small voids augment their relative presence with respect to the medium and large voidage as the post-fill pressure increases. This is consistent with the disruption of the pressure balance between the air pressure inside the void and the pressure surrounding the void (i.e. post-fill pressure).

3.6 References

1. Johnston N. J., In: *Book of Abstracts, Composites 2000: An International Symposium on Composite Materials*. University of Delaware, 2000.
2. Fong L. and Advani S., In: *Resin Transfer Molding - Technical Report CCM 95-09*. University of Delaware Center for Composite Materials. 1995
3. Roychowdhury S., *Void Formation and Growth in Amorphous Thermoplastic Polymeric Materials*, PhD Thesis, University of Delaware, Newark, DE. 1995
4. Judd N. C. W., and Wright W. W., *SAMPE Journal*, 14(1), 10, 1978.
5. Thomason, J. L., *Composites*, 26(7), 467, 1995.
6. Patel N., Rohatgi V., and Lee J. L., *Polymer Engineering and Science*, 35(10): 837, 1995.
7. Patel N. and Lee J. L., *Polymer Composites*, 17(1), 104, 1996.
8. Young W. B., *Journal of Composite Materials*, 30(11), 1191, 1996.
9. Chen Y. -T., Davis H. T., and Macosko C. W., *AICHE J.*, 41 (10), 2261, 1995.
10. Lundström T. S. and Gebart B. R., *Polymer Composites*, 15(1), 25, 1994.
11. Blackmore B., Li D., and Gao J., *Journal of Colloid and Interface Science*, 241(2), 514, 2001.
12. Varna J., Joffe R., Berglund L., and Lunström T. S., *Composites Science and Technology*, 53(2), 241, 1995.
13. Olivero K. A., Barraza H. J., O'Rear E. A., and Altan M. C., *Journal of Composite Materials*, 36(16), 2011, 2002.
14. Mahale A. D., Prud'homme R. K., and Rebenfeld L., *Polymer Engineering and Science*, 32(5), 319, 1992.

15. Ghiorse S. R., *SAMPE Quarterly*, 24(2), 54, 1993.
16. Howe C. A., Paton, R. J. and Goodwin A. A., In: *Proc. of ICCM-11*, Vol. 4, 46, 1997.
17. Wisnom M. R., Reynolds T., and Gwilliam N., *Composites Science and Technology*, 56(1), 93, 1996.
18. Gebart R. and Strömbeck L., In: *Processing of Composites*, Davé R.S. and Loos A.C. (Eds.), Hanser Publishers, Munich, 2000.
19. Shamsuddin I., Siegel M. C., Sadler R. L. and Avva V. S., In: *International SAMPE Technical Conference*, 27, 457, 1995.
20. Stabler W. R., Tatterson G. B., Sadler R. L., and El-Shiekh A. H. M., *SAMPE Quarterly*, 23(2): 38, 1992.
21. Pantelidis N. G., Bikas A., and Kanarachos A. E., In: *Annual Technical Conference - Society of Plastics Engineers*, 58 (2), 2351, 2000.
22. Nowak T. and Chun J. H., In: *Proc. of Materials Research Society Symposium*, 305: 241, 1993.
23. Strömbeck A., In: *Proc. of the 9th International Conference of Composite Materials*, 3, 497, 1993.
24. Lee C. H. and Wei K. H., *Journal of Applied Polymer Science*, 77(10), 2149, 2000.
25. Lee C. H. and Wei K. H., *Polymer Engineering Science*, 40 (4), 935, 2000.
26. Larson B. and Drzal L., *Composites*, 25 (7), 711, 1994.
27. Chui W. K., Glimm J., Tagerman F. M., Jardine A., Madsen J. S., Donellan T., and Leek R., *SIAM Review*, 39 (4), 714, 1997.

28. Barraza H. J., Hwa M. J., Blakely K., O'Rear E. A., and Grady B. P., *Langmuir*, 17 (17), 5288, 2001.
29. Kang M. K., Lee W. I., and Hahn H. T., *Composites Science and Technology*, 60, 2427, 2000.
30. Ghiorse S. R., *A Comparison of Void Measurement Methods for Carbon/Epoxy Composites*. U. S. Army Materials Technology Laboratory, Report MTL TR 91-13, 1991.
31. Russ J., *Practical Stereology*, 1st Ed., Plenum Press, New York, 1986.
32. Chan A. W., Larive D. E., and Morgan R. J., *Journal of Composite Materials*, 27(10), 996, 1993.
33. Palmese G. R. and Karbhari V. M., *Polymer Composites*, 16(4), 313, 1995.
34. Rohatgi V., Patel N., and Lee J., *Polymer Composites*, 17(2): 161-170. 1996

4 Through-The-Thickness Morphological Void Distribution of the RTM composite Molded at Zero Packing Pressure*

4.1 *Abstract*

Performance of composite materials usually suffers from process-induced defects such as dry spots and microscopic voids. While effects of void content in molded composites have been studied extensively, knowledge of void morphology and spatial distribution of voids in composites manufactured by resin transfer molding (RTM) remains limited. In this study, through-the-thickness void distribution for a disk-shaped, E-glass/epoxy composite part manufactured by resin transfer molding is investigated. Microscopic image analysis is conducted through-the-thickness of a radial sample obtained from the molded composite disk. Voids are found to concentrate primarily within or adjacent to the fiber preforms. More than 93% of the voids are observed within the preform or in a so-called transition zone, next to a fibrous region. In addition, void content was found to fluctuate through-the-thickness of the composite. Variation up to 17% of the average void content of 2.15% is observed through-the-thicknesses of the eight layers studied. Microscopic analysis revealed that average size of voids near the mold surfaces is slightly larger than those located at the interior of the composite. In addition, average size of voids that are located within the fiber preform is observed to be smaller than those located in other regions of the composite. Finally, proximity to the surface is found to have no apparent effect on shape of voids within the composite.

* Material in this chapter is published in Journal of Engineering Materials and Technology, 2004.

4.2 *Introduction*

Due to its versatility and low cost, resin transfer molding has been a popular method for manufacturing near-net-shape, geometrically complex, composite parts. Although the majority of load-bearing structural composite components in aerospace industry are fabricated by traditional autoclave process, the automotive industry utilizes RTM for structural or semi-structural parts due to lower operational cost and higher production rates [1]. Resin transfer molding and its variants consist of injecting a thermosetting polymeric resin into a mold cavity preloaded with a multi-layer, fibrous reinforcing preform. During mold filling, the resin wets individual fibers and pushes air out of the mold cavity through the exit gates. As the fluid front impregnates the fibrous preform, dry spots and microscopic voids may be formed in or near the fiber tows due to incomplete wetting of the preform. The formation of such microscopic voids during resin injection is one of the major barriers to larger scale usage of these molding processes.

Detrimental effect of voids on mechanical performance of composites is well established. Judd and Wright [2], for example, reported that a void content as low as 1% results in a decrease in strength up to 30% in bending, 3% in tension, 9% in torsional shear, and 8% in impact. In a more recent study of voidage effects on mechanical properties, Goodwin et al. [3] reported a 7% reduction in interlaminar shear strength per 1% increase in voidage up to 10% for a resin transfer molded composites containing 5-harness satin preform. In addition, the authors observed that failure cracks initiate from medium to large sized voids with sharp corners, but not from small spherical voids. Voidage is also

known to affect both the rate and equilibrium level of moisture absorption in composite parts [4].

Lowering or totally eliminating voids in RTM parts involves understanding mechanics of void formation during filling of the mold cavity. In resin transfer molded composites, voids are reported to originate primarily from mechanical entrapment during mold filling [5-8]. In some cases, voids can also emerge from volatilization of dissolved gases in the resin, partial evaporation of mold releasing agent into the preform, and initial air bubble content in the resin [9]. The mechanical entrapment is believed to arise from the presence of alternative paths for resin flow as a result of non-homogeneous preform permeabilities. The non-homogeneity in preform permeability leads to the following two different flow fields: (a) viscous flow through the opening between fiber bundles, and (b) capillary flow where resin penetrates into fiber bundles. At slower injection flow rates, the capillary flow within the fiber tows leads the viscous flow and promotes inter-tow void entrapment at the interstices of the tow structure. In contrast, high injection flow rates promote intra-tow void entrapment within fiber bundles as viscous flow leads capillary flow during preform impregnation. A comprehensive analysis of this phenomenon has often been performed [5-9] using the capillary number, Ca , defined as the non-dimensional ratio of the viscous forces to the capillary forces:

$$Ca = \frac{\mu V}{\gamma}, \quad (4.1)$$

where μ , V , and γ are the impregnating resin viscosity, the macroscopic fluid front velocity, and the resin surface tension, respectively.

A correlation between overall void content and capillary number is well-established in the literature [5-9]. Mahale et al. [6] reported that below a certain capillary number critical value (i.e. $Ca < 2.5 \times 10^{-3}$), void content increases exponentially with decreasing capillary number during planar radial flow into non-woven multifilament glass networks. Moreover, if capillary number is above this critical value, negligible void entrapment was reported. Incorporating the liquid-fiber-air contact angle into the non-dimensional capillary number was found to help generalize the analysis by preventing discrepancies caused by material variation. The resulting modified capillary number, Ca^* , has been defined by Patel et al. [7] and Rohatgi et al. [8] as:

$$Ca^* = \frac{\mu V}{\gamma \cos \theta}, \quad (4.2)$$

where θ is the advancing contact angle. Both references reported the existence of a single master curve of void content plotted as a function of the modified capillary number. Experimentally measured data followed this master curve for various model fluids injected at different fluid velocities. The authors also reported the existence of a preferential range of modified capillary number between 10^{-3} and 10^{-2} , within which inter-tow macro-voids and intra-tow micro-voids coexist. Below this preferential range ($Ca^* < 10^{-3}$), voids are primarily inter-tow macro-voids, and above the second critical value of 10^{-2} , voids are mainly micro-voids trapped inside fiber bundles.

In order to predict void formation during mold filling, a number of authors developed theoretical and numerical models [10-15]. Most of the proposed models introduced

numerous assumptions, and often considered simplified preform architectures. For instance, Chan and Morgan [10] developed a model that predicts localized void formation at the resin front region, but only for unidirectional preforms with parallel flow. Chui et al. [11], on the other hand, proposed a theoretical model predicting a voidage-pressure dependence in RTM processes. Although the model was based on a simple unsaturated flow in porous media, the voidage-pressure dependence was confirmed experimentally by Lundström [12]. Patel and Lee [13,14] also developed a model for void formation in liquid composite molding (LCM) processes based on the multi-phase Darcy's law. Furthermore, a simple analytical model for tow impregnation when the macroscopic flow is parallel to the fiber axis was developed by Binetruy et al. [15]. Additionally, several researchers [16,17] investigated bubble motion through constricted micro-channels to characterize void transport through fiber reinforcement. Lundström [16] reported that voids are more prone to mechanical entrapment within fiber bundles than between bundles. Shih and Lee [17] found that bubble mobility depends on both bubble size and the resin-fiber contact angle.

Proposed void reduction methods for RTM composites in the literature include vacuum assistance [18], continuing the resin flow after complete wet out [5], compressing mold walls during injection [19], and applying a permanent post fill pressure after injection [20,21]. Nevertheless, the most effective technique for void reduction cannot be established without thorough understanding of the spatial void distribution throughout the composite part. To the best of the authors' knowledge, such detailed spatial void characterization has not yet been available for resin transfer molded composites. In the current work, we study the spatial void distribution and void morphology in a disk-

shaped, E-glass/epoxy composite fabricated by resin transfer molding. A radial sample from this disk is analyzed through-the-thickness by an optical microscope. In addition, since void size and shape are critical both in failure mechanisms [3] and in void mobility during injection [17], their variations in the thickness direction are investigated.

4.3 Experimental Studies

4.3.1 Procedure for Composite Manufacturing

An epoxy resin, EPON 815C (Shell Chemicals) is chosen as the molding material. Attractive characteristics of this resin include low toxicity and low viscosity, suitable for effective preform impregnation and lower injection pressures. The gel time of about 20 minutes is obtained by choosing the curing agent EPICURE 3282 (Shell Chemicals). As depicted in Fig. 4.1, the apparatus used to fabricate resin transfer molded disks comprises a molding press and a disk-shaped mold cavity. The molding press contains a 40-ton hydraulic press (ARCAN, Model CP402), and two hollow cylinders, designed for resin and curing agent, respectively. The internal diameters of the two stainless steel cylinders are machined to 55.47 and 25.53 mm in order to realize the exact mix ratio of 4.7 to 1 by volume of resin to curing agent.

When the hydraulic press is activated, the attached plungers progress at a constant linear velocity of 2×10^{-3} m/s. The flows from the two cylinders coalesce through a T-connector. Subsequently, the resin and curing agent mixture pass through a Statomix® static inline mixer (ConProTec, Inc., 32 segments. L=155 mm, ID= 5 mm, OD= 8mm). The mixture is afterwards injected through the center of the disk-shaped cavity at a constant injection rate of $5.32 \text{ cm}^3/\text{s}$.

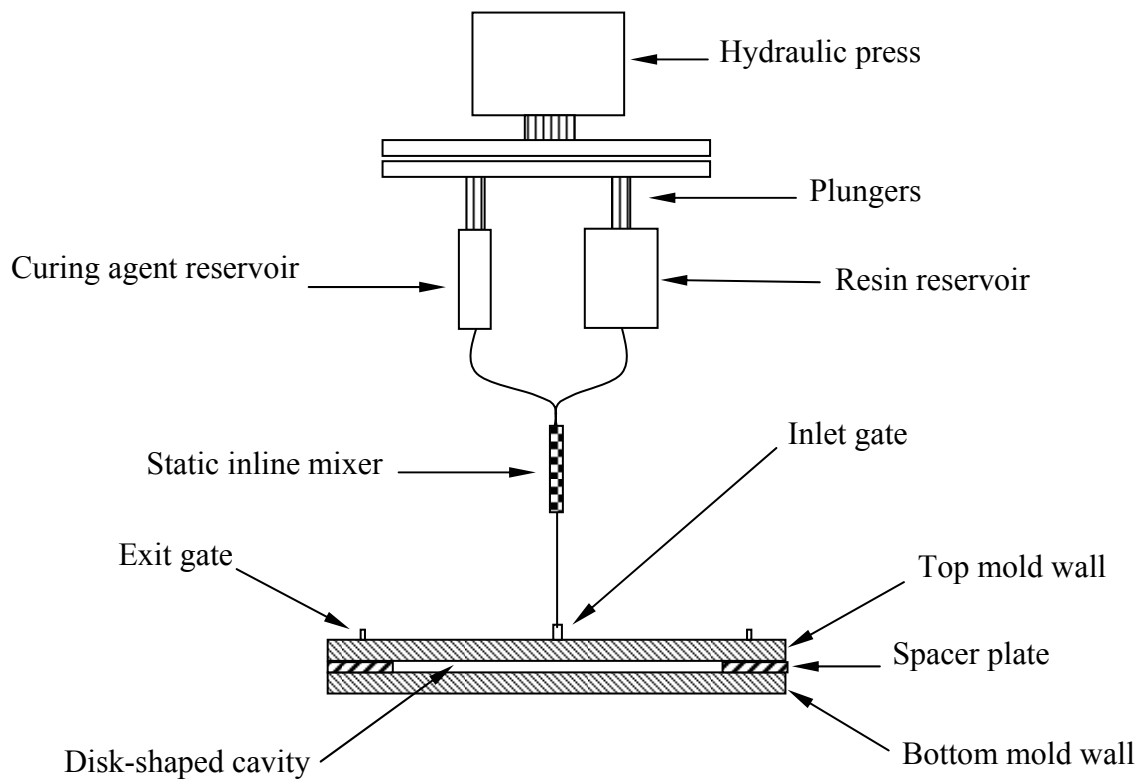


Figure 4.1: Experimental molding apparatus used to fabricate RTM composite disks.

The mold cavity, as shown in Fig. 4.1, is built by placing a 3.18 mm-thick aluminum spacer plate between two 12.6 mm-thick aluminum mold walls. A 152.4 mm diameter circle is cut from the center of the spacer plate to form the disk-shaped cavity. A centered inlet gate and four symmetrically positioned vents are placed on the top mold wall. Leakage is prevented by placing 4-mm O-rings into machined grooves in each mold wall. The filling pressure steadily increases as the flow front advances radially outward towards the exit vents by impregnating random-fiber preform. The exit vents are intentionally placed at a diameter of 177.8 mm to force the resin into the narrow opening between mold walls and spacer plate. Hence, after the mold cavity is full, the pressure increases at a very steep rate as the resin creeps inside this tight space. The pressure reaches a maximum inside the mold, as higher pressure is expected to ensure the full impregnation of the dry preform, help reduce voidage [11-12], and facilitate void mobility [17].

Once the pressure reaches a high-enough value, resin starts to come out of the exit vents. Resin injection is then immediately stopped, and exit vents are left unclamped to allow continued discharge of the resin until the driving pressure gradient becomes zero. The reinforcement used in this study is a chopped-strand, randomly-oriented E-glass fiber mat, having a planar density of 0.459 kg/m^2 (Fiberglast, part #250). Four layers of preform are cut into 152.4 mm diameter circles and placed into the mold cavity preceding filling, yielding a fiber volume fraction of 18.1%. This moderately low fiber content is chosen to lower the pressure levels experienced during resin injection. However, the capillary analysis and the obtained results are believed to be applicable to higher fiber

contents and even to other liquid molding processes for composite materials where similar flow kinematics exists during mold filling. After resin comes out of all four exit vents, the part is left to cure in the mold for 48 hours before demolding. The part is then post cured at room temperature for two extra weeks to achieve total cross-linking. The resulting product is a 3.88 mm-thick resin transfer molded composite disk having 152.4 mm diameter, with an 18.1% fiber volume fraction. Because of the planar randomness of the preform and the disk axisymmetry, the void morphology within the sample is expected to be independent of the angular position. Therefore, spatial void distribution is investigated only through-the-thickness, across the radius of a radial specimen from the molded disk.

4.3.2 Capillary Number Determination

As discussed in the introduction, void content is known to correlate well with the capillary number [5-8]. In addition, the modified capillary number is helpful in understanding the effect of micro-scale flow during fluid front progression. Determining the modified capillary numbers involved in mold filling is needed to identify void formation mechanisms, and consequently spatial void distribution within the molded disk.

Determining the modified capillary number requires, as described in Eq. (4.2), quantifying the resin viscosity, μ , the macroscopic fluid front velocity, V_{ave} , the resin surface tension, γ , and the advancing contact angle, θ . Both the surface tension and the advancing contact angle are measured in an earlier study for the same system of resin, curing agent, and E-glass-fibers [21]. The respective measured values of the surface

tension and advancing contact angle are 36.3×10^{-3} N/m, and 34° . The viscosity of the resin-curing agent mixture is measured using a Brookfield viscometer (Model DV-II +). Even though the mixture's viscosity changes a great deal towards the end of the 20 minute gel time, its value remains reasonably stable around $0.96 \text{ N}\cdot\text{s}/\text{m}^2$ during the first few minutes of mixing. The macroscopic fluid front velocity can be determined from the injection flow rate and the mold geometry as:

$$V_{ave} = \frac{Q}{A} = \frac{Q}{2\pi H r(1-V_f)}, \quad (4.3)$$

where Q is the resin flow rate, H is the thickness of the mold, r is the radius at which the capillary number is calculated, A is the cross-sectional area of the resin flow at r , and V_f is the fiber volume fraction. Substituting Eq. (4.3) in Eq. (4.2), the modified capillary number becomes a function of the radial distance from the injection gate:

$$Ca^* = \frac{\mu Q}{2\gamma\pi H(1-V_f)\cos\theta} \cdot \frac{1}{r}. \quad (4.4)$$

4.3.3 Void Characterization

Microscopic image analysis is utilized to investigate average void content and spatial void distribution through-the-thickness of the composite disk. Microscopic image analysis is chosen since it is believed to be among the most accurate methods for measuring the true void content [22]. Moreover, image analysis offers the advantage of providing detailed information of other important parameters such as void location and void shape and size distribution that cannot be assessed by any other method. However,

voidage measurement by optical imaging is generally performed on limited sample surface area. Statistical averaging is also commonly used from random acquisition of pictures over the larger area of interest. Image analysis in the current work, on the other hand, is performed over the entire cross-sections studied, and hence all identifiable voids at the working magnification are included in the void analysis.

In order to investigate the void distribution through-the-thickness, a radial specimen is cut from the cured composite disk. The length and thickness of the specimen are 75 and 3.88 mm, respectively. Once embedded into a quick cure acrylic resin (Allied High Tech. Products, part # 170-10000), the sample is polished in six successive steps with a series of polishing pastes (Clover Compound) with grits sizes ranging from 180 (e.g. 80 μm average particle diameter) to 1200 (15 μm). After each step, the sample is sonicated for 40 minutes in an ultrasonic cleaner (50 kHz) to remove all residues of the polishing compound.

The optical image analysis starts by dividing the 3.88 mm-thick specimen into eight layers through-the-thickness (seven 0.5 mm-thick layers and one 0.38 mm-thick bottom layer). Frames captured from different 0.5 mm-layers are used to assess the voidage distribution through the specimen thickness. Each layer is then entirely scanned at 200x magnification using a MEIJI optical microscope. At this particular magnification, every frame displayed about $0.71 \times 0.53 \text{ mm}^2$ area. Hence, scanning across the sample thickness at a particular radial location needs the capture of eight frames. Images of each layer containing an identified void are captured using a PC-based CCD camera. A total of approximately 460 frames containing voids are captured during this analysis. Each

picture is processed using the image analysis software UTHSCSA Image Tool[®], which allows the measurement, for each void, of the area, A , and the maximum length, L_{max} . Void contents of different layers are then calculated.

4.4 Results and Discussion

4.4.1 Location of Voids and Average Void Content

The voids observed in the molded part are located in three different void zones. First zone is defined as those areas that are rich in matrix and not comprising any fiber preform. Voids located in this zone are completely surrounded by the epoxy matrix and referred to as matrix voids. Second zone is defined as fiber rich-region where the area is dominantly composed of reinforcing preform. Voids in this region are situated within fiber bundles and are referred to as preform voids. Finally, transition zone is defined as the zone between the two other zones herein defined. Voids located in this zone are referred to as transition voids and are always positioned adjacent to fiber bundles but not inside the preform.

Figure 4.2 depicts sample images containing voids obtained from the three defined zones at 200x magnification. In Fig. 4.2a, the continuous polymeric matrix appears as a gray background, the white circular and elliptical objects correspond to glass fibers oriented perpendicularly and in an angle, respectively, to the cross-section. The white parallel stripes represent glass fibers parallel to the studied cross-section. Based on the void locations defined earlier, the two voids present in Fig. 4.2b are matrix voids. The five voids appearing in Fig. 4.2c, on the other hand, fall into the category of preform voids. Finally, the adjacent void to fibers seen in Fig. 4.2d is considered a transition void.

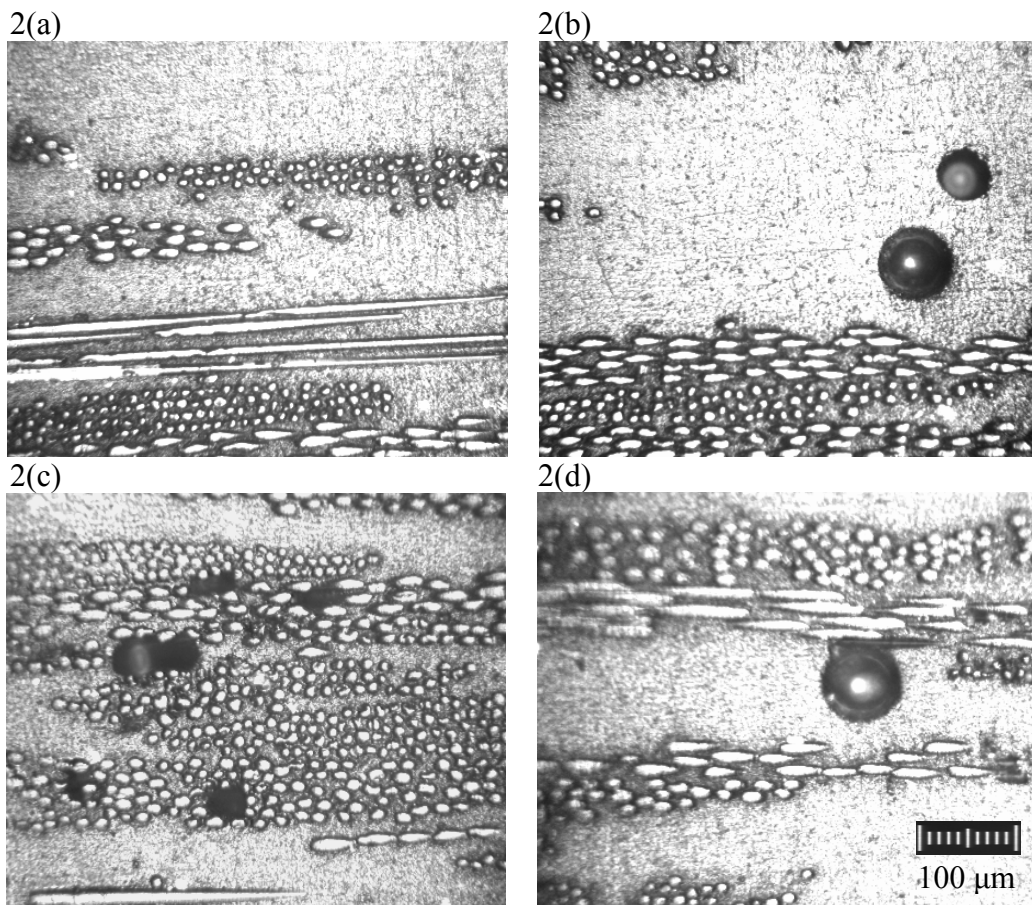


Figure 4.2: Representative microscopic images obtained at 200 x magnifications from the RTM composite molded without post-fill pressure at 17.5% fiber content depicting examples of voids from different zones: (a) typical composite cross-section with different fiber orientations; (b) two matrix voids; (c) five preform voids; (d) one transition void.

Voids from these three different zones are identified and their respective contributions to the overall void content determined in order to investigate likelihood for void mobility. In addition, classifying voids based on their proximity to fibers can help estimate their primary effect on mechanical properties. It is known that matrix voids only reduce the load-bearing composite cross-section, while preform and transition voids also weaken local fiber-matrix adhesion.

Combining all through-the-thickness layers, an average void content of 2.15% is calculated. As depicted in Fig. 4.3, matrix voids make up only 0.15%, thus form only 6.98% of the total voidage of 2.15%. On the other hand, most voids formed in the composite disk are encountered in the transition and preform locations, contributing with 1.31 and 0.72%, respectively to the overall void content. The modified capillary number, as discussed in the introduction, can be used to help understand the void formation mechanisms involved in the micro-scale flow during fluid front progression leading to this specific zone distribution. Substituting the previously measured values of 36.3×10^{-3} N/m for surface tension, and 34° for advancing contact angle in Eq. (3.4), the modified capillary number is found to vary between 0.13 and 1.15 along the radial distance from the injection gate. Those values suggest that the formed voids should be mostly intra-tow micro-voids [7], which is consistent with the results seen on Fig. 4.3. As Fig. 4.3 illustrates, preform and transition voids combined represent 93.02% of the total voidage formed within the composite part.

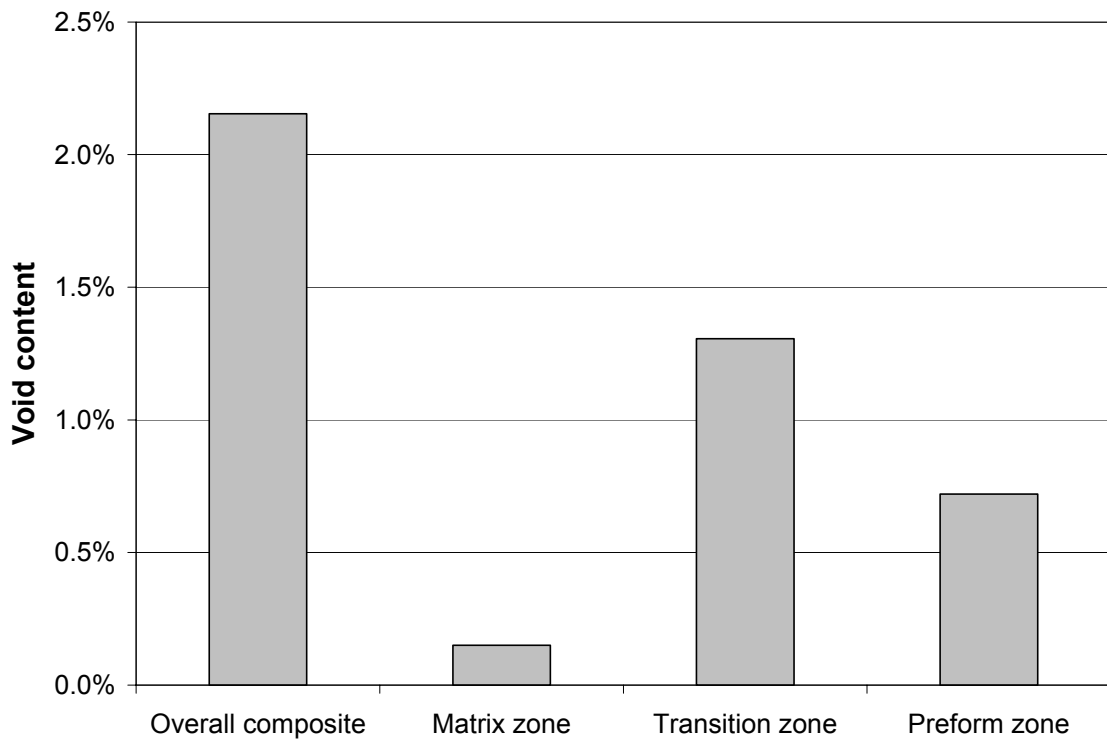


Figure 4.3: Void content contributions of different locations (void zones) within the composite disk molded without post-fill pressure at 17.5% fiber content.

4.4.2 Variation of Void Content Through-The-Thickness

Non-uniformity in voidage through-the-thickness of the composite disk can arise from uneven spaces between the preform layers, or between the preform and the mold walls. It can also originate from the possible change in the velocity of fluid front between mid-plane and other planes. Another plausible cause can be the poor wettability of the aluminum mold walls pretreated with Teflon mold releasing agent. To quantify the void content change through the specimen's thickness, eight layers are defined as described earlier, with the first layer defined as the very top 0.5 mm-thick layer. Note that the eighth layer is only 0.38 mm-thick. Void contents obtained for these eight different layers are shown in Fig. 4.4.

Void contents are found to vary significantly from one layer to another, between a maximum of 2.62% in layer 4 and a minimum of 1.25% in the eighth layer. A standard deviation of 0.53% was calculated yielding a 95% confidence interval of 0.37%, which represents 17.21% of the average void content. Consequently, the commonly used statistical averaging of void contents calculated from randomly acquired pictures may introduce 17% error in the overall void content. Thus, scanning the whole cross-section may be needed in order to obtain an accurate overall void content.

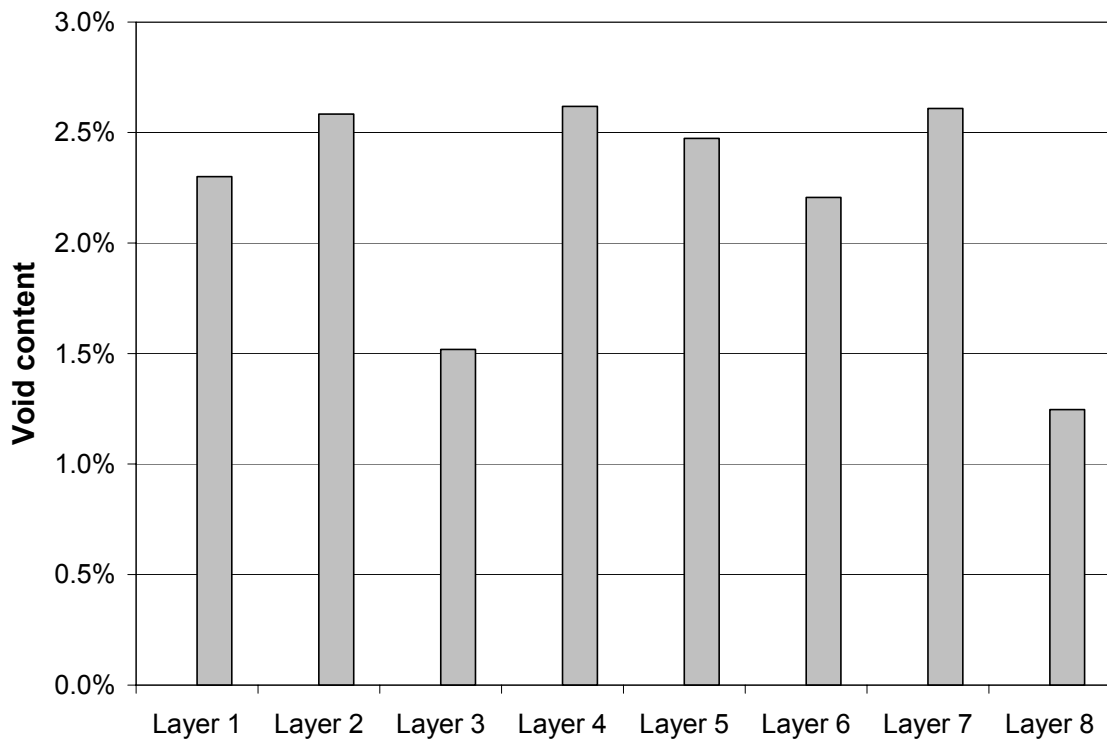


Figure 4.4: Variation in void content through-the-thickness of the composite disk molded without post-fill pressure at 17.5% fiber content.

For the remaining part of the study, the eight layers are combined into two major layers to summarize the results as we focus on other voidage aspects. The first layer is combined with the seventh and eighth layers to define a surface layer, which represents the composite regions right next to the mold walls surface. Voids found within these layers are referred to as surface voids. The second, third, fourth, fifth, and sixth layers are combined into an inner layer representing the layers within the composite's core, away from mold walls effects. Voids encountered within these layers are called inner voids.

4.4.3 Variation of Void Size

Classifying void sizes is essential in the choice of void removal method as size is reported to affect void mobility [17]. Larger voids have longer perimeters and thus have higher adhesion force; small voids, on the other hand, have lower adhesion force and therefore become more mobile. Captured void surface area data, measured earlier, are utilized in order to quantify void sizes. An equivalent diameter, D_{eq} , is defined to classify the void size for each void as:

$$D_{eq} = \sqrt{\frac{4A}{\pi}}, \quad (4.5)$$

where A is the measured area of the void. Size distributions of inner and surface voids based on D_{eq} are shown in Fig. 4.5. Both distributions are one-tailed distributions, contrasting with typical bimodal void distributions observed in fiber reinforced molded composites [14], where the first peak represents intra-tow micro-voids and the second

inter-tow macro-voids. As mentioned earlier, the range of modified capillary numbers that are calculated as 0.13 to 1.15 implies that the formed voids are primarily intra-tow micro-voids [8], which explains the presence of fewer large macro-voids. However, size distributions of inner and surface voids are considerably different. The size distribution of inner voids presents a larger peak, with a higher maximum frequency of 21.96% for voids with equivalent diameter between 30 and 40 μm , and a narrower tail, with no voids having an equivalent diameter larger than 140 μm . The size distribution of surface voids depicts a maximum frequency of 18.56% for voids with equivalent diameter between 50 and 60 μm , and existence of voids even larger than 200 μm . These size distributions show clearly that surface layer voids are generally larger than inner voids. Surface layer also contains some very large voids (over 200 μm) in contrast with inner layer that does not contain any void with an equivalent diameter larger than 138 μm .

This difference in size distribution of the two layers is compensated by an opposite difference in void density. Inner voids shows a void density of 10.75 voids per mm^2 , while surface voids shows a void density of 9.76 voids per mm^2 , thus yielding comparable average void contents of 2.28 and 2.05% for inner and surface layers, respectively. These results are expected as uneven spaces between the preform and the mold walls, and the variation of fluid front velocity between mid-plane and other planes, coupled with poor wettability of the aluminum mold wall pretreated with Teflon mold releasing agent lead to variation in voidage through-the-thickness of the composite disk.

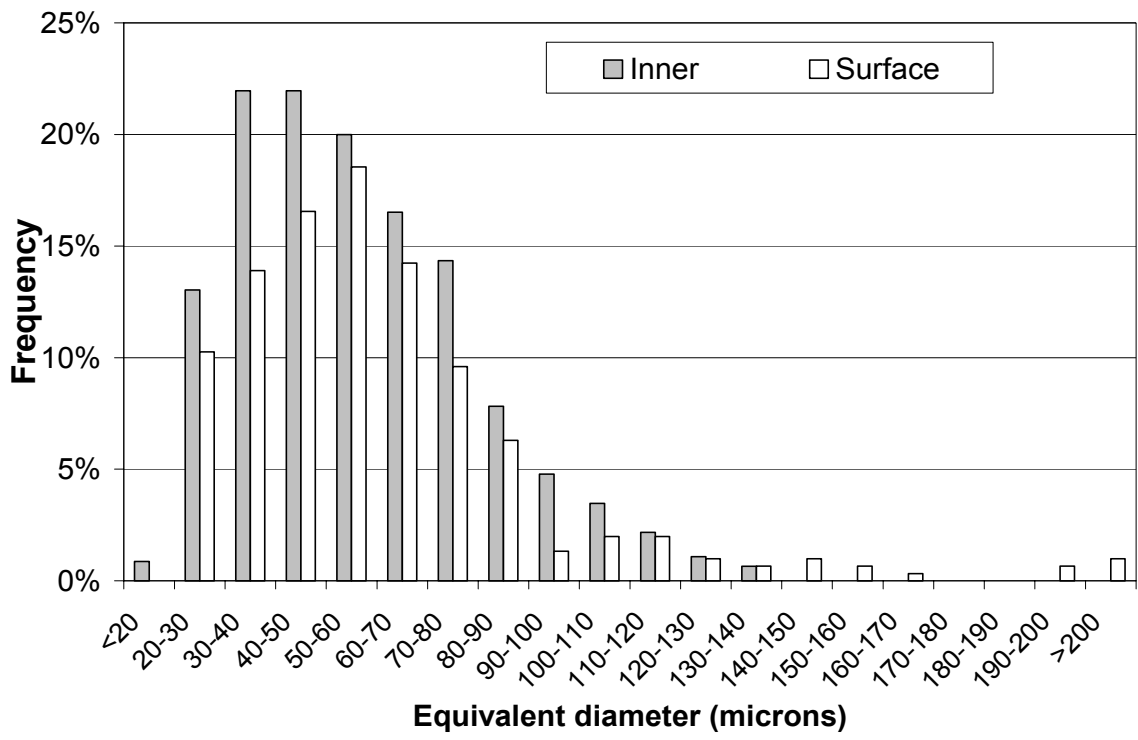


Figure 4.5: Void size distributions based on equivalent diameter at the surface (next to mold walls) and inner layers of the RTM composite molded without post-fill pressure at 17.5% fiber content.

In order to categorize the observed differences in void sizes, three different sizes are defined. Large voids are defined as those voids with an equivalent diameter greater than $100\ \mu\text{m}$, i.e. $D_{eq} > 100\ \mu\text{m}$; while voids with an equivalent diameter lower than $50\ \mu\text{m}$ are regarded as small voids. Intermediate equivalent diameter values, i.e. $50\ \mu\text{m} < D_{eq} \leq 100\ \mu\text{m}$, correspond to medium size voids. Figure 4.6 depicts representative small, medium, and large voids as defined above.

Figure 4.6a shows an example of a large void with an equivalent diameter of $142\ \mu\text{m}$. In contrast, Fig. 4.6b depicts two small voids and one barely medium void. The equivalent diameter of the void at the bottom half of Fig. 4.6b is measured as $57\ \mu\text{m}$, while the other two voids are measured as 41 and $35\ \mu\text{m}$, respectively. Fig. 4.6c depicts a medium and a small void. The medium void, $D_{eq} = 81\ \mu\text{m}$, is caught between two fiber tows. It should be noted that the void in Fig. 4.6c is also considered a transition void since it is only adjacent to fiber bundles. With an equivalent diameter of only $D_{eq} = 23\ \mu\text{m}$, The small void trapped inside the fiber tow located in the bottom of Fig. 4.6c is considered a preform void. The image shown in Fig. 4.6d comprises voids with different sizes (equivalent diameters of $31, 123, 123, 69,$ and $38\ \mu\text{m}$ –from top to bottom).

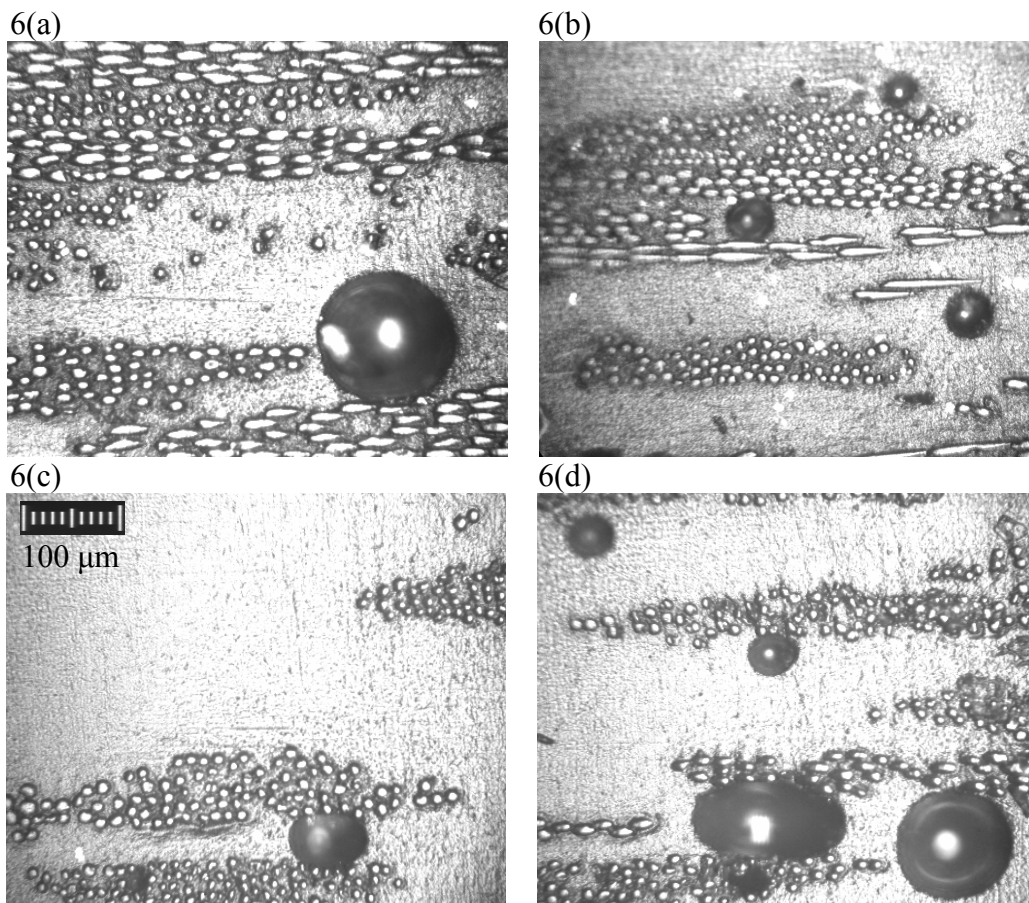


Figure 4.6: Representative microscopic images obtained at 200 x magnifications from the RTM composite molded without post-fill pressure at 17.5% fiber content depicting voids with different sizes: (a) example of a large void adjacent to a fiber bundle; (b) two small and a barely medium void (from top to bottom); (c) a medium void; (d) voids from different size categories.

Furthermore, using these three different void sizes, voids from different zones within the composite show a substantial difference in size distribution. This variation in size distribution is shown in Fig. 4.7. The relative percentage of large voids is almost the same for all the composite zones. However, the presence of medium voids in the preform zone shows a substantial difference compared to the matrix and transition zones. Medium voids form only 28.65% of all voids in preform zone, while they form 61.29 and 67.13% of all voids in matrix and transition zones, respectively. At the same time, an opposite difference in relative percentage of small voids is registered. Small voids make up 65.99% of all voids observed in the preform, while they form only 33.33 and 24.30% of all voids in matrix and transition zones, respectively. This finding concurs with previous studies showing that inter-tow voids are usually larger than the intra-tow voids [6,13,14]. However, due to the higher range of modified capillary number in the present study, the sizes of observed inter-voids are closer to those observed for intra-tow voids.

4.4.4 Variation of Void Shape

Since voids with different shapes are known to induce different failure mechanisms [3], shape distribution within a load-bearing composite becomes important in predicting a part's performance. As Figs. 4.2 and 4.6 depict, different void shapes are encountered in the composite sample. Voids shown in Figs. 4.2b, 4.2d, 4.6a, and 4.6b are mostly circular. In contrast, the void captured in Fig. 4.6c, and the void caught between fiber bundles in Fig. 4.6d are more elliptical. The small void entrapped within the preform in the latter figure and those depicted in Fig. 4.2c present a different asymmetrical geometry.

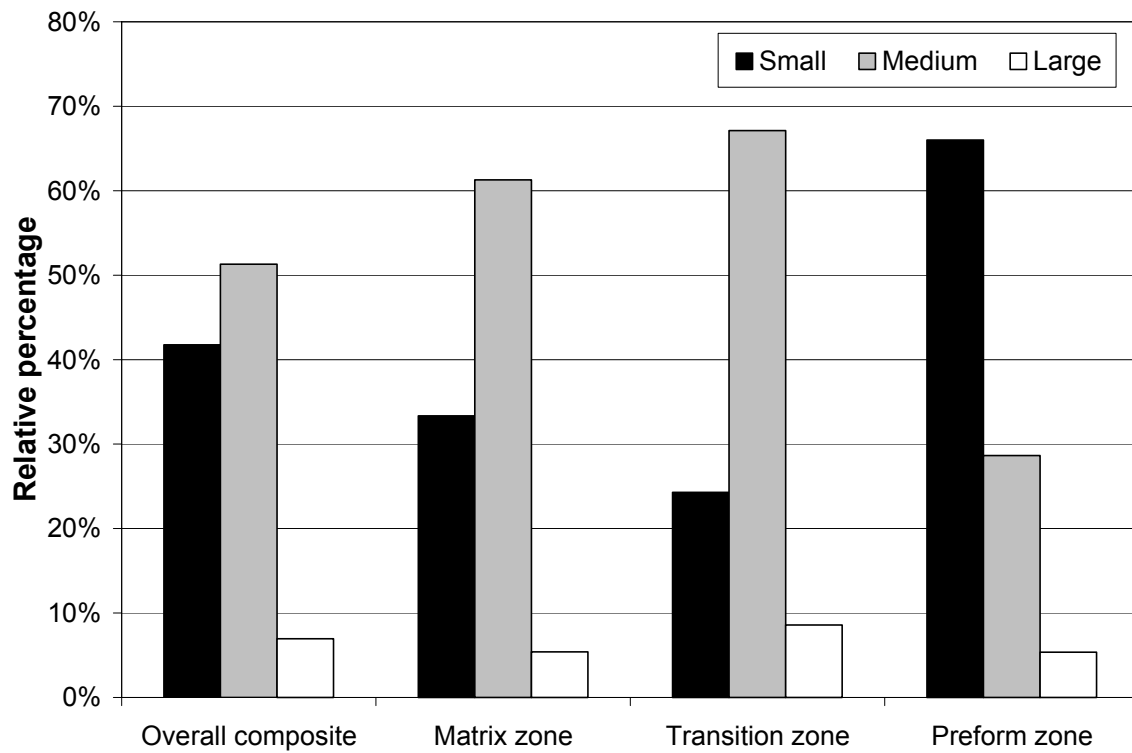


Figure 4.7: Size distributions of voids from different locations (void zones) within the composite disk molded without post-fill pressure at 17.5% fiber content.

In order to quantify these differences and categorize void shapes, both geometrical and quantitative void characteristics are combined. First, based on the observed shape, voids are divided into two groups: irregular and regular shapes. Irregular void shapes are defined as those presenting a non-convex planar surface area, that is, one can find two different points within the void that can be connected in a straight line that goes outside the void. The remaining voids are defined as regular.

A quantitative measure of geometrical circularity of regular voids is introduced to distinguish between circular and elliptical voids. The data obtained from captured voids is further processed by introducing the shape ratio, R_s , defined for each void as the equivalent diameter obtained from Eq. (5) divided by the maximum measured length L_{max} , within a void:

$$R_s = \frac{D_{eq}}{L_{max}}. \quad (4.6)$$

Since an ideal circle is represented by $R_s = 1$, only voids with shape ratios above 0.95 ($0.95 < R_s \leq 1$) are considered as circular voids (the void shown in Fig. 4.6a for instance). Voids with shape ratios lower than 0.95 comprise a minor axis smaller than the maximum length. The circular symmetry is lost, and they are better classified as elliptical voids. For example, the void caught between preform bundles in Fig. 4.6d has a shape ratio of 0.78. Relative percentages of voids with different shapes are depicted in Fig. 4.8.

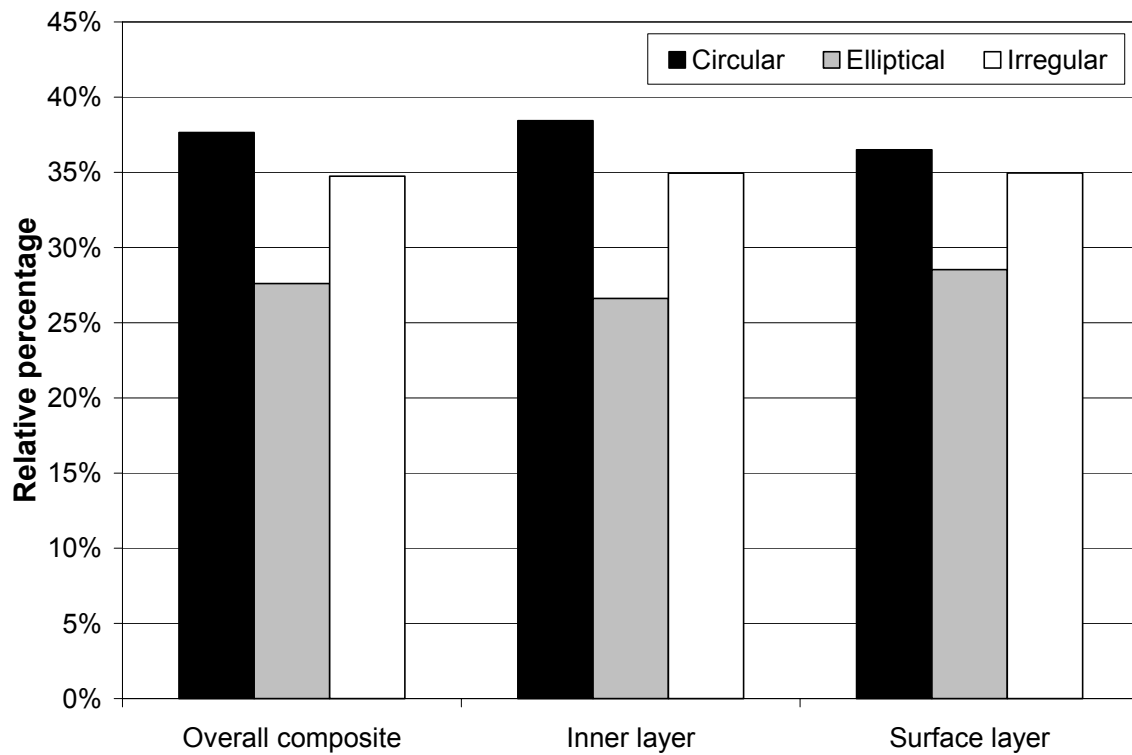


Figure 4.8: Void content contributions of voids with different shapes encountered in the RTM composite molded without post-fill pressure at 17.5% fiber content.

Considering the overall composite disk, circular and irregular voids have relative percentages of 37.65 and 34.75%, respectively. Elliptical voids, on the other hand, have the lowest relative occurrence at 27.60%. The inner and surface shape distributions are also investigated in order to determine any potential difference in shape distribution caused by the surface non-uniformity. Figure 4.8 includes shape distributions of voids encountered within the inner and surface layers. Both layers show a very similar shape distribution of voids. Relative percentages of elliptical voids in inner and surface layers are 26.61 and 28.54%, whereas frequency of circular voids in inner and surface layers is 38.44 and 36.50%, respectively. These results suggest that proximity to the mold surface seem to have no effect on void shape distribution.

Finally, using the shape criteria for voids presented earlier, relative contributions of voids with different sizes to circular, elliptical, and irregular shaped voids are calculated. The resulting relative percentage of voids having different sizes based on shape is presented in Fig. 4.9. A distinct difference in size distribution between the three defined void geometries is observed. As the occurrence of large voids is more or less the same for all the shapes (around 7%), relative percentage of small void jumps from a low 25.31% for circular voids to a high 57.47 % for irregular voids. Medium voids see an opposite trend as their relative percentage goes from a high 67.78% for circular voids to 50.38% for elliptical voids, and to even a low 36.00% for irregular voids. Size distribution of elliptical voids is found similar to the overall size distribution shown in Fig. 4.7. Circular and irregular voids, on the other hand, display different size distributions as they are in average larger and smaller, respectively, than the overall void size average.

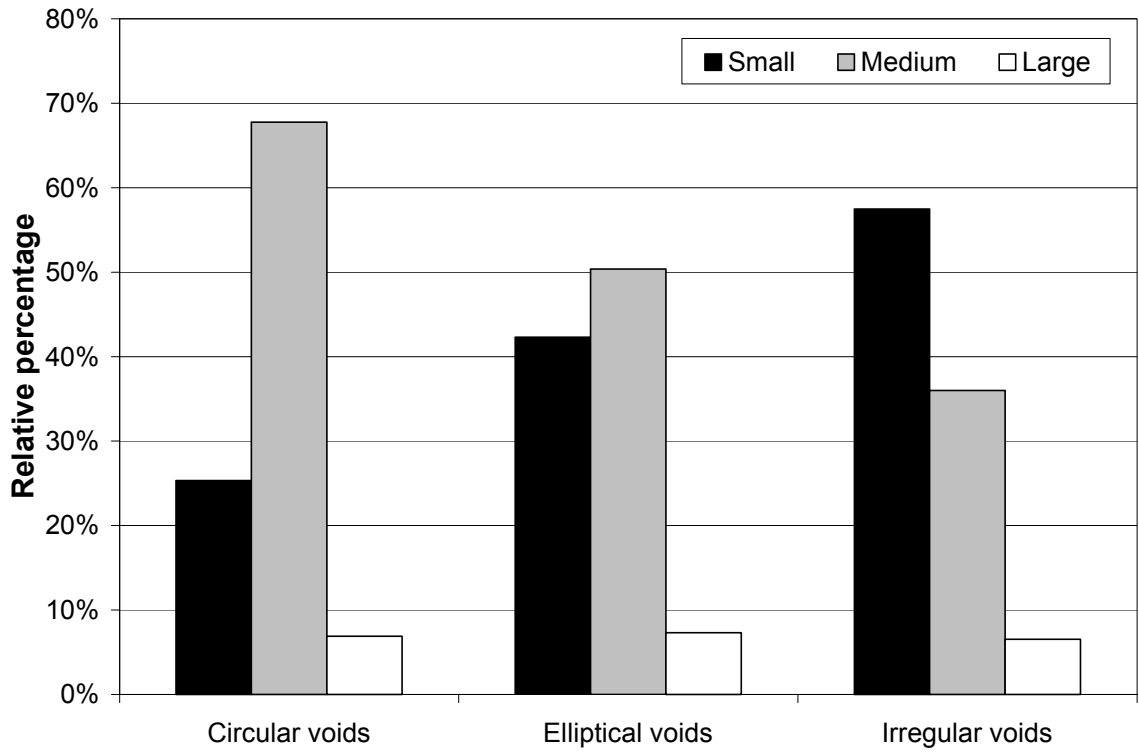


Figure 4.9: Size distribution of voids with different shapes encountered in the RTM composite molded without post-fill pressure at 17.5% fiber content.

Figure 4.9 also reveals that irregular voids are mostly small, while circular voids are mostly medium voids. These results can be better understood if zone locations of voids with different shapes are considered. Irregular voids are mostly encountered in the preform zone. Therefore, they are expected to be smaller than the circular voids, which occur mostly in matrix or preform zones.

4.5 Concluding Remarks

Voidage distribution is important for resin transfer molded composites since it dictates overall performance of the product. Microscopic image analysis is utilized to investigate through-the-thickness void distribution for a resin transfer molded, disk-shaped, E-glass/epoxy composite. The results indicate significant void variation through the composite's thickness. Void content, for instance, was found to fluctuate through-the-thickness of the part with a variation as much as 17% of the overall 2.15% void content. Primarily, micro-scale voids are encountered since the mold filling is conducted at relatively high modified capillary numbers. Furthermore, voids are found to be mostly concentrated within or right next to the preform with more than 93% of voids occurring in preform and transition zones. Voids occurring next to the mold surface are found to be larger in average than inner voids, whereas voids within the preform are observed to be smaller in average than voids from other composite zones. Finally, mold walls are found to have no apparent effect on shape distribution of voids through-the-thickness of the composite.

4.6 References

1. Abraham D., Matthews S., and McIlhagger R., *Composites Part A*, 29, 795, 1998.
2. Judd N. C. W., and Wright W. W., *SAMPE Journal*, 14(1), 10, 1978.
3. Goodwin A. A., Howe C. A., and Paton R. J., *Proc. of ICCM-11*, M. L. Scott, Ed, *Australian Composite Structures Society*, Vol. IV, 11, 1997.
4. Harper B. D., Staab G. H., and Chen R. S., *Journal of Composite Materials*, 21, 280, 1987,
5. Patel N., and Lee L. J., *Polymer Composites*, 16(5), 386, 1995.
6. Mahale A. D., Prud'Homme, R. K., and Rebenfeld, L., *Polymer Engineering and Science*, 32(5), 319, 1992.
7. Patel N., Rohatgi V., and Lee J. L., *Polymer Engineering and Science*, 35(10), 837, 1995.
8. Rohatgi V., Patel N., and Lee J. L., *Polymer Composites*, 17(2), 161, 1996.
9. Stabler W. R., Tatterson G. B., Sadler R. L., and El-Shiekh A. H. M., *SAMPE Quarterly*, 23(2), 38, 1992.
10. Chan A. W., and Morgan R. J., *SAMPE Quarterly*, 23(4), 48, 1992.
11. Chui W. K., Glimm J., Tangerman F. M., Jardine A. P., Madsen J. S., Donnellan T. M., and Leek R., *Proc. of the 9th International Conference of Numerical Methods in Thermal Problems*, 1323, 1995.
12. Lundström T. S., *Composites Part A*, 28, 201, 1997.
13. Patel N., and Lee J. L., *Polymer Composites*, 17(1), 96, 1996.
14. Patel N. and Lee J. L., *Polymer Composites*, 17(1), 104, 1996.

15. Binetruy C., Hilaire B., and Pabiot J., *Journal of composite Materials*, 32(3), 223, 1998.
16. Lundström T. S., *Polymer Composites*, 17(6), 770, 1996.
17. Shih C.-H., and Lee L. J., *Polymer Composites*, 23(1), 120, 2002.
18. Lundström T. S., and Gebart B. R., *Polymer Composites*, 15(1), 25, 1994.
19. Choi J. H. and Dahran C. K. H., *Journal of Composite Materials*, 36(19), 2267, 2002.
20. Olivero K. A., Barraza H. J., O'Rear E. A., and Altan M. C., *Journal of Composite Materials*, 36(16), 2011, 2002.
21. Barraza H. J., Hamidi Y. K., Aktas L., O'Rear E. A., and Altan M. C., *Journal of Composite Materials*, 38, 195, 2004.
22. Ghiorse S. R., U. S. Army Materials Technology Laboratory, Report MTL TR 91-13, 1991.

5 Three-Dimensional Features of Void Morphology in Resin Transfer Molded Composites^{*}

5.1 *Abstract*

Detailed analyses of shape, size, and spatial variations of void morphology are presented for a disk-shaped, resin transfer molded (RTM), E-glass/epoxy composite. The disk is molded at constant injection rate and contains 17.5% E-glass random fiber mats. Voids throughout the composite are evaluated by microscopic image analysis of through-the-thickness and planar surfaces obtained from adjacent radial samples of the molded disk. The void content of 2.15% is obtained from the analysis of through-the-thickness images and believed to be representative of the actual void content in the studied part. Relatively large cylindrical voids are observed in cigar shapes in the planar surfaces, whereas these voids only appear as small irregular or elliptical voids on through-the-thickness surfaces. Along the radial direction, combined effects of void formation by mechanical entrapment and void mobility are shown to yield a complex radial void distribution. It is shown that fewer voids are trapped mechanically with increasing distance from the inlet and most of the medium and small voids that are mobile migrate towards the exit during resin injection. These findings are believed to be applicable not only to RTM, but generally to liquid composite molding processes with varying fluid front velocities.

* Material in this chapter was submitted to Composites Science and Technology, 2004.

5.2 *Introduction*

Resin transfer molding (RTM) and structural reaction injection molding (SRIM), among other liquid composite molding (LCM) processes, are being used in manufacturing near-net-shape, geometrically complex composite parts. These liquid molding processes have been regarded in the last decade as successful alternatives to the traditional autoclave-based composite manufacturing. In addition to the process versatility and wide range of possible molding materials, attractive features of these liquid molding processes are lower operational costs, and higher production rates compared to autoclave process [1]. Resin transfer molding consists of placing a dry fibrous preform composed of multiple layers into a mold cavity. Subsequently, a thermosetting resin mixed with a curing agent is injected into that mold cavity. During injection, the resin displaces air out of the mold cavity and impregnates the preform before the curing reaction begins. One of the current obstacles to a larger scale application of this process is the formation of defects such as dry spots and voids during resin injection.

Despite several advancements in voidage predictions via modeling and simulations, void formation mechanisms in RTM and similar processes are still not fully understood [2]. This is primarily due to the complexity of the advancing fluid front through intricate preform architectures. Void presence in composites, even in small amounts, is detrimental to their mechanical performance. In an earlier article, Judd and Wright [3] summarized adverse effects of voidage on mechanical properties of composites for a variety of resins, fibers, and fiber surface treatments. The authors reported that regardless of the utilized materials, void presence induces reduction in mechanical

properties of a composite part. The properties affected include interlaminar shear strength, tensile and flexural strength and modulus, torsional shear, fatigue resistance, and impact. Ghiorse [4] indicated, for carbon/epoxy composites, that each 1% increase in void content induced a 10% reduction in flexural and interlaminar shear strength, and a 5% reduction in flexural modulus.

In more recent studies, voidage effects on mechanical properties of resin transfer molded composites were investigated. Olivero et al. [5] reported that doubling the void content from 0.35 to 0.72% by volume resulted in a 15% decrease in ultimate tensile strength and 14% decrease in stiffness for resin transfer molded composites reinforced with randomly-oriented preforms at 21% fiber volume fraction. Goodwin et al. [6] reported a 7% reduction in interlaminar shear strength per 1% increase in voidage up to 10% for a RTM composite containing 57% 5-harness satin preform. In addition, the authors observed that failure cracks initiated from medium to large sized voids with sharp corners, but not from small spherical voids. Voidage is also known to affect both the rate and equilibrium level of moisture absorption in composites [7,8]. Harper et al. [7] reported that an increase from 1 to 5% in void volume fraction induces an increase of around 280% in the initial absorption rate, and 50% in the equilibrium mass gain for an AS4/3502 graphite/epoxy composite. Hoppel et al. [8] also reported that minor variations in void volume fraction can increase the moisture diffusion rate by a factor of 6. Consequently, controlling void presence in molded parts is very critical to achieve acceptable performance.

Controlling void presence in resin transfer molded composites involves two different steps: Understanding void formation mechanisms during injection, and developing effective methods for void removal. Possible void formation sources in RTM parts are: (a) mechanical entrapment; (b) volatilization of dissolved gas in the resin during mold filling or curing; (c) partial evaporation of mold releasing agent into the preform; and (d) initial air bubble content in the resin mixture [9]. Most of these void sources can be eliminated by choosing adequate resin systems (i.e., involving fewer volatiles during molding) and degassing prior to injection, thus leaving mechanical air entrapment as the primary cause of void formation in RTM composites [10-12]. On a macro-scale, the preform is often treated as a porous medium, and the flow is presumed to follow Darcy's law. However, on the micro-scale, i.e. fiber scale, the preform is far from regular and fingering may occur. At the fiber tow level (i.e., scale of the spacing between tows), the flow is driven by viscous forces. In contrast, flow impregnating fiber tows is driven by capillary forces, which at a single fiber scale, becomes dominant over viscous forces. Depending on injection pressure, resin viscosity, fluid front velocity, and other molding parameters, either viscous or capillary flow is likely to lead the other, causing mechanical entrapment of air bubbles. A more detailed analysis of this phenomenon (i.e., fingering) has often been achieved using the capillary number, Ca , defined as the non-dimensional ratio of viscous forces to capillary forces [10-13]:

$$Ca = \frac{\mu V}{\gamma}, \quad (5.1)$$

where μ , V , and γ are the impregnating resin viscosity, the macroscopic fluid front velocity, and the resin surface tension, respectively. At lower Ca , capillary flow leads,

thus promoting inter-tow void entrapment in the macro-space between fiber tows. At higher Ca , on the other hand, viscous flow leads, thus promoting intra-tow void entrapment within fiber tows [10-13].

Mahale et al. [11] studied void entrapment during planar radial flow into non-woven multifilament glass fiber networks, and reported the existence of a critical capillary number value of 2.5×10^{-3} , below which void content increases exponentially with decreasing capillary number. Above this critical value, much less void entrapment was observed. However, these critical capillary number values remain specific to the set of material used in their experiment. To avoid such dependence on material, a modified capillary number, Ca^* , has been defined by introducing liquid-fiber contact angle (a measure of the wetting between resin and fibers), θ , into the non-dimensional number as [12,13]:

$$Ca^* = \frac{\mu V}{\gamma \cos \theta} . \quad (5.2)$$

The authors argued that the incorporation of the contact angle allowed the generalization of the capillary number definition for any type of liquid-fiber system. They based their argument on experimental observations of measured void contents for various model fluids injected at different velocities. When plotted as a function of modified capillary number, all the experimental voidage data followed a single master curve. This master curve also indicated the existence of a preferential range of modified capillary number between 2.5×10^{-3} and 2.5×10^{-2} , within which the void content is minimal (suggesting a micro-equilibrium between viscous and capillary flows). In addition, the authors

reported the coexistence of both inter-tow macro-voids and intra-tow micro-voids in this preferential range. For molding processes with $Ca^* < 2.5 \times 10^{-3}$, void content increases exponentially with decreasing Ca^* . Moreover, voids encountered within this range are primarily macro-voids. And for $Ca^* > 2.5 \times 10^{-2}$, void content increases at a slower rate with increasing Ca^* . Voids observed at this range, on the other hand, are dominantly micro-voids.

The definite correlation between modified capillary number and void content confirms that voids originate principally from mechanical entrapment during filling. Based on this finding, a number of authors [14-20] developed theoretical and numerical models, often for simplified architectures, to predict void formation during injection, and consequently propose techniques for void removal. Chan and Morgan [14] developed a one-dimensional model for the impregnation of unidirectional preforms with parallel flow based on Darcy's law. This model predicts a localized void formation at the resin front region but is weakened by the assumption of a simplified fiber arrangement pattern. Chui et al. [15] proposed a theoretical model based on a simple unsaturated flow in porous media, predicting a voidage-pressure dependence in RTM processes. Chui's model thus suggests that increases in local pressure would reduce porosity. This voidage-pressure dependence was confirmed experimentally by Lundström [16], who reported that high pressure, high local flow rate, and low initial gas concentration in resin are favorable parameters for void dissolution in RTM process. Patel and Lee [17,18] also developed a model for void formation in LCM processes based on the multi-phase Darcy's law. In addition, they offered a criterion based on the local pressure, void size, and contact angle for the movement of trapped voids. Binetruy et al. [19], on the other hand, developed a

simple analytical model for tow impregnation when the macroscopic flow is parallel to the fiber axis. More recently, Kang et al. [20] formulated a mathematical model to describe microscopic perturbations in the resin flow front that induce void formation during injection.

Once voids are formed, they will be subjected to transport phenomena during filling that alter their spatial distribution and geometrical morphology. To understand void transport mechanics through fiber reinforcement, bubble motion through constricted micro-channels has been investigated by several researchers [17-18,21-22]. Based on his theoretical results, Lundström [21] argued that voids are more likely to be trapped within fiber bundles than between bundles. Furthermore, both bubble size and the resin-fiber contact angle are reported to affect their mobility [22,23]. Adhesion force between bubbles and fibers originates from the surface tension and the difference between advancing and receding contact angles [22]. In addition, larger voids exhibit larger perimeters and thus have larger adhesion force [22,23].

Several investigations that suggest ways to reduce void occurrence in RTM composites have been presented [10,24-29]. Vacuum assistance has been shown to reduce voidage by eventual collapse of formed voids as they have no internal pressure [24]. Resin bleeding is also performed at the end of mold filling in order to purge the voids inside the composite [10,25]. Another method used to reduce void occurrence is filling the edge gap between preform and mold cavity prior to injection, a.k.a. gating [26]. Articulated tooling consists of successively compressing parts of mold walls during injection and is utilized to minimize voids in RTM composites [27,28]. A different method is packing,

which consists on applying a permanent post-fill pressure after injection [5,29]. However, determining the best method to reduce voidage involves an in-depth understanding of spatial distribution and detailed morphological characterization of voids throughout the composite. Very few studies explored such detailed void characterization in RTM. In earlier studies, we investigated different aspects of void occurrence and reduction for RTM composites manufactured by procedures similar to the one used in the current study [5,29-31]. Spatial void morphology distribution within such composites was first investigated by Hamidi et al. [30], and significant spatial variations were observed in void content and morphology, correlating well with the local fluid front velocity during filling. Through-the-thickness void distribution for the disk-shaped, E-glass/epoxy RTM composite used in the current study was also investigated [31]. Microscopic analysis revealed that average size of voids near the mold surfaces is slightly larger than those located at the interior of the composite and that void content fluctuates considerably through-the-thickness of the composite. Note that for Ref. [31], only the distribution of void content through the composite thickness was investigated, and no assessment of voidage was obtained from the planar view, nor was any information obtained on radial distribution of void content and morphology.

Microscopic image analysis was chosen not only because it allows the assessment of void location, shape, and size, but also since it has been demonstrated to be among the most accurate methods for measuring void contents [32-35]. However, three-dimensionality of the voids is an important aspect of void morphology that is often overlooked in the literature. With all the advantages of microscopic image analysis, one can only assess void morphology two-dimensionally, which does not fully reveal the actual three-

dimensional void shapes and sizes. In the current work, we further investigate the morphology and spatial distribution of voids in a disk-shaped, RTM composite based on both planar and through-the-thickness cross-sections. The investigation is performed on two adjacent samples cut along a radial line of the composite. The first sample is analyzed through-the-thickness, while the second is utilized to examine the planar voidage distribution, thus assessing the three-dimensional features of the void morphology. In addition to contrasting the results obtained from both views, more interest is drawn upon radial variation of void content and morphological features of voids to help identify dominant void formation mechanisms.

5.3 *Experimental Setup*

5.3.1 Molding Procedure

The experimental molding setup utilized to manufacture resin transfer molded disks is depicted in Fig. 5.1. The apparatus consists of a molding press assembly that injects a two-part thermosetting resin at a constant flow rate, and a disk-shaped mold cavity. The entire setup is mounted on a hydraulic press (ARCAN, Model CP402, 80,000 lb), that contains two hollow cylinders, designed as reservoirs for resin and curing agent, respectively. Due to its low toxicity and low viscosity, an epoxy resin, EPON 815C (Shell Chemicals), is selected as the molding resin. The low viscosity of $0.96 \text{ N}\cdot\text{s}/\text{m}^2$ (960 cP) facilitates high injection speeds at moderate pressures. The adequate gel time of about 20 minutes is achieved by selecting EPICURE 3282 (Shell Chemicals) as the curing agent. In order to achieve the appropriate mix ratio (4.7 to 1 by volume of resin to curing agent), the inner diameters of the two stainless steel cylinders are machined to 55.47 and 25.53 mm. Operating the press moves the attached plungers equal amounts,

thus injecting the resin and curing agent out of the cylinders. The flow coming out of the two cylinders merges through a T-connector, and then passes through a Statomix[®] motionless inline mixer (ConProTec, Inc. part # MC-05 32). Thorough mixing of the two fluids is ensured by 32 alternating helical segments inside the 155 mm-long polypropylene Statomix[®] mixer (ID= 5 mm, OD= 8 mm). The mixture then passes through a pressure transducer before being injected into the disk-shaped cavity through its center. The press progresses at a constant linear velocity of 2×10^{-3} m/s, yielding a constant injection rate of approximately 5.32×10^{-6} m³/s.

The mold cavity, as shown in Fig. 5.1, is constructed by placing a 3.18 mm-thick aluminum spacer plate between two 12.6 mm-thick aluminum mold walls. An inlet gate, is drilled and tapped for a polypropylene hose fitting (ID=6.2mm) at the center of the top mold wall. Four vents are also drilled on the top mold wall and tapped for hose fittings (ID=1.6 mm). Vents are positioned symmetrically around the cavity at a radius of 88.9 mm. A 152.4 mm-diameter circle is cut from the center of the spacer plate to form the disk-shaped cavity. In order to prevent leakage after filling and to seal the mold, 4-mm O-rings are placed in previously machined 3 mm-deep grooves in each mold wall. Note that the exit vents are located at R=88.9 mm, before the O-ring grooves (located at R=91.3 mm) but further out from the edge of the spacer plate at R=76.2 mm, as illustrated in Fig. 5.1.

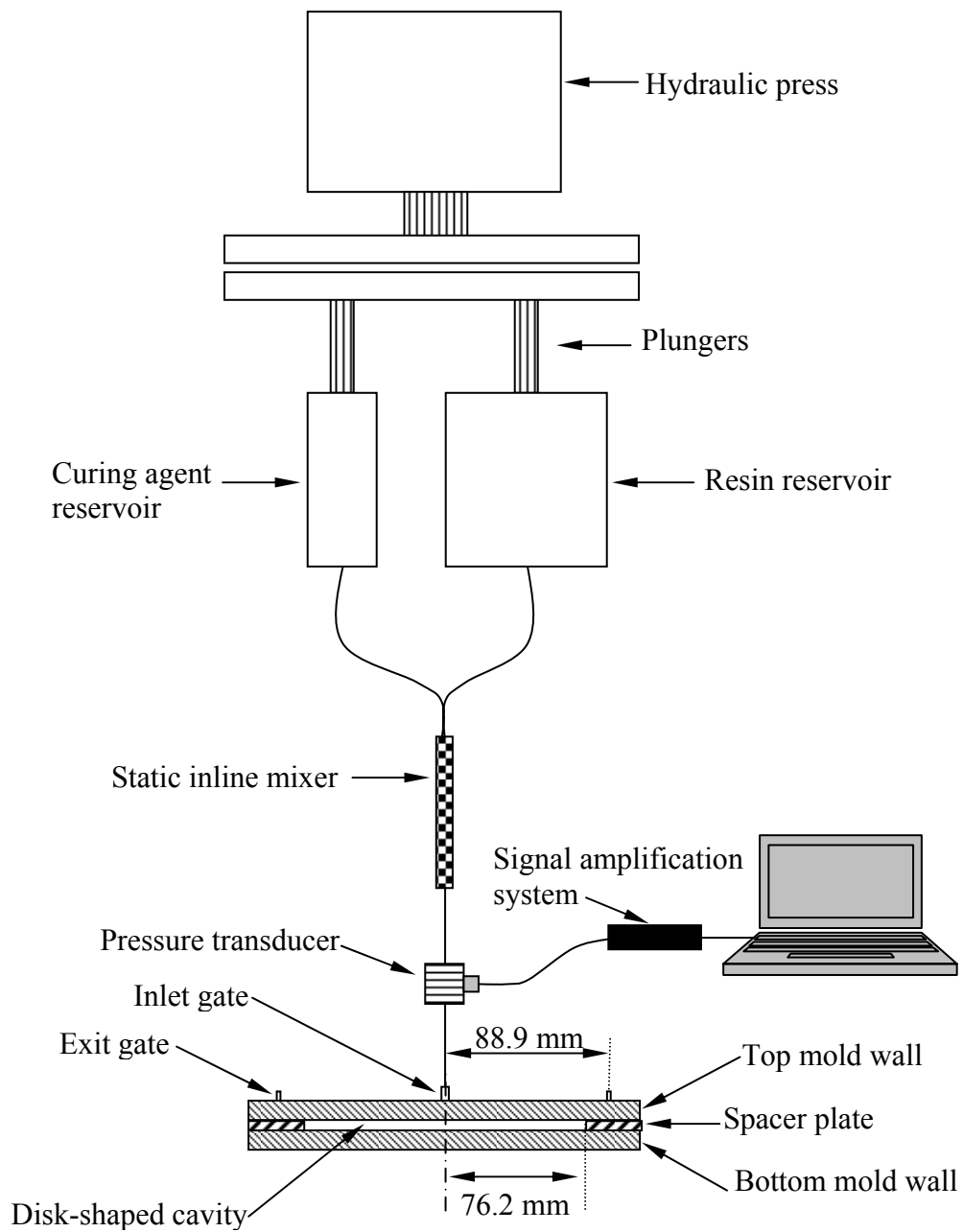


Figure 5.1: Experimental molding setup used to manufacture the RTM composite disk.

Four layers of chopped-strand, E-glass fiber mats having randomly-oriented, planar fibers, and a planar density of $0.4356 \text{ kg/m}^2 \pm 0.0449 \text{ kg/m}^2$ (Fiberglast part #250) are utilized in this study. Preforms are cut into 152.4 mm diameter circles and placed in the mold cavity prior to filling. In order to facilitate demolding, the mold walls are also sprayed with Teflon release agent (Miller-Stephenson MS-122DF) prior to filling. After the mold is completely filled, the press is run for a few additional seconds until resin creeps inside the narrow gap between spacer plate and mold walls, and comes out of all four exit vents. After injection is complete, the part is left to cure in the mold for 48 hours before demolding. The part is then post cured at room temperature for two additional weeks to ensure the completion of cross-linking. The final product is a 3.88 mm-thick resin transfer molded composite disk having 152.4 mm diameter, with a fiber volume fraction of 17.5%.

5.3.2 Transient Filling Pressure Measurement

During filling, transient inlet pressure is measured using a flush diaphragm, stainless steel pressure transducer (Sensotec BP357BR Model S, 100 psi max, 0.1% accuracy) mounted inline between the mixer and the mold inlet as shown in Fig. 5.1. The pressure transducer is attached to a custom built signal amplification circuit based on an AD620 in-amp, which conditions the signal for data acquisition system by amplifying the voltage and isolating the signal. Pressure data is recorded at 10 Hz using an Omega Daqbook data acquisition system installed on a laptop computer. Pressure monitoring is continued for a few minutes after the mold cavity is completely full, as the exit hoses are left unclamped to allow continued discharge of the resin.

5.3.3 Capillary Number Determination

As discussed in the introduction, void content is shown to correlate with modified capillary number [10-13]. In addition, capillary number and modified capillary number are useful tools in understanding the micro-scale flow during fluid front progression, as well as void formation mechanisms. If modified capillary number changes spatially, one might expect to see not only spatial variations in void content within a composite part, but also variations in void sizes and shapes. Therefore, determining the range of capillary number involved during an RTM process can be vital to understanding void formation mechanisms, and consequently spatial void distribution and void morphology throughout the molded part.

As defined in Eq. (5.2), modified capillary number calculation requires quantifying the impregnating resin viscosity, μ , the macroscopic fluid front velocity, V_{ave} , the resin surface tension, γ , and the advancing contact angle, θ . The viscosity of the resin-curing agent mixture is measured using a Brookfield viscometer (Model DV-II+). Although the mixture's viscosity increases rapidly at the end of the 20 minute gel time as the cross-linking starts, its value remains mostly stable around $0.96 \text{ N}\cdot\text{s}/\text{m}^2$ several minutes after the mixing. Both the surface tension and the advancing contact angle were measured in an earlier study for the same system of resin, curing agent, and random glass-fibers [29]; and their respective values were measured to be $36.3 \times 10^{-3} \text{ N}/\text{m}$, and 34° . These values compare well with measured values of similar systems published in the literature [32-34]. Finally, the macroscopic fluid front velocity can be determined from the injection rate and the mold geometry as:

$$V_{ave} = \frac{Q}{A} = \frac{Q}{2\pi H r(1-V_f)}, \quad (3)$$

where Q is the volumetric resin flow rate, H the thickness of the mold cavity, r the radius at which the capillary number is calculated, A the cross-sectional area of the resin flow at r , and V_f the fiber volume fraction. Substituting Equation (3) into Equation (2), the modified capillary number becomes a function of the radial distance from the injection gate:

$$Ca^* = \frac{\mu Q}{2\gamma\pi H(1-V_f)\cos\theta} \cdot \frac{1}{r}. \quad (4)$$

5.3.4 Void Characterization

Void content in composite materials is measured using a multitude of methods that can be classified into three major categories: (i) density measurement methods such as relative density, burn-off, and acid digestion; (ii) non-destructive methods such as water absorption, ultrasonic, and radiography; and (iii) optical-microscopy based methods. Density measurement methods are simple, standardized, and provide overall void contents based on a small sample, but have a low accuracy and give no information on size, shape, location, or distribution of voids. Non-destructive methods are particularly attractive since they present the advantage of inspecting the whole composite without inducing any adverse effects. In the C-scan ultrasonic technique for instance, a sound wave is transmitted through the composite. The void content is calculated by measuring the attenuation in the sound wave caused by passage through the material [25,33-34].

However, to obtain quantitative void content readings calibration is needed by using results from another method. It is believed that the accuracy of ultrasonic void inspection methods is not better than $\pm 0.5\%$ void content [25]. Moreover, attenuation levels are influenced by preform architecture, fiber volume fraction, resin degree of cure, and also by the fiber/matrix interface [25,33-34]. Thus, ultrasonic measurements are usually used for comparison purposes [34].

Optical image analysis provides detailed information on void size, shape, and location. In addition to these important parameters, void contents and areal densities are quantified from microscopic images usually conducted on highly localized areas that are assumed to be representative of the whole composite. By assuming an unstructured void pattern perpendicular to the image plane, the statistical average of void percentages in the processed images is taken as equivalent to the void volume fraction. The method is so far considered the most accurate for measuring the true void content [33-35].

However, voids can have spatial patterns and non-random distributions due to different molding parameters as was observed in our earlier studies [5,29-31]. These spatial patterns undermine the assumption of random void distribution throughout the composite, thus lowering the accuracy of obtained void contents. In a study on void content measurement in commingled E-glass/polypropylene composites using optical image analysis, Santulli et al. [38] correlated the error originating from statistical averaging to the number of cross-sections used. Although optical image analysis offers a compromise between adequate accuracy and sufficient resolution, error was observed to steadily decrease with increasing number of cross-sections reaching 0.05% only after examining

half of the composite. However, the authors argued that for composites with higher void occurrence and due to possible void concentration in a localized part of the composite, the entire composite needs to be processed in order to obtain acceptable accuracies.

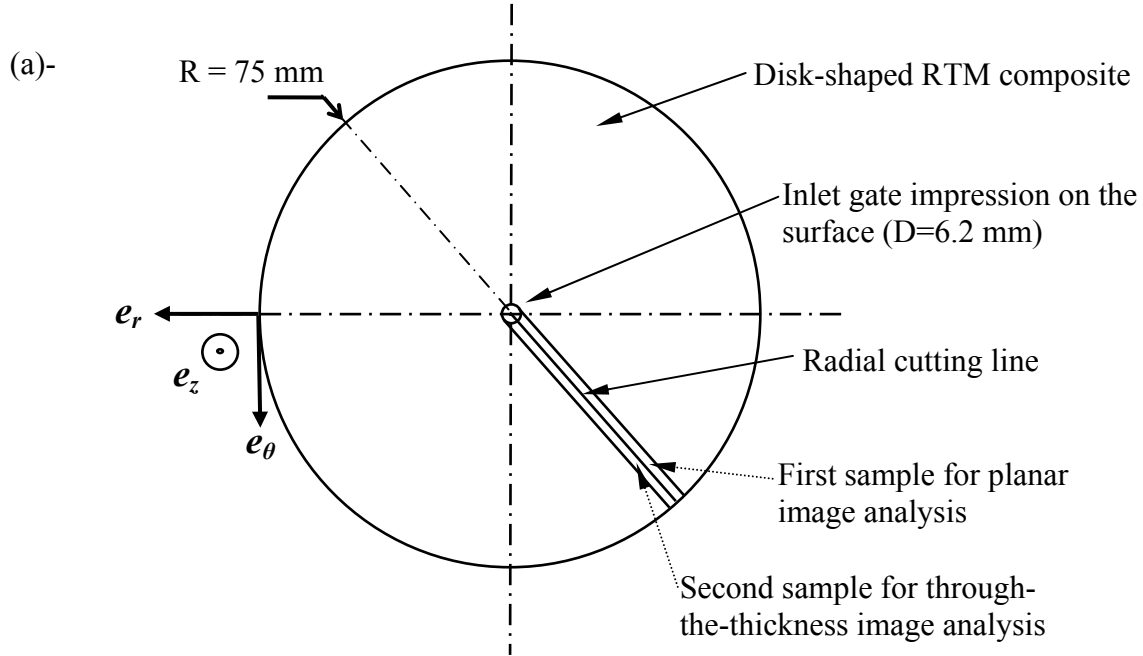
In the current work, instead of statistically averaging randomly selected images, microscopic image analysis is performed over the entire cross-sectional area of the composite using a sufficiently high magnification (i.e., 200x), which enables the identification of voids as small as the radius of a single fiber. Consequently, all identifiable voids at the working magnification throughout the investigated cross-sections are included in the analysis of void content, morphology, and spatial distribution.

Due to the planar isotropy of the preform and axisymmetric shape of the mold, the flow is assumed to depend only on the radial location. In order to fully characterize void distribution, two adjacent radial specimens are cut from the fully cured composite disk. Figure 5.2 depicts the spatial arrangement of the two investigated samples. The first sample is selected to investigate the planar void distribution (i.e. the θ plane in the cylindrical coordinates shown in Fig. 5.2), while the second is used for a more traditional through-the-thickness void analysis in the r - z plane. The two specimens present an average length and thickness of 75 and 3.88 mm, respectively, and were separately embedded into a quick cure acrylic resin (Allied High Tech. Products, part # 170-10000). Once embedded, the planar sample was further machined on a vertical mill to remove a thin composite surface layer and avoid surface irregularities. Then, the two samples were polished with a series of polishing pastes (Clover Compound) with grit sizes ranging from 180 (e.g. 80 μm average particle diameter) to 1200 (15 μm) in six successive steps.

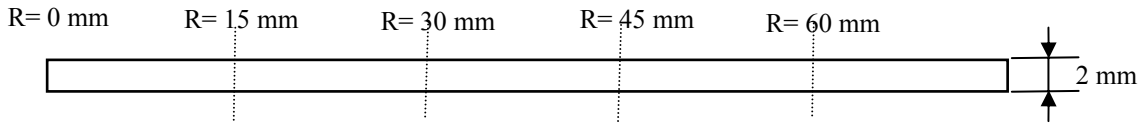
After each step, the samples were sonicated for 40 minutes in an ultrasonic cleaner (50 kHz) to remove all residues of the polishing compound. As a result of surface machining and subsequent polishing, a total of 0.67 mm-thick layer is removed from the top of the first composite sample reserved for planar void analysis.

Microscopic optical image analysis is started by dividing the first 75 mm-long sample into five 15 mm-long regions along the radial direction as shown in Fig. 5.2b. Given that the inlet has an outer diameter of 6.2 mm, only a 2 mm-wide strip is investigated. The strip width of 2 mm, as shown in Fig. 5.2a, is chosen to remain within the axisymmetry of the disk. Each 15 mm x 2 mm cross-section is then entirely scanned at 200x magnification using a MEIJI optical microscope. At this particular magnification, every frame displays approximately 0.71 mm x 0.53 mm, which requires the capture of four image frames to scan across the sample width at a particular radial location. Images of each radial region containing identified voids are captured using a PC-based CCD camera.

In addition to planar image analysis, void distribution through-the-thickness of the second specimen is also recorded. To accomplish that, five radial regions, with a surface area equivalent to those regions defined for the planar sample, are investigated. As shown in Fig. 5.2c, only 8 mm x 3.88 mm cross-sections located at the center of corresponding radial regions are investigated (i.e., 7.5, 22.5, 37.5, 52.5, and 67.5 mm radial distance from the injection gate).



(b)-First sample, top view



(c)-Second sample, through-the-thickness view

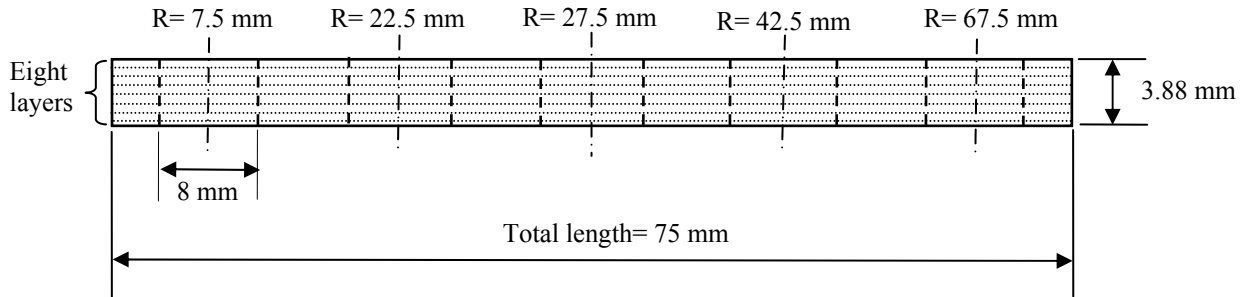


Figure 5.2: Spatial arrangement of investigated samples of the RTM composite molded without post-fill pressure at 17.5% fiber content: (a) location of samples within the composite disk, (b) First sample partitioned into five 15 mm-long radial regions for planar void analysis, (c) Second sample partitioned into five 8 mm-radial regions and eight through-the-thickness layers.

As described before, the images of voids entrapped at each spatial location are captured using a PC-based CCD camera attached to the optical microscope. At each particular radial location, scanning across the full sample thickness requires the capture of eight frames. In addition, voids located at different thickness locations of the sample are differentiated to permit void characterization through-the- thickness of the composite. A total of 960 frames are scanned and 826 frames containing voids are stored from the two samples analyzed. Each one of the 826 frames is processed using the image analysis software UTHSCSA Image Tool[®], which allows the measurement of area, A , and maximum length, L_{max} , of each void. Void contents for different radial regions of the two samples are then calculated as the ratio of the total void area to the entire scanned area of that region. Furthermore, in order to quantify the change in void content through the sample's thickness, eight layers were defined as described in Fig. 5.2c, with the first layer defined as the very top 0.5mm-thick layer, then the second as the adjacent layer, and so forth. Note that the eighth layer is only 0.38 mm-thick.

5.4 Results and Discussion

5.4.1 Inlet Filling Pressure

Impregnation of porous fiber preform during liquid composite molding is usually described by a flow through porous media model given by Darcy's law. In the present study, operating the hydraulic press, as described earlier, ensures that the injection of the impregnating resin mixture takes place at a constant volumetric rate at the center of the circular mold cavity. Therefore, the filling pressure steadily increases as the flow front advances radially outward through the fiber preform towards the exit vents. Due to the circular mold geometry, and the planar isotropy of the preform, an axisymmetric flow front is expected.

The transient inlet pressure profile during molding of the composite disk is shown in Fig. 5.3. During mold filling, the pressure increases at a steep rate until all the preform is impregnated, reaching 380 kPa in less than 9 seconds. When the mold cavity is full, the pressure increases at a higher rate as the resin creeps inside the tight space between mold walls and the spacer plate. The exit vents were placed intentionally between the spacer plate edge and the O-ring seal to force the resin into this narrow opening, hence increasing the maximum pressure inside the mold. The high pressure reached at the inlet is expected to ensure complete impregnation of the dry preform, help reduce voidage [15,16], and facilitate void mobility [22]. As the resin is forced to creep inside the tight opening between spacer plate and mold walls, the pressure attains its highest value of 565 kPa. After the resin starts coming out of the four exit vents, injection is immediately stopped, and exit vents are left unclamped to allow continued discharge of the resin.

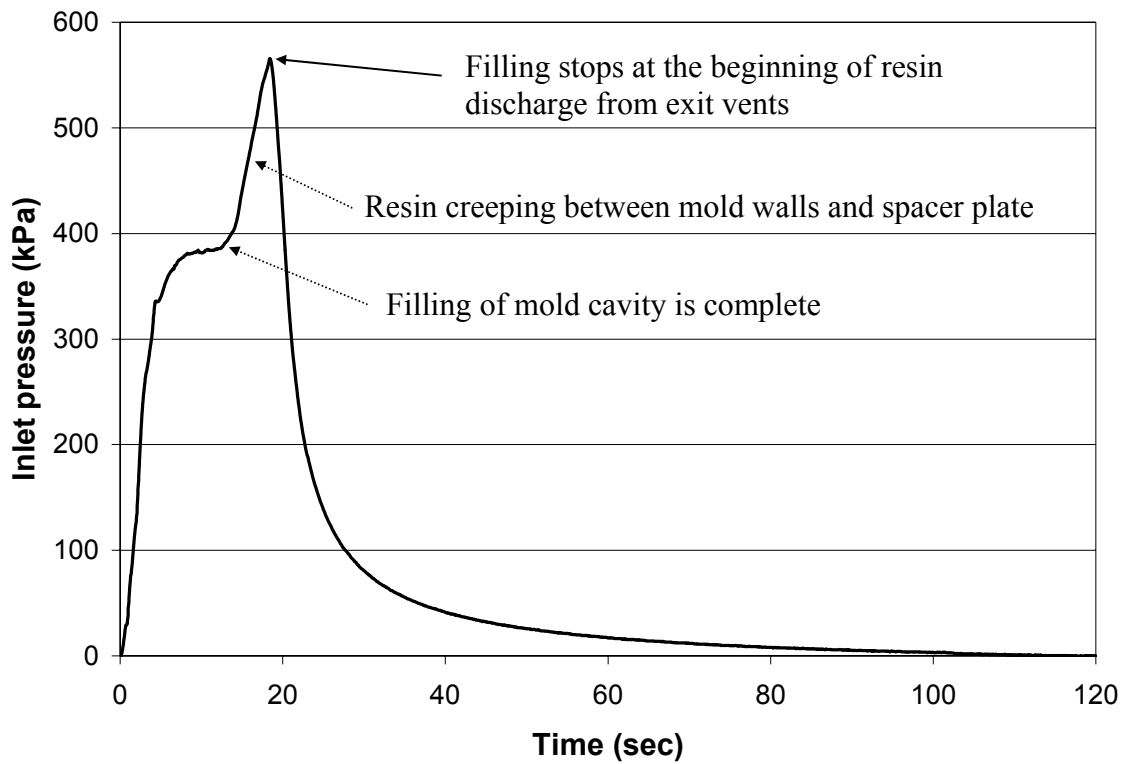


Figure 5.3: Inlet pressure profile during mold filling of the composite disk molded without post-fill pressure at 17.5% fiber content.

5.4.2 Average Void Content

Most, if not all, void studies characterize void morphology two-dimensionally, which limits the understanding of void distribution, formation and mobility mechanisms in RTM composites. Post-cure studies investigating void size and shape often use microscopic image analysis only through-the-thickness of the composite [4-6,20,22,25,29-31,35,38]. While other investigations, with a focus on void formation, determine void content, morphology, and distribution during mold filling via monitoring flow front progression from the planar view [1,10-13,17-18,26,33-34,36,39]. Nevertheless, and to the best knowledge of the authors, no study combines the two views to assess three-dimensional features of void morphology. As illustrated by lower magnification (i.e., 50x) images shown in Fig. 5.4, fiber orientation distributions and fiber clustering for the two views (i.e., planar and through-the-thickness) are fundamentally different: Fibers are seen as more homogeneously distributed through the composite thickness (Figs. 5.4a, 5.4c, and 5.4e), while the planar view offers zones with very high fiber concentration (Fig. 5.4f), and large matrix-rich regions (Fig. 5.4d). The way successive preform layers are arranged inside the mold cavity prior to mold filling is a plausible cause for the observed difference in architecture between the two views of the same composite. Another conceivable source for these architectural discrepancies may be related to up to 77% variation in planar densities of the utilized reinforcement. Planar density of utilized preforms was found to vary between 0.3141 to 0.5564 kg/m², thus yielding significant variations of spatial fiber concentration. These values were calculated from more than five hundred circular preforms cut from the same randomly-oriented fiber glass roll used in this study.

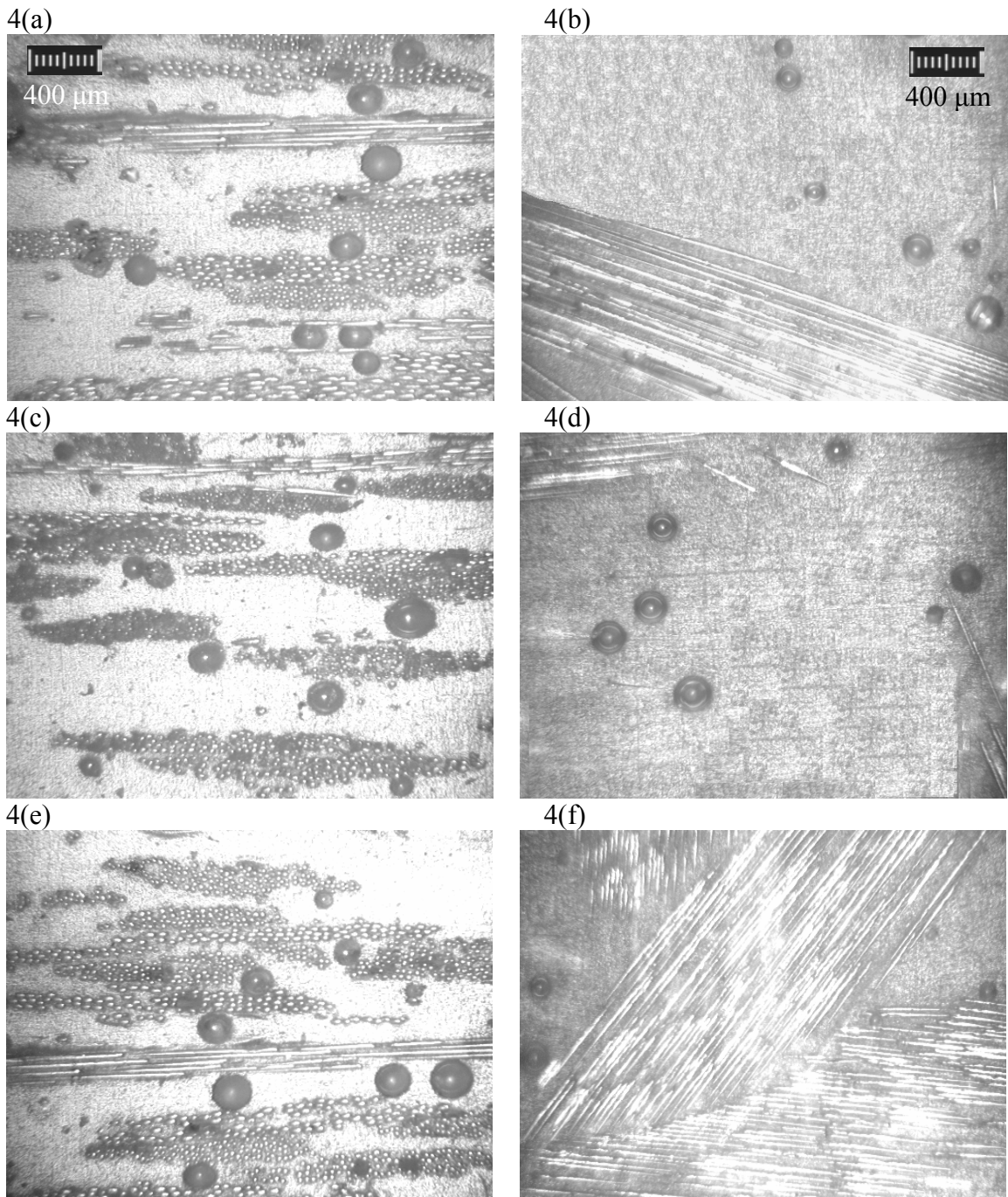


Figure 5.4: Representative microscopic images obtained at 50x magnification from through-the-thickness (left column) and planar (right column) views of the RTM composite molded without post-fill pressure at 17.5% fiber content.

Void contents obtained for the eight through-the-thickness layers depicted in Fig. 5.2c are shown in Table 5.1:

Table 5.1: Variation in voidage through-the-thickness of the composite disk molded without post-fill pressure at 17.5% fiber content.

	Layer 1	Layer 2	Layer 3	Layer 4	Layer 5	Layer 6	Layer 7	Layer 8
Thickness (mm)	0.50	0.50	0.50	0.50	0.50	0.50	0.50	0.38
Void content	2.30%	2.58%	1.52%	2.62%	2.47%	2.21%	2.61%	1.25%
Planar void density (Void / mm ²)	10.78	11.51	9.25	11.51	10.84	10.67	12.12	6.37

The void content is found to vary between 1.25 and 2.62% through-the-thickness. This non-uniformity can arise from uneven spaces between the four preform layers, or between the preform and the mold walls. It can also originate from the potential variations in the fluid front velocity across the thickness of the mold cavity. Thus, considerable differences in overall void content obtained from the two samples are also expected. After processing all the void data, planar and through-the-thickness average void contents of 2.56 and 2.15% are calculated, respectively. However, average void content obtained from the planar view can only be compared to void content in the same layer of the composite. Since a 0.67 mm-thick layer was machined from the top of the planar sample; the obtained planar void content of 2.56% should be compared to that of 2.58% obtained from the second layer (Table 5.1). The two values are clearly very similar; suggesting that void contents obtained from planar views would depend primarily on the through-the-thickness location of the plane studied, and thus may vastly

vary from one layer to the other. On the other hand, void contents obtained from through-the-thickness view, when the entire composite thickness is examined for voids, are not prone to such variations [38]. Consequently, the void content determined from through-the-thickness view would be more representative of the actual void content in RTM composites.

5.4.3 Location of Voids

Void proximity to fibers can be assessed differently from planar and through-the-thickness views. Voids seen in matrix-rich areas from the planar view can in fact be in contact with fibers in other layers below the polished surface. To study this morphological feature, we introduced a classification of voids based on their proximity to fibers and analyzed both planar and through-the-thickness sections. In addition, this classification can help estimate possible adverse effects of each void on mechanical properties. Voids located only in the matrix reduce the load bearing cross-section of the composite, while those located in contact with fibers are also detrimental to fiber/matrix adhesion. Three void locations are defined: The first location is defined as areas rich in matrix and not comprising any fibers. Voids encountered in this location are totally surrounded by the epoxy matrix and are referred to as *matrix voids*. The second location is defined as areas rich in fibers, where the area is primarily composed of reinforcing preform. Voids in these locations are situated within fiber bundles (i.e., intra-tow voids) and are referred to as *preform voids*. Finally, a transition location is defined as the remaining locations other than the other two defined above. Voids found in this location are referred to as *transition voids* and are always positioned adjacent to the preform but not inside fiber tows.

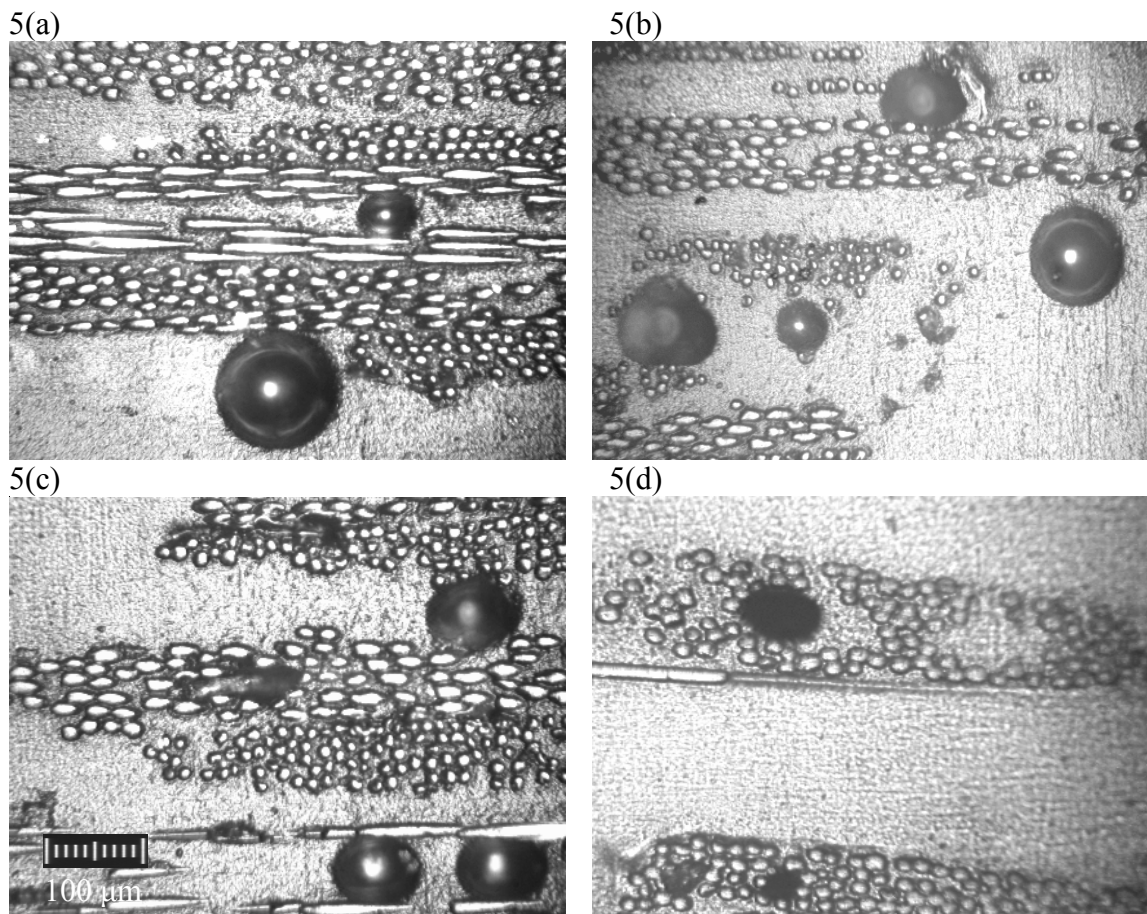


Figure 5.5: Representative microscopic images obtained at 200x magnification from the RTM composite molded without post-fill pressure at 17.5% fiber content depicting examples of voids from different zones: (a) typical composite cross-section with different fiber orientations and two *transition voids*; (b) examples of *transition* and *matrix voids*; (c) three *transition voids* and two *preform voids*; (d) three *preform void*.

Figure 5.5 depicts sample images obtained from through-the-thickness view containing voids obtained from the three zones defined above at 200x magnification. In Fig. 5.5a, the continuous polymeric matrix appears as a gray background, the white circular and elliptical objects correspond to glass fibers oriented at an angle to the cross-section. Based on the categories defined earlier, the two adjacent voids to fibers seen in Fig. 5.5a are *transition voids* along with similar voids from Figs. 5.5b and 5.5c. The two voids seen inside fiber tows in Fig. 5.5c and the three voids appearing in Fig. 5.5b, on the other hand, are *preform voids*. Finally, the void depicted at the right side of Fig. 5.5d is considered a *matrix void*.

Figure 5.6 depicts the contributions of voids encountered within different locations to the average void content of the whole composite. From the planar view, voids seem to be concentrated in the matrix rich zone with almost 57.4% to the 2.56% overall void content (i.e., 1.5%) located in the matrix. At the same time, intra-tow voids, located inside the preform, do not seem to constitute a significant portion of the voidage of the whole composite. Only 17.6% of the 2.15% overall voidage (i.e., 0.43%) is identified as *preform voids*. Through-the-thickness voidage distribution, on the other hand, shows a different distribution. While the *transition voids* showed the highest contribution at 1.31%, the *preform* and *matrix voids* contributed 0.72% and 0.15%, respectively. Hence 94.4% of the total voidage is found to be concentrated either inside or right next to the preform when through-the-thickness view is used.

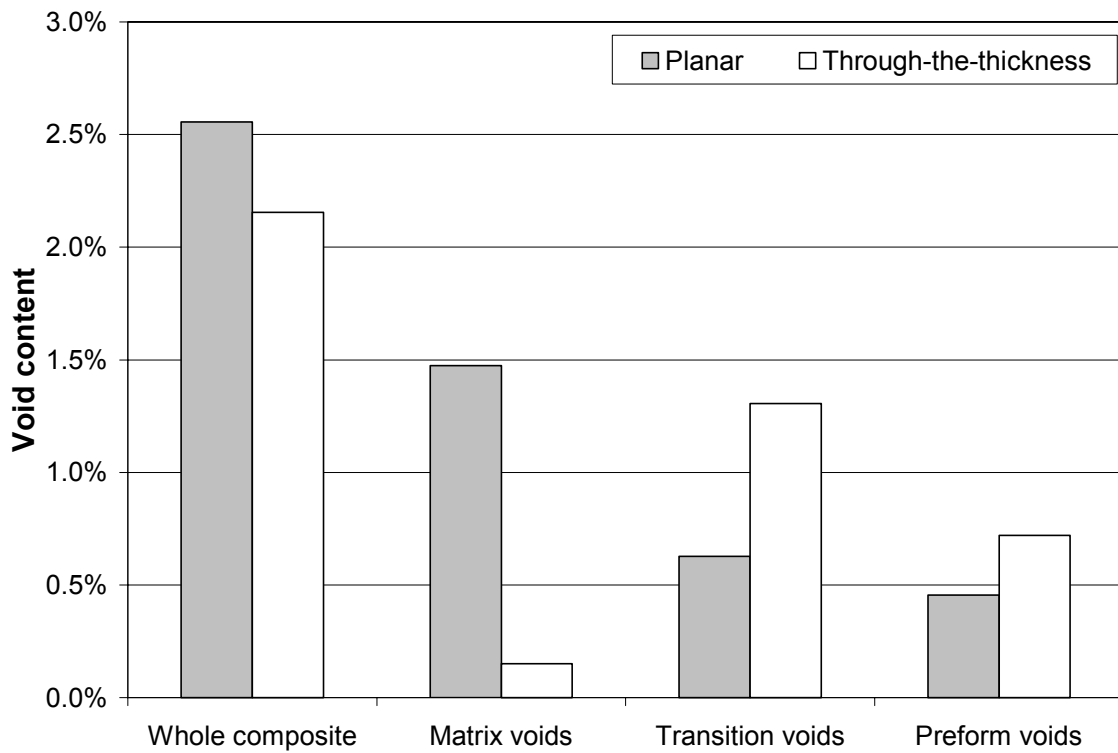


Figure 5.6: Planar and through-the-thickness void content contributions of voids located at different locations of the composite molded without post-fill pressure at 17.5% fiber content.

Due to the difference in fiber orientation patterns between planar and through-the-thickness views described above, classification of void locations based on through-the-thickness view is believed to better characterize the actual locations of voids throughout the composite. For instance, many voids that are classified as *matrix voids* in the planar view might be in contact with fibers at composite layers above or below the observed plane, thus belonging in reality to *transition voids* category. As depicted in Figs. 5.4a, 5.4c, and 5.4e, the stacking of preform layers does not leave adequate space between fiber tows to have a significant occurrence of *matrix voids*.

Utilizing the modified capillary number can help understand formation mechanisms of voids involved in the micro-scale flow during fluid front progression. Using Eq. (5.4) and the measured values of resin viscosity, surface tension, and advancing contact angle (i.e., 0.96 N·s/m², 36.3 x 10⁻³ N/m, and 34 °, respectively), the modified capillary number is calculated to change along the radial distance from the injection gate between 0.13 and 1.15 as depicted in Table 5.2:

Table 5.2: Modified capillary number variation along the radial flow direction.

Radial distance from the injection gate (mm)	7.5	22.5	37.5	52.5	67.5
Modified capillary number (Ca^*)	1.150	0.382	0.229	0.164	0.127

These high values of modified capillary number suggest that voids formed during filling should be mostly intra-tow, micro-voids [12,13]. As predicted for this range of modified

capillary numbers [12,13], through-the-thickness view incidentally describes the voids as primarily intra-tow voids, thus affirming through-the-thickness view as a better representation of actual void locations with respect to the fibers.

5.4.4 Variation of Void Size

Void size is reported to affect void mobility [22], such that larger voids have longer perimeters and thus yielding larger adhesion forces. Small voids, on the other hand, have lower adhesion forces and therefore become more mobile. Consequently, identifying void size distribution can prove useful in the choice of void removal methods. To quantify void sizes, the surface area, A , of each captured void is measured using the image analysis software UTHSCSA Image Tool[®]. An equivalent diameter, D_{eq} , is defined to classify void sizes as:

$$D_{eq} = \sqrt{\frac{4A}{\pi}}, \quad (5.3)$$

where A is the measured area of the void.

Planar and through-the-thickness size distributions based on D_{eq} are represented in Fig. 5.7. Both are lognormal distributions with only one peak, unlike typical bi-modal void distributions in fiber reinforced composites that exhibit two peaks [18]. The first peak often represents intra-tow micro-voids while the second inter-tow macro-voids. As discussed previously, the calculated range of modified capillary numbers of 0.13 to 1.15 implies that the formed voids are primarily intra-tow micro-voids [12,13], which explains why only few large macro-voids were encountered within the composite.

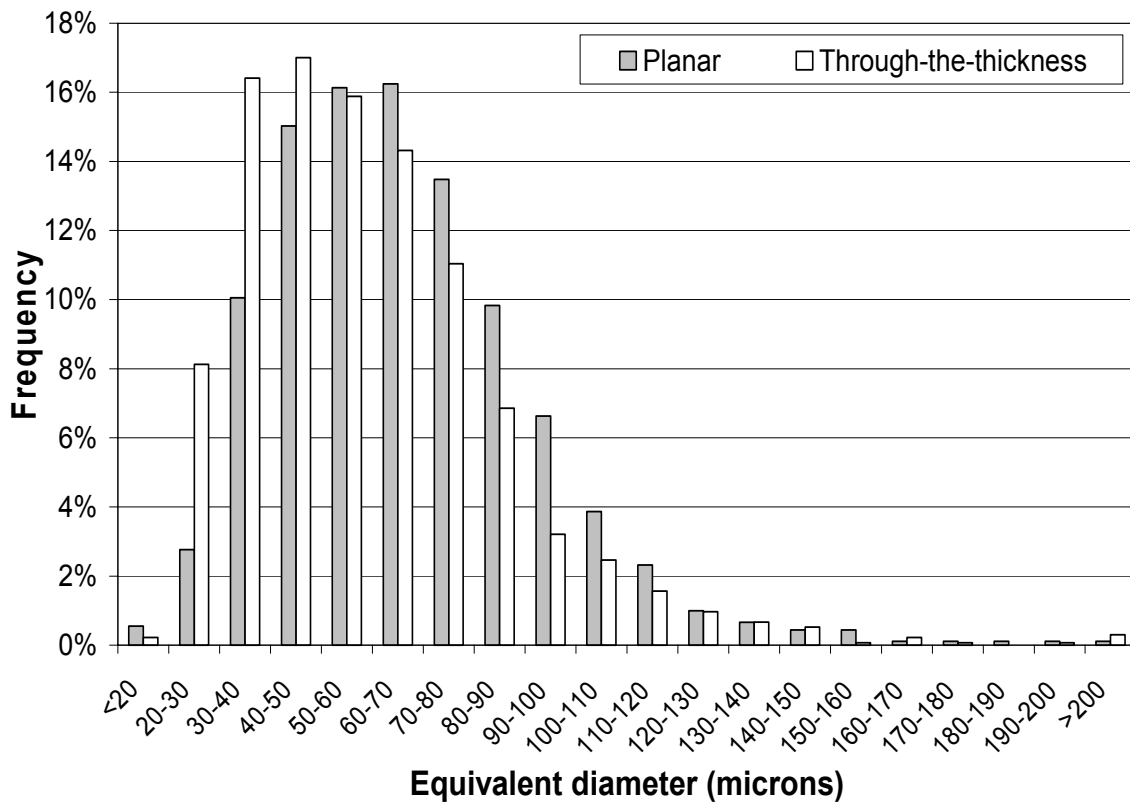


Figure 5.7: Planar and through-the-thickness size distributions based on equivalent diameter of voids encountered in the RTM composite molded without post-fill pressure at 17.5% fiber content.

Although the standard deviations of both distributions appear comparable, a slight “shift” of the distribution towards smaller voids is observed from the planar to the through-the-thickness view. The two size distributions present different mean values of 59 μm for the through-the-thickness view and 66 μm for the planar view, but have very the same standard deviations of 27 μm . This variation in the size distribution viewed from two planes is compensated by an opposite variation in areal void density. Through-the-thickness view showed a void density of 9.83 voids/ mm^2 , while the planar view showed only 6.33 voids/ mm^2 in areal void density. In short, voids are seen in average slightly fewer but larger in the planar view. The observed difference in void size distribution when seen from the two views, especially the mean equivalent diameter, can be explained by the existence of long cigar-shaped intra-tow voids inside fiber bundles (Fig. 5.8b and 5.8d). The preform is mostly planar, thus these cigar-shaped voids are seen only as small intra-tow voids when observed from through-the-thickness view, but are seen in full in the planar view.

In order to categorize void sizes, three different size ranges are defined. Large voids are defined as those voids with an equivalent diameter greater than 100 μm , i.e. $D_{eq} > 100 \mu\text{m}$; while voids with an equivalent diameter lower than 50 μm are regarded as small voids. Intermediate equivalent diameter values, i.e. $50 \mu\text{m} < D_{eq} \leq 100 \mu\text{m}$, correspond to medium size voids. Using these categories, concise planar and through-the-thickness void size distributions are obtained as shown in Fig. 5.9. Void size distributions for the whole composite and for the *preform voids* only are presented in Fig. 5.9 for both samples.

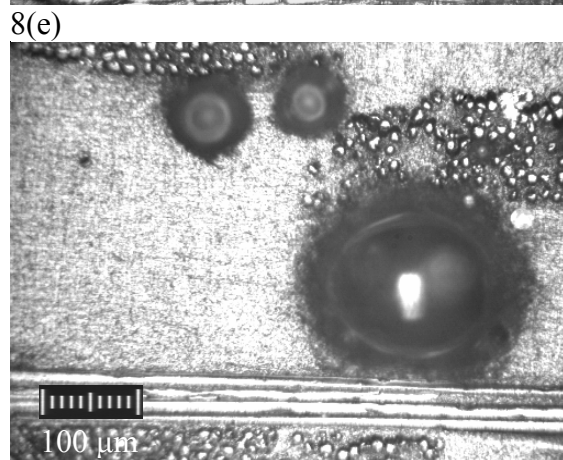
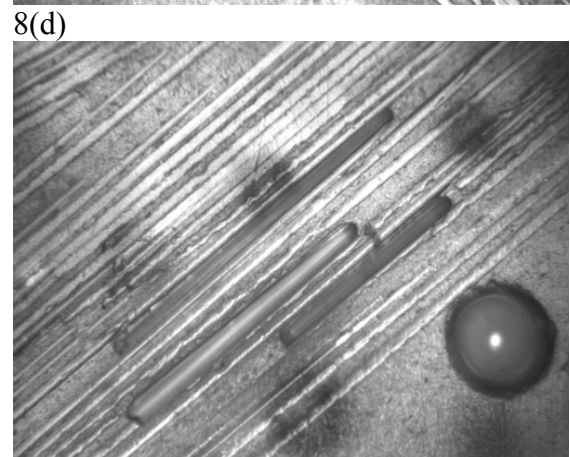
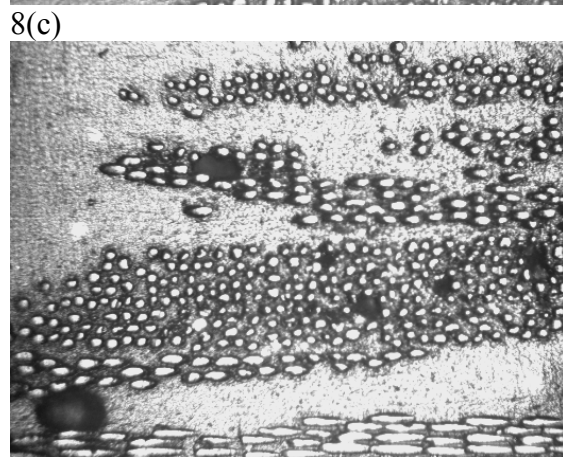
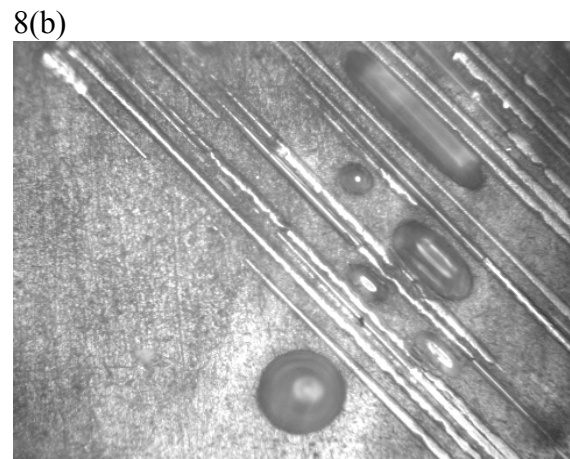
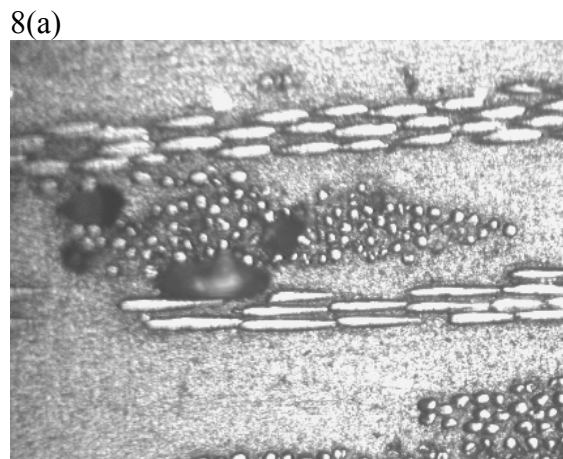


Figure 5.8: Representative microscopic images obtained at 200x magnifications from the through-the-thickness view (left column), and planar view (right column) samples of the RTM composite molded without post-fill pressure at 17.5% fiber content.

The decrease in average void size from the planar view to through-the-thickness view for the whole composite, presented earlier in detail, can still be seen as the relative percentage of small voids increases from 28.4 to 41.7% between planar and through-the-thickness distributions.

The relative percentages of *matrix* and *transition voids* are found to remain mostly similar for planar and through-the-thickness views. Therefore only size distributions of *preform voids* are shown in Fig. 5.9. Small voids encountered within the preform rise from a 40% of the total voids for the planar view to more than 66% for through-the-thickness view. This steep increase in relative percentage of small voids found within the preform combined with almost no change in *matrix* and *transition voids* size distributions confirms that only *preform voids* cause the change in average void size between the two views, yielding the 13% increase in average void size observed in Fig. 5.7. Based on these findings, the actual void size distribution seems to be revealed better by the planar view as some of the larger voids are not fully seen in through-the-thickness-view.

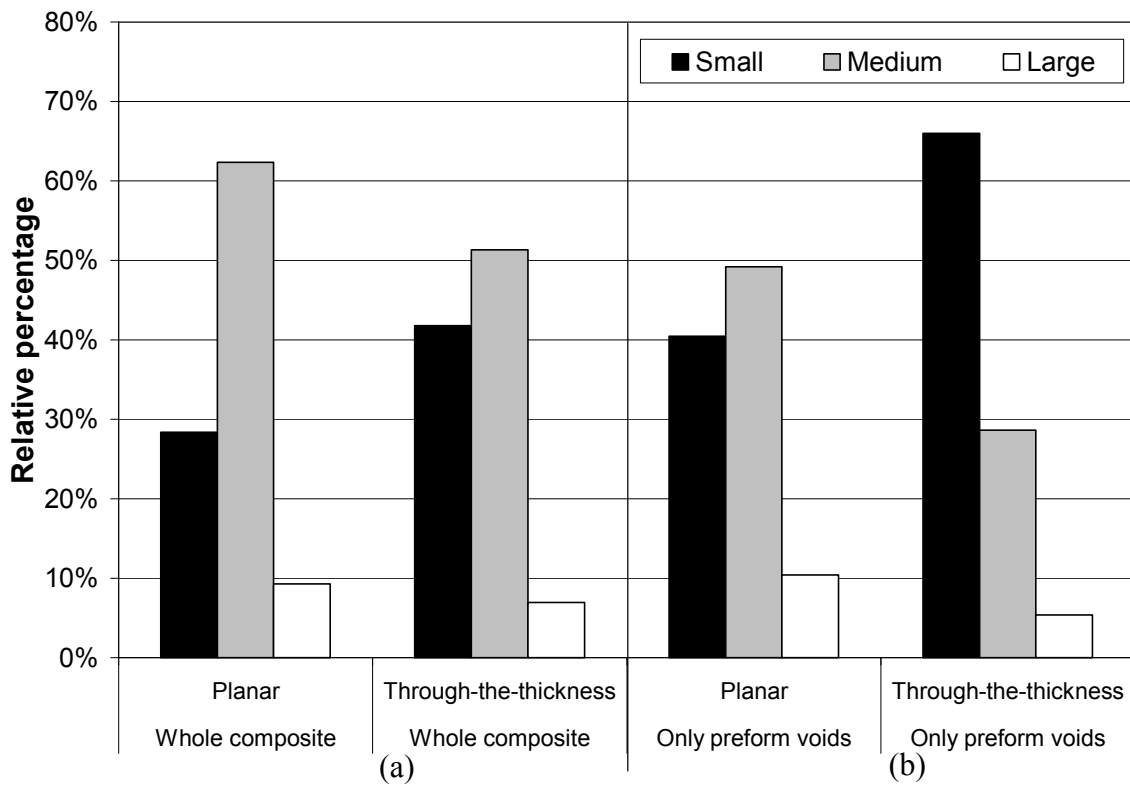


Figure 5.9: Size distribution of voids obtained from planar and through-the-thickness views of the RTM composite molded without post-fill pressure at 17.5% fiber content when: (a) considering the whole composite; (b) considering only *preform* voids.

5.4.5 Variation in Void Shape

In a study on void induced reduction in interlaminar shear strength, Wisnom et al. [40] reported that the commonly observed void induced decrease in interlaminar shear strength of glass fiber and carbon fiber/epoxy composites is due to a combination of two phenomena: (i) reduction of cross-sectional area from the overall voidage; and (ii) initiation of failure from larger elongated voids. Similar results were reported by Goodwin et al., who identified larger voids with sharper corners as inducers of early crack formation [6]. Thus, shape distribution of voids becomes essential in predicting structural integrity of a composite part. As Figs. 5.4, 5.5 and 5.8 depict, different void shapes are encountered in the two views of the composite. Voids shown in Figs. 5.4b, 5.4d, at the bottom of 5.5a, and at the right of 5.5b, and those seen at the bottom of 5.8b and top of 5.8d are mostly circular. In contrast, voids trapped between fiber bundles at the bottom of Fig. 5.5c, and in Figs. 5.8b, and 5.8d, and the void captured in Fig. 5.8f are more elongated. Voids entrapped within the preform in Figs. 5.8a and 5.8c present a different asymmetrical geometry.

In order to quantify these differences and categorize void shapes, both geometrical and quantitative void characteristics are combined. First, based on the observed shape, the voids are divided into three groups: Irregular, cylindrical, and spherical voids. Irregular voids are defined as those presenting a non-convex planar surface area, that is, one can find two different points within the void that can be connected by a straight line that leaves the void boundary. Additionally, cylindrical voids are defined as cigar-shaped voids, observed almost exclusively inside fiber tows when seen from the planar view

(Figs. 5.8b and 5.8d). Excluding those two categories, remaining voids are mostly spherical (Figs. 5.8e and 5.8f), although some of them do not present a perfect circular symmetry (Fig. 5.8f).

To classify this variation in voids' roundness, a quantitative measure of geometrical circularity of voids is used. The data obtained from captured voids is further processed by introducing the shape ratio, R_s , defined for each void as the equivalent diameter obtained from Equation (3) divided by the measured maximum length, L_{max} , within a void:

$$R_s = \frac{D_{eq}}{L_{max}}. \quad (4)$$

Using this shape ratio, spherical voids are divided into two categories: circular voids, and elliptical voids. Since an ideal circle is represented by $R_s = 1$, only voids with shape ratios above 0.95 ($0.95 < R_s \leq 1$) are considered circular voids (bottom of Fig. 5.8b). Voids with shape ratios lower than 0.95 comprise a minor axis that could be significantly smaller than the maximum length. Thus, the circular symmetry is lost, the voids appear as ellipses, and are defined as elliptical voids (Fig. 5.8f). Typical examples of small irregular voids are presented in Figs. 5.8a and 5.8c, with equivalent diameters raging between 17 and 50 μm . Similar intra-tow voids are seen as cylindrical voids in the planar view as shown in Figs. 5.8b and 5.8d. A large circular void is seen at the bottom of Fig. 5.5a ($D_{eq} = 119 \mu\text{m}$ and $R_s = 0.96$), and medium circular voids are depicted at the right of Fig. 5.5d ($D_{eq} = 95 \mu\text{m}$ and $R_s = 0.98$), and at the bottom of figure 8(b) ($D_{eq} = 85 \mu\text{m}$ and $R_s = 0.99$). Finally, figure 8(f) exemplifies a large elliptical void exhibiting an equivalent diameter of 250 μm and a 0.91 shape ratio.

As voids with different shapes are known to affect the mechanical performance of the composite differently [6,40], the number of voids having a detrimental shape is more important than their contribution to the void content obtained for the whole composite. Therefore, areal void density is used here to present planar and through-the-thickness shape distributions. The resulting shape-voidage distribution is presented in Fig. 5.10.

Areal void densities obtained from the two samples are considerably different. The areal void density of 6.33 voids/mm² in the planar view is only 64.4% of the through-the-thickness areal void density of 9.83 voids/mm². As shown in Fig. 5.10, cylindrical voids are not observed through the composite thickness. Since the sample used for through-the-thickness analysis is cut at an angle to most fiber bundles - potential beds for cylindrical voids - all cylindrical voids are truncated at an angle with respect to their longitudinal axis, and are seen as either small irregular, or small elliptical voids. This can explain the considerable increase in areal void density of elliptical voids from 7.58 to 29.60% of the planar to through-the-thickness elliptical void density obtained for the whole composite, respectively. In addition, irregular areal void density jumps from 0.25 voids/mm² in the planar view to 3.48 voids/mm² in through-the-thickness view. This increase can also be explained, in addition to the presence of cylindrical voids, by the difference in fiber placement and orientation patterns for the two views illustrated in Fig. 5.4.

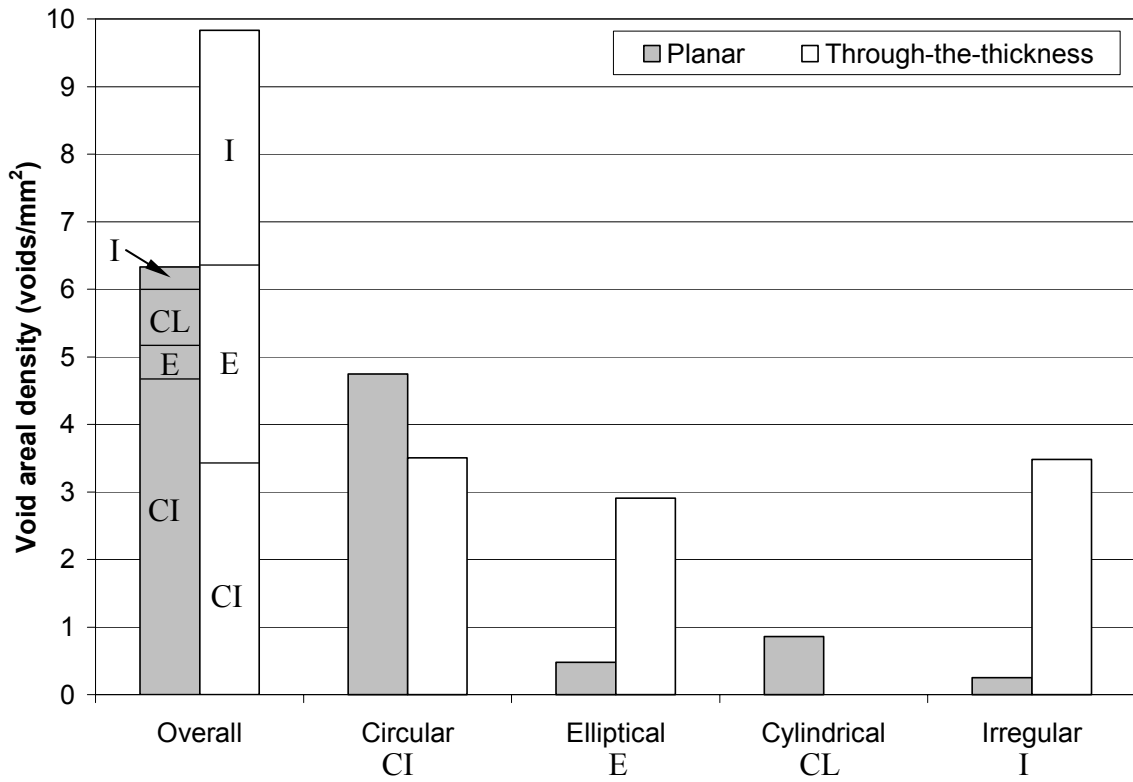


Figure 5.10: Planar and through-the-thickness areal void density distributions for different void shapes encountered in the RTM composite molded without post-fill pressure at 17.5% fiber content.

As argued earlier, many voids that are seen in the matrix in a particular planar view are in reality in contact with fiber tows at composite layers above or below the observed plane. Therefore, even if the planar view of a void is circular, the void may in fact present an irregularity where it comes in contact with fiber bundles, and is seen as an irregular void through-the-thickness. This latter fact can also explain the drop in circular areal void density from 4.75 in planar view to 3.50 voids/mm² in through-the-thickness view. These findings imply that neither planar nor through-the-thickness views can fully represent the actual void shape distribution. A combination of the two must be incorporated in order to fully assess the three-dimensional shape morphology of the voids.

Voids with different shapes are expected to have different planar and through-the-thickness size distributions. However, planar and through-the-thickness size distributions of both circular and elliptical voids are found almost identical. In addition, through-the-thickness view did not comprise any cylindrical voids. The size distribution of different void shapes is given in Fig. 5.11. In this figure, relative size distributions for all void shape categories observed in the planar view, and size distribution of irregular voids observed in through-the-thickness view are depicted. In the planar view, circular and cylindrical voids are observed as mostly medium size. Elliptical voids are observed to be slightly smaller since 45.59% of the total elliptical voids encountered are small. Nevertheless, small and medium size voids together represent 90% or more of the circular, elliptical, and cylindrical voids.

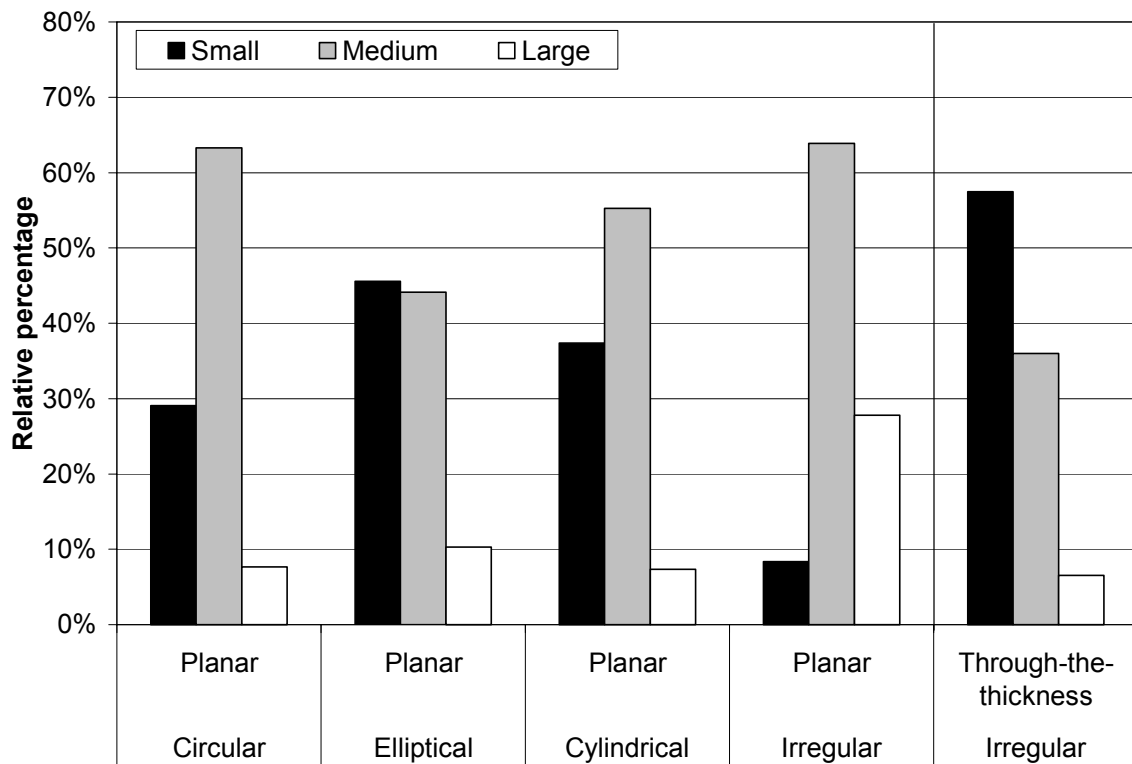


Figure 5.11: Average planar and through-the-thickness size distributions of voids with different shapes encountered in the RTM composite molded without post-fill pressure at 17.5% fiber content.

Consequently, size distributions of voids from these three shape categories remain consistent with the size distribution for the whole composite presented in Fig. 5.9. Irregular voids, on the other hand, display different size distribution profiles when analyzed using planar and through-the-thickness views. The majority of irregular voids shift from medium or large size in the planar view to small or medium size if viewed through the part's thickness. The increase in average void size is 13%, which is an additional proof for the analysis argued earlier, that states the difference in cylindrical voids seen in planar and through-the-thickness views as the reason of the difference in average void size observed in Fig. 5.7.

5.4.6 Voidage Variation Along the Radius of the Molded Disk

In addition to molding speed, other factors are known to change void content and distribution inside a molded composite part. When resin injection is performed at a constant volume flow rate through a constant mold cross-section, the fluid front velocity, and subsequently the capillary number, does not depend on the distance from the injection inlet. Consequently, the voidage along the composite part may not vary much with respect to the inlet distance. In contrast, the impregnation in the current case is carried out at constant volume flow rate for a center-gated disk-shaped cavity. Hence, as formulated in Eqs. (5.3) and (5.4), the fluid front velocity and the capillary number change as the flow progresses. This change in capillary number is likely to yield a radially non-uniform void distribution. This latter case is not the only configuration where spatially non-uniform void distribution is expected, constant inlet pressure

molding, a commonly used RTM method, is also carried out at decreasing fluid front velocity. Thus similar void distribution trends are expected in such composites.

In a previous study [29], packing effects on void contents and spatial void distribution were investigated in composites molded under parameters similar to those utilized in this study. Radial void distribution was also investigated. Packing was found to induce void migration along the radius of the composite. This void migration was believed to result from several transport mechanisms such as shearing forces and void compression and dissolution. This behavior contrasted with that encountered in composites molded without packing, where the voids preferentially concentrated at the center of the part. However, radial distribution of voids and void morphology prior to the application of any void reduction method has not been available. Hence, detailed radial void distribution and void morphology characterization are believed to be the key to understanding void formation and migration mechanisms, as well as assessing the effectiveness of various void reduction methods.

To determine the effect of radial distance on voidage and void morphology, five equivalent radial regions were defined as shown in Fig. 5.2 for both samples studied. Figure 5.12 depicts planar and through-the-thickness void content distributions along the radial direction (i.e., the direction of the flow during mold filling). Each radial region is referred to using the radial distance from the injection gate to its center. The modified capillary numbers are calculated for each region and the resulting values are shown in Table 5.2. At this range, (i.e., $Ca^* > 2.5 \times 10^{-2}$), void content is expected to increase moderately with increasing modified capillary number [12,13]. Accordingly, void

content is predicted to decrease with increasing radial distance from the injection gate. Moreover, at longer distances from the injection gate (i.e., lower capillary number), slower moving fluid front is expected to trap smaller, more circular, and fewer voids [30]. Nevertheless, both planar and through-the-thickness void content radial distributions, given in Fig. 5.12, do not show any clear trend. It even appears that void content increases with increasing radial distance. The absence of a clear trend in radial void content distribution can be the result of different factors with contrasting influences on void formation during filling.

To understand the mechanisms behind this radial distribution, void contents from different void locations (i.e., *matrix*, *transition*, and *preform voids*) are segregated. Since through-the-thickness view is believed to better represent the actual location distribution of voids, only through-the-thickness results are utilized here. Figure 5.13 depicts radial distribution of *matrix*, *transition*, and *preform voids* taken from through-the-thickness view. As seen in Fig. 5.13, radial distance does not seem to have an effect on the distribution of *matrix voids*. However, clear trends are observed for the relative content of *transition* and *preform voids*, especially from the third radial region outward. The relative contribution of *preform voids* (voids within a fiber tow) to the overall void content decreases from 47.23% in the third region to 14.55% in the fifth region. In contrast, contribution of *transition voids* (voids right next to fibers but not inside fiber tows) increases from 37.50% in the third region to 77.40% in the fifth region.

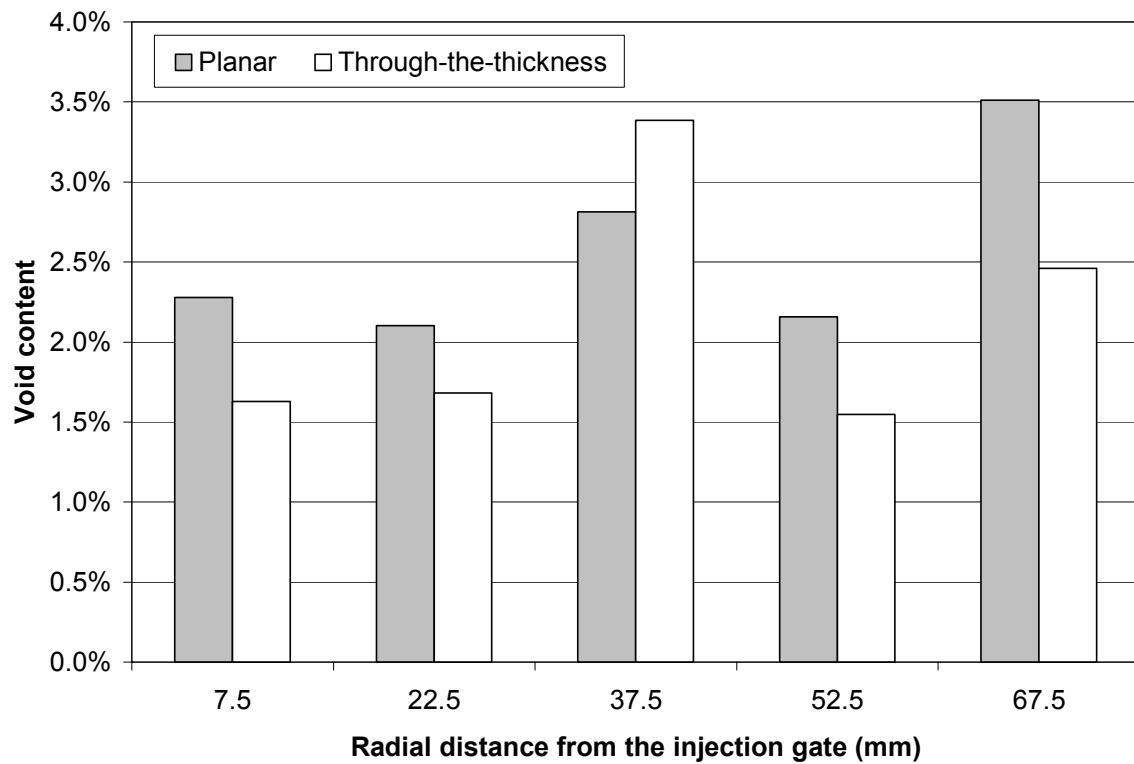


Figure 5.12: Planar and through-the-thickness radial distributions of void content within the RTM composite molded without post-fill pressure at 17.5% fiber content.

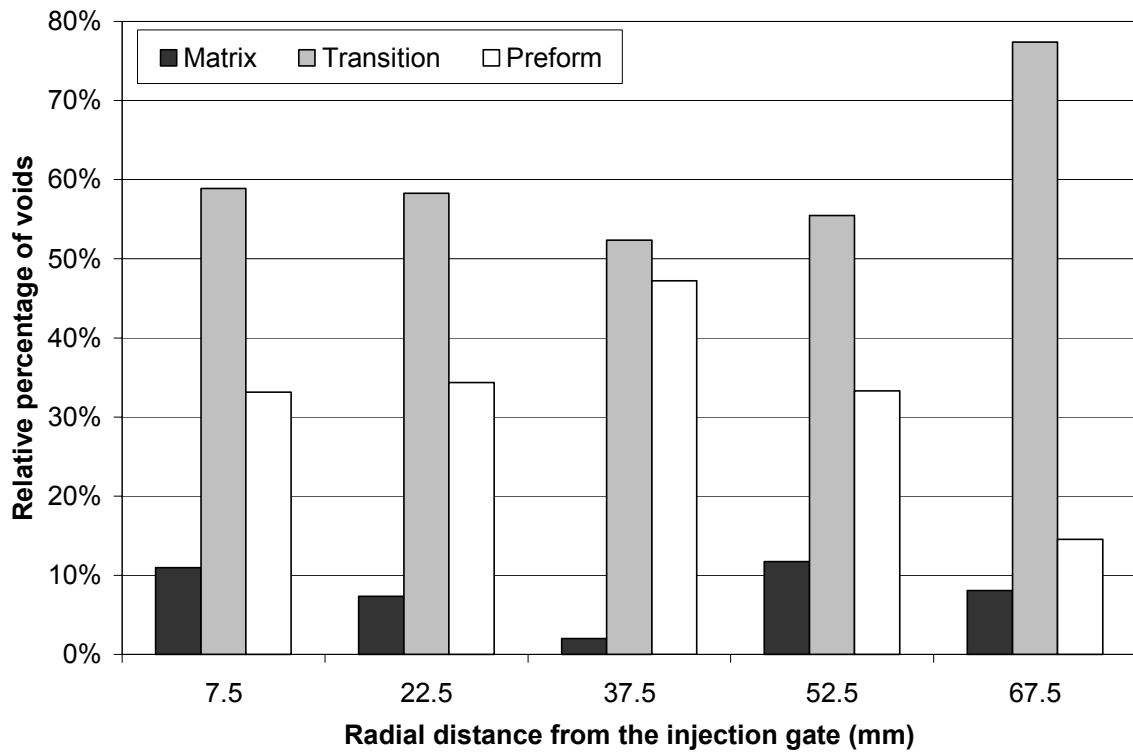


Figure 5.13: Through-the-thickness radial voidage distribution for different void locations in the RTM composite molded without post-fill pressure at 17.5% fiber content.

Reduction in *preform void* content along the flow direction is in agreement with the predicted void behavior based on capillary number analysis discussed earlier. On the other hand, higher pressure inside the mold would force the voids to shrink or even dissolve into the resin [36,37]. Therefore, void sizes during mold filling - where pressure levels reach 500 to 600 kPa - and after the pressure inside the mold cavity dropped to atmospheric levels at the end of mold filling would be different. Hence, voids would have been much smaller during mold filling and expand to larger sizes as the pressure drops after filling is complete. Unlike *preform voids* that are trapped inside fiber tows, *transition* and *matrix voids* are relatively free to move during mold filling, particularly if they are sufficiently small [22,23]. Consequently, there is an elevated probability of their transport towards the exit vents. Moreover, closer to the injection gate, voids experience flow and are subject to shear deformation as well as increasing pressure for longer durations. Therefore, although *matrix* and *transition voids* may have formed as predicted by the capillary number analysis, their radial distribution might have been rearranged during mold filling.

To better understand this phenomenon, a closer look at the radial distribution of *preform voids* can be of great assistance. If the void formation mechanisms follow the capillary number analysis, one can expect “immobile” voids trapped within the preform to show the expected trend, hence becoming smaller with increasing radial distance from the injection gate. Figure 5.14 illustrates planar size distribution of *preform voids* in the radial direction. Planar view is used here since cylindrical voids with very different sizes

would appear the same when sectioned by through-the-thickness view, hence giving a misleading representation of the investigated morphological feature.

The faster moving fluid front in the first radial region, led by viscous flow, is expected to trap larger *preform voids*. As the radial distance from the injection gate increases, slower fluid fronts are anticipated to capture fewer and smaller *preform voids*, yielding lower void contents at higher radial distances from the injection gate. In figure 5.14, the gradual shift towards smaller trapped intra-tow voids is obvious as the relative percentage of small *preform voids* increases - almost linearly - from 31.03 to 46.34% between the first and fifth radial regions, registering almost 50% increase. The increase in the contribution of small *preform voids* with increasing radial distance from the injection gate is balanced by an opposite trend seen in the contribution of medium *preform voids*. Medium *preform void* relative percentage sees a 34.97% decrease between the second and fifth radial regions (i.e., 60 to 39 %). The observed change in radial size distribution of *preform voids* is accompanied by a decrease in average *preform void* size from 69 μm in the first radial region to 61 μm in the fifth. In addition, figure 5.15 shows the planar preform voidage variation along the flow direction. Clear trends of decreasing *preform* void content as well as preform void areal density away from the inlet verifying the formation by mechanical entrapment of fewer *preform* voids at higher radial distances from the injection gate. These definite trends prove that voids - at least at the formation stage - correlate well with the predictions based on the capillary number analysis.

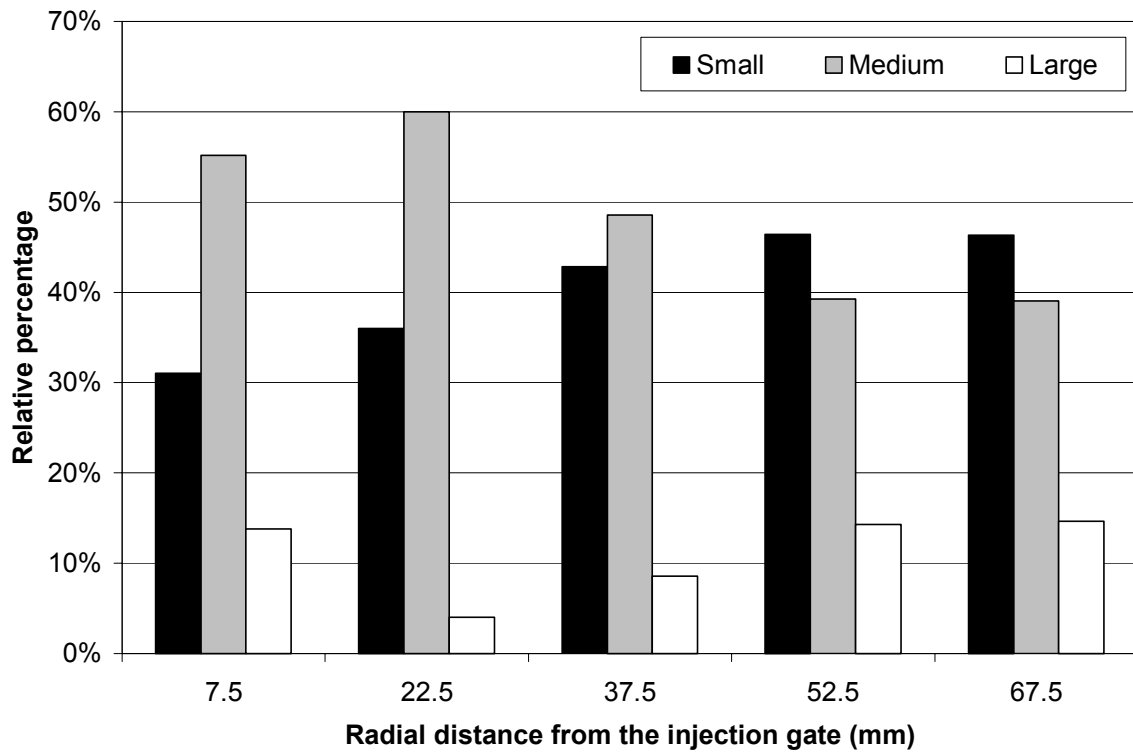


Figure 5.14: Planar *preform void* size distribution along the flow direction in the RTM composite molded without post-fill pressure at 17.5% fiber content.

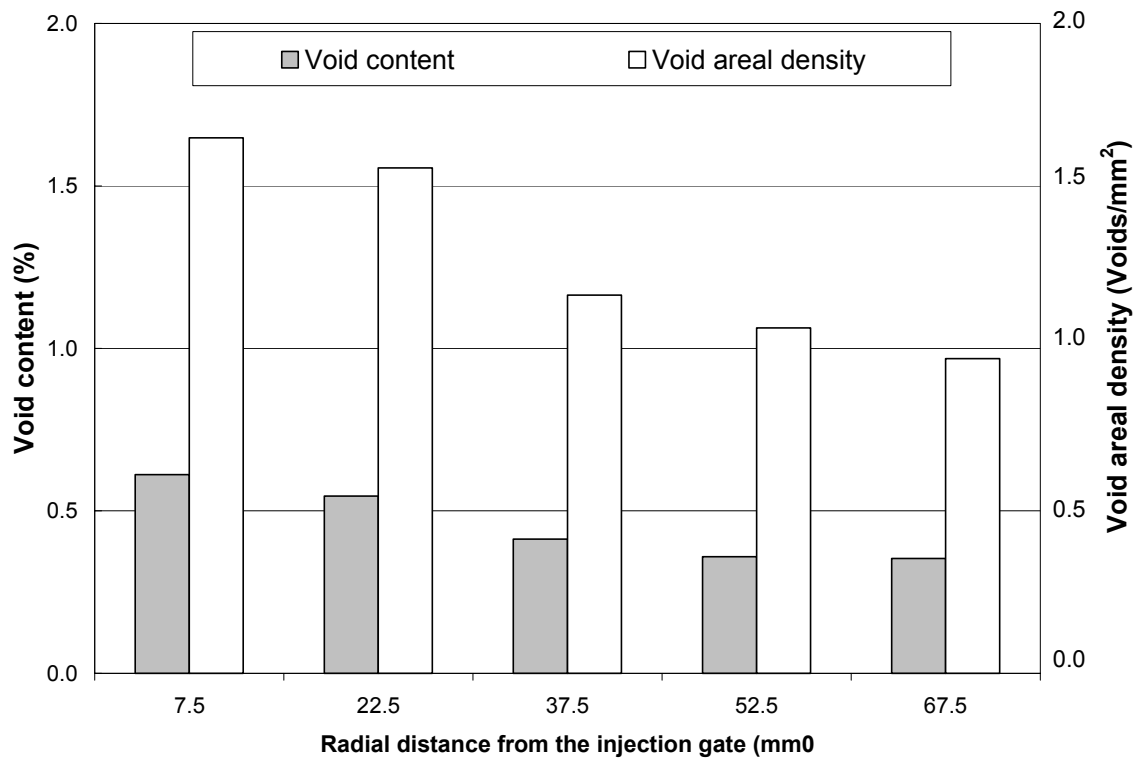


Figure 5.15: Planar *preform* void content and void areal density variation along the flow direction in the RTM composite molded without post-fill pressure at 17.5% fiber content.

However, once voids are formed at a radial location, they are subjected to increasing pressures and shear stresses during filling, making them prone to become smaller and move radially away from the inlet. *Preform voids* cannot move since they are trapped inside fiber bundles. Hence, only *matrix* and *transition voids* are potential mobile voids. Radial size distributions of *matrix* and *transition voids* are investigated to characterize the behavior of mobile voids in the flow direction. Combined matrix and transition areal void densities along the flow direction are depicted in Fig. 5.16.

Large voids are less likely to move during resin injection since they have higher adhesion force caused by their longer perimeters [22,23]. Therefore, large voids, even in few numbers, tend to resist transport and stay where they were initially formed. Hence, radial distribution of large mobile voids would be another good indicator of void formation mechanisms. Considering the five radial regions combined, the average areal density of large mobile voids is at almost 0.5 voids/mm². However, the areal density of large mobile voids is observed to decrease steadily with increasing distance from the injection gate, from 0.67 to 0.22 voids/mm² between the first and fifth radial region. The observed trend of decreasing large mobile voids with increasing radial distance from the inlet (i.e., with decreasing modified capillary number) confirms the effect of capillary number on void formation.

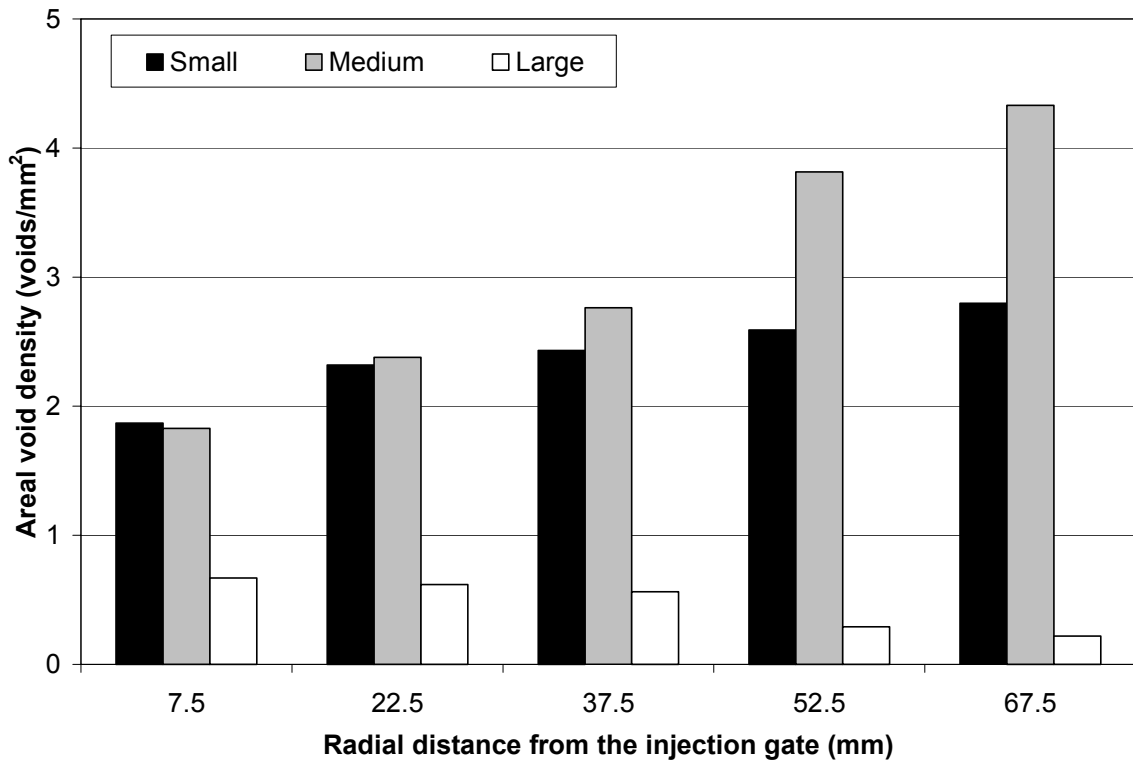


Figure 5.16: Areal density of different-sized mobile voids (i.e., combined matrix and transition) along the flow direction based on through-the-thickness view of the RTM composite molded without post-fill pressure at 17.5% fiber content.

Contrary to the radial distribution of large mobile voids, medium and small mobile voids show an opposite trend, that is, their respective contributions augment away from the inlet. Small and medium mobile areal void densities increase both steadily along the flow from 1.87 and 1.83 voids/mm² at 7.5 mm from the injection gate, respectively, to 2.80 and 4.33 voids/mm² at 67.5 mm from the injection gate. However, the contribution of medium mobile voids shows a higher increase of almost 140%, while small mobile voids showed a more modest 50% increase between the first and fifth radial regions. Therefore, spatial distributions of medium and small mobile voids in a molded composite are essentially dictated by their mobility. In summary, most voids encountered in RTM composites are formed according to the local capillary number, and a large number of potential mobile voids (i.e., matrix and *transition voids*) are then transported during mold filling leading to a complex spatial distribution.

Finally, since large irregular voids are more likely to induce failure cracks [6], irregular void size distribution is investigated along the radial flow direction. Contribution of irregular voids to the overall through-the-thickness void content is 29.30%. Due to their non-convexity, any void classified as irregular presents a potential weakening location for the composite as failure cracks are known to initiate from medium to large irregular voids with sharp corners [6]. As discussed earlier, voids seen in the planar view as cylindrical, circular, or elliptical shaped voids can present an irregularity when they come in contact with a preform layer. Therefore, through-the-thickness void size distribution is used at this point. Figure 5.17 represents size distribution of irregular voids along the flow direction determined from through-the-thickness view.

Combining all radial regions, the average irregular void size distribution obtained from through-the-thickness view has been presented in Fig. 5.11. Almost 58% of the irregular voids are made of small voids with an equivalent diameter less than 50 μm . Moreover, almost 36% of the irregular voids encountered have an equivalent diameter between 50 and 100 μm . However, size distribution of irregular voids shows clear radial trends. While relative percentage of large irregular voids barely reaches 12% in the third radial region, small and medium irregular voids show differing trends along the radial flow direction. Contribution of small voids sees a 38% decrease from 72.45% at 22.5 mm from the injection gate to 45.16% at 67.5 mm, whereas medium voids show a 90% increase over the same radial distance, passing from 25.51 to 48.39%. These radial distributions imply that irregular voids become larger away from the injection gate.

These results must be interpreted in conjunction with those results presented in Figs. 5.14, 5.15, and 5.16. *Preform void* sizes are seen to decrease with increasing distance from the injection gate, while matrix and transition void sizes are observed to increase over the same range. Thus, preform irregular voids are not contributing to the size enlargement depicted in Fig. 5.17, and only mobile irregular voids are responsible for this phenomenon. A plausible explanation can be based on void mobility during resin injection. As *matrix* and *transition voids* are compressed under injection pressure, they become mobile and are thought to be moved radially as inter-tow voids. As the injection is completed, the pressure drops to zero allowing these voids to expand to their original size. These voids become irregular during expansion because of geometrical constraints. As a result, the molded composite presents a higher risk of failure away from the inlet as the concentration of larger, irregular voids increases radially outward.

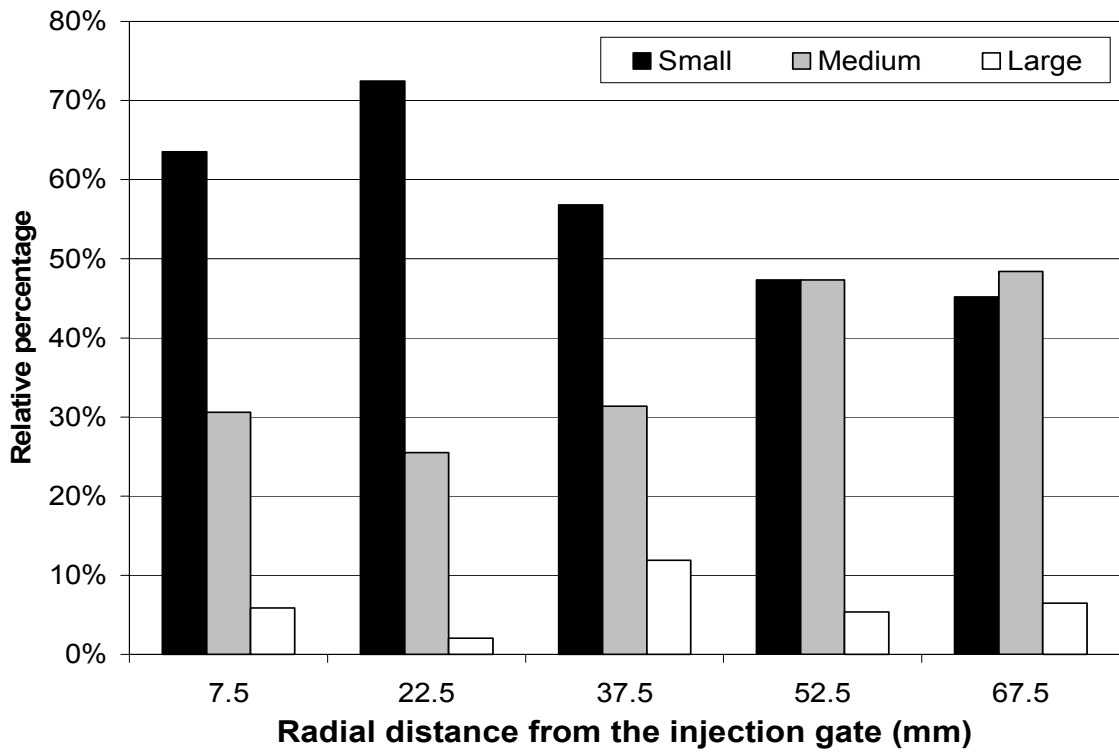


Figure 5.17: Irregular void size distribution along the flow direction, determined from through-the-thickness view of the RTM composite molded without post-fill pressure at 17.5% fiber content.

5.5 Conclusions

Three-dimensional features of void morphology in resin transfer molded composites are investigated. Voids are assessed via microscopic image analysis from both planar and through-the-thickness surfaces of a disk-shaped, E-glass/epoxy composite with a fiber content of 17.5%. A 2.15% void content is obtained from the through-the-thickness surface and is believed to be representative of the actual void content in the studied part. The planar void content of 2.56%, on the other hand, compares well with the 2.58% void content obtained from the corresponding through-the-thickness layer. The two investigated views also revealed differences in void morphology. Relatively large cylindrical voids, observed in cigar shapes in the planar surface, appear only as small irregular or elliptical voids on through-the-thickness surface. These observed differences in void morphology led to a 13% decrease in the average void size from planar to through-the-thickness views. Moreover, in the planar view, 57.4% of the voidage is observed to be surrounded completely by the matrix; whereas 94.4% of the total voidage in through-the-thickness surface is found to be either inside or right next to fiber tows. Along the radial direction, combined effects of void formation by mechanical entrapment and void mobility formed a complex radial void distribution. 33% fewer inter-tow voids are observed to be trapped mechanically near the exit compared to the inlet region. Most of the medium and small mobile voids (i.e., *matrix and transition voids*) seem to migrate towards the exit during resin injection, thus yielding a 93% increase of such voids near the exit. These findings are believed to be applicable not only to RTM, but generally to other composites manufactured by liquid molding processes with similar flow kinematics.

5.6 References

1. Abraham D., Matthews and S., McIlhagger R., *Composites Part A*, 29, 795, 1998.
2. Shojaei A., Ghaffarian S. R., and Karimian S. M. H., *Polymer Composites*, 24(4), 96, 2003.
3. Judd N. C. W., and Wright W. W., *SAMPE Journal*, 14(1), 10, 1978.
4. Ghiorse, S. R., *SAMPE Quarterly*, 24(1), 54, 1993.
5. Olivero K. A., Barraza H. J., O'Rear E. A., and Altan M. C., *Journal of Composite Materials*, 36(16), 2011, 2002.
6. Goodwin A. A., Howe C. A., and Paton R. J., In: *Proc. of ICCM-11, Australian Composite Structures Society*, M. L. Scott, Ed., Vol. IV: 11, 1997.
7. Harper B. D., Staab G. H., and Chen R. S., *Journal of Composite Materials*, 21, 280, 1987.
8. Hoppel C., Bogetti T., and Newill J. F., In: *Proc. of the American Society for Composites*, 1094, 2000.
9. Stabler W. R., Tatterson G. B., Sadler R. L., and El-Shiekh A. H. M., *SAMPE Quarterly*, 23(1), 38, 1992.
10. Patel N., and Lee L. J., *Polymer Composites*, 16(5), 386, 1995.
11. Mahale A. D., Prud'Homme R. K., and Rebenfeld L., *Polymer Engineering and Science*, 32(5), 319, 1992.
12. Patel N., Rohatgi V., and Lee J. L., *Polymer Engineering and Science*, 35(10), 837, 1995.
13. Rohatgi V., Patel N., and Lee J. L., *Polymer Composites*, 17(2), 161, 1996.
14. Chan A. W., and Morgan R. J., *SAMPE Quarterly*, 23(4), 48, 1992.

15. Chui W. K., Glimm J., Tangerman F. M., Jardine A. P., Madsen J. S., Donnellan T. M., and Leek R., In: *Proc. of the 9th International Conference of Numerical Methods in Thermal Problems*, 1323, 1995.
16. Lundström T. S., *Composites Part A*, 28, 201, 1997.
17. Patel N., and Lee J. L., *Polymer Composites*, 17(1), 96, 1996.
18. Patel N., and Lee J. L., *Polymer Composites*, 17(1), 104, 1996.
19. Binetruy C., Hilaire B., and Pabiot J., *Journal of Composite Materials*, 32(3), 223, 1998.
20. Kang M. K., Lee W. I., and Hahn H. T., *Composite Science and Technology*, 60, 2427, 2000.
21. Lundström T. S., *Polymer Composites*, 17(6), 770, 1996.
22. Shih C-H., and Lee L. J., *Polymer Composites*, 23(1), 120, 2002.
23. Blackmore B., Li D., and Gao J., *Journal of Colloid and Interface Sciences*, 241(2), 514, 2001.
24. Lundström T. S., and Gebart B. R., *Polymer Composites*, 15(1), 25, 1994.
25. Shih C-H., *Liquid Composite Molding of Tackified Fiber Reinforcement: Preforming and Void Removal*. PhD Thesis, Ohio State University, Department of Chemical Engineering, 2000.
26. Abraham D. and McIlhagger R., *Composites Part A*, 29, 533, 1998.
27. Ikegawa N., Hamada H., and Maekawa Z., *Polymer Engineering and Science*, 36(7), 953, 1996.
28. Choi J. H., and Dahran C. K. H., *Journal of Composite Materials*, 36(19), 2267, 2002.

29. Barraza H. J., Hamidi Y. K., Aktas L., O'Rear E. A., and Altan M. C., *Journal of Composite Materials*, 38(3), 195, 2003.
30. Hamidi Y. K., and Altan M. C. *Journal of Material Science Letters*, 22(24): 1813, 2003.
31. Hamidi Y. K., Aktas L., and Altan M. C., *Journal of Engineering Materials and Technology*, in press, 2004.
32. Blake J. W., *Studies in Reaction Injection Mold Filling*, PhD Thesis, University of Minnesota, Department of Chemical Engineering & Material Science, 1987.
33. Patel N., *Micro Scale Flow Behavior, Fiber Wetting and Void Formation in Liquid Composite Molding*, PhD Thesis, Ohio State University, Department of Chemical Engineering, 1994.
34. Rohatgi V., *Liquid Molding of Textile Reinforcements: Analysis of Flow Induced Voids and Effects of Powder Coating on Preforming and Moldability*, PhD Thesis, Ohio State University, Department of Chemical Engineering, 1995.
35. Ghiorse S. R., *A Comparison of Void Measurement Methods for Carbon/Epoxy Composites*, U. S. Army Materials Technology Laboratory, Report MTL-TR: 91, 1991.
36. Chen Y-T., Davis H. T., and Macosko C. W., *AIChE Journal*, 41(10): 2261, 1995.
37. Roychowdhury S., *Void Formation and Growth in Amorphous Thermoplastic Polymeric Materials*, PhD Thesis, University of Delaware, Department of Material Science & Engineering, 1995.
38. Santulli C., Garcia Gil, R., Long A. C., and Clifford M. J., *Science and Engineering of Composite Materials*, 10(2), 77, 2002.

39. Han K., and Lee L. J., *Journal of Composite Materials*, 30(13), 1458, 1996.
40. Wisnom M. R., Reynolds T., and Gwilliam N., *Composite Science and Technology*, 56(1), 93, 1996.

6 Effect of Packing on Void Morphology in Resin Transfer Molded E-Glass/Epoxy Composites*

6.1 *Abstract*

Effects of applying a packing pressure on void content, void morphology, and void spatial distribution are investigated for resin transfer molded (RTM) E-glass/epoxy composites. Packing pressures of zero and 570 kPa are respectively applied to center-gated composites containing 17.5% randomly-oriented, E-glass fiber preform. Radial samples of these disk-shaped composites are utilized to evaluate voidage via microscopic image analysis. Two adjacent surfaces are cut from each molded disk in order to evaluate void presence from both through-the-thickness and planar views. The packed composite is found to contain almost 92% less void content than the unpacked composite. While void fractions of 2.2 and 2.6% are measured respectively from the through-the-thickness and planar surfaces of the unpacked composite, only 0.2% void content is observed in the packed composite from both surfaces. Digital images obtained from through-the-thickness surface showed that average void size dropped from 59.3 μm in the unpacked composite to 31.7 μm in the packed composite. A similar reduction in average void size from 66.7 to 41.1 μm is observed from the planar surfaces. Circular voids are found to experience higher removal rates at 99%, followed by cylindrical and elliptical voids at 83 and 81%, respectively; while irregular voids show slightly lower void removal rates at 67%. Void proximity to fiber bundles is also observed to affect void reduction as voids located inside fiber tows experience lower void reduction rates. Along

* Material in this chapter was submitted to Polymer Composites, 2004.

the radial direction of the molded disks, removal of voids with different proximities to fibers seems to depend on their arrangement at the end of the filling stage. These findings are believed to ascertain packing as an effective void removal method for RTM and similar liquid composite molding processes.

6.2 Introduction

Liquid composite molding (LCM) processes such as RTM have been established in the automotive and aerospace industries as versatile technologies for manufacturing medium to large composite parts with complex geometries [1-3]. RTM consists on injecting a reactive liquid resin into a closed mold cavity pre-loaded with layers of fibrous preform. After cure reaction is complete, the solidified composite part is removed from the mold. The relatively high occurrence of process-induced defects such as poor wet-out and voids during mold filling often limits the increased use of LCM and RTM in composites industry. Presence of void is known to shorten the service life of composites by reducing their thermo-mechanical performance [4-12] and adversely affecting their response to environmental effects [13-14]. Despite the importance of voids, methods of void removal and their effectiveness are not fully established for LCM and RTM processes [3-6,8,12,15-26].

Voids in RTM are primarily formed by the impregnation mechanisms of the unsaturated fibrous media during mold filling. Although the preform impregnation at macro-scale is commonly described by a Darcy flow [27,28], two different flows develop at different scales: (i) a viscous flow between fiber tows; and (ii) a capillary flow inside each fiber bundle, driven by capillary forces. When these two flows are advancing at disparate

front velocities, voids form by so-called mechanical entrapment [18-26]. At higher fill rates, the viscous flow leads the impregnation, and voids are mostly formed inside fiber tows via fingering or lead-lag phenomena, resulting in microscopic intra-tow voids. In contrast, at slower injection velocities, the capillary flow leads the impregnation, and macroscopic inter-tow voids are formed between fiber tows. A minimum void occurrence can be obtained when both flows are advancing at comparable front velocities. Numerous researchers used flow visualization to monitor air entrapment during filling and documented this micro-scale flow behavior in detail [18-22].

In order to analyze the equilibrium between these two flows, Mahale et al. [19] used the capillary number, defined as the ratio of viscous to capillary forces. The authors reported that if the filling is performed at a capillary number of 2.5×10^{-3} , void formation will be minimal. Patel et al. [21], and Rohatgi et al. [22] generalized the non-dimensional capillary number by introducing the liquid-fiber contact angle. Several researchers explained their experimental void formation data with the modified capillary number [24,29,31], thus establishing the capillary number analysis as an available method for predicting void formation in RTM and LCM composites. Other theoretical and numerical models have been offered for predicting void occurrence in liquid injection processes [32-37]. Yet, these models have limited range of application as they are generally developed for simplified preform architectures.

Although acceptable void levels can be achieved at optimum capillary numbers [8,17-22], attaining such values often requires a range of injection rates slower than those used in the industry [29]. Slow injection rates increase mold filling time, and hence reduce

RTM applicability to large scale production. Thus, there is a need for effective void reduction or removal methods suitable for RTM processes involving fast injection rates.

Numerous techniques have been used to reduce void presence in composites manufactured by RTM and its variants [3,8,18-22,25-29,39-42]. Lundsstrom et al. [25,26], among others, utilized vacuum assistance to lower void content. Mold cavity is vacuumed before injection to lower the internal air pressure, hence facilitating void dissolution into the resin, and also enhancing void mobility during molding. Increasing the pressure difference between the inlet and outlet of the mold cavity from 0.17 to 0.50 MPa resulted in a decrease in void content from 6.5 to 3.8%. Yet, low void contents are only reached when costly, very high vacuum levels are used [25].

Degassing the injected resin is also used to reduce voidage in molded composites, since high initial bubble content results in elevated void presence [3,4,12,39]. However, resin degassing does not address entrapment by the fluid front, the primary cause of void formation for these processes. Another commonly used method for void removal is bleeding, which consists of continuing resin discharge after impregnation is completed to purge formed voids [18,25,40]. Bleeding might be useful when the formed voids are transportable, i.e. when voids are dominantly inter-tow voids. However, inter-tow voids are formed mostly at slow injection rates not seen in most industrial molding applications [19-22]. In addition, intra-tow voids formed in RTM processes with faster impregnation rates are found very difficult to purge by bleeding [22].

Another void removal method is compression, which consists on compressing mold walls after resin injection is complete [41]. Squeezing mold walls is anticipated to expel voids and help fabricate void-free composites. The method drives out voids only to the end of the cavity [11], and yet requires expensive tooling that might make the molded parts much more expensive. Articulated tooling, a variant of compressing mold walls, was recently proposed by Choi and Dharan [42]. This technique calls for a segmented articulated mold wall, utilized to sequentially impregnate dry preform areas in a step-wise sequential manner. A five fold reduction in mold fill time and reduced void generation were observed [42]. Nonetheless, like compression, articulated tooling requires higher initial investment, and possibly yields undesirable surface marks and defects.

Packing is performed by a sudden increase in pressure after the molding cavity is filled. This method has also been used to reduce void occurrence in RTM composites [8,18,25,29]. Forcing more resin into a previously filled mold cavity would shrink the existing voids or even dissolve them into the resin matrix. In an earlier study by Olivero et. al [8], void content was found to decrease exponentially with increasing applied packing pressure up to 700 kPa for resin transfer molded glass/epoxy composites at 21% fiber content [8]. In a different study performed at higher injection rates [29], applying a packing pressure as low as 300 kPa resulted in a drop of more than 70% in void content. Packing facilitates void removal for RTM and similar processes without additional tooling or investment. Hence, packing can be a cost-effective void removal technique that might improve most LCM processes. Concerns with packing reside in the possible spatial concentration of voidage or creation of large irregular voids with sharp corners that are prone to early failure cracks [11,13]. To address this issue, a thorough

investigation of the effects of packing on void morphology is needed. To the best of the authors' knowledge, no such study is available in the literature.

There are primarily two types of void studies relevant to molded polymeric composites: (a) post-cure studies, conducted on actual molded composites; and (b) void formation studies, conducted by monitoring flow front progression during impregnation process. Investigation of voids in molded composites can be conducted by a multitude of methods. However, void morphology is usually assessed by microscopic image analysis. Although microscopic image analysis is reported as one of the best methods to measure void contents [8,43,44], the obtained void morphology is only two-dimensional as void data are generally collected from a polished through-the-thickness surface of the composite [7-9,24,28-30,43,44]. On the other hand, most studies on the mechanisms of void formation are conducted by monitoring flow front progression from the planar view [1,2,19,21-23,33,35]. In addition, filling process is usually carried out by using model fluids such as glycerine, ethylene glycol, and silicone and diphenyl-octyl-phthalate (DOP) oils. Although this technique provides valuable insight on void formation mechanisms such as fingering and led-lag, it only captures two-dimensional features of voids. Furthermore, model fluids do not cure and continue micro-scale impregnation due to capillary forces even after complete mold filling. Thus, the obtained void morphology might be affected by phenomena that are not present in curing resin mixtures.

In the current study, effects of applying a 570 kPa packing pressure on void content, void morphology, and void spatial distribution are investigated for resin transfer molded E-glass/epoxy composites. Voidage is assessed by microscopic image analysis of planar

and through-the-thickness surfaces of the studied composites. Difference in void content and void areal density between the molded composites is evaluated. In addition, changes in void morphology (i.e. size and shape) due to packing are investigated. Furthermore, radial variations in void content are examined, as well as changes in reduction rates based on void proximity to fibers.

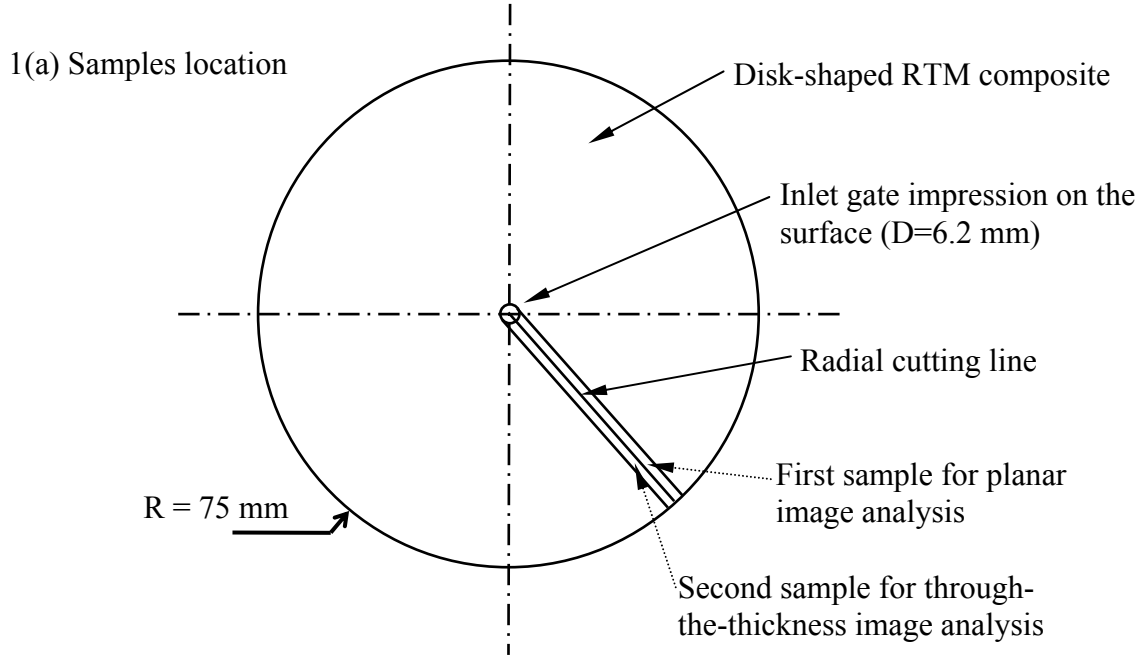
6.3 *Experimental Setup*

6.3.1 Molding Procedure

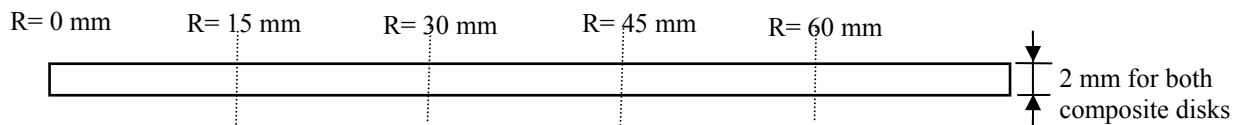
The composite disks used in this study are fabricated by a custom made experimental molding setup composed of a hydraulic press; two reservoirs for resin and curing agent; a static mixer; and a disk-shaped mold cavity. Operating the molding press forces the EPON 815C resin and EPICURE 3282 (Shell Chemicals) curing agent out of the reservoirs into the mold cavity at a constant flow rate. Thorough mixing of these fluids is ensured by the 32 alternating helical segments of a static mixer, yielding a gel time of approximately 20 minutes. Preforms placed in the mold cavity prior to filling are composed of four layers of the randomly-oriented, chopped-strand, E-glass fiber mats with a planar density of $0.4356 \text{ kg/m}^2 \pm 0.0449 \text{ kg/m}^2$ (Fiberglast part #250). The details of the molding procedure and experimental setup are described in detail elsewhere [28-31]. The first resin transfer molded disk is manufactured without applying any packing pressure, and is referred to as the unpacked composite. The second disk, referred to as the packed composite, is manufactured by applying a 570 kPa post-fill pressure. The packing process forces additional resin into the mold cavity and induces a 2% increase in average composite thickness from 3.88 mm in the unpacked composite to 3.96 mm in the packed one. Both composites have around 17.5% fiber content by volume.

6.3.2 Sample Preparation for Microscopic Image Analysis

The planar isotropy of the fibrous preform and the mold axisymmetry simplify the impregnation into a purely radial flow. Hence, the molded composite disks are examined along their radii. In order to prepare specimens for microscopic image analysis, two adjacent radial strips are cut from each disk. One of the strips is utilized for voidage assessment using its planar surface, and the other is used for void analysis based on its through-the-thickness surface. Figure 6.1 illustrates the spatial arrangement of these two strips obtained from both packed and unpacked composites. The first 2 mm-wide samples (Fig. 6.1b) are selected to investigate voidage from a planar surface, while the second ones (Fig. 6.1c) are utilized for void analysis from the through-the-thickness surface. All samples are 75 mm-long, while the unpacked and packed composites have an average thickness of 3.88 and 3.96 mm, respectively. Radial variation of voidage is assessed by dividing each 75 mm-long sample into five 15 mm-long regions along the radial direction as shown in Figs. 6.1b and 6.1c. Composite strips are embedded separately into a quick cure acrylic resin (Allied High Tech. Products, part # 170). The samples containing the planar composite surfaces are machined on a vertical mill to remove a thin layer and eliminate near-surface non-uniformities. For polishing, a series of polishing pastes is applied (Clover Compound) with grit sizes ranging from 180 (i.e. 80 μm average particle diameter) to 1200 (15 μm) in six successive steps. To remove paste residues after each step, 40 minutes of subsequent cleaning periods are performed in an ultrasonic bath at 50 kHz. After all polishing steps are completed, a 0.67 mm-thick layer is removed from the top of both planar composite samples. At the end of polishing and cleaning, the samples become ready for microscopic image analysis.



1(b) Planar sample



1(c) Through-the-thickness sample

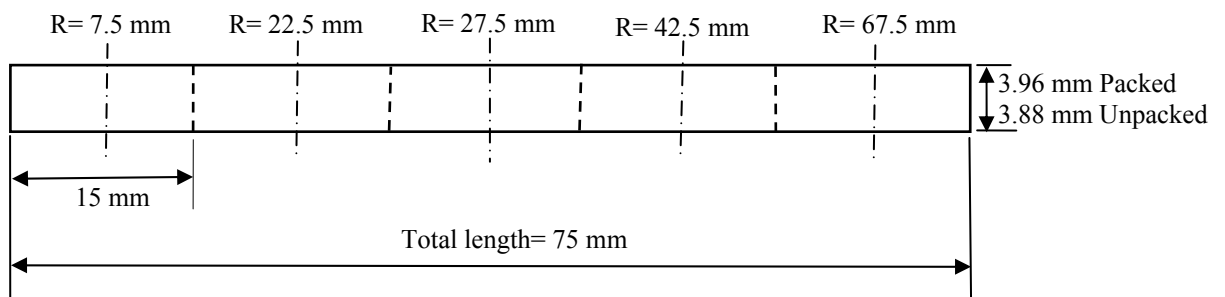


Figure 6.1: Spatial arrangement of investigated samples for both packed and unpacked composite disks: (a) sample locations within the composite disk, (b) Planar sample partitions of five 15 mm-long radial regions, (c) Through-the-thickness sample partitions of five 15 mm-long radial regions.

6.3.3 Void Characterization

Microscopic image analysis is considered among the most precise methods for measuring void contents [8,29,43,44]. In addition, this technique provides detailed information on other vital parameters such as void location, shape, and size that cannot be assessed by other methods. Often, microscopic image analysis is used by averaging randomly selected images [43,44]. In the current investigation however, the entire studied composite cross-sections are scanned in order to accurately estimate void content, morphology, and their spatial variations. Voidage features are obtained from images acquired at 200x magnification using a PC-based CCD camera mounted on a MEIJI optical microscope. At this particular magnification, every frame displays approximately a 0.71 mm x 0.53 mm area. The selected magnification of 200x enables the assessment of voids as small as the radius of a single fiber of 7 μm . Consequently, all identifiable voids throughout the entire composite samples are included in the analysis of void content and morphology. Each captured frame is processed using the image analysis software UTHSCSA Image Tool[®], which allows the measurement of voids' area, A , and maximum length, L_{max} .

6.4 Results and Discussion

6.4.1 Inlet Mold Filling Pressure

Temporal variation of molding pressure is monitored with a flush diaphragm pressure transducer (Sensotec[®] BP357BR Model S, 0.1% accuracy), attached between the static mixer and the mold inlet. Due to the circular mold geometry and the preform planar isotropy, the resin front has a circular shape and advances radially through the preform.

Molding takes place at a constant flow rate, thus closer to the injection gate, the resin front moves at higher velocities. The constant flow rate forces the inlet pressure to increase in order to impregnate a larger preform area as the flow front moves radially outward. Inlet pressure data recorded during filling of both packed and unpacked composite disks are shown in Fig. 6.2.

During the first 9 seconds of mold filling, the inlet pressures increase at similar rates for unpacked and packed composites. Thereafter, pressure readings show minor discrepancies due to slight variations in the constricted channel spacing between mold walls and spacer plates. Once the resin reaches the exit vents, the molding press is turned off, stopping resin injection. As seen in Fig. 6.2, when the injection is stopped, a monotonic decrease in pressure is recorded. This decrease is consistent with the natural pre-disposition of the system to reach a balance between inlet and outlet pressures. In the case of unpacked composite, exit vents are left open, and hence the pressure continues decaying asymptotically to atmospheric pressure during 100 seconds. The same behavior is observed for the packed composite during the 4 seconds between the time injection is stopped and all vents are securely closed, thus sealing the mold. Thereafter, the pressure is monitored for 60 seconds. The pressure levels-off to a plateau of 370 kPa, and remains constant until packing.

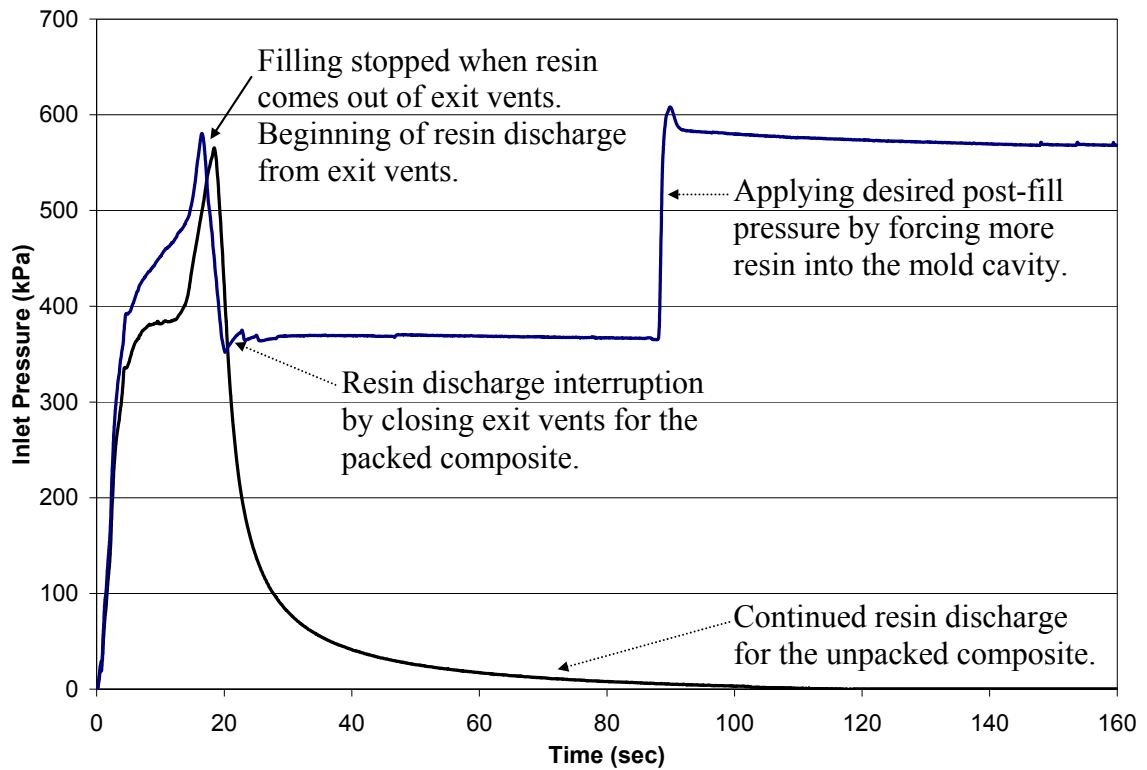


Figure 6.2: Inlet pressure profiles during mold filling of the unpacked and packed composite disks containing 17.5% fiber content by volume.

Applying the desired post-fill pressure of 570 kPa is achieved by forcing additional resin into the mold cavity, which requires operating the molding press for 3 additional seconds. Inlet pressure is again monitored for 60 seconds to ensure that no leaking occurs. Several minutes after the post-fill pressure is applied, the injection port is securely clamped, and the composite is allowed to cure at the desired packing pressure. The slight pressure difference observed during filling of packed and unpacked composites is not likely to affect void morphology at the end of the filling stage. However, the application of the 570 kPa packing pressure is expected to reduce void content, and induce major changes in void morphology and spatial distribution.

6.4.2 Assessment of Void Removal

Void contents from both unpacked and packed composites are assessed via microscopic image analysis. Representative images obtained at 200x magnification from both planar and through-the-thickness views of the unpacked and packed composites are depicted in Fig. 6.3. The continuous gray background in Fig. 6.3 represents the epoxy matrix; while the white circular and elliptical objects are glass fibers oriented perpendicularly and at an angle, respectively, to the cross-section. The single white parallel stripe in Fig. 6.3c and all others in Fig. 6.3d represent glass fibers parallel to the investigated cross-section. Figures 6.3a through 6.3d also depict the basic difference in fiber orientation and clustering observed on planar and through-the-thickness surfaces of an RTM composite.

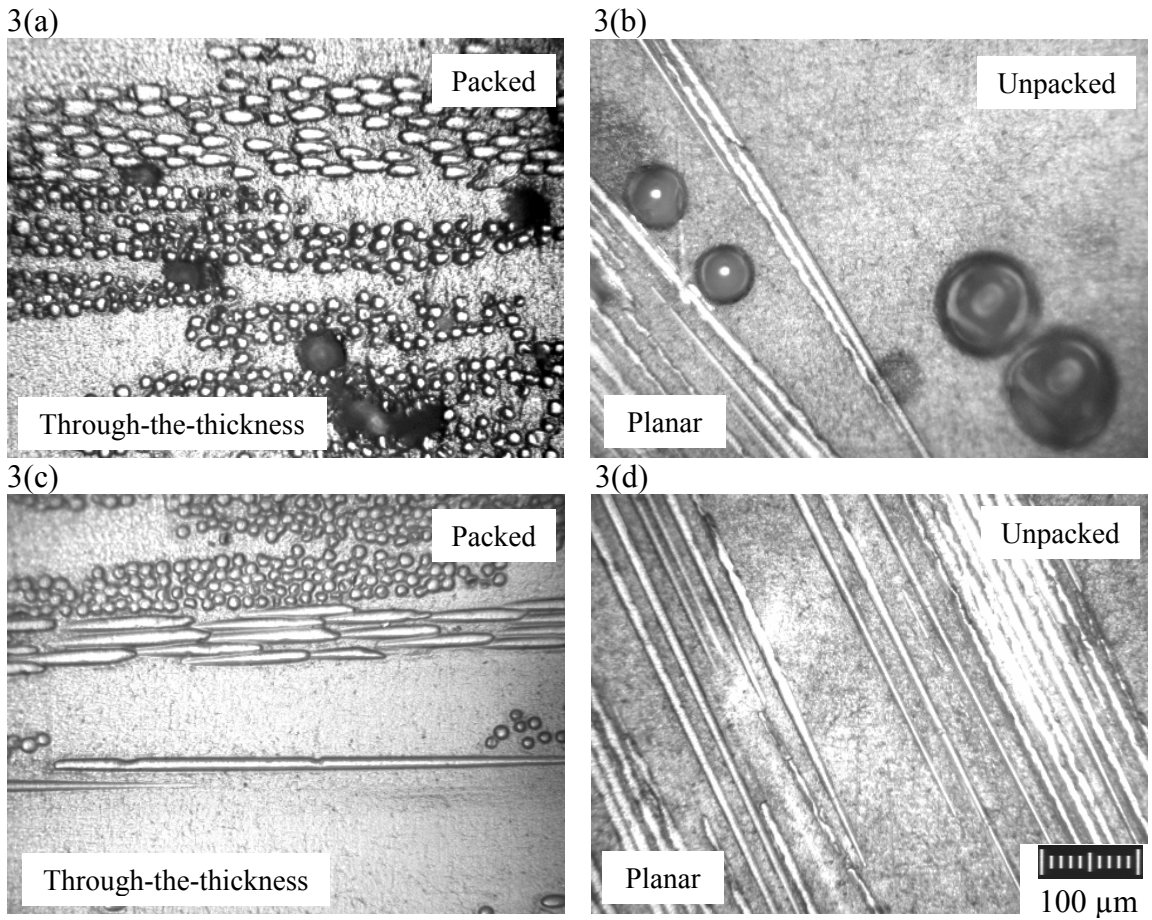


Figure 6.3: Representative image of voids in different composite locations obtained at 200x magnification from through-the-thickness (left column) and planar (right column) views of the unpacked (top row) and packed (bottom row) composite disks.

Fibers are seen as more homogeneously distributed through the composite thickness; while the planar view offers large matrix-rich regions and other zones with high fiber concentration. Hence, different morphological features of voids are expected to become prominent when observed on these two orthogonal planes.

Void contents and void areal densities of the unpacked and packed composites are shown in Fig. 6.4. Results obtained from both planar and through-the-thickness views of each composite disk are presented. Analysis of through-the-thickness surfaces reveals that applying a 570 kPa post-fill pressure resulted in 91.2% reduction in the void content dropping from 2.2 to 0.2%. When the void contents obtained from planar surfaces are compared, a similar 91.8% decrease from 2.6 to 0.2% is observed. This reduction in void content is accompanied with more than 83 and 97% reduction in void areal density when assessed from the through-the-thickness and planar views, respectively. This large diminution in voidage is attributed primarily to void shrinkage and dissolution due to pressure differential between the resin and air trapped inside the voids. Packing is hereby ascertained as an efficient void reduction technique that removes the majority of voids formed during impregnation in liquid injection processes. Additional investigation is needed in order to understand relevant removal mechanisms, as well as the effects of packing on void morphology.

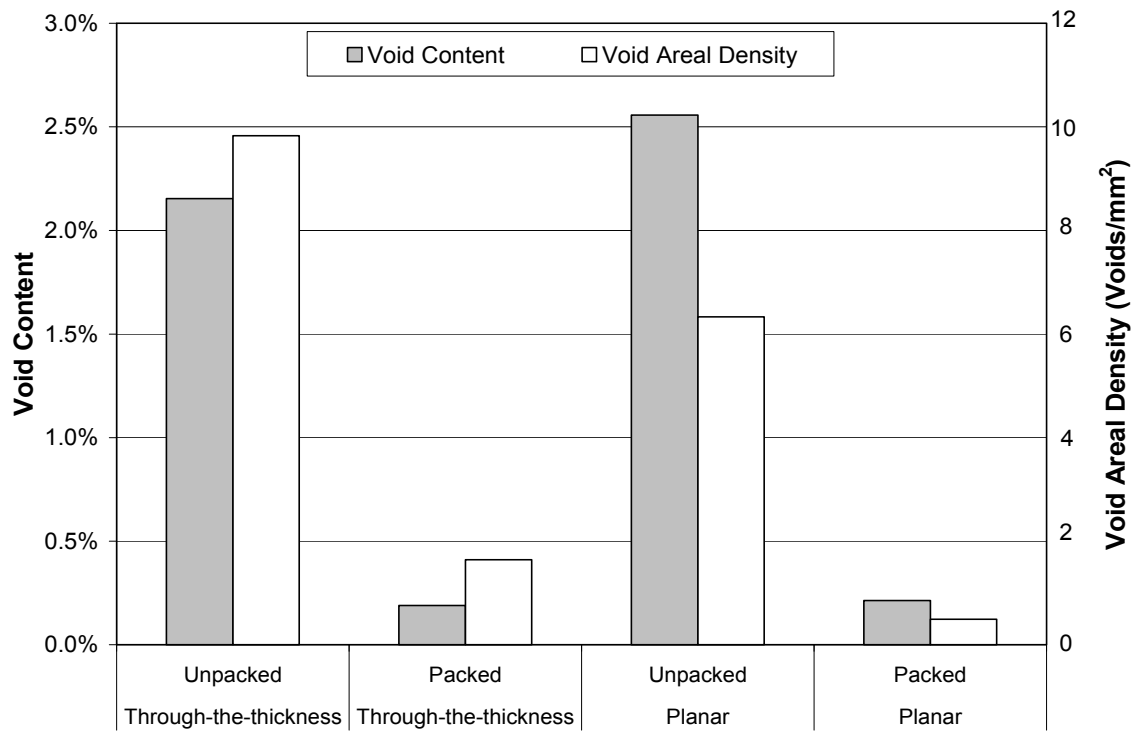


Figure 6.4: Through-the-thickness and planar void contents and void areal densities for the unpacked and packed composite parts.

6.4.3 Effect of Packing on Void Location

As illustrated in Fig. 6.3, voids are seen at three different locations within the molded composites. First location is defined as areas rich in matrix away from fibers. Voids encountered in this location are completely surrounded by the epoxy matrix and are referred to as matrix voids. Second location is defined as areas rich in preform, where the area is primarily composed of reinforcing fibers. Voids in this region are intra-tow voids situated within fiber bundles and are referred to as preform voids. Finally, the third location is defined as the transitional areas between the two other locations herein defined. Voids in this location are referred to as transition voids and are always positioned next to fiber bundles but not within the fiber preform. Based on the locations defined above, all voids present in Fig. 6.3a are preform voids. The two voids appearing in the left half of Fig. 6.3b are considered transition voids. Finally, the remaining two voids seen in the right of Fig. 6.3b are categorized as matrix void. Voids from these three different locations in the four composite samples are identified and their respective contributions to the total void content determined.

Figure 6.5 shows reduction in void content in different locations of the packed composite, including results from both planar and through-the-thickness views. When assessed from the planar view, the 91.8% reduction in overall composite void content presented in Fig. 6.4 is not equally distributed among voids from the three locations defined above. Matrix and preform voids seem to experience higher reduction rates of 96.6 and 93.3%, respectively; while only a 79.4% reduction is observed for transition voids. The percentage reduction in void content observed through-the-thickness is also different

among the three void locations. Both matrix and transition voids are reduced at a slightly higher rate of 93.3 and 94.7%, respectively. In contrast, preform voids are reduced only by 84.7%.

This difference in perceived reduction of voids from different locations is believed to originate from the difference in void location distribution between planar and through-the-thickness views of the unpacked composite. Due to the planar architecture of the reinforcing preform, many voids that are classified as matrix voids in the planar view might be in contact with fibers at composite layers above or below the observed plane, belonging in fact to transition voids as shown in Fig. 6.5b. Therefore, distribution of void location based on through-the-thickness surface is believed to be more representative of the actual distribution. Hence, the actual locations of voids throughout the composite would be better characterized from the through-the-thickness view. In addition, location of voids based on the through-the-thickness view reveals that voids are concentrated either inside or right next to fiber bundles, as predicted for the local capillary number values [30-31]. On the contrary, location distribution of voids based on the planar view depicts voids as mainly inter-tow, matrix voids.

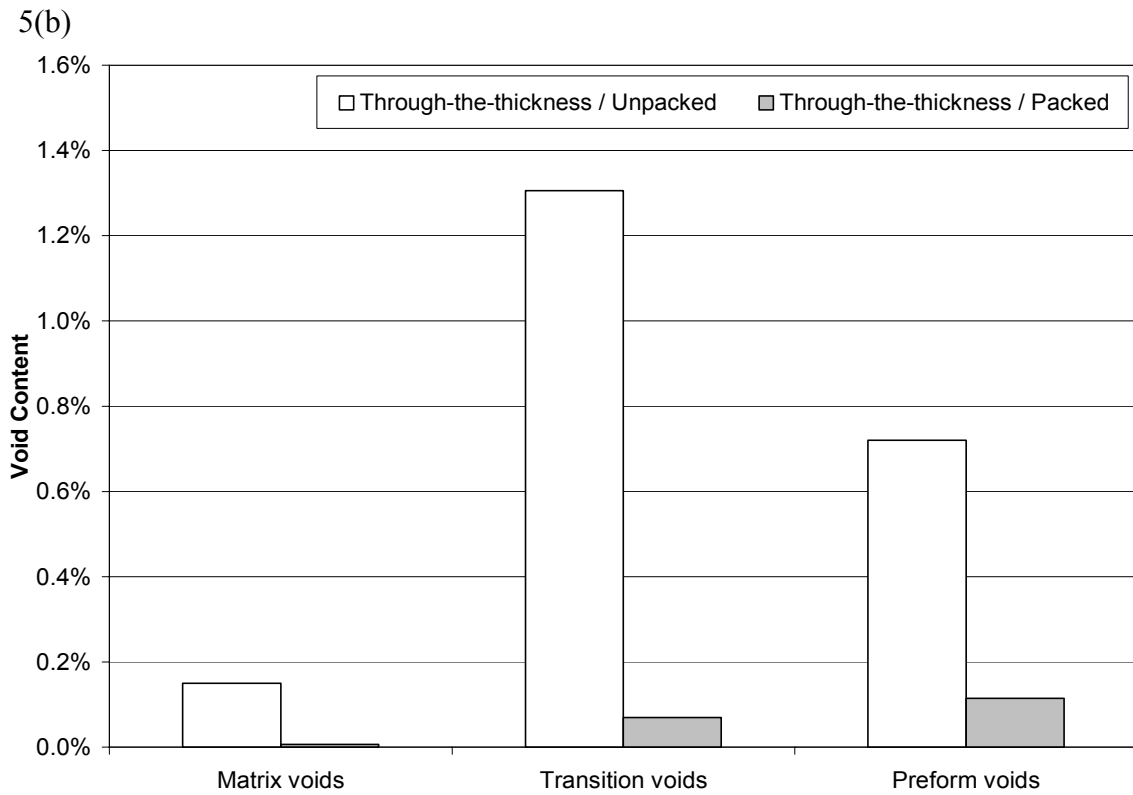
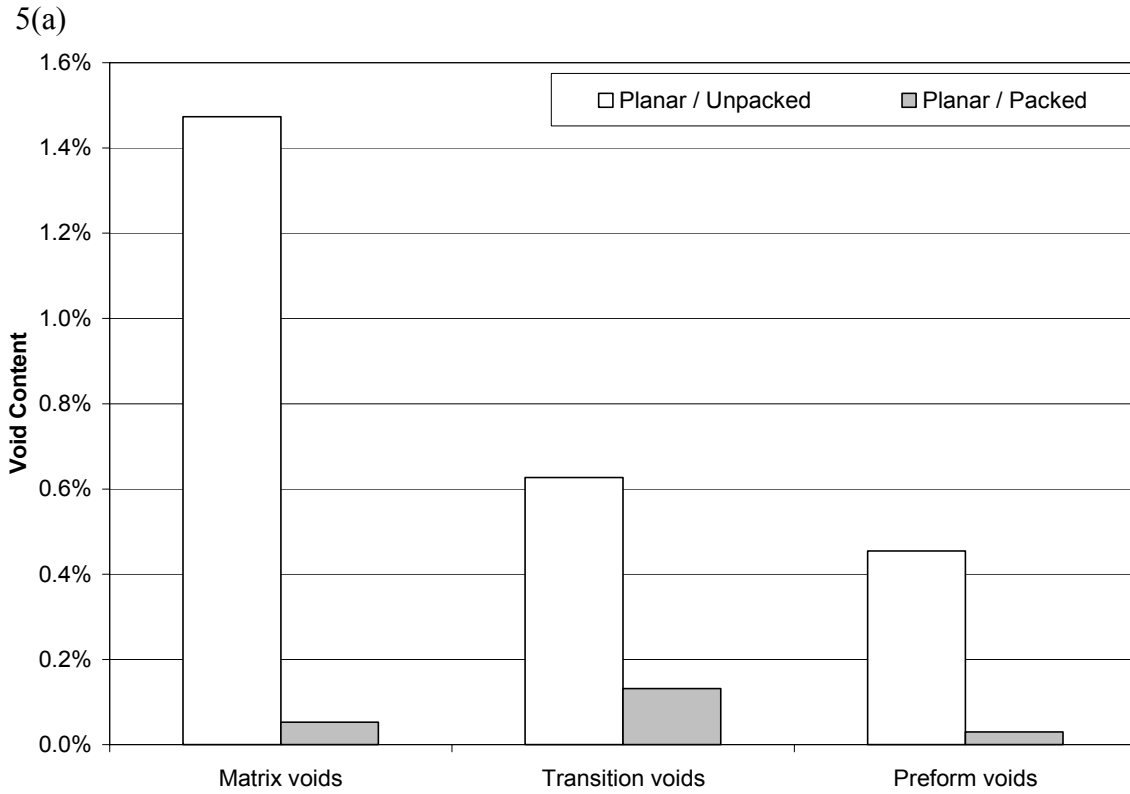


Figure 6.5: Contributions from voids in different locations within the composite disks to the void contents of unpacked and packed parts viewed from: (a) the planar view, and (b) the through-the-thickness view.

In terms of void areal density, the void content reduction rates seen in Fig. 6.5b translate to 84.9 and 86.6% removal rates for matrix and transition voids, respectively; while preform voids are removed slightly less at 78.8%. This is expected since intra-tow preform voids, once formed, are known to be more difficult to eliminate than inter-tow voids [10,18,22,29], as they are trapped in the constricted narrow spacing within fiber bundles. As a result, preform voids see more than a 70% jump in their relative contribution to the total void content due to packing, increasing from 33.5 to 57.9% of the total voids.

6.4.4 Effect of Packing on Void Size

To classify void sizes, an equivalent diameter, D_{eq} , is defined for each void as:

$$D_{eq} = \sqrt{\frac{4A}{\pi}}, \quad (6.1)$$

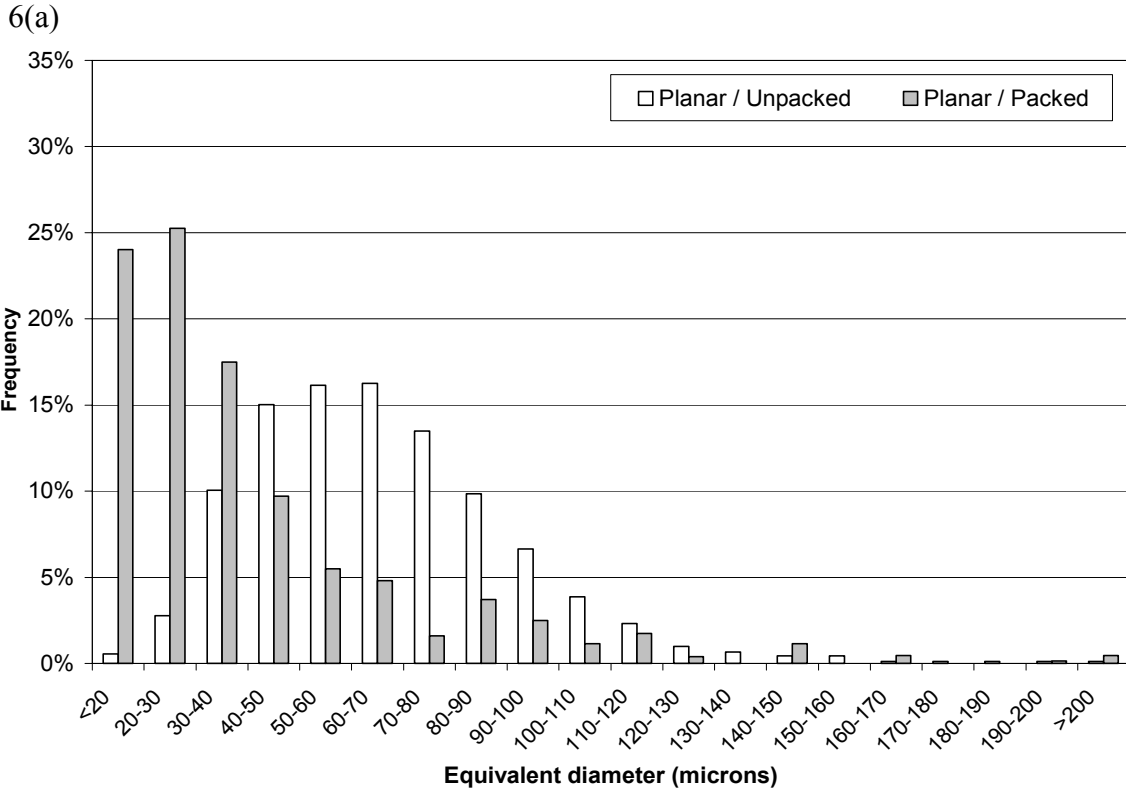
where A is the void area measured via image analysis software UTHSCSA Image Tool®. Similar methods are commonly used to characterize grain size in a multitude of materials such as metals [45,46], ceramics [47-50], and polycrystalline materials [51,52].

Figure 6.6a, obtained from images of the planar surface, illustrates void size distributions based on D_{eq} for both unpacked and packed composites. As a result of applying the 570 kPa packing pressure, the size distribution of voids is significantly changed. A large shift in void size distribution is observed as average void size is reduced from 67 μm in the unpacked composite to 41 μm in the packed composite. The highest void occurrence frequency changed from 16.2% for voids with D_{eq} between 60 and 70 μm in the

unpacked composite to 25.3% for voids with D_{eq} between 20 and 30 μm in the packed composite.

Similarly, void size distributions obtained from the through-the-thickness view for both unpacked and packed composites are represented in Fig. 6.6b. Compared to Fig. 6.6a, a larger shift in void size distribution is observed as average void size decreases from 59 to 32 μm . The highest void occurrence frequency changed from 17.0% for voids with D_{eq} between 40 and 50 μm in the unpacked composite to 30.6% for voids with D_{eq} less than 20 μm in the packed composite.

In order to focus on other aspects of void size distributions, three different size ranges are defined. Large voids are defined as those with an equivalent diameter greater than 100 μm , i.e. $D_{eq} > 100 \mu\text{m}$; while voids with an equivalent diameter lower than 50 μm are regarded as small voids. Intermediate equivalent diameter values, i.e. $50 \mu\text{m} < D_{eq} \leq 100 \mu\text{m}$, correspond to medium size voids. Data obtained from voids in different composite locations are reprocessed using these three void sizes to quantify the effects of packing on size distribution of voids encountered in each composite location. Size distributions of matrix, transition, and preform voids obtained from planar surface data of unpacked and packed composites are presented in Fig. 6.7a. Likewise, size distributions of matrix, transition, and preform voids obtained from through-the-thickness surface data of unpacked and packed composites are presented in Fig. 6.7b.



6

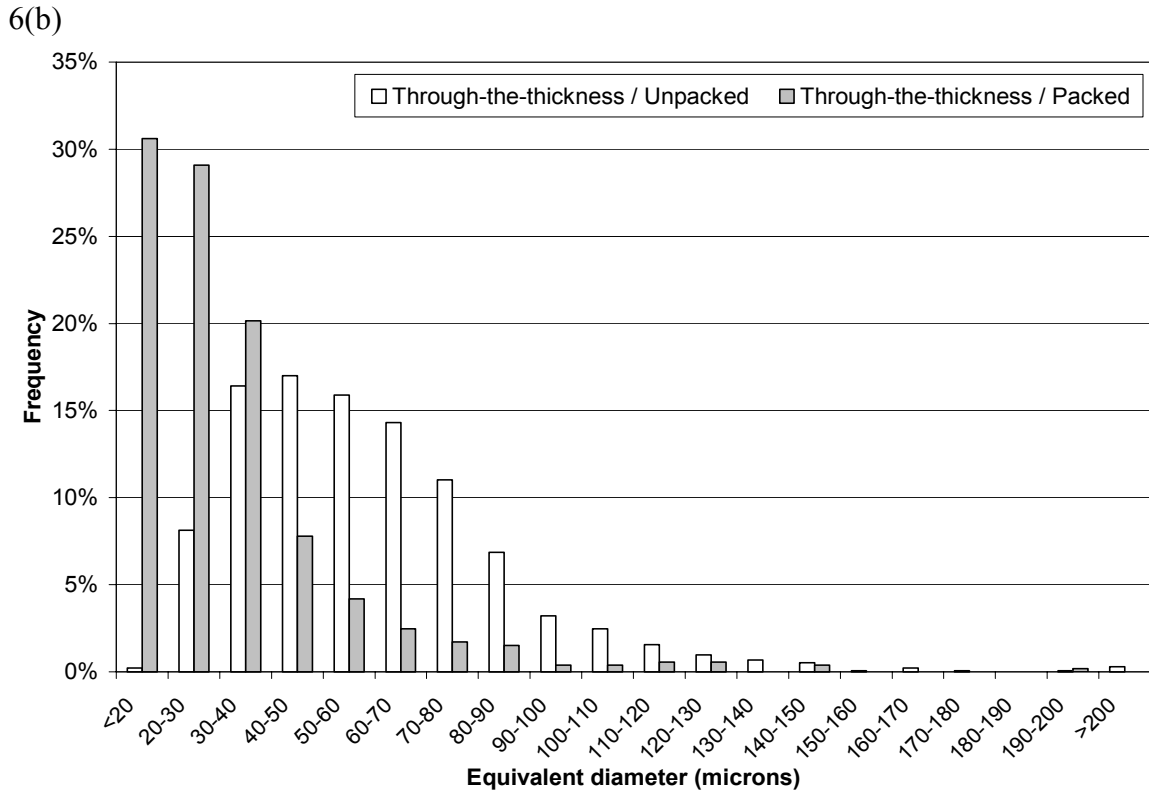
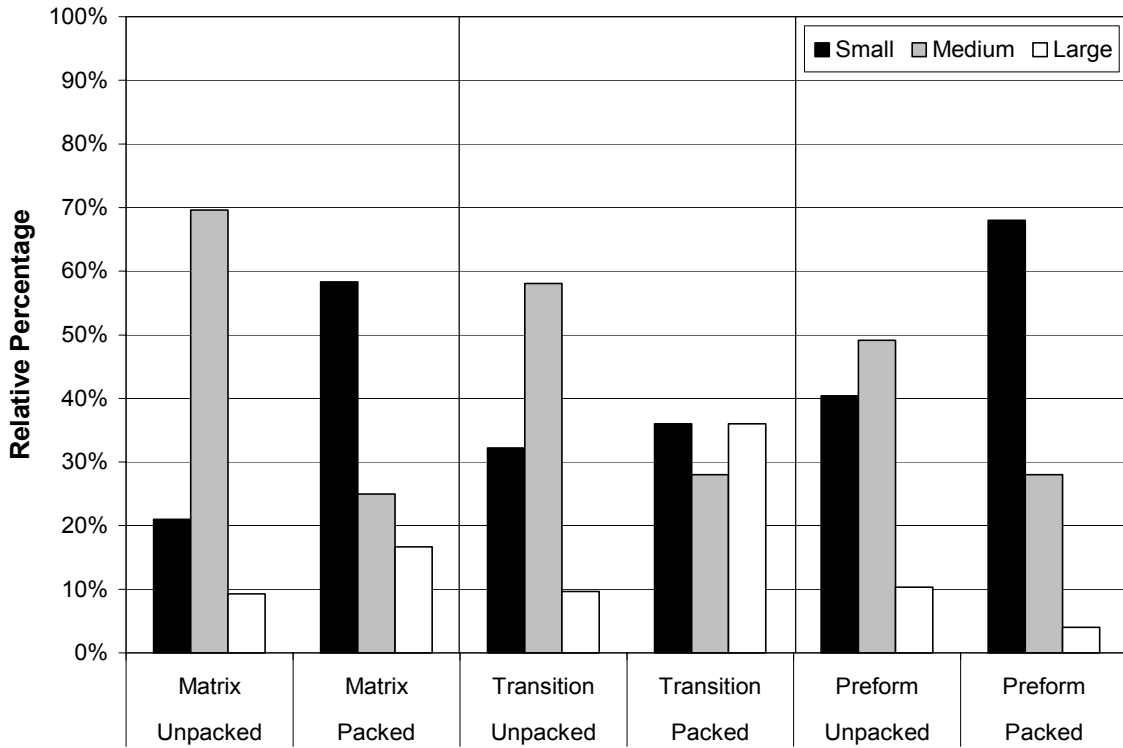


Figure 6.6: Void size distributions for the unpacked and packed composite disks from: (a) the planar view; and (b) the through-the-thickness view.

When assessed from the planar view, i.e. Fig. 6.7a, small voids encountered within the matrix increase from 21.0% in the unpacked composite to more than 58% in the packed composite, while medium voids see their contribution reduced from 69.6 to 25.0%. This 77.4% increase in relative percentage of small voids found within the matrix along with the 64.0% decrease in medium matrix voids is a direct result of void shrinkage. From through-the-thickness view, i.e. Fig. 6.7b, an even accentuated trend is observed as small matrix voids augment from a relative frequency of 33.3% in the unpacked composite to almost 97% in the packed one. Medium matrix void contribution is dramatically reduced due to packing from 61.3 to merely 3.0%; while large matrix voids completely disappeared in the packed composite.

As shown in Fig. 6.7a, size distribution of preform voids show a similar trend due to packing. Relative contribution of small preform voids, obtained from the planar view, depict a considerable increase from 40.4 to 68.0%. An opposite trend is observed for both medium and large voids, whose relative percentages drop from 49.2 and 10.4% to 28.0 and 4.0%, respectively. A decrease in average size of preform voids is also observed from through-the-thickness view in Fig. 6.7b. Small intra-tow voids exhibit a 30.0% increase from 66.0% in the unpacked composite to 86.0% in the packed composite. Medium and large voids contributions, however, are decreased from 28.7 and 5.4% to 10.0 and 4.1%, respectively.

7(a)



7(b)

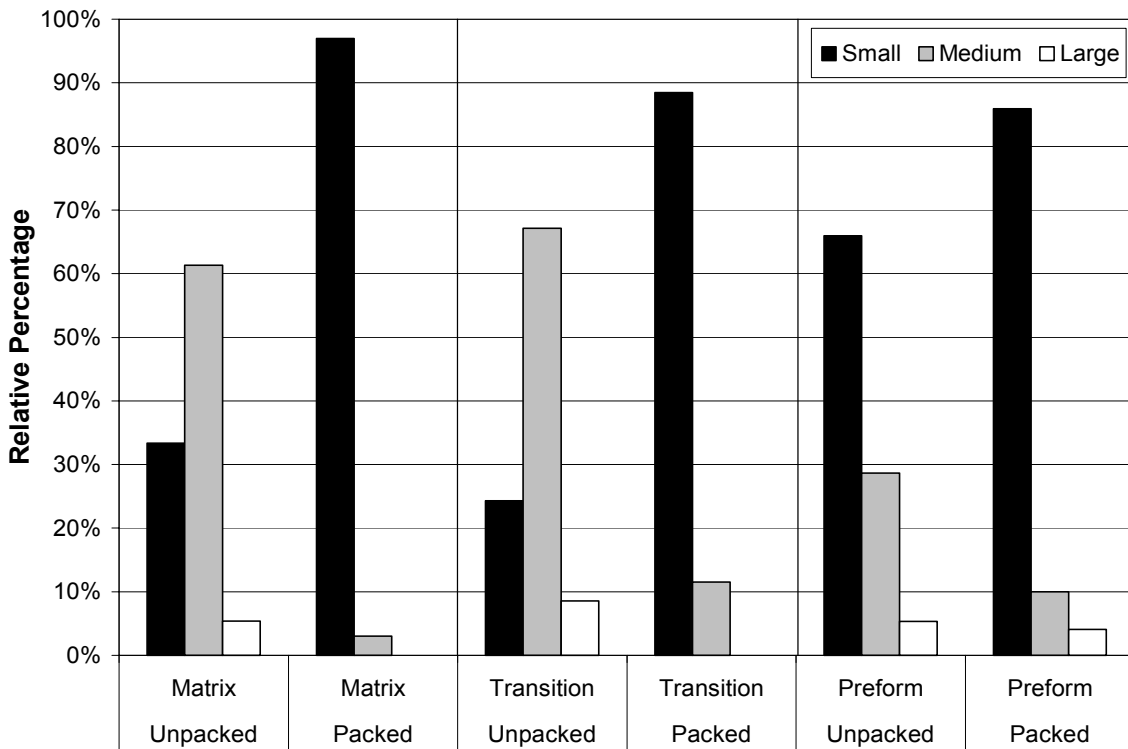


Figure 6.7: (a) Planar and (b) through-the-thickness size distributions of voids observed in different locations in the unpacked and packed composite disks.

This relatively smaller reduction in size of preform voids as compared to that of matrix voids seen from both views can be expected since since intra-tow voids are physically trapped inside fiber tows, and hence might not be fully subjected to the higher packing pressure.

The difference between planar size distributions of transition voids of unpacked and packed composites, depicted in Fig. 6.7a, is the most interesting. Unexpectedly, large void frequency is observed to increase from merely 9.7% to 36.0%. At the same time, medium voids occurrence is reduced from 58.1% to 28.0% and small void contribution is modestly increased from 32.3 to 36.0%. A more reasonable decrease in contribution of transition voids is observed from through-the-thickness view, i.e. Fig. 6.7b. Small transition voids augmented from 24.3% in the unpacked composite to 88.4% after packing. Medium transition voids contribution is considerably reduced from 67.1 to 11.6%; while no large transition voids are encountered in the through-the-thickness surface of the packed composite. These findings suggest that large voids trapped right next to the fiber bundles are more difficult to remove by packing than matrix voids, and maybe that some transition voids consolidate together between planar preform layers into larger elongated voids. Although no explanation is found for this phenomenon solely based on Figs. 6.7a and 6.7b, a more careful look into the captured microscopic images of the packed composite shows that indeed most large transition voids - seen from the planar view - are deformed into irregular shapes, while no large transition voids are observed from through-the-thickness view. Nevertheless, these voids only sum up to less than 0.003% void content, which is by all means an insignificant occurrence that is not

likely to alter the composite's mechanical performance. In summary, the investigation of void size distributions in both packed and unpacked composites shows that voids encountered in different composite locations do not respond equally to packing, but more importantly, that no critical adverse effect is introduced by applying a packing pressure.

6.4.5 Effect of Packing on Void Shape

Due to variations in void sizes and locations, a variety of void shapes are encountered in RTM composites [4,20-25]. Howe et al. [4] reported the existence of two major void shapes for RTM woven carbon/epoxy composites at 59% fiber content. The first comprises spherical to elliptical voids with a diameter of 100 to 200 μm , and the second represents larger voids confined to the preform. These irregularly-shaped voids have a height of 150 to 400 μm and a length of 250 μm to 4 mm. Patel and Lee [20] investigated effects of fiber architecture on void formation in LCM by monitoring the mold filling from a planar plane using model fluids. Although no quantifications were given, they reported the formation of voids with different shapes for both bidirectional stitched fiberglass and 4-harness woven fiberglass preforms. These different void shapes observed in RTM and LCM composites can originate from different wetting mechanisms for different preform architectures. For instance, a fast flow impregnating unidirectional fiber tows in the transverse direction is expected to trap cylindrical intra-tow voids; while voids trapped around a preform stitch by a slow impregnating flow are reported to be mostly irregular [22-25].

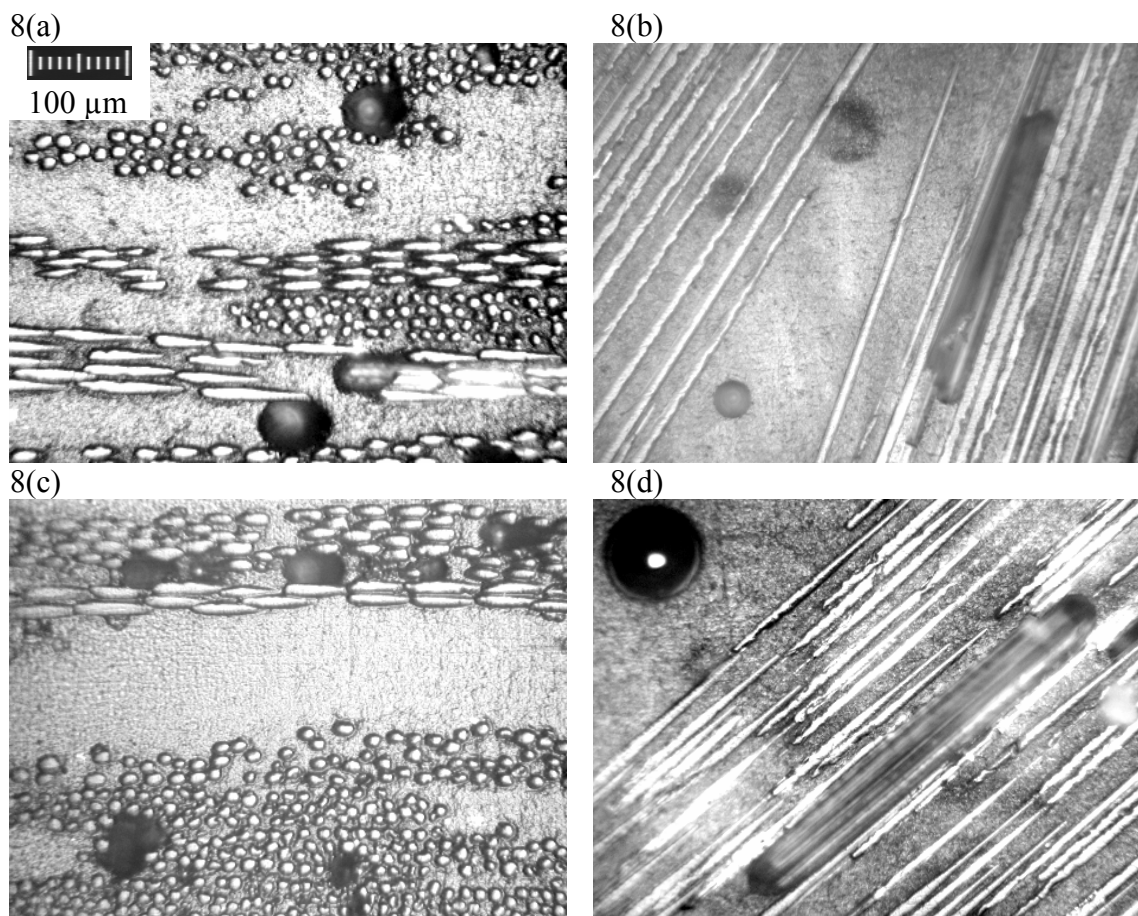


Figure 6.8: Representative image of voids with different shapes obtained at 200x magnification from through-the-thickness (left column) and planar (right column) views of the unpacked composite disk molded without post-fill pressure at 17.5% fiber content.

Figure 6.8 depicts representative images of different shapes of voids encountered in the unpacked composite obtained at 200x magnification from through-the-thickness and planar views. Voids seen in Fig. 6.3b and top left of Fig. 6.8d are mostly circular. In contrast, voids trapped between fiber bundles in bottom of Fig. 6.8a and top of Fig. 6.8c are more elliptical. Voids entrapped within the preform in Fig. 6.3a and bottom of Fig. 6.8c present a different irregular geometry. Another void shape is large, cigar-shaped, preform voids observed only in the planar view as seen in Figs. 6.8b and 6.8d. These cylindrical voids appear only as smaller truncated voids when observed from a through-the-thickness surface.

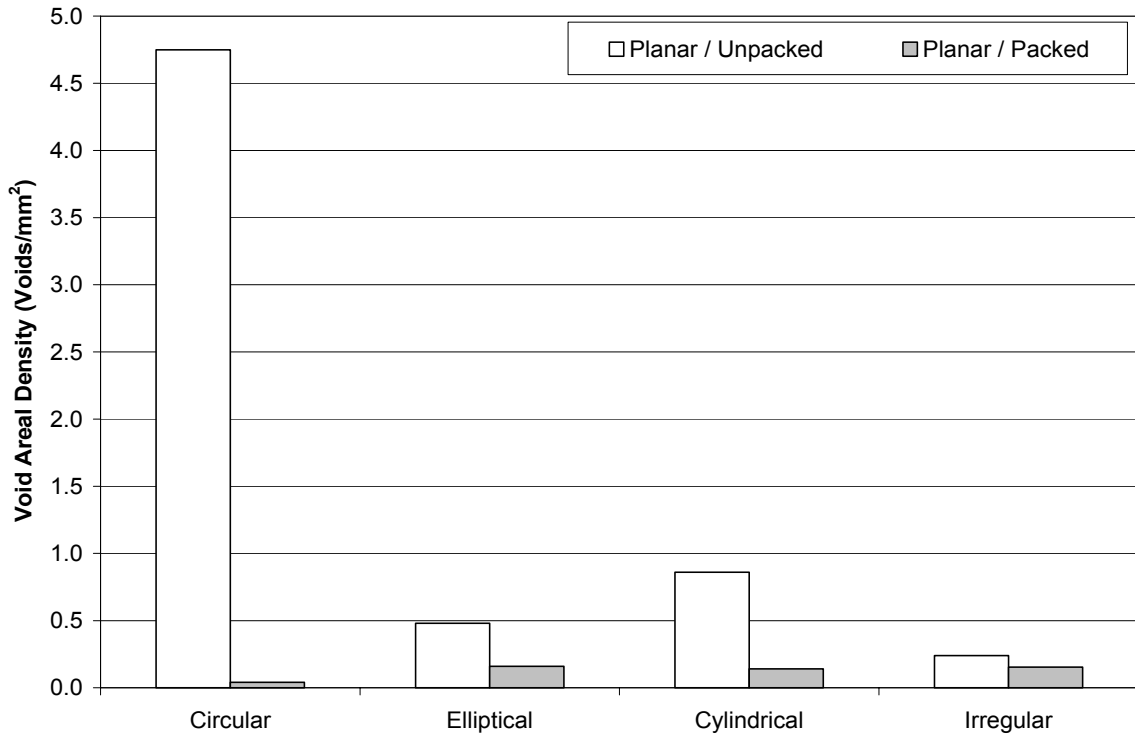
First, based on the observed shapes, voids are separated into three groups: Irregular, cylindrical, and spherical voids. Irregular voids are defined as those presenting a non-convex planar surface area, that is, two different points exist within the void that can be connected by a straight line that intersects the void boundary. Cylindrical voids are defined as cigar-shaped voids, found exclusively inside fiber bundles (Figs. 6.8b and 6.8d). Excluding those two categories, remaining voids are mostly spherical, even though most of them do not present a perfect circular symmetry. To classify this variation in voids' roundness, void data is further processed by introducing the shape ratio, R_s , defined for each void as the equivalent diameter obtained from Eq. (1) divided by the maximum measured length, L_{max} , within a void:

$$R_s = \frac{D_{eq}}{L_{max}}. \quad (6.2)$$

Note that ideal circles are represented by $R_s = 1$, and as the shape ratio gets smaller, voids become more elongated. Using this shape ratio, spherical voids are further segregated into two categories: Circular voids with shape ratios above 0.95 ($0.95 < R_s \leq 1$), and elliptical voids with shape ratios lower than 0.95. Different shape parameters are utilized for roundness measurement of voids in composites [8,28-31], or pores in both ceramics [47,50] and metals [53].

Using the criteria defined above, contributions to void content from voids with different shapes are calculated. The resulting shape distributions of voids observed in unpacked and packed composites are presented in Figs. 6.9a and 6.9b. Shape distributions based on void areal densities obtained from both planar and through-the-thickness surfaces are simultaneously analyzed in order to assess the accurate void morphology. Circular voids are almost completely removed with a 99.2% reduction in void areal density when assessed from the planar views. An equally high, void removal rate of 98.0% is observed for circular voids when evaluated using the through-the-thickness view. Cylindrical voids can only be seen in the planar view as through-the-thickness sample is cut perpendicularly to most fiber bundles - potential beds for cylindrical voids. Packing is found to reduce the void areal density of cylindrical voids from 0.86 to 0.14 voids/mm², registering an 83.0% reduction rate.

9(a)



9(b)

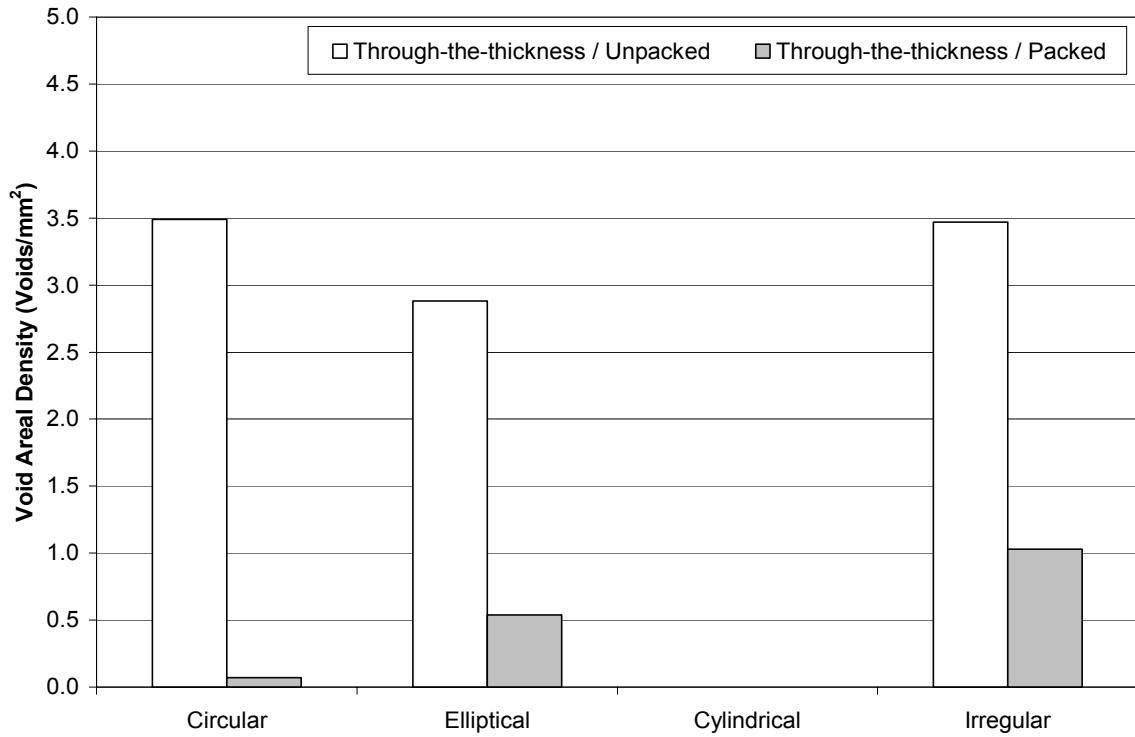


Figure 6.9: (a) Planar and (b) through-the-thickness void shape distributions for the unpacked and packed composite disks.

Elliptical and irregular voids both show a slightly different percentage reduction in void areal densities. Contribution of elliptical voids to planar void areal density decreases from 0.9 voids/mm² in the unpacked composite to 0.2 voids/mm² in the packed composite, while its through-the-thickness counterpart drops from 2.9 to 0.6 voids/mm². These reductions of 66.7 and 81.1% are significant voidage removal levels even if they are lower than those observed for circular and cylindrical voids. Likewise, although areal densities of irregular voids assessed from both surfaces drop considerably (i.e. 37.5% in the planar surface and 70.3% in the through-the-thickness view), these removal rates do not reach the reduction levels of circular and cylindrical voids. These findings show that voids with different shapes do not have the same likelihood of removal under packing. Irregular and elliptical voids are found to be less sensitive to packing than cylindrical and circular voids.

Data of irregular voids obtained from all four samples are further processed to obtain their size distribution. The resulting size distributions of irregular voids in unpacked and packed composites are depicted in Fig. 6.10. Based on through-the-thickness data, all irregular voids with different sizes are observed to decrease. As a result of packing, irregular small voids dropped from 2.0 to 0.9 voids/mm². Medium and large voids experienced even higher removal rates, decreasing respectively from 1.3 and 0.2 voids/mm² to 0.1 and 0.03 voids/mm², which corresponds to 81.6 and 76.9% reductions.

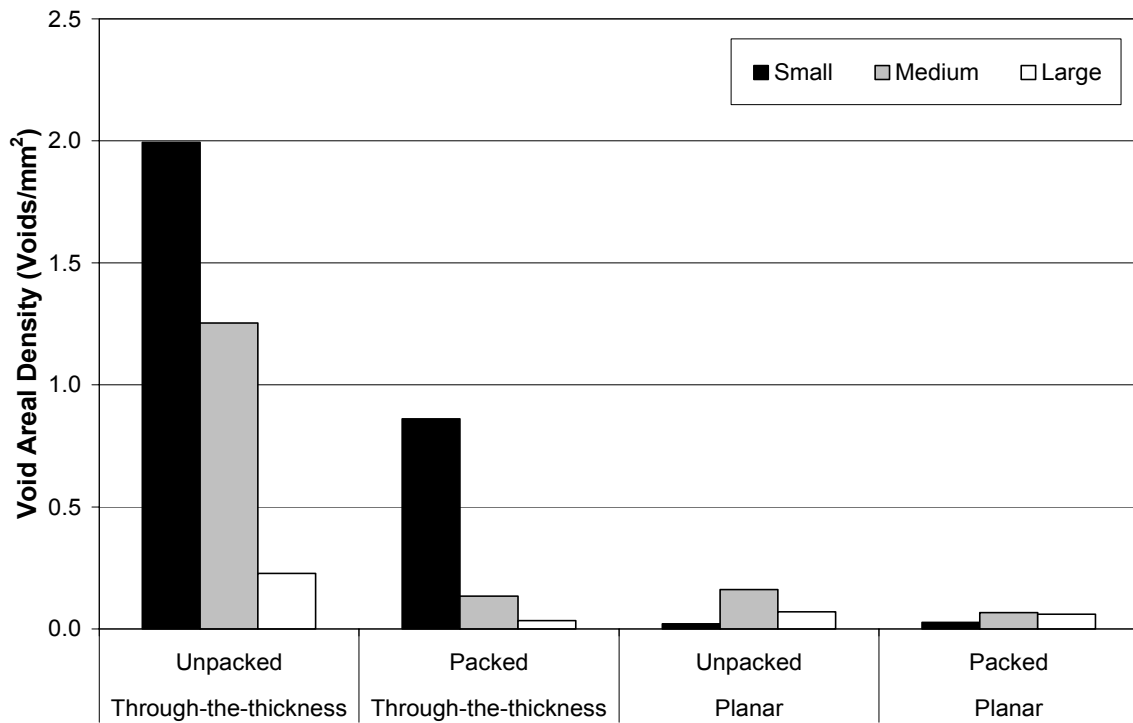


Figure 6.10: Through-the-thickness and planar size distributions of irregular voids obtained from the unpacked and packed composite disks.

The very low planar areal densities of irregular voids are also depicted in Fig. 6.10 to ascertain that no increase in large irregular voids occurs in the packed composite. These results show that insignificant occurrences of large irregular voids are present in the packed composite, and in any case, their incidence level is significantly lower than those experienced in the unpacked composite.

The shape ratio defined earlier can help monitor void elongation due to shear induced by packing. An analysis using the shape ratio is undertaken to shed some light on the size distribution of transition voids depicted in Fig. 6.7. Using planar data of all voids from both unpacked and packed composites, average shape ratios of both total and transition voids are calculated and presented in Table 6.1, along with their respective 95% confidence intervals and standard deviations. Packing is found to produce in average more elongated voids, as the average shape ratio dropped from 0.84 to 0.67, given that circular voids with the highest shape ratios are almost entirely eliminated as shown in Fig. 6.9. Transition voids see a more accentuated elongation due to packing since their average shape ratio is reduced from 0.98 to 0.66, possibly due to shear deformation of the voids restrained by the neighboring fibers.

Table 6.1: Effect of applying a 570 kPa post-fill pressure on shape ratio distribution for the overall composite and for transition voids.

	Overall voids	Transition voids
Unpacked composite	Average shape ratio: 0.8347 ± 0.0097 Standard deviation: 0.1798	Average shape ratio: 0.9778 ± 0.0063 Standard deviation: 0.0487
Packed composite	Average shape ratio: 0.6658 ± 0.0174 Standard deviation: 0.2031	Average shape ratio: 0.6577 ± 0.0724 Standard deviation: 0.1847

6.4.6 Effect of Packing on Radial Voidage Variation

Variation of void content in the radial direction in both composites is examined to assess packing effects on spatial void distribution, and ensure that anomalies in void concentration are not formed. Five radial regions of equal length, covering the entire composite samples, are defined as shown in Figs. 6.2b and 6.2c for both the planar and through-the-thickness surfaces, respectively. Figure 6.11 illustrates the variation of void content in the radial direction obtained from planar and through-the-thickness surfaces for the unpacked and packed composites. The radial variation of void content of the unpacked composite seems to show a very slight increase in the voidage away from the injection gate. Concurrently, the packed composite depicts different radial trends of void content from both views. From the planar view, void content in the packed composite slightly increases through the first three radial regions from 0.3 to 0.4%, and then drops dramatically in the last two regions. In contrast, from through-the-thickness view, void content in the packed composite, with the exception of the first radial region, is observed to increase almost linearly with radial distance from the injection gate, doubling from 0.1 to 0.2% between the second and fifth region. We submit that the spatial variation of voidage in the packed composite can be attributed to the voids' existing pre-dispositions to removal before packing, influenced by their proximity to fibers. Note that proximity to fibers was classified based on the location of voids earlier in this paper. Still, voidage levels are very low in all radial regions of the packed composite and voids do not seem to concentrate radially at any particular region and a structurally weak radial position is not expected.

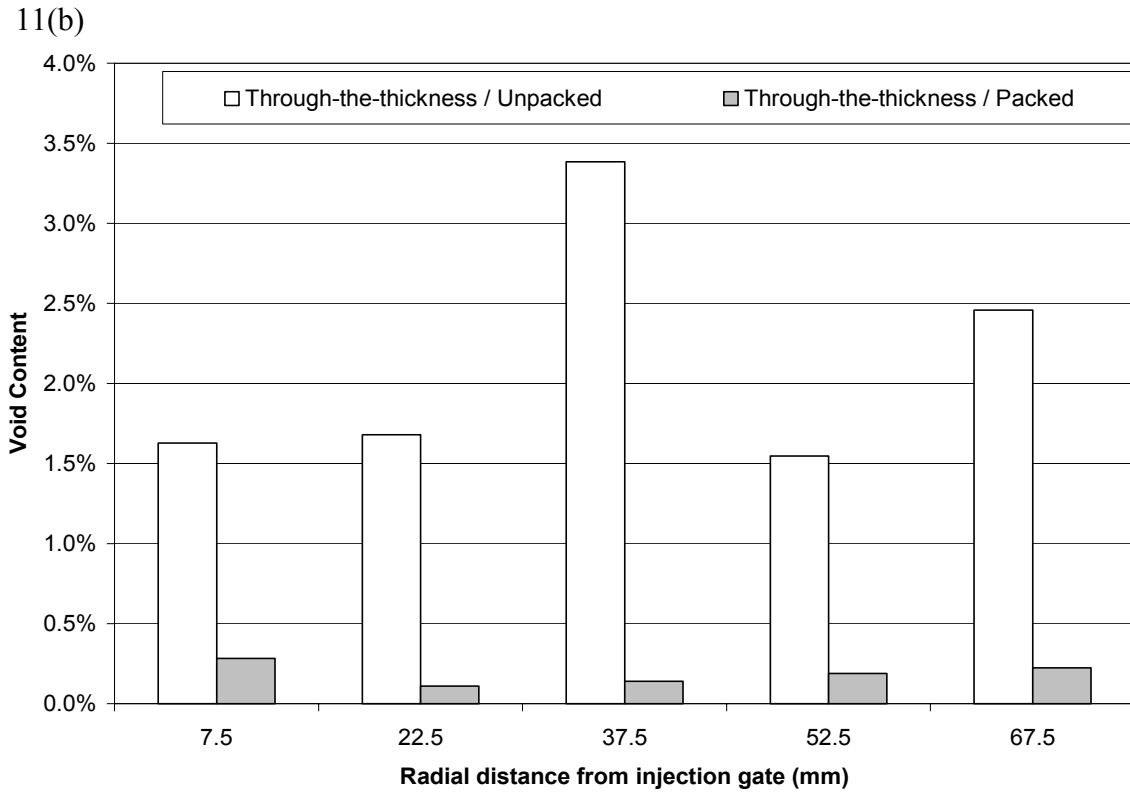
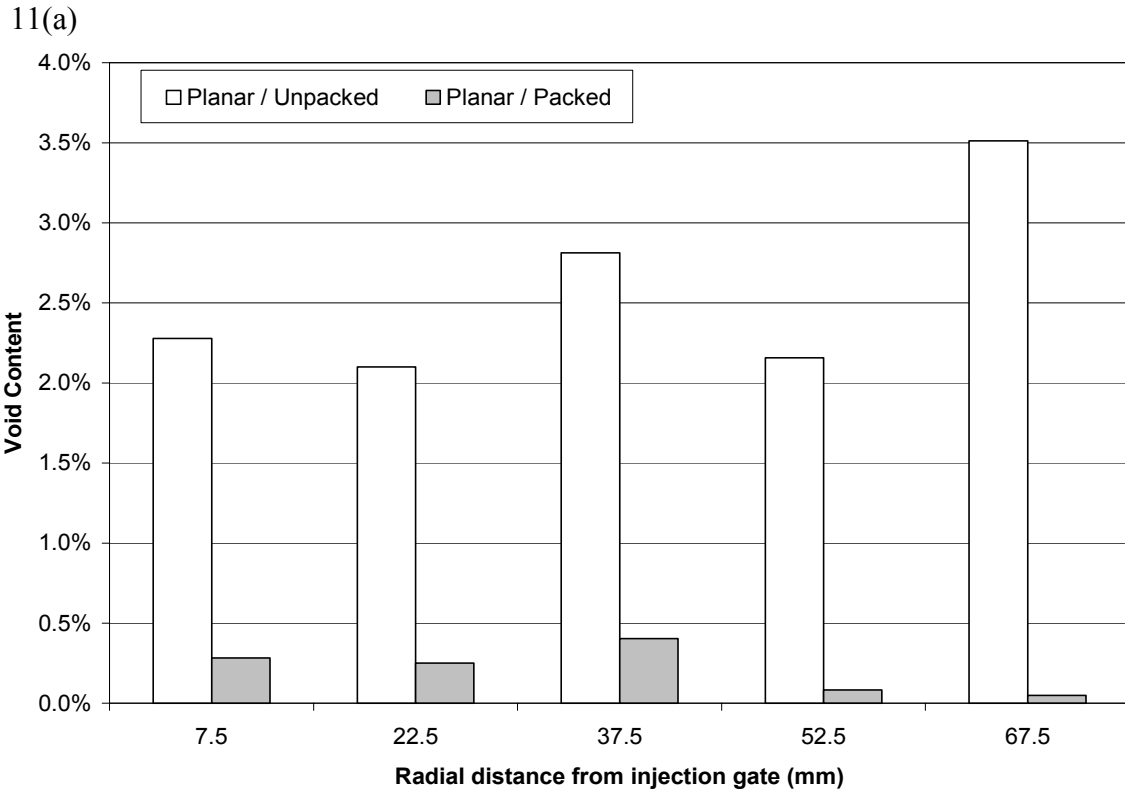


Figure 6.11: Radial variation of void content in the unpacked and packed composite disks: (a) obtained from the planar surface, and (b) obtained from the through-the-thickness surface.

To further investigate the radial variation of void content in the packed composite, contribution of voids from different locations to the overall void content is considered. As discussed earlier in this paper, through-the-thickness surface is likely to better represent the distribution of void locations. Thus, only through-the-thickness void data are utilized in the following analysis. The effect of location of voids on reduction rates in each radial region can be studied by introducing a *conformity parameter*, $C_{i,l}$, defined as:

$$C_{i,l} = \frac{R_{i,l} - R_i}{R_i}, \quad (6.3)$$

where R_i is the reduction rate for all voids at the radial region i , and $R_{i,l}$ the reduction rate for voids formed at a particular location l . Note that there are five regions, $i = 1$ to 5, and three void locations, $l =$ matrix, transition, or preform. A positive *conformity parameter* means that voids at that particular location have experienced a higher reduction rate than the reduction rate experienced by all voids combined in that radial region, and *vice versa*. Figure 6.12 depicts radial variations of *conformity parameter* for matrix, transition, and preform voids obtained from the through-the-thickness surface. The first observation is that void content reduction rates of voids formed in different locations, depicted in Fig. 6.5b, are not uniform at a particular region or along the radius of the composite. Voids in different locations of the composite respond differently to packing. For instance, in the second radial region, transition voids are more prone to removal by packing than matrix and preform voids. In addition to voids' proximity to fibers, their radial position seems to affect the reduction rates. Unlike the first region, matrix voids have a much higher reduction rate than transition and preform voids in the fourth and fifth regions.

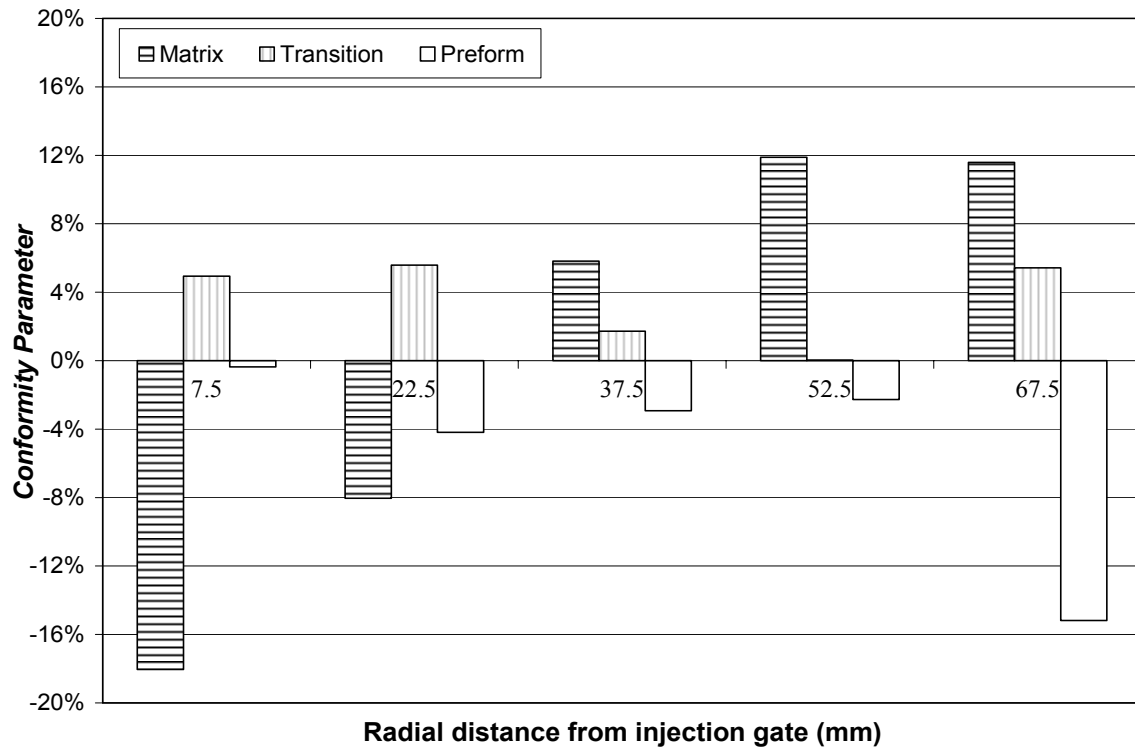


Figure 6.12: Through-the-thickness radial variation of *conformity parameter* from average void content reduction rates due to the application of 570 kPa post-fill pressure.

Figure 6.12 depicts radial variations of *conformity parameter* for matrix, transition, and preform voids obtained from the through-the-thickness surface. The first observation is that void content reduction rates of voids formed in different locations, depicted in Fig. 6.5b, are not uniform at a particular region or along the radius of the composite. Voids in different locations of the composite respond differently to packing. For instance, in the second radial region, transition voids are more prone to removal by packing than matrix and preform voids. In addition to voids' proximity to fibers, their radial position seems to affect the reduction rates. Unlike the first region, matrix voids have a much higher reduction rate than transition and preform voids in the fourth and fifth regions.

Conformity parameter of matrix voids shows a steady increase from a -18.1% in the first radial region, to a high of 11.6% in the fifth. Matrix voids experience a considerably lower reduction rate than transition and preform voids in the first radial region. Along the radial direction, matrix voids gradually see their reduction rate increase reaching a much higher rate than transition and preform voids in the fifth region. This monotonic raise is attributed to pre-existing voidage arrangement in the composite disk prior to packing. Data collected from the unpacked composite show that matrix voids become smaller away from the injection gate. Smaller matrix voids, in turn, are easier to dissolve under pressure. Therefore, more matrix voids might be dissolved into the matrix near the exit vents. One should keep in mind, nonetheless, that matrix voids are a very small portion (less than 7%) of all voids existing in the unpacked composite.

Preform voids show negative values of *conformity parameter* in all radial regions; while transition voids are observed to have solely positive values. As seen in Fig. 6.5b, preform voids are less prone to removal by packing. Therefore, negative values of preform *conformity parameter* are expected. Transition voids are also anticipated to be more susceptible to pressure induced shrinkage or removal than preform voids since they are directly subjected to the higher packing pressure. The highest negative *conformity parameter* for preform voids, i.e. 15.2%, is observed at 67.5 mm away from the injection gate. Region five has the lowest occurrence of preform voids prior to packing with mostly small voids. Small preform voids, situated well inside fiber tows, might be more difficult to remove since they are shielded from the packing pressure. In contrast, large preform voids often wrap around a large part of the fiber tow making them more susceptible to the packing pressure. Incidentally, preform voids show their lowest *conformity parameter* in the first radial region, which experiences the highest fluid front velocity during injection, and thus has the maximum occurrence of large preform voids. A similar analysis can be conducted on transition voids for all radial regions. In short, the levels of removal of voids with different proximities to fibers, although comparable, are governed by their pre-existing arrangement at the end of the filling stage, i.e. prior to packing. This finding further stresses the importance of understanding spatial void morphology in LCM composites in order to implement proper void removal methods.

6.5 *Conclusions*

Effects of applying a post-fill pressure on void content, void morphology, and void spatial distribution are presented for RTM E-glass/epoxy composites containing 17.5% fibers. The composite molded with a 570 kPa packing pressure showed almost 92% drop in void content compared to an unpacked composite. Microscopic image analysis was utilized to examine voidage from both through-the-thickness and planar surfaces of the two molded disks. Only 0.2% void content was registered in the packed composite, whereas the unpacked composite showed void contents of 2.2 and 2.6% in the through-the-thickness and planar surfaces, respectively. In addition, the average void size was observed to decrease from 59.3 μm in the unpacked composite to 31.7 μm in the packed composite when observed from through-the-thickness surface. A comparable reduction rate was observed on the planar surface from 66.7 to 41.1 μm in average void size. Furthermore, reduction rates of voids appear to be affected by their shapes. While circular voids experienced the highest removal rate of 99%, cylindrical and elliptical voids registered lower but still significant reduction rates of 83 and 81%, respectively. Irregular voids, on the other hand, showed a slightly lower void removal rate at 67%. Proximity of voids to fiber bundles was also observed to affect their removal rates as voids located inside fiber tows sustained slightly lower reduction rates. Along the radial direction, removal of voids with different proximities to fibers seems to depend on their arrangement at the end of the filling stage. These findings are believed to be relevant to RTM and LCM processes with similar flow kinetics. Finally, packing did not induce any spatial void concentration or other adverse effects, thus validating packing as an effective void removal method.

6.6 References

1. Abraham D., and McIlhagger R., *Composites Part A*, 29, 533, 1998.
2. Abraham D., Matthews S., and McIlhagger R., *Composites Part A*, 29, 795, 1998.
3. Johnson C. F., *Composite Materials Technology- Process and Properties*, Hanser Publisher, NewYork, Ch. 5, 1990.
4. Howe C. A., Paton R. J., and Goodwin A. A., *Proc. of ICCM-11, Composites Processing and Microstructure*, Australian Composite Structures Society, Gold Coast, Australia, 46, 1997.
5. Judd N. C. W., and Wright W. W., *SAMPE Journal*, 14, 10, 1978.
6. Govindarjan S., and Langrana N. A., *Finite Elements in Analysis & Design*, 23, 333, 1996.
7. Ghiorse S. R., *SAMPE Quarterly*. 23(1), 54, 1993.
8. Olivero K. A., Barraza H. J., O'Rear E. A., and Altan M. C., *Journal of Composite Materials*, 36, 2011, 2002.
9. Goodwin A. A., Howe C. A., and Paton R. J., *Proc. of ICCM-11, Composites Processing and Microstructure*, Australian Composite Structures Society, Gold Coast, Australia, 11, 1997.
10. Pearce N., Guild F., and Summerscales J., *Composites Part A*, 29, 141, 1998.
11. Wisnom M. R., Reynolds T., and Gwilliam N., *Composites Science and Technology*, 56, 93, 1996.
12. Bowles K. J. and Frimpong S., *Journal of Composite Materials*, 26, 1487, 1992.
13. Harper B. D., Staab G. H., and Chen R. S., *Journal of Composite Materials*, 21, 280, 1987.

14. Hoppel C., Bogettiand T., and Newill J. F., *Proc. of the American Society for Composites*, APG, MD, USA, 1094, 2000.
15. Gebart R. and Strömbeck L., *Principles of Liquid Composite Molding*, Carl Hanser Verlag, Munich, Germany, 358, 2000.
16. Shim S.-B., Seferis J. C., and Hudson, W., *Journal of Advanced Materials*, 28, 26, 1997.
17. Thomas M. M., Joseph B., and Kardos J. L., *Polymer Composites*, 18, 283, 1997.
18. Han K., and Lee L. J., *Journal of Composite Materials*, 30, 1458, 1996.
19. Mahale A. D., Prud'Homme R. K., and Rebenfeld L., *Polymer Engineering and Science*, 32, 319, 1992.
20. Patel N., and Lee L. J., *Polymer Composites*, 16, 386, 1995.
21. Patel N., Rohatgi V., and Lee L. J., *Polymer Engineering and Science*, 35, 837, 1995.
22. Rohatgi V., Patel N., and Lee L. J., *Polymer Composites*, 17, 161, 1996.
23. Patel N. and Lee L. J., *Polymer Composites.*, 17, 96, 1996.
24. Kang M. K., Lee W. I., and Hahn H. T., *Composites Science and Technology*, 60, 2427, 2000.
25. Lundstrom T. S., and Gebart B. R., *Polymer Composites*, 15, 25, 1994.
26. Lundstrom T. S., Gebart B. R., and Lundemo C. Y., *Journal of Reinforced Plastics and Composites*, 12, 1339, 1993.
27. Darcy H. P. G., *Les Fontaines Publiques de la Ville de Dijon*, Delmont, Paris, 306, 1856.
28. Olivero K. A., Hamidi Y. K., Aktas L., and Altan M. C., *Journal of Composite Materials*, 38, 937, 2004.

29. Barraza H. J., Hamidi Y. K., Aktas L., O'Rear E. A., and Altan M. C., *Journal of Composite Materials*, 38, 195, 2004.
30. Hamidi Y. K., Aktas L., and Altan M. C., *Composites Science and Technology*, in review, 2004.
31. Hamidi Y. K., Aktas L., and Altan M. C., *Journal of Engineering Materials and Technology*, in press, 2004.
32. Chan A. W., and Morgan R. J., *SAMPE Quarterly*, 23(4), 48, 1992.
33. Patel N., and Lee L. J., *Polymer Composites*, 17, 104, 1996.
34. Binetruy C., Hilaire B., and Pabiot J., *Journal of Composite Materials*, 32, 223, 1998.
35. Han K., and Lee L. J., *Journal of Composite Materials*, 30, 1458, 1996.
36. Chang C.-Y., and Hourng L.-W., *Polymer Engineering and Science*, 38, 809, 1998.
37. Breard J., Saouab A., and Bouquet G., *Composites Part A*, 34, 517, 2003.
38. Shojaei A., Ghaffarian S. R., and Karimian S. M. H., *Polymer Composites*, 24, 525, 2003.
39. Stabler W. R., Tatterson G. B., Sadler R. L., and El-Shiekh A. H. M., *SAMPE Quarterly*, 23(1), 38, 1992.
40. Chui W. K., Glimm J., Tangerman F. M., Jardine A. P., Madsen J. S., Donnellan T. M. and Leek R., *Proc. of the 9th International Conference of Numerical Methods in Thermal Problems*, Atlanta, 1323, 1995.
41. Ikegawa N., Hamada H., and Maekawa Z., *Polymer Engineering and Science*, 36, 953, 1996.
42. Choi J. H., and Dharan C. K. H., *Journal of Composite Materials*, 36, 2267, 2002.
43. Ghiorse S. R., U.S. Army Mat. Tech. Lab. Report MTL TR, 91-13, 1991.

44. Santulli C., Garcia Gil R., Long A. C., and Clifford M. J., *Science and Engineering of Composite Materials*, 10, 77, 2002.
45. Jiang H., Bowen P., and Knott J. F., *Journal of Materials Science*, 34, 719, 1999.
46. Singh M., Trivedi M. K., and Bellare J., *Journal of Materials Science*, 34, 5315, 1999.
47. Kawai C., *Journal of Materials Science*, 36, 5713, 2002.
48. Chaim R., and Hafetz M., *Journal of Materials Science*, 39, 3057, 2004.
49. Rice R. W., *Journal of Materials Science*, 34, 2769, 1999.
50. Fukasawa T., Deng Z.-Y., Ando M., Ohji T., and Goto Y., *Journal of Materials Science*, 36, 2523, 2001.
51. Sun Y., Liu G., and Wang C., *Journal of Materials Science*, 39, 2553, 2004.
52. Song X. and Liu G., *Journal of Materials Science*, 34, 2433, 1999.
53. Kubicki B., Sundhar V., and Kubicki M., *Journal of Materials Science*, 37, 3959, 2002.

7 Effect of Nanoclay Content on Void Morphology in Resin Transfer Molded Composites

7.1 Abstract

Effect of nanoclay content on morphology and spatial distribution of voids in resin transfer molded nanoclay/E-glass/epoxy composite disks are investigated. Cloisite[®]25A nanoclay loads of 2, 5, and 10 wt% are mixed by sonication with a low-viscosity epoxy resin prior to filling the mold cavity containing 13.6% E-glass preform by volume. A disk without nanoclay is also molded. Once the molded composites are cured, voids are evaluated via microscopic image analysis of radial samples. The addition of nanoclay is found to result in a significant increase in the apparent viscosity of the clay-epoxy mixture, thus increasing the molding pressure. Void occurrence is observed to increase considerably with increasing nanoclay content from 2.1% in the composite without nanoclay to 5.1 and 8.3% in the composites molded with 5 and 10 wt% nanoclay, respectively. However, the composite with 2 wt% nanoclay yields the lowest void content of 0.7%. Voids are observed to be, in average, smaller after the addition of nanoclay at all nanoclay concentrations. Presence of nanoclay in the impregnating resin induces at least 60% reduction in voids located inside fiber tows, which are trapped by the fluid front motion during impregnation. Irregularly shaped voids are also observed to decrease with increasing nanoclay content. A nonuniform void content and morphology is observed radially, which seems to be affected by the flow kinematics as well as possible breakdown and filtration of clay clusters.

7.2 Introduction

In recent years, usage of nanoscale fillers in polymers and fiber-reinforced composites has attracted considerable interest. Such nanoscale fillers frequently exhibit larger surface area per unit volume and thus enhance the performance of the fabricated composite. One of the most promising of these nanoscale particles is the abundantly available layered silicate, a.k.a. nanoclay. Individual nanoclay particles are silicate platelets that typically range from 1 to 10 nm in thickness and 1 to 13 μm in length [1]. Although nanoclay was first introduced to reinforce thermoplastics such as nylon 6 [2-7], its utilization has been expanded to reinforce thermosetting resins due to their wider industrial usage, higher strength, and lower viscosity [8]. Nanoscale fillers have been also added to fiber-reinforced composites with well established manufacturing processes in order to improve the mechanical and barrier properties.

Researchers from Toyota [2-7] pioneered the utilization of nanoclay in thermoplastics. They studied effects of adding uniformly-dispersed nanoclay into nylon 6 on the mechanical and thermal properties, flame retardancy, as well as water absorption and gas permeability resistance. Usuki et al. reported that the addition of 4 wt% nanoclay induced a 100% increase in stiffness and 50% in strength [5]. A 40% reduction in maximum water absorption was reported for similar nanocomposites [6]. Kojima et al. [7] also reported an increase in glass transition temperature, T_g , of nylon 6 containing 4.7 wt% nanoclay.

Improved properties are obtained only when nanoclay is intercalated and/or exfoliated into the polymeric matrix [2-4]. When the clay is well mixed with the polymer matrix,

the polymer swells the spacing between platelets and the nanocomposite is called intercalated. When individual clay layers are further dispersed as single platelets into the polymeric matrix, the nanocomposite is called exfoliated. Alexandre and Dubois [9], for instance, showed that mechanical and barrier properties, transparency, and toughness are directly proportional to the degree of exfoliation. Nanoclay dispersion into epoxies also induces significant enhancements in mechanical properties. For example, Advani and Shonaike [10] observed more than 100 and 120% increase in tensile modulus and strength respectively after the addition of 5 wt% nanoclay into an epoxy adhesive. Furthermore, Shah et al. [11] reported a reduction in moisture absorption diffusivity after the introduction of Cloisite[®] 10A nanoclay into a molded Derkane epoxy part. A nanoclay load as low as 0.5 wt% reduced moisture diffusivity by more than 50%, while a 5 wt% clay load resulted in an 86.4% reduction in moisture diffusivity. Increases in T_g and tensile modulus with increasing nanoclay contents were also reported [11]. Kinloch and Taylor [12] studied T_g improvements in an epoxy due to the introduction of 10 wt% of nanoclay. The authors reported a small improvement from 78 to 79°C for exfoliated Nanomer[®] I30E, and a higher T_g of 85°C for intercalated Cloisite[®] 25A.

Akkapeddi [13], on the other hand, studied both short and continuous glass-fiber-reinforced clay-polyamide 6 nanocomposites manufactured by a melt compounding technique. The author reported improved flexural modulus, strength, and heat distortion temperature under load as well as improved moisture resistance at 2 and 5 wt% nanoclay contents. Haque et al. [14] reported significant improvements in mechanical and thermal properties of S2-glass/epoxy composites with low nanoclay contents manufactured by vacuum assisted resin infusion molding (VARIM). The authors observed that dispersing

1 wt% clay resulted in a 26°C increase in T_g as well as 44, 24, and 23% improvement in interlaminar shear strength, flexural strength, and fracture toughness, respectively. Hussain and Dean [15] utilized the VARIM process to fabricate a series of S2-glass/vinylester nanocomposites containing 0.5, 1, 2, 5 and 10 wt% clay. They reported significant improvements in T_g , interlaminar shear strength, flexural strength, flexural modulus, and fracture toughness [15]. Becker et al. [16] investigated intercalated clay-epoxy nanocomposites reinforced with 49% unidirectional carbon fibers. The addition of layered silicate to the prepregs resulted in tougher composites with more than 50% increase in fracture energy reported for composites containing 2.5, 5, and 7.5 wt% nanoclay.

Based on the recent results, one can conclude that the addition of nanoclay into a polymeric matrix often yields significant improvements in the mechanical and thermal properties while enhancing moisture resistance. A similar statement can be made for the case of conventional, fiber-reinforced composites; however, the extent of improvements still remains uncertain in commercial applications. The effectiveness of using nanoclay-polymer mixtures in current fabrication methods for conventional composites needs to be investigated. For example, the addition of nanoclay increases the bulk viscosity of the polymer, which might require excessive injection pressure for molded composites. For higher nanoclay contents, adequate dispersion and purging of air pockets embedded in clay clusters might not be achieved, even for low viscosity epoxy resins commonly used in liquid composite molding (LCM) processes.

The successful resolution of such fabrication difficulties would facilitate the wider use of nanoclay in both thermosetting and thermoplastic composites. Of particular interest is the resin transfer molding (RTM) process due to the possibility of achieving improved performance at a reduced cost. Resin transfer molding is a well established, versatile process for manufacturing near-net-shape, geometrically complex composite parts. RTM typically involves injecting a reacting polymeric resin into a closed mold containing a dry fiber preform. Although large spatial variations in fluid velocity are not observed at the macroscale, local microscale velocities can be very different. Wide disparities between local permeabilities and local capillary pressures within the preform often lead to a non-uniform impregnation inside and outside the fiber bundles. This non-uniform velocity field with large spatial variations of velocity gradients leads to the formation of voids in the fabricated composites [17-19]. At higher front velocities, resin flow outside fiber tows is much faster than inside, and voids are primarily formed inside the fiber bundles, a.k.a. intra-tow voids. At slower filling rates, on the other hand, capillary flow inside fiber tows leads the impregnation and most of the voids are inter-tow voids formed outside the fiber bundles. Various researchers reported the existence of an optimum resin velocity at which void formation is minimal and both inter- and intra-tow voids coexist [17-23]. In addition to the described void formation by mechanical entrapment, other void formation mechanisms in RTM composites include initial air bubble content in the resin mixture, volatilization of dissolved gas in the resin during mold filling or curing, and partial evaporation of mold releasing agent into the preform [24]. While mechanical entrapment is inevitable in RTM, the remaining sources of void formation can be eliminated by degassing and proper selection of the resin/preform systems. With the

addition of nanoclay however, initial void content in the resin might be augmented due to the presence of air pockets inside larger clay clusters.

Unfortunately, void presence in composites always yields severe degradation of the mechanical properties [23-26] and resistance to moisture absorption [27-28]. For instance, Ghiorse [25] reported that each 1% increase in void content induces a 10% reduction in flexural and interlaminar shear strength, and a 5% reduction in flexural modulus for carbon/epoxy composites. Goodwin et al. [26] also reported a 7% reduction in interlaminar shear strength per 1% increase in voidage up to 10% for RTM composites containing 57% 5-harness satin preform. In addition, even a minor variation in void content is reported to increase the moisture diffusion rate by a factor of 6 [28]. Consequently, void occurrence in RTM composites can be critical in predicting their mechanical performance.

The effect of adding nanoscale fillers on void formation in RTM composites has not yet been studied. In a recent study, Chisholm et al. [29] investigated property enhancement due to the introduction of nanosized SiC fillers into a carbon/epoxy vacuum assisted resin transfer molded composite. The authors reported qualitatively that nanoparticles tend to reduce void content of the fabricated composites. However, no information on void morphology or spatial void distribution was offered. Understanding void occurrence, morphology, and distribution within the resin transfer molded nanoclay/E-glass/epoxy composites is believed to be the first step in developing fabrication procedures yielding lower void occurrences in such composites. To the best of the authors' knowledge, no such investigation is available in the literature.

In the current study, we investigate the effect of nanoclay on void content, morphology, and spatial void distribution in resin transfer molded, nanoclay/E-glass/epoxy composites. The composite disks containing 13.6% E-glass preform by volume and 2, 5, and 10% Cloisite®25A nanoclay by weight are fabricated. A composite disk containing only 13.6% E-glass preform is also molded. In addition to comparing the void contents obtained at different nanoclay loads, more interest is drawn upon morphological features and radial variation of voids to help identify dominant void formation mechanisms.

7.3 Experimental

7.3.1 Materials

The nanoclay used in this study is Cloisite®25A supplied by Southern Clay Products, Inc. Cloisite®25A is a natural montmorillonite modified with a quaternary ammonium salt in order to increase the organophilicity of its gallery region, thus improving its dispersion in various types of resins. Typical particle sizes range from 1 to 13 μm in length and 1 to 10 nm in thickness, and its specific gravity is reported as 1.87 kg/m^3 [1]. The low viscosity epoxy resin EPON 815C is utilized together with the EPICURE 3282 curing agent commercialized by Shell Chemicals. Preforms used in this study are layers of randomly-oriented, chopped-strand, E-glass fibers with a planar density of 0.21 ± 0.015 kg/m^2 supplied by Fiberglast (part #248).

7.3.2 Preparation of the Clay-Epoxy Mixtures

Prior to the RTM process, the EPON 815C epoxy resin is mixed with the desired amount of Cloisite®25A nanoclay. The stochastic ratio of 5 to 1 of resin to curing agent by weight

is considered in order to achieve exact contents of 2, 5, and 10 wt% of nanoclay in epoxy-curing agent system. Initially, clay-epoxy blends are prepared by sonication. Cloisite[®]25A is first gradually added to the epoxy at room temperature while stirring with a glass rod in a beaker for 5 minutes. Thereafter, thorough mixing of the blend is performed at 60°C in an ultrasonic bath at a frequency of 42 KHz. After 60 minutes, no visual change in the clay-epoxy mixture is observed and the sonication is stopped. The high mixing temperature is selected as higher temperatures normally yield lower viscosities, and thus a better dispersion of the nanoclay. After sonication, the mixture is degassed at room temperature for one additional hour to remove a thin bubble layer formed at top surface. Note that before molding of the composite disk without clay, the epoxy resin is subjected to the same sonication process to ensure identical pre-molding conditions for all molded composites. After degassing, the viscosity of each clay-epoxy mixture is measured at 26°C using a Brookfield viscometer (Model DV-II+). Note that for clay-epoxy mixtures with 5 and 10 wt% nanoclay, one hour degassing did not eliminate all micro air bubbles at the top. In order to minimize sedimentation of clay clusters, additional degassing time was not allowed.

7.3.3 Molding Procedure

Nanocomposite disks used in this study are fabricated by a custom-made experimental molding setup composed of a hydraulic press; two reservoirs for clay-epoxy mixture and curing agent; a static mixer; and a center-gated, disk-shaped mold cavity. Operating the molding press forces the clay-epoxy blend and the curing agent out of the reservoirs into the mold cavity at a constant flow rate. Thorough mixing of these fluids is ensured by a disposable static mixer, yielding a gel time of about 20 minutes. Six layers of fiber

preform are placed in the 3-mm thick mold cavity prior to filling for all disks manufactured in this study. The details of the molding procedure and experimental setup are described in detail elsewhere [21-22]. At the end of mold filling, resin injection is stopped and no further post-fill operations are performed in order not to alter void morphology or spatial distribution formed during filling. Molded composite parts are then cured for 48 hours at room temperature before demolding, and sequentially oven-cured for 24 hours at 40°C. The final molded parts are four composite disks loaded with 0, 2, 5, and 10 wt% Cloisite[®]25A nanoclay, and each containing 13.6% E-glass fibers by volume. Average thickness and radius of the composite disks are 3.1 and 75.0 mm, respectively.

7.3.4 Microscopic Image Analysis

The preform planar isotropy and mold axisymmetry simplify the impregnation into a purely radial flow. Consequently, only radial composite samples are examined. A radial specimen is cut from each disk for voidage assessment. Radial variation is assessed by dividing each 75-mm long sample into five 15-mm long regions along the radial direction as shown in Fig. 7.1.

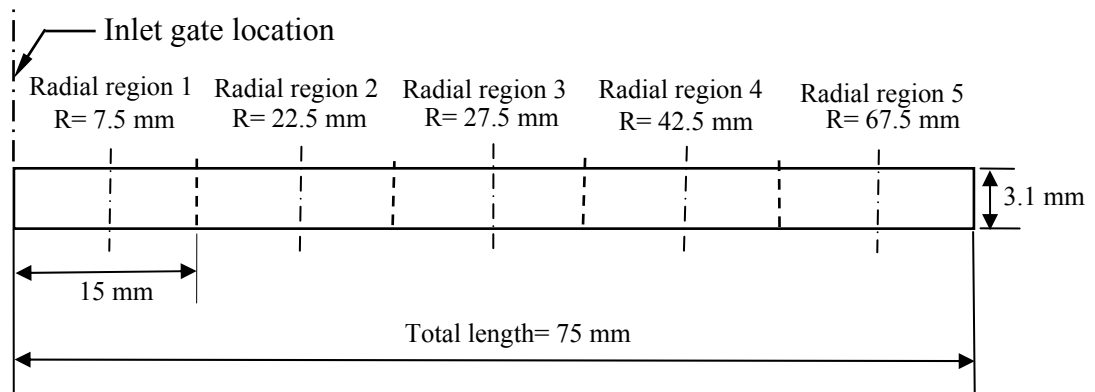


Figure 7.1: Spatial arrangement of nanocomposite samples into five radial regions for microscopic analysis.

Microscopic image analysis is considered among the most precise methods for measuring void contents [21-25,30-31]. In addition, this technique provides detailed information on other important parameters such as void location, shape, and size that cannot be assessed by other methods. Often, microscopic image analysis is used by averaging randomly selected images [30-31]. In the current investigation, however, the studied composite cross-sections are entirely scanned in order to accurately assess void content and morphology. Voidage features are obtained from images acquired at 200x magnification using a PC-based CCD camera mounted on a MEIJI optical microscope. At this particular magnification, every frame displays approximately 0.71 mm x 0.53 mm. Hence, 720 frames are captured for each composite sample: 6 frames through the thickness and 120 across the length. The selected magnification of 200x enables the assessment of voids as small as the radius of a single fiber, i.e. 7 μm . Consequently, all visually identifiable voids throughout the entire composite samples are included in the analysis of void content and morphology. A total of 15,250 voids are captured manually from the four studied composite samples. Each captured frame is manually processed using the image analysis software Image Tool[®], which allows the measurement of the area, A , and the maximum length, L_{max} for each void.

7.4 Results and Discussion

7.4.1 Effect of Nanoclay Content on Mold Filling Parameters

Figure 7.2 depicts the effect of nanoclay content on the viscosity of the epoxy. Both nanoclay volume fraction and relative viscosity values are shown with their respective 95% confidence intervals. The apparent dynamic viscosity increases moderately from

0.65 Pa·s for the neat resin to 1.12 Pa·s for the 5 wt% nanoclay suspension. A much steeper increase is observed for concentrated blends. For instance, the viscosity of the mixture reaches 3.69 Pa·s at 10 wt% clay content. For low clay concentrations (i.e. ϕ up to 5%), the relative viscosity, μ / μ_0 , shows linear behavior consistent with the Einstein regime:

$$\frac{\mu}{\mu_0} = 1 + [\eta]\phi, \quad (7.1)$$

where μ is the suspension apparent viscosity, μ_0 the viscosity of the liquid resin, and ϕ the filler content. A linear fit to the data yields a value of $[\eta]=8.7$, significantly higher than the value for spheres of 2.5, which indicates that the nanoclay cluster sizes are quite irregular [33].

As the nanoclay concentration rises, additional dissipative effects are introduced during the flow yielding an increase in the apparent viscosity of the suspension. Suspensions with elevated filler contents are reported in the literature to exhibit non-Newtonian behavior and yield higher viscosities [32-35]. Several methods extending the Einstein description into the nonlinear, concentrated regime can be used to predict the relative viscosity of resin-filler blends. A popular choice is the semi-empirical Krieger and Dougherty model, used recently by different researchers for nanoclay fillers [32-34]:

$$\frac{\mu}{\mu_0} = \left(1 - \frac{\phi}{\phi_{\max}}\right)^{-[\eta]\phi_{\max}}, \quad (7.2)$$

where the relative viscosity, μ / μ_0 , diverges asymptotically as the maximum filler content ϕ_{\max} is approached. Rather than fitting the data simultaneously with a two parameter nonlinear procedure, the value of $[\eta]$ was taken as that obtained earlier, then a single-parameter nonlinear fit was performed to obtain ϕ_{\max} . The solid line in Fig. 7.2 represents the best fit to the data, which yields $\phi_{\max} = 65\%$.

The significant increase in apparent bulk viscosity shown in Fig. 7.2 will affect the injection pressure. Knowing that the injection pressure is directly proportional with the apparent viscosity [36], one might expect more than two fold increase in molding pressure for the resin containing 5 wt% nanoclay. This increase will be as high as 6- to 10-fold if in excess of 10 wt% clay is added. Such substantial increases in injection pressure may facilitate the formation of smaller voids throughout the composite. However, effective degassing of a highly viscous clay-polymer suspension poses a serious problem. In higher clay loadings, breaking down clay clusters, removing micro-air pockets, and achieving full dispersion might not be possible by mechanical mixing or sonication. Hence, addition of nanoclay above a critical level may adversely affect the final void content in a molded composite.

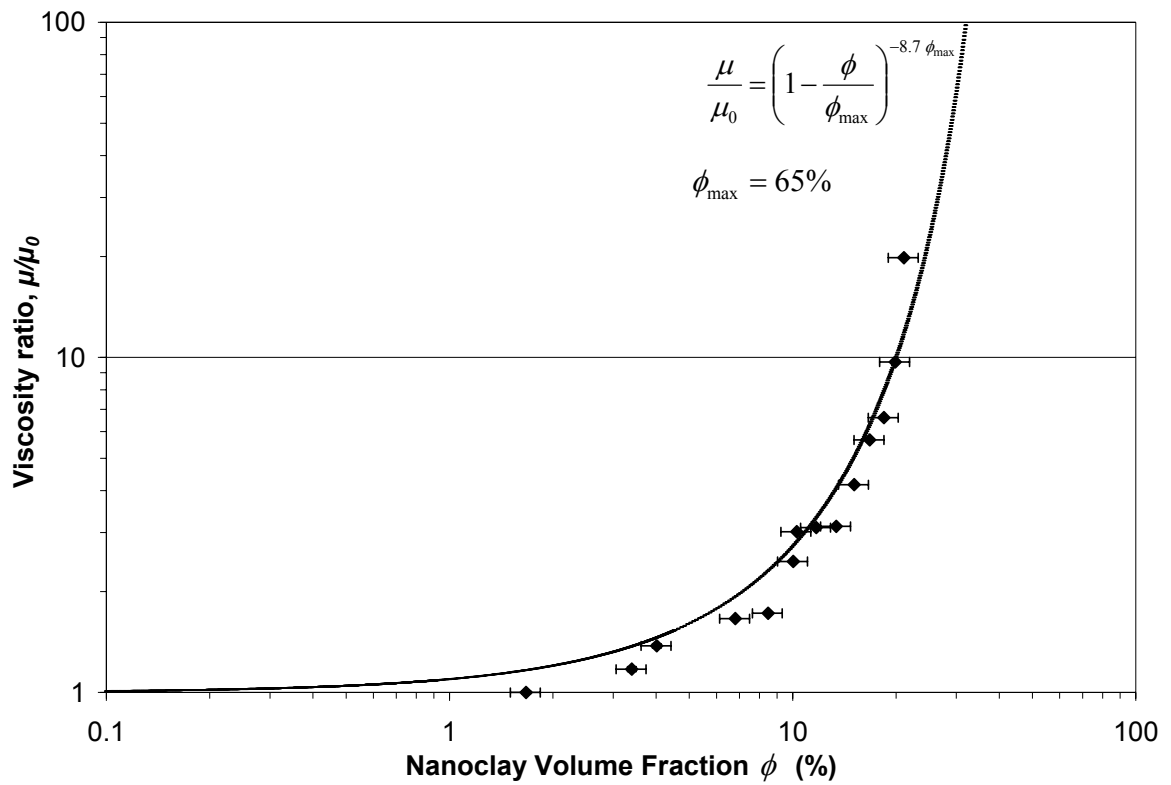


Figure 7.2: Effect of nanoclay volume fraction on the viscosity of the clay-epoxy mixture. Epoxy viscosity, $\mu_0 = 0.65$ Pa·s.

The apparent viscosity is not the only parameter affected by filler content, the surface tension, γ , of the clay-epoxy mixture and the contact angle, θ , between fiber and clay-epoxy mixture are affected as well [33-35]. Surface tension and contact angle will change the modified capillary number, $Ca^* = \mu V / \gamma \cos \theta$, during molding [17-22]. Furthermore, the change in Ca^* will dictate the dominant void morphology. For example, increase in the viscosity will increase Ca^* , thus fostering the presence of intra-tow voids inside fiber tows [17-19]. However, increases in surface tension and contact angle can counterbalance these effects and facilitate the formation of larger inter-tow voids.

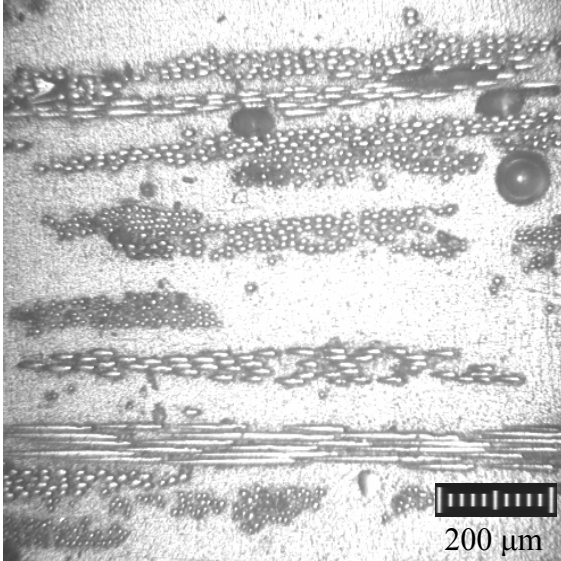
7.4.2 Effect of Nanoclay Content on Void Occurrence

Void occurrence of the composites loaded with different nanoclay contents are assessed by microscopic image analysis. Figure 7.3a depicts a microscopic image obtained at 50x magnification from the composite molded without nanoclay. In order to illustrate differences in nanoclay contents, scanning electron microscope (SEM) images obtained at 50x magnification from the 2%-, 5%-, and 10%-nanocomposites are shown in Figs. 7.3b, 7.3c, and 7.3d, respectively. Dispersed nanoclay clusters appear as light grey objects of various sizes in Figs. 7.3b, 7.3c, and 7.3d.

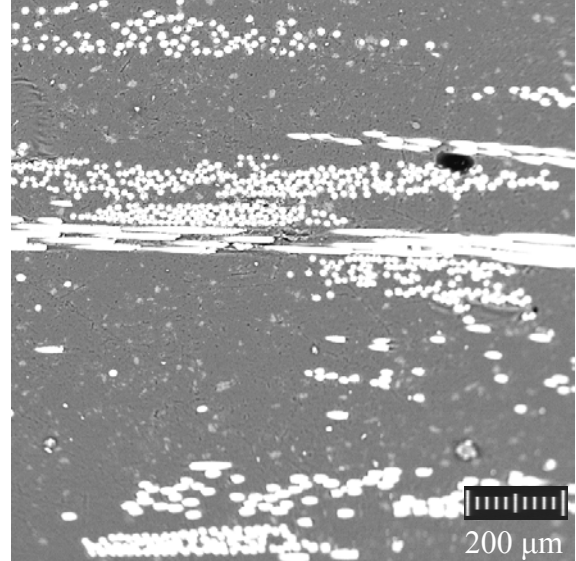
Resulting void contents and void areal densities of all molded composites are presented in Fig. 7.4. Void occurrence is observed to increase significantly with increasing nanoclay content. In the composite without nanoclay, 2.1% void content is obtained; whereas with 5 and 10 wt% nanoclay, void contents are increased to 5.1 and 8.3%,

respectively. However, void content is observed to decrease to 0.7% in the composite with 2 wt% nanoclay. This initial reduction in void occurrence suggests that the addition of 2 wt% nanoclay possibly shifts the modified capillary number to a more favorable range, thus helping reduce the void fraction. As discussed in the introduction, impregnation performed at a higher modified capillary number range is known to augment formation of intra-tow microvoids [17-22]. Reducing void formation in these cases can only be attained by lowering the modified capillary number, which implies a balance between the viscous flows outside fiber tows and the capillary flow inside fiber tows. If such a favorable balance is achieved, then the fluid front inside and between fiber tows progress at the same rate, thus minimizing entrapment of voids by the advancing fluid front. Above 2 wt% nanoclay however, void content increases significantly. In addition, void areal densities of 16.6 and 41.6 voids/mm² attained in the composites containing 5 and 10 wt% nanoclay, respectively, are sharp increases from the 5.2 voids/mm² registered in the composite molded without nanoclay. These steep increases in void occurrence might be a result of the initial bubble content or the formation of additional voids via mechanical entrapment. Detailed analysis of void morphology might help understand dominant void formation mechanisms for each nanoclay concentration.

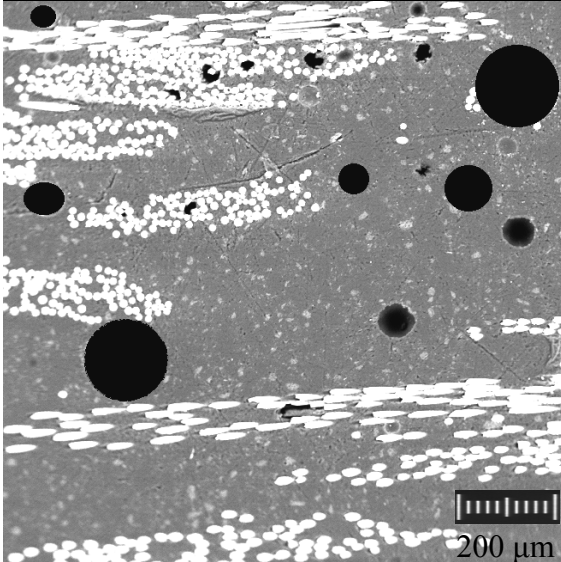
(3a) composite molded without nanoclay



(3b) 2%-nanocomposite



(3c) 5%-nanocomposite



(3d) 10%-nanocomposite

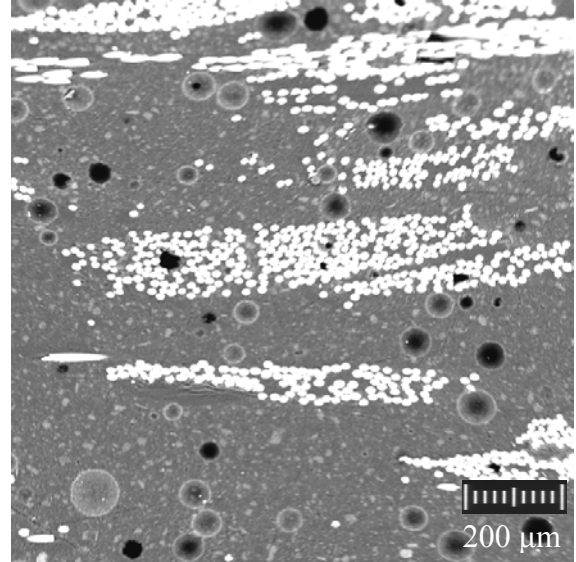


Figure 7.3: (a) A representative microscopic image obtained at 50x from the composite molded without nanoclay at 13.6% fiber content by volume; and representative SEM images obtained at 50x from nanocomposites with (b) 2, (c) 5, and (d) 10% nanoclay content by weight.

7.4.3 Effect of Nanoclay Content on Void Location

Proximity of voids to fiber tows can help understand their formation mechanisms as discussed in the introduction. Three different void locations are thus introduced in order to classify observed voids in the molded parts. First location is defined as areas primarily composed of reinforcing fibers. Voids in this region are intra-tow voids situated within fiber bundles and are referred to as preform voids. Second location is defined as areas rich in matrix without fibers. Voids encountered in this location are totally surrounded by the clay-epoxy blend and are referred to as matrix voids. The third location is defined as the transitional areas between the two other locations defined here. Voids situated in this location are referred to as transition voids and are always positioned adjacent to, but not within fiber bundles.

Figure 7.5 depicts contributions from voids encountered at different locations to the total voidage of the composites molded with different clay contents. Matrix voids are negligible in both the 0%- and the 2%-nanocomposite as they contribute with almost 0.1% to their respective void content. However, matrix voids are observed to increase significantly above 2 wt% clay content reaching 1.59% and 5.81% for the composites containing 5 and 10 wt% nanoclay, respectively. Similar trends are observed for void areal densities. This exponential increase in matrix voids occurrence at higher clay concentration can only be explained by elevated initial air bubble levels prior to injection since matrix voids are not likely to form by mechanical entrapment. Apparently, mechanical mixing followed by sonication and degassing were not effective in removing the micro-air pockets within clay clusters when the clay content exceeded 5 wt%. On the

other hand, sonication and 60 minutes of degassing led to almost void free resins containing 0 and 2 wt% clay content.

Preform voids, entirely formed by mechanical entrapment, show a different trend. The addition of clay seems to induce a large reduction in void content originating from preform voids. Preform void content is observed to drop from 0.83% in the composite without clay to 0.20, 0.30 and 0.34%, in the 2%-, 5%-, and 10%-nanocomposites, respectively. Simultaneously, preform void areal density slightly increases from 2.49 to 2.61, 5.34, and 5.12 voids/mm². These large drops (more than 60%) in preform void content after the addition of nanoclay to the resin, coupled with slight increases in void areal density indicate that preform voids became significantly smaller at higher clay concentrations. This reduction in the average size of preform voids is likely due to the increased molding pressure experienced during impregnation. One can also deduce that adding nanoclay to the resin helps reduce voids formed by mechanical entrapment due to a lower range of modified capillary number as discussed earlier.

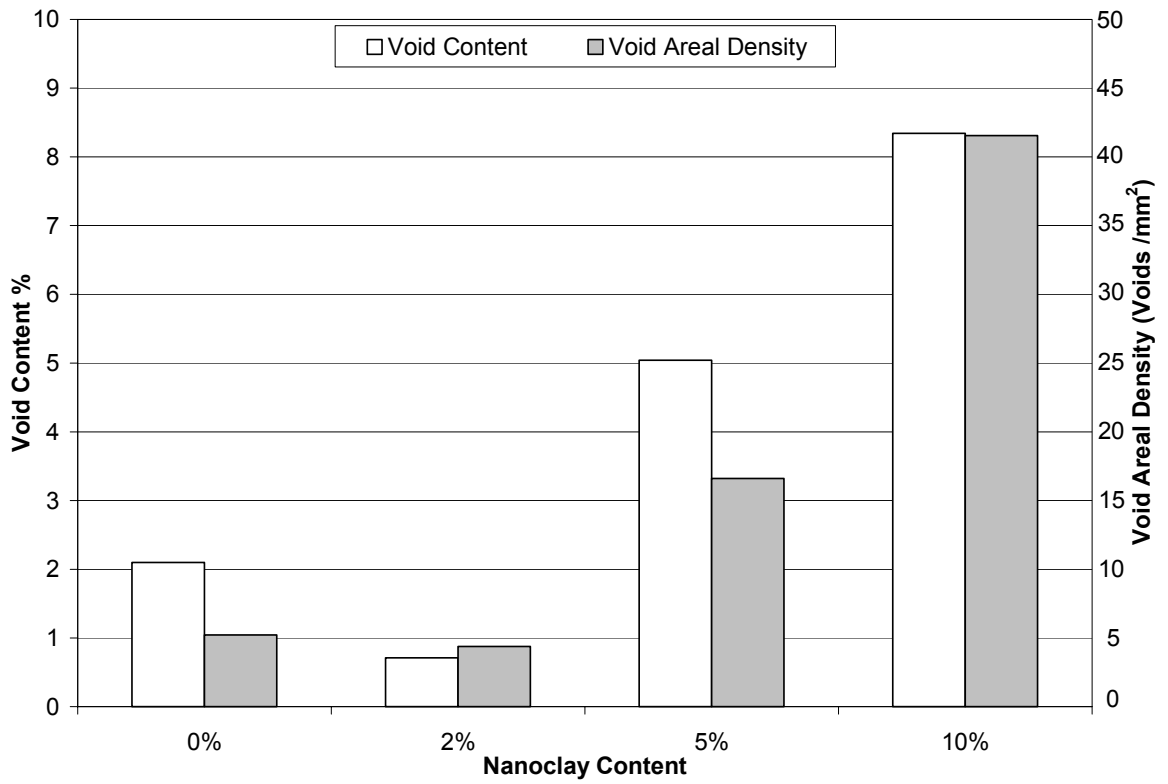


Figure 7.4: Void contents and void areal densities of composites with different clay contents molded with 13.6% volume fraction of E-glass fibers.

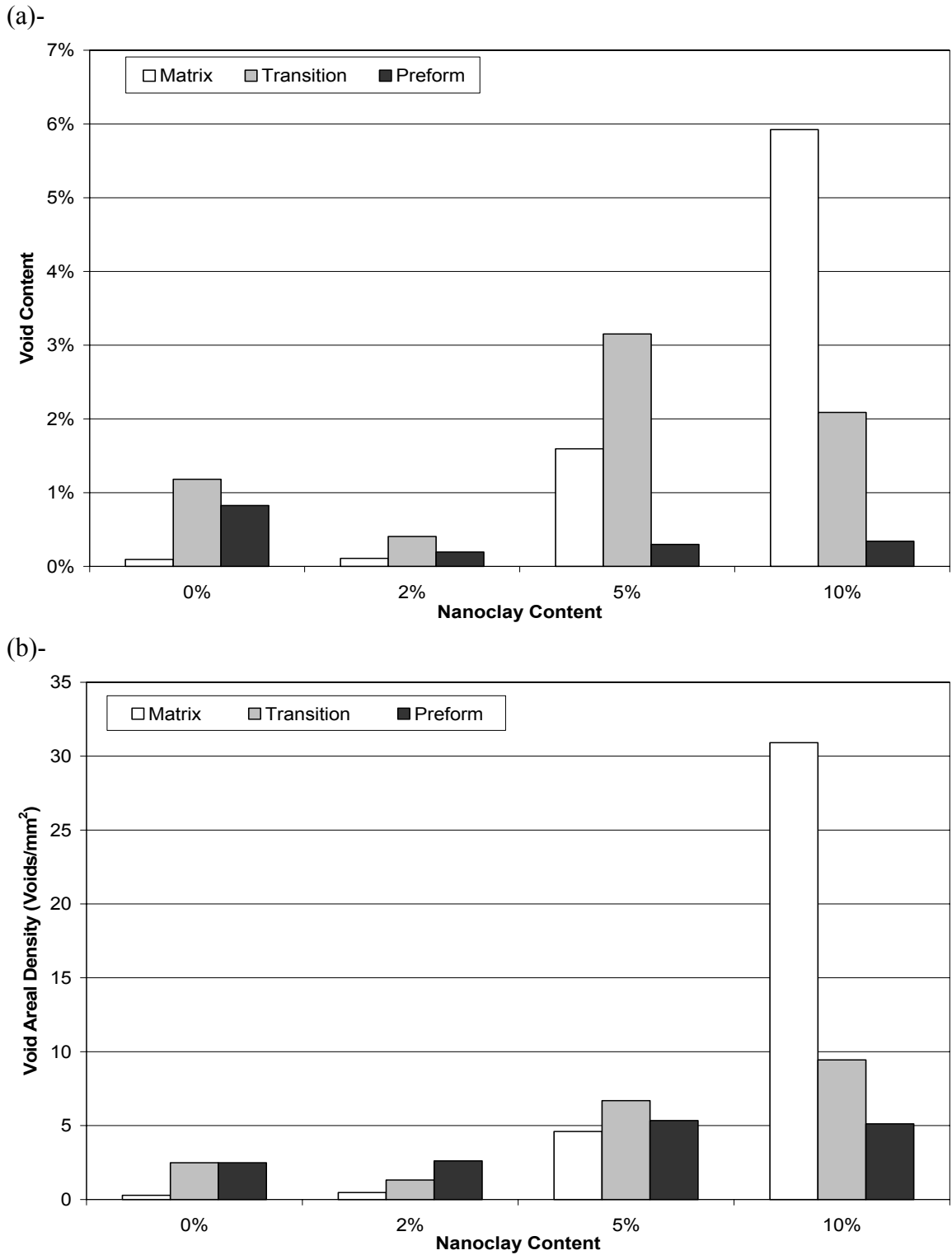


Figure 7.5: Contributions from voids encountered at different locations to overall voidage in nanocomposites with different clay contents: (a) void content, (b) void areal density.

7.4.4 Effect of Nanoclay Content on Void Size

In order to investigate void size distributions within the molded composites and verify the explanations elaborated above, an equivalent diameter, D_{eq} , is introduced using the measured void area, A :

$$D_{eq} = \sqrt{\frac{4A}{\pi}}. \quad (7.3)$$

The void size distributions for the different composites are presented in Fig. 7.6. The composite molded without nanoclay has an average void size of 60 μm with a standard deviation of 39 μm ; and the highest frequency of 17.70% is registered for voids with equivalent diameters between 30 and 40 μm . The composite with 2% nanoclay has a lower average void size of 39 μm with a standard deviation of 23 μm , and registered the highest frequency of 21.76% for voids with equivalent diameters between 20 and 30 μm . The 5%-nanocomposite, on the other hand, has an average void size of 50 μm with a standard deviation of 37 μm . The highest frequency of 18.24% is registered for voids with equivalent diameters between 20 and 30 μm . The 10%-nanocomposite has an average void size of 44 μm with a standard deviation of 21 μm . The highest frequency of 24.77% occurs for voids with equivalent diameters between 40 and 50 μm .

Voids are observed to be, in average, smaller after the addition of nanoclay at all concentration levels. This finding is expected since higher clay content would result in higher viscosity and thus a proportionally higher molding pressure. A higher molding pressure is in turn known to shrink formed voids, leading to smaller voids [20-22]. The

apparent viscosity of the impregnating resin increased by 17.37, 72.37, and 467.54% after the addition of 2, 5, and 10 wt% nanoclay, respectively, which would translate into the same increases in molding pressure. However, average size of voids formed in the 2%-nanocomposite are found to be considerably smaller than those formed in the 5%- and 10%-nanocomposites. To investigate this further, the size distributions of voids encountered at different locations need to be studied. Figure 7.7 depicts average sizes of voids encountered in different location of each composite, along with their standard deviations. First, note that preform voids are always smaller, in average, than transition and matrix voids. In addition, preform void size is observed to decrease with increasing clay content as described earlier. However, matrix and transition voids do not exhibit a similar steep reduction. For instance, the average void sizes calculated for voids from the matrix and transition locations of the 5%-nanocomposite are very similar to those calculated for the composite molded without nanoclay. Therefore, higher average void sizes observed in the 5%- and 10%-nanocomposites are attributed to much higher occurrences of matrix and transition voids, which are on average much larger than preform voids.

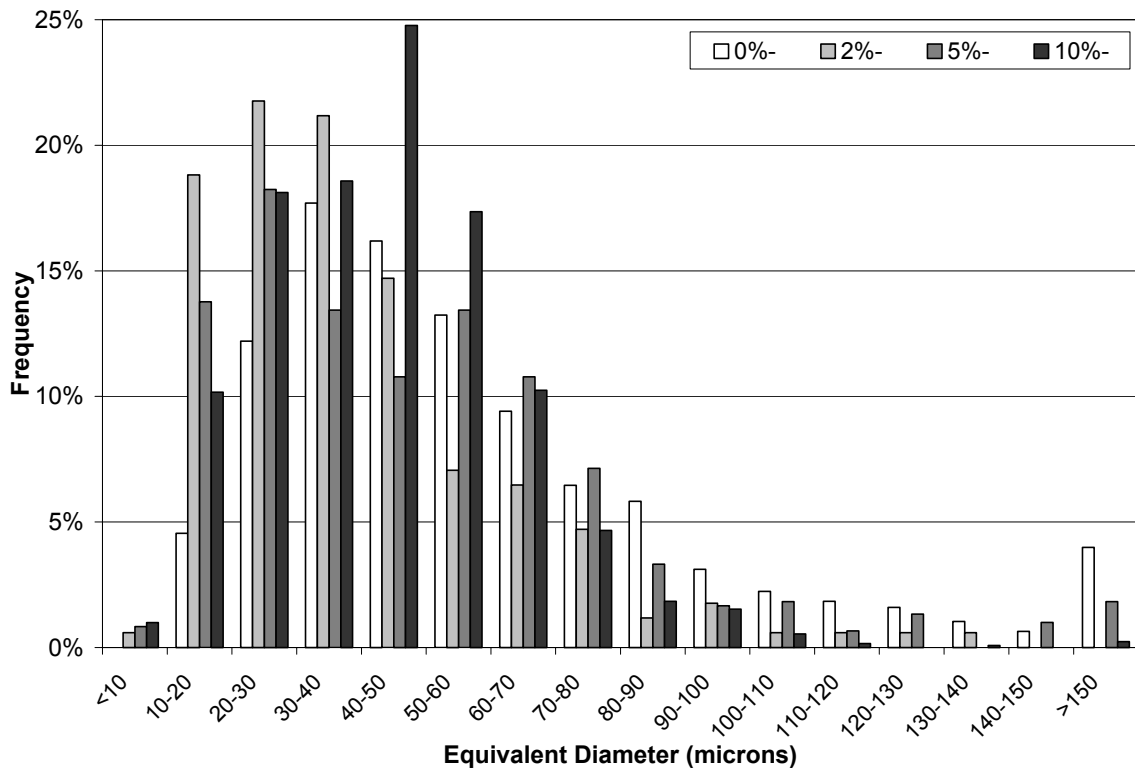


Figure 7.6: Void size distributions for the composites containing different nanoclay contents molded with 13.6% volume fraction of E-glass fibers.

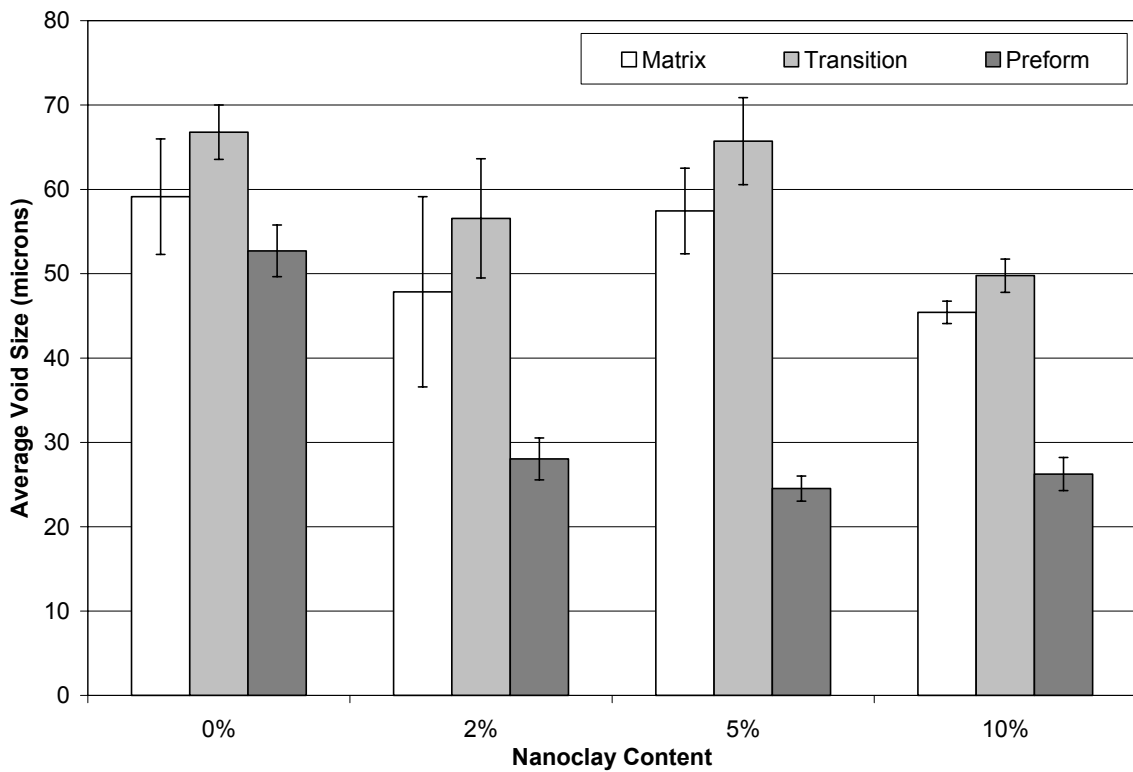


Figure 7.7: Effect of nanoclay content on average void sizes and on their respective standard deviation for voids encountered in different location of all nanocomposites molded with 13.6% volume fraction of E-glass fibers.

7.4.5 Effect of Nanoclay Content on Void Shape

Figure 7.8 shows representative microscopic images of different voids encountered within the molded composites obtained at 200x magnification. As seen in Fig. 7.8, different void shapes are observed within the studied composites. For example, Fig. 7.8a, obtained from the composite molded without nanoclay, depicts a mostly circular matrix void and an irregularly shaped preform void. Figure 7.8b, obtained from the 2%-nanocomposite, depicts a circular transition void and a medium elongated transition void. Void shapes are quantitatively analyzed by categorizing them into two groups: irregular and spherical voids. Irregular voids are defined as those within which there exist two different points that can be connected in a straight line that intersects the void boundary. The remaining voids are mostly spherical, although most of them do not present a perfect circular symmetry. To classify this variation in roundness, a shape ratio, R_s , is introduced for each void as the equivalent diameter obtained from Eq. 3 divided by the maximum measured length, L_{max} , within a void:

$$R_s = \frac{D_{eq}}{L_{max}}. \quad (7.4)$$

Note that $R_s = 1$ represents ideal circles, and as the shape ratio decreases, voids become more elongated. Using this shape ratio, spherical voids are further divided into two categories: circular voids with shape ratios above 0.95 ($0.95 < R_s \leq 1$), and elliptical voids with shape ratios lower than 0.95. For instance, the elongated transition void in Fig. 7.8b and the top large elongated transition void in Fig. 7.8c both present an $R_s = 0.76$, while the smaller elongated void shown in Fig. 7.8c has an $R_s = 0.91$.

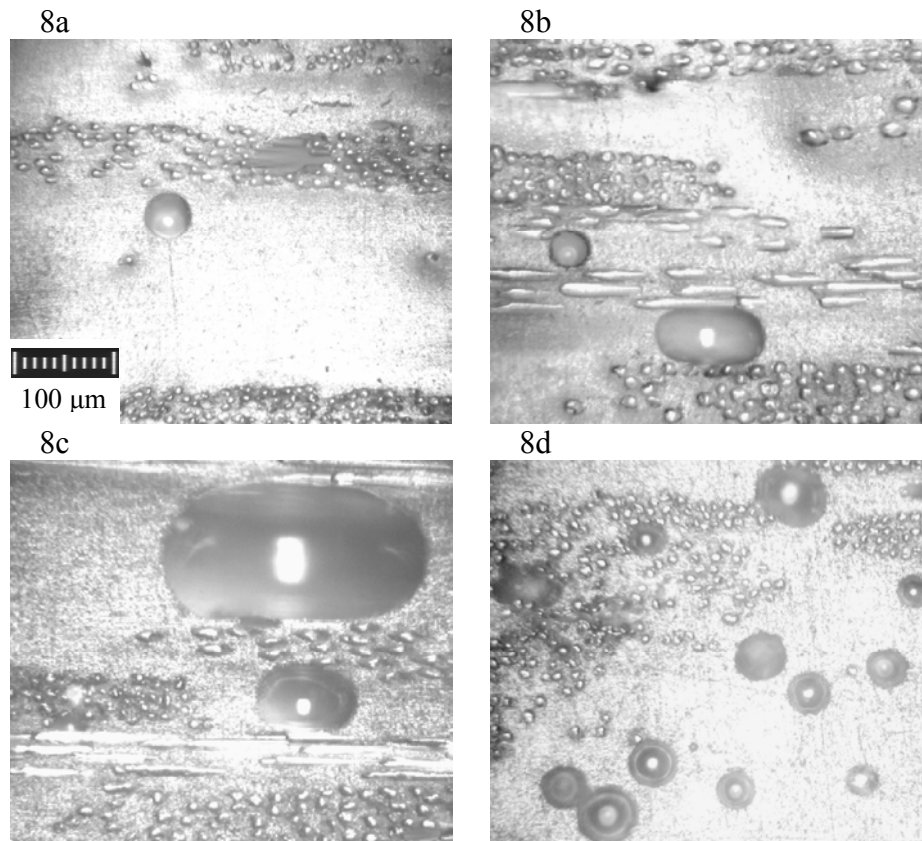


Figure 7.8: Representative images obtained at 200x magnification of different voids encountered within the composite molded with 13.6% volume fraction of E-glass fibers and containing: (a): 0%; (b): 2%; (c): 5%, and (d): 10% nanoclay by weight.

Using the shape classification defined above, contributions to void content from voids with different shapes are calculated. The resulting shape distributions of voids encountered within the studied composites are presented in Fig. 7.9. Circular and elliptical void content are observed to increase considerably with increasing nanoclay content; conversely, irregular void content is observed to decrease.

For the composite molded without nanoclay, circular and elliptical voids contribute respectively 0.48 and 0.45% to the total void content. Circular voids increase dramatically reaching 2.56% in the 5%-nanocomposite and 5.90% in the 10%-nanocomposite, while elliptical void content increases only to 2.21 and 2.16%. Further analysis of void data indicates that in the 5%-nanocomposite, more than 95% of circular voids are encountered within the matrix or transition locations (45.74% and 49.61% respectively). Similarly, more than 75% elliptical voids in the 5%-nanocomposite are concentrated in the matrix or transition regions. Even a higher percentage of circular and elliptical voids found within the 10 wt%-nanocomposite are categorized as matrix or transition voids. More than 98% of circular voids and 92% of elliptical voids are encountered within the matrix or transition locations. Since the vast majority of circular and elliptical voids in both 5%- and 10%-nanocomposites are located in matrix or transition regions, one can conclude that the voidage increases experienced by voids with both circular and elliptical voids shown in Fig. 7.9 originate from the micro-air pockets embedded in larger nanoclay clusters, which are transported by the clay epoxy mixture during impregnation.

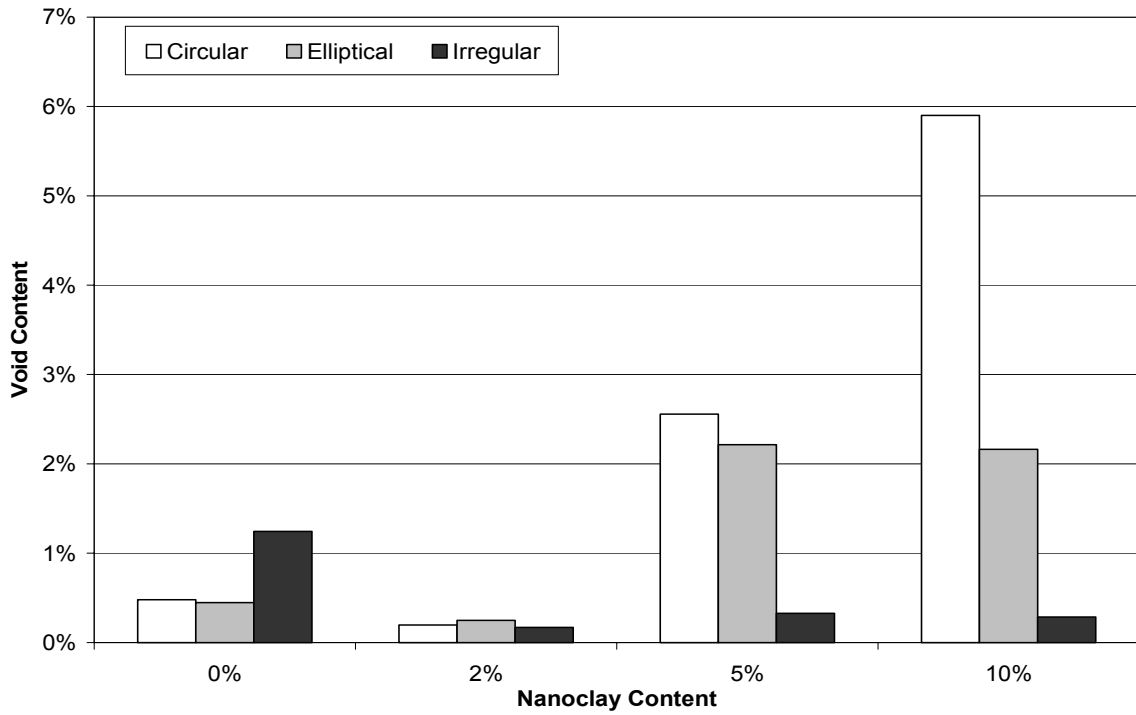


Figure 7.9: Contributions to void content from voids with different shapes as a function of nanoclay content.

On the other hand, irregular voids contribute with 1.24% to the total void content of the composite molded without nanoclay, i.e. more than 50% of the total void content. After the addition of 2, 5, and 10 wt% nanoclay, the contribution of irregular voids to the total void content drops significantly to 0.17, 0.33 and 0.29%, respectively. These observed drops can be attributed to the changes induced in preform voids since most preform voids are confined to the narrow spacing between single fibers and thus present irregular geometries. As observed earlier in Fig. 7.5, preform voids become much smaller after the addition of nanoclay, thus representing a smaller percentage of the total voids. Most likely, the increase in molding pressure at higher clay levels also contributes to the formation of more circular voids as the void deformation induced by flow is counterbalanced by pressure.

7.4.6 Effect of Nanoclay Content on Radial Voidage Variation

Radial variation of voidage in the molded composites is examined in order to assess the effect of nanoclay content on spatial void arrangements. Each composite sample is divided into five 15 mm-long radial regions as shown in Fig. 7.2, and void content in each region is calculated. Figure 7.10 depicts radial variations of void content in the molded composites. Void contents in the composites containing nanoclay do not seem to show clear radial trends. However, radial void contents of the composite molded without nanoclay appear to follow predictions of the capillary analysis [17-22,37-38]. Because the mold filling is performed at a constant injection rate, the fluid front velocity decreases with increasing distance from injection gate. For the range of modified capillary number, Ca^* , of the composite molded without nanoclay, the viscous flow leads the capillary flow

[21-22]. Thus, slower fluid front velocity is expected to trap fewer and smaller voids inside fiber bundles towards the outer edges of the disk [37-38]. This latter fact might explain the sharp decrease of void content from 3.96 to 1.26% between the first and third radial regions of the composite molded without nanoclay. Matrix and transition voids formed during mold filling are relatively free to move and might be transported to the last two radial regions by the flow yielding slightly higher void contents of 1.55 and 1.70% in the fourth and fifth regions, respectively. The 2%-nanocomposite, on the other hand, exhibits lower void contents limited between a minimum of 0.51% at the third radial region and a maximum of 0.88% in the fourth. These comparable low void occurrences are consistent with an equilibrium between the viscous and capillary flows during mold filling as suggested earlier. Finally, no clear radial trend in void content could be detected for the 5%- and 10%-nanocomposites since the air bubbles embedded in clay clusters dominate the void morphology, as well as size and location distributions.

In order to investigate the radial variation of voids formed during the impregnation process, only those voids formed by mechanical entrapment by the fluid front are utilized. Hence, the effect of pre-existing voids embedded in or trapped by the larger clay clusters is eliminated. This is achieved by considering the radial variation of only preform voids as presented in Fig 7.11. Preform void content for the composite molded without nanoclay is observed to decrease gradually from 2.09% in the first region to 0.35% in the fifth as predicted by the capillary number analysis. For the 2%-nanocomposite, preform void content is also observed to decrease from 0.30 to 0.16% between the first and fifth regions. The much lower void occurrences corroborate that a certain equilibrium is reached between viscous and capillary forces as suggested earlier.

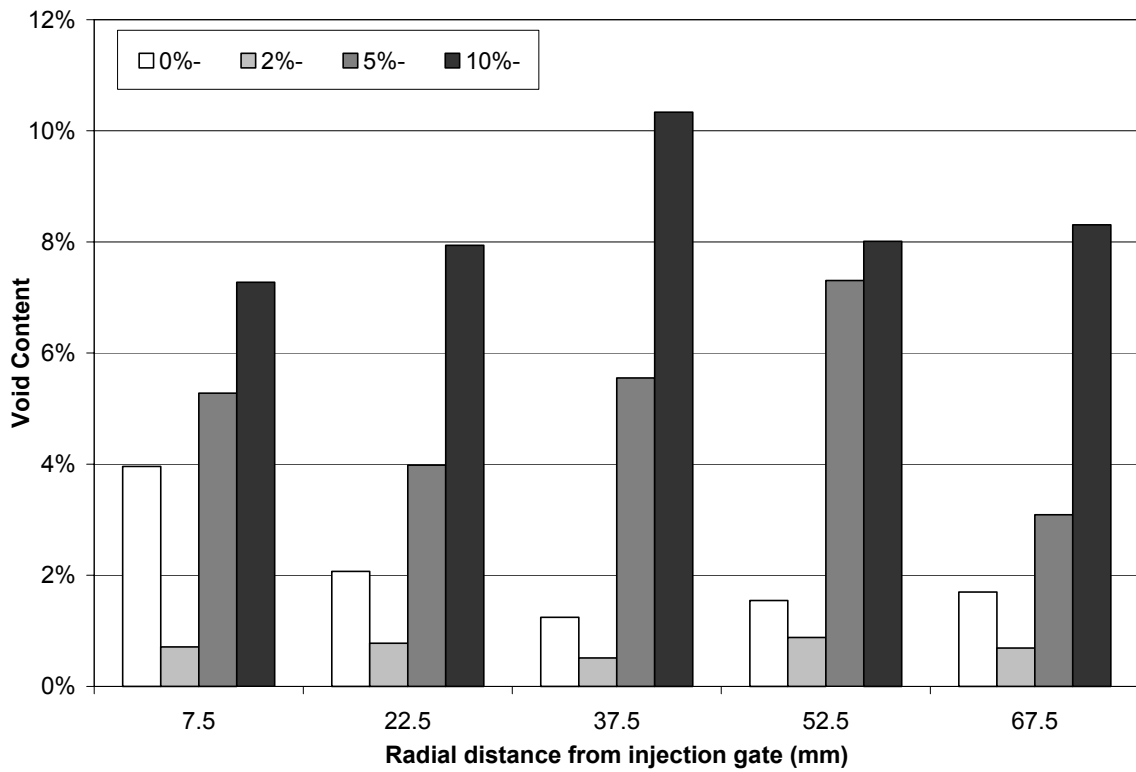


Figure 7.10: Radial variation of void content in the composites molded with 13.6% volume fraction of E-glass fibers and containing 0, 2, 5, and 10% nanoclay.

According to the capillary number analysis, void content of voids formed by mechanical entrapment (i.e. preform voids) is expected to decrease with decreasing fluid front velocity, i.e. away from the inlet [21-22,37-38]. Yet, radial variations of the preform void content obtained from both 5%- and 10%-nanocomposites show a slight increase with increasing radial distance. Preform voids gradually increase from 0.24 to 0.38% along the five radial regions of the 5%-nanocomposite, while a similar 45% increase from 0.27 to 0.39% is observed for the 10%-nanocomposite. Again, the low occurrence of preform voids implies the existence of an equilibrium between viscous and capillary flows. However, the radial increases can be a result of changes in the bulk properties of the impregnating fluid such as the apparent viscosity, contact angle, and surface tension yielding higher voids entrapment inside the preform. Breakdown of nanoclay cluster in the radial direction has been reported for similar composite disks [39], which would contribute to the variation of bulk fluid properties during mold filling. Clay filtration is also probable, especially for 5 and 10 wt% nanoclay content, yielding lower concentrations of clay in the impregnating fluid towards the outer edge of the molded disks. Thus, nonuniform values of apparent viscosity, surface tension, and contact angle are expected at the fluid front during mold filling. These changes in bulk fluid properties and the radially decreasing fluid front velocity slightly augment mechanical entrapment of voids at higher clay concentrations as shown in Fig. 7.11.

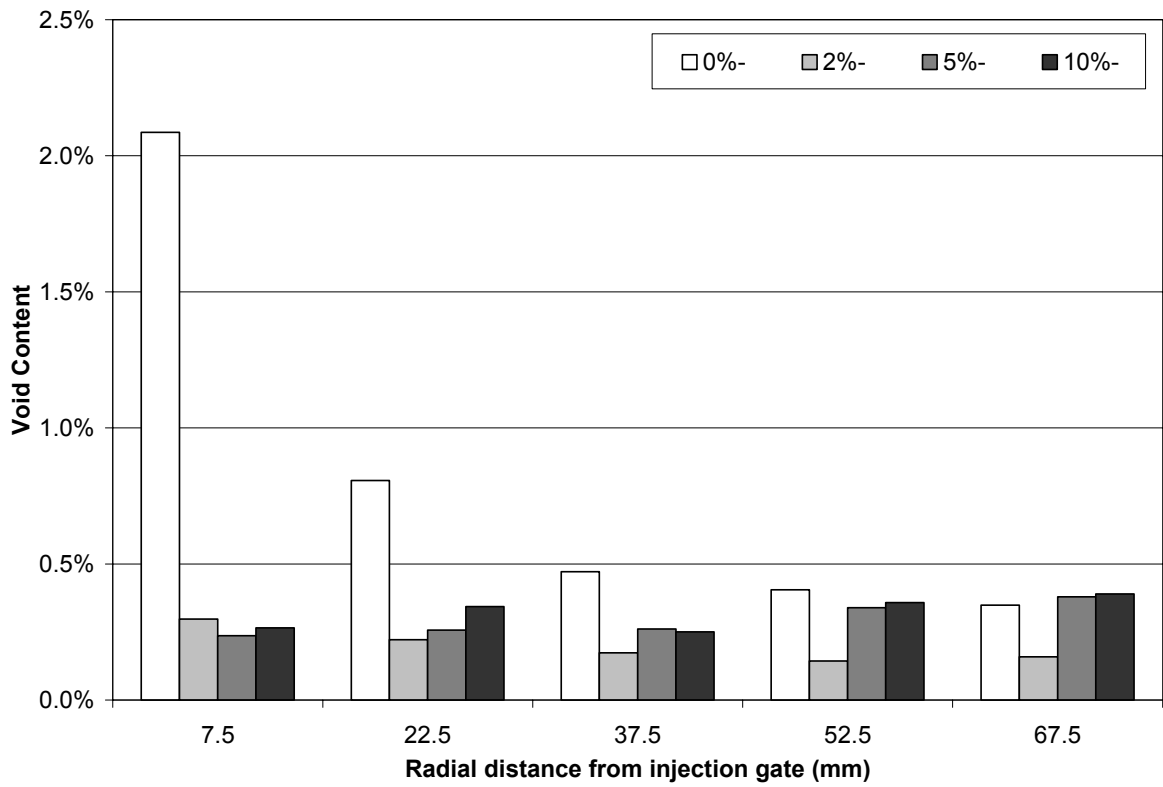


Figure 7.11: Radial variation of preform void content in the composites molded with 13.6% volume fraction of E-glass fibers and containing 0, 2, 5, and 10% nanoclay.

7.5 *Conclusions*

Effect of adding nanoclay on the formation, morphology, and spatial distribution of voids in resin transfer molded nanoclay/E-glass/epoxy composite disks are presented. Mixing of Cloisite[®] 25A nanoclay with the low viscosity EPON 815C resin leads to a significant increase in the resin viscosity, and thus in the injection pressure. Almost six-fold increase in the injection pressure is estimated for the resin containing 10 wt% nanoclay. Overall void content is observed to increase from 2.1% in the composite disk molded without nanoclay to 5.1 and 8.3% in the composites containing 5 and 10 wt% nanoclay, respectively. The addition of 2 wt% nanoclay yields the lowest void content at 0.7%. The increased void content in composites molded with 5 and 10 wt% clay is due to the pre-existence of air pockets embedded in clay clusters, which could not be removed by mechanical mixing, sonication, or degassing. These air pockets usually appear as 40- to 60- μm , circular voids surrounded by the epoxy resin, thus forming bulk of so-called matrix voids. Voids are observed to be smaller on average after the addition of nanoclay at all concentrations. Presence of nanoclay in the resin induced at least 60% reduction in voids located within the fiber preform. Irregularly shaped voids are also observed to decrease with increasing nanoclay content. Along the radial direction of the molded disks, an increase in preform voids, which are formed by mechanical entrapment, is observed at higher nanoclay levels.

7.6 References

1. Typical Physical Properties Bulletin, Southern Clay Products, Inc. 2004.
2. Usuki, A., Kawasumi, M., Kojima, Y., Okada, A., Kurauchi, T., and Kamigaito, O., *Journal of Material Research*, **8**, 1174, 1993.
3. Usuki A., Kojima Y., Kawasumi M, Okada A., Fukushima Y., Kurauchi T., and Kamigaito O., *Journal of Material Research*, **8**, 1179, 1993.
4. Kojima Y., Usuki A., Kawasumi M, Okada A., Kurauchi T., and Kamigaito O., *Journal of Polymer Science, Part A: Polymer Chemistry*, **31**, 2493, 1993.
5. Kojima, Y., Usuki, A., Kawasumi, M., Okada, A., Kurauchi, T., and Kamigaito, O., *Journal of Polymer Science, Part A: Polymer Chemistry*, **31**, 1755, 1993.
6. Kojima Y., Fukumori K., Usuki A., Okada A., Kurauchi, T., *Journal of Materials Science Letters*, **12**, 889,1993.
7. Kojima Y., Usuki A., Kawasumi M, Okada A., Fukushima Y., Kurauchi T., and Kamigaito O., *Journal of Material Research*, **8**, 1185, 1993.
8. Isik I., Yilmazer U., and Bayram G., *Polymer*, **44**, 6371, 2003.
9. Alexandre M., and Dubois P., *Materials Science and Engineering*, **28**, 1, 2000.
10. Advani S. G. and Shonaike G. O., *Advanced Polymeric Materials: Structure Property Relationships*, CRC Press, 349, 2003.
11. Shah A. P., Gupta R. K., Gangarao H. V. S., and Powell C. E., *Polymer Engineering and Science*, **42**, 1852, 2002.
12. Kinloch A. J., and Taylor A.C., *Journal of Materials Science Letters.*, **22**, 1439, 2003.
13. Akkapeddi M. K., *Polymer Composites*, **21**, 576, 2000.

14. Haque A., Shamsuzzoha M., Hussain F., and Dean, D., *Journal of Composite Materials*, **37**, 1821, 2003.
15. Hussain F. and Dean, D., *International SAMPE Technical Conference (M&P-Ideas to Reality)*, **34**, 692, 2002.
16. Becker O., Vareley R. J., and Simon G. P., *Journal of Materials Science Letters*, **22**, 1411, 2003.
17. Patel N., and Lee L. J., *Polymer Composites*, **16**, 386, 1995.
18. Mahale A. D., Prud'Homme R. K., and Rebenfeld L., *Polymer Engineering and Science*, **32**, 319, 1992.
19. Patel N., Rohatgi V., and Lee J. L., *Polymer Engineering and Science*, **35**, 837, 1995.
20. Rohatgi V., Patel N., and Lee J. L., *Polymer Composites*, **17**, 161, 1996.
21. Barraza H. J., Hamidi Y. K., Aktas L., O'Rear E. A., and Altan M. C., *Journal of Composite Materials*, **38**, 195, 2003.
22. Hamidi Y. K., Aktas L., and Altan M. C., *Journal of Engineering Materials and Technology*, 126, 420, 2004.
23. Olivero K. A., Barraza H. J., O'Rear E. A., Altan M. C., *Journal of Composite Materials*, **36**, 2011, 2002.
24. Stabler W. R., Tatterson G. B., Sadler R. L., and El-Shiekh A. H. M., *SAMPE Quarterly*, **23**, 38, 1992.
25. Ghiorse S. R., *SAMPE Quarterly*, **23**, pp. 54, 1993.
26. Goodwin A. A., Howe C. A., and Paton R. J., *Proc. ICCM-II, Australian Composite Structures Society*, **IV**, 11, 1997.

27. Harper B. D., Staab G. H., and Chen R. S., *Journal of Composite Materials*, **21**, 280, 1987.
28. Hoppel C., Bogetti T., and Newill J. F., *Proc. the American Society for Composites*, 1094, 2000.
29. Chisholm N., Mahfuz H., Rangari V. K., Ashfaq A., and Jeelani S., *Composite Structures*, **67**, 115, 2005.
30. Ghiorse S. R., U.S. Army Materials Technology Laboratory, Report MTL-TR 91-13, 1991.
31. Santulli C., Garcia Gil R., Long A. C., and Clifford M. J., *Science and Engineering of Composite Materials*, **10**, 77, 2002.
32. Wang H., Elkovitch M., Lee L. J., and Koelling K. W., *Proc. 58th Annual Technical Conference - Society of Plastics Engineers*, **2**, 2402, 2000.
33. Kugge C. and Daicic J., *Journal of Colloid and Interface Science*, **271**, 241, 2004.
34. Kislenko V. N and Verlinskaya R. M., *Journal of Colloid and Interface Science*, **244**, 405, 2001.
35. Khil M. S., Kim H. Y., Kim M. S., Park S. Y., and Lee D.-R., *Polymer*, **45**, 295, 2004.
36. Olivero K. A., Hamidi Y. K., Aktas L., and Altan M. C., *Journal of Composite Materials*, **38**, 937, 2003.
37. Hamidi Y. K., and Altan M. C., *Journal of Materials Science Letters*, **22**, 1813, 2003.
38. Hamidi Y. K., Aktas L., and Altan M. C., *Composite Science and Technology*, in review, 2004.

39. Aktas L., Hamidi Y. K., and Altan M. C., *Journal of Engineering Materials and Technology*, in review, 2004.

8 Conclusions and Recommendations

RTM is a successful process in manufacturing near-net-shape, geometrically complex composite parts. However, RTM composites usually suffer from the formation of flow-induced defects such as voids and dry regions. Voids are formed during mold filling step of RTM and similar LCM processes because of two simultaneous competing flows. One is the flow through the larger gaps between fiber tows, and the second in the capillary penetration of the resin inside fiber tows. For these LCM processes to reach full potential, better and faster molding cycles must be developed and the quality of molded composites must be improved. In this study, a systematic analysis has been performed on void formation and removal in such composites. In addition, in light of the reported performance enhancements in polymers modified with clay silicates, nanoclay effects on void formation are investigated. It is hoped that this study would provide useful guidelines for the development of the optimal molding process. Results obtained in this study are believed to be general in nature and are applicable to the other LCM processes with similar flow kinematics. Major conclusions that can be drawn from this study are presented henceforth.

- **Analysis of flow-induced voids through modified capillary number:**

The formation of flow-induced voids in RTM composites was studied for different injection rates through the modified capillary number analysis. Void contents presented in chapter 3 agree well with results given in other studies for the same values of modified capillary number. In addition, more than 93% of the voids formed in the composite studied in chapter 4 are observed within the preform or next to a fibrous region, corroborating expected results from the modified capillary number analysis. Therefore,

modified capillary number analysis reveals to be a powerful tool in predicting void formation by mechanical entrapment.

- **Establishing packing as an effective void reduction technique for molded composites:**

Packing, i.e. applying a post-fill pressure, helped significantly reduce void contents. For instance, overall void content dropped more than 92% with the application of a post-fill pressure as low as 570 kPa. In addition, packing helped reduce average void size from 59.3 μm in the unpacked composite to 31.7 μm in the packed composite. Irregular void occurrence was also reduced considerably after applying the 570 kPa post-fill pressure. Thus, packing not only reduces the overall void content, but also reduces considerably the occurrence of large irregular voids, potential inducers of early crack growth. In addition, applying higher packing pressures resulted in lower void occurrence as presented in chapter 3, although an optimum post-fill pressure should exist before drastic measures would be needed to ensure mold sealing. These results establish packing as an effective method for void reduction in molded composites.

- **Complexity of spatial void distribution:**

During mold filling, void formation and transport mechanisms often interact resulting in complex void spatial distributions. Along the flow direction of the studied composites, combined effects of void formation by mechanical entrapment and void mobility are shown to yield a complex radial void distribution. It is shown that fewer voids are trapped mechanically with increasing distance from the inlet and most of the medium and small voids that are mobile migrate towards the exit during resin injection. In addition, Variation up to 17% of the average void content of 2.15% is observed through-the-

thicknesses of the studied RTM composite. These results underline the importance of considering both void formation and transport mechanisms in predicting void spatial arrangement within molded composites.

- **Importance of void three-dimensionality:**

Voids are often considered two-dimensional since most void measurement techniques that allow assessment of void size, shape, and spatial distribution only use specimen surfaces. However, this simplification is found to critically affect our perception of void actual morphology distributions. Features of void three-dimensionality were assessed by considering both through-the-thickness and planar adjacent surfaces of studied composites. Analyzing void distributions from both views allowed a better understanding of void actual morphology and arrangements. For instance, relatively large cylindrical voids were observed in cigar shapes in the planar surfaces, whereas these voids only appear as small irregular or elliptical voids on through-the-thickness surfaces. These findings underscore the importance of developing adequate methods for considering void three-dimensionality, especially when correlating void occurrence with the composite performance.

- **Addition of nanoclay up to 10 wt% is found to result in the formation of fewer voids by mechanical entrapment:**

Addition of nanoclay to the impregnating liquid significantly increases its viscosity, yielding higher molding pressures, which in turn results in the formation of smaller voids, and facilitates void shrinkage and transport. Nanoclay addition is also believed to lower the range of modified capillary number values experienced during molding, thus leading to the formation of fewer voids by mechanical entrapment. However, the overall void

content increased at higher clay concentrations due to preexisting air bubbles in the clay-epoxy mixture that can be eliminated by developing better mixing techniques. Thus, nanoclay addition is believed to help reduce void formation by mechanical entrapment in molded composites, in addition to its potential performance enhancement reported in the literature.

Understanding the effects of different parameters on void formation in RTM and LCM composites can help develop powerful predicting tools, and ultimately help develop the optimal molding process. In order to accomplish this latter goal, the following studies, among others, are recommended for future work:

- Investigate the effect of other parameters such as fiber content and preform architecture on void formation and morphology in RTM composites.
- Study the effect of exit vents placement on void morphology within the same molded composite.
- Characterize actual three-dimensional void morphology distribution in RTM composites.
- Correlate void morphology distribution to composite properties such as stiffness, moisture absorption, and others through finite element analysis.
- Compare packing to other popular void reduction techniques such as bleeding.
- Investigate nanoclay filtration along the flow direction in RTM clay/fiber/epoxy composites and its effect on void morphology distribution.